ISSN 2712-8172

MAGAZINE OF CIVIL ENGINEERING

Magazine of Civil Engineering

ISSN 2712-8172

Online peer-reviewed open-access scientific journal in the field of Civil and Construction Engineering

Founder and Publisher: Peter the Great St. Petersburg Polytechnic University

This journal is registered by the Federal Service for Supervision of Communications, Information Technology, and Mass Media (ROSKOMNADZOR) in 2020. Certificate El No. FS77-77906 issued February 19, 2020.

Periodicity: 8 issues per year

Publication in the journal is open and free for all authors and readers.

Indexing: Scopus, Web of Sceince (ESCI, RSCI), DOAJ, Compendex, Google Academia, Index Copernicus, ProQuest, Ulrich's Serials Analysis System, CNKI

Corresponding address: 29 Polytechnicheskaya st., Saint Petersburg, 195251, Russia

Chief science editor:
D.Sc., Galina L. Kozinetc

Deputy chief science editors:
D.Sc., Sergey V. Korniyenko

Executive editor: Ekaterina A. Linnik

Translator, editor: Irina Ye. Lebedeva

Proofreader: Philipp Chrysanthes S. Bastian

DT publishing specialist:
Anastasiya A. Kononova

Contacts:
E-mail: mce@spbstu.ru
Web: http://www.engstroy.spbstu.ru

Date of issue: 10.111111.2025

Contents

Magazine of Civil Engineering

ISSN 2712-8172

journal homepage: http://engstroy.spbstu.ru/

Research article

UDC 69

DOI: 10.34910/MCE.139.1

Mechanical properties of concrete made with waste fine and coarse ceramic aggregates

A.A. Alkraidi[1], ***M.R. Aldikheeli***[1], ***Q.A. Alatiya***[2], ***L.A. Alasadi***[1]✉, ***R.A. Aljazaari***[2], ***T.M. Almusawi***[1]
Department of Structures and Water Resources Engineering, Faculty of Engineering, University of Kufa, Najaf, Iraq

[2]*Department of Civil Engineering, Faculty of Engineering, University of Kufa, Najaf, Iraq*

✉*laitha.alasadi@uokufa.edu.iq*

Keywords: waste aggregate, waste fine, coarse ceramic, compressive, tensile, flexural strength, modulus of elasticity

Abstract. This study aims to produce a new type of waste aggregate concrete by using fine and coarse waste ceramic as aggregate; the waste ceramic used in this study was in 2 types: red ceramic, which has a red colour and is produced from waste ceramic tiles, and white ceramic, which produced from the waste of tableware. Replacing ordinary fine and coarse aggregate with a ceramic waste aggregate improved the mechanical properties of concrete, compressive, tensile, flexural strength, and modulus of elasticity of normal concrete by using waste ceramic as aggregates. 20, 40,60, 80, and 100 % replacement by weight of aggregates are studied. Total replacement of normal aggregate with white ceramic aggregates led to an increase in compressive strength from 42.2 to 52.1 MPa; tensile strength also increased from 2.9 to 4.8 MPa, flexural strength increased from 4.3 to 8.7 MPa, and static modulus of elasticity has risen from 25.6 to 32.8 GPa. The mechanical properties of red ceramic increased until 60 % replacement; a slight decrement in mechanical properties was found after 60 % replacement. Studies show that waste white ceramic has better mechanical properties than red clay ceramic.

Citation: Alkraidi, A.A., Aljazaari, R.A., Aldikheeli, M.R., Alasadi, L.A., Almusawi, T.M., Alatiya, Q.A. Mechanical properties of concrete made with waste fine and coarse ceramic aggregates. Magazine of Civil Engineering. 2025. 18(7). Article no. 13901. DOI: 10.34910/MCE.139.1

1. Introduction

Waste materials have been widely used in recent years, such as plastics, waste iron filing, and chips, waste copper, waste glass, waste bricks, waste tiles, waste old concrete, etc. The benefit of using waste materials in concrete is to have lower costs of concrete production to obtain a cleaner environment and less environmental pollution, as well as some increment in mechanical properties, such as compressive, tensile, and flexural strength of concrete. Some waste materials also reduce the density of concrete, which is very useful for decreasing dead loads on foundations and achieving low cost in building construction, such as using bricks as coarse aggregate [1, 2]. Waste plastics are also used as fibers in concrete and can improve concrete's tensile and flexural strength [3, 4]. Recycled plastics can reduce concrete density to 1800 kg per cubic meter [5], which gives valuable benefits in construction, such as lowering deadloads of buildings and more economic structures. Waste ceramic can improve some mechanical properties of concrete, such as compressive strength; Murali Dharan & Mohan [6] studied ceramic waste as aggregate in concrete with different cement content and improved compressive strength; with 350 kg cement content, the compressive strength increased from 24 to 31 MPa. Singh & Srivastava [7] use waste ceramics as fine and coarse aggregates in concrete and states that replacing normal aggregates with waste ceramic

aggregate leads to decreased compressive strength, tensile strength, and flexural strength. Ramadevi [8] study the Effect of using waste ceramic as fine aggregate in concrete and found that using ceramic increases concrete compressive and tensile strength until 75 % replacement. Waste rubber is also used in some research to achieve new concretes with specified properties and benefit nature because burning such waste can cause several problems to the heart or harmful gasses. This study aims to use a waste ceramic with two types (red and white ceramic) as fine and coarse aggregate in concrete and study the Effect of replacement on the mechanical properties of concrete.

2. Methods

2.1. Materials Used in The Study

Ordinary Portland cement was used in this study for all mixes; average coarse aggregate was used in the study with grading shown in Table 1 and confirming Indian standards specifications of aggregates IS-383 [9, 10] with maximum size aggregate equal to 16 mm. Ordinary yellow sand is used in reference and partially replacement mixes confirming Zone 4. Table 2 shows a sieve analysis of fine aggregate. Fig. 1 shows the grain size distribution curve for fine aggregates used in the study. The waste ceramic is coarse and fine aggregate and uses white clay ceramic and red clay ceramic. Some properties of waste white ceramic are shown in Table 3. Also, some properties of red ceramic are given in Table 4. Fig. 2 shows the waste of red and white ceramics used.

2.2. Mixes Proportion

Table 5 shows the mix proportions and ingredients used in the study, and it contains using materials like cement, fine and coarse aggregate, water in kilograms for each cubic meter of concrete, and using 1.8 liters of Superplasticizer for each 100 kg of cement (10.8 liters for each cubic meter of concrete) for all mixes. In this study, the replacement values by weight of fine and coarse waste ceramic aggregates were 0, 20, 40, 60, 80, and 100 %.

2.3. Specimens And Tests:

Cubic steel molds with 10×10×10 cm were used to cast concrete, and three specimens for each mix were cast to find average compressive strength. All specimens were tested after 28 days. The tensile strength test is done by cylinders with 10 cm diameter and 20 mm height and tested after 28 days from the cast for splitting test method according to Eq. (1):

$$Ft = \left(2 \times p\right) \Big/ \left(\pi \times D \times L\right), \tag{1}$$

where Ft – tensile strength of the concrete specimen; p – maximum load causing failure; D – diameter of the cylinder; L – height of cylinder.

A flexural strength test was done using 10×10×40 cm beams and tested for third point loading according to British standards specification BS-1881 [11]. Also, three beams for each mix were tested after 28 days from casting and then finding the average value. The value of flexural strength can be found in Eq. (2):

$$Fb = \pi\left(P \times L\right) \Big/ \left(b \times d^2\right), \tag{2}$$

where Fb – flexural strength of the concrete specimen; P – maximum load; b and d – width and depth of the beam; L – length of the beam.

Fig. 3 shows a cubic concrete specimen after the compression test. Figs. 4 and 5 show the concrete beam after failure in testing for flexure strength. Modulus of elasticity was done using 150×300 mm specimens and mechanical strain gauges;Fig. 6 shows tensile strength and modulus of elasticity tests.

Table 1.Sieve analysis of coarse aggregate.

Sieve size	% Passing by weight	% PassingconfirmingIS-383 limits
20 mm	100 %	100 %
16 mm	93.5 %	90–100 %
10 mm	63.9 %	30–70 %
5 mm	5.7 %	0–10 %

Table 2.Sieve analysis of fine aggregate.

Sieve size, mm,micron	% Passing by weight	% Passing confirming IS-383 limits
10 mm	100 %	100 %
4.75 mm	100 %	95–100 %
2.36 mm	100 %	95–100 %
1.18 mm	98.2 %	90–100 %
600 micron	92.6 %	80–100 %
300 micron	39.7 %	15-50 %
150 micron	3.4 %	0–15 %

Table 3. Someproperties of white ceramic used in the study.

Properties	Specific gravity	Compressive strength	Tensile strength	Modulusof elasticity	Flexural strength	Absorption
Value	2.3	252 MPa	12.7 MPa	19200 MPa	25.9 MPa	0.2 %

Table 4.Some properties of red ceramic as waste aggregate.

Red ceramic property	Color	Density	Compressive strength	Flexural strength	Absorption
details	Red-brown	1.90 g/cm^3	43.2 MPa	22.4 MPa	1.91 %

Table 5.Ingredients of concrete used in the study forone cubic meter of concrete (reference mix).

Cement	Sand	Gravel	Water	Superplasticizer
600 kg	600 kg	1000 kg	150 kg	10.8 liter

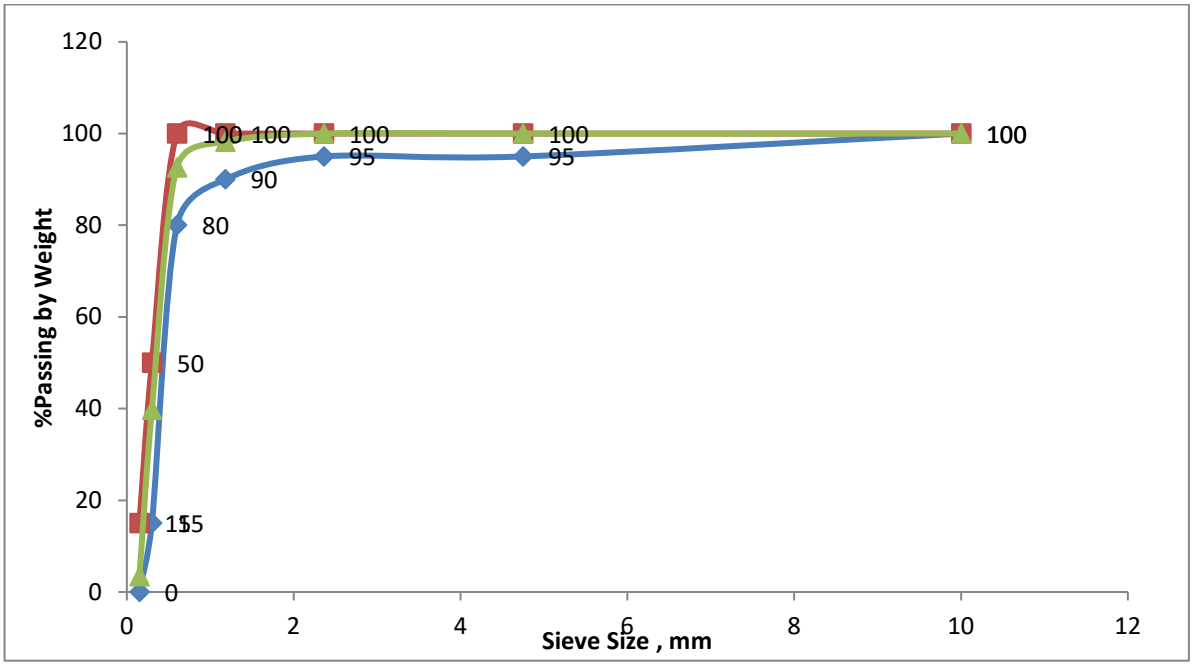

Figure 1.Grain size distribution curve for fine aggregates (the red and blue curves are the maximum and minimum limits) obtained from sieve analysis.

Figure 2. Red ceramic and white ceramic used in the study.

Figure 3. White waste ceramic concrete after compression test.

Figure 4. Flexural strength test shows ductile failure for white ceramic aggregate concrete.

Figure 5. 100 % white ceramic as waste aggregate (replacement) after flexure test.

Figure 6. Specimens under modulus of elasticity and tensile strength tests.

3. Results and Discussion

Tables 6 and 7 show the mechanical properties obtained from experimental work consisting of compressive strength, flexural strength, tensile strength, and static modulus of elasticity of reference mixes for both red ceramic and white ceramic, respectively, and also show reference mixes and mixes with 20, 40, 60, 80 %, and total replacement with waste ceramics as fine and coarse aggregates. As shown in Table 6, the compressive strength increases slightly until 60 % replacement, then decrease slightly after 60 % replacement for both fine and coarse ceramic waste aggregates. Decreasing in higher ratios of replacement can be attributed to the lower strength of red ceramic compared with natural gravel. The increment can be attributed to fine ceramics consistingof silica particles that can react with some products liberated from cement hydration and form an additional gel.

Also, from the same table, tensile, flexural, and modulus of elasticity increased using waste red ceramic until 60 % replacement. Table 7 shows good increment for the mechanical properties, by using white ceramic, compressive strength increased from 42.2 MPa for reference mix to 52.1 MPa for 100 % replacement, there is no decrement in compressive strength by using waste white ceramic until 100 % replacement and that can be attributed to excellent mechanical properties for white ceramic as shown in Table 3 comparing to red ceramic properties, tensilestrength,flexural strength, and modulus of elasticity also increased by using white ceramic until 100 % replacement, the flexural strength increased from 4.3 MPa for reference mix to 8.7 MPa for mixes with 100 % replacement, and modulus of elasticity increased from 25.6 to 32.8 GPa by using 100 % replacement and that can be attributed to the increment of compressive strength[12, 13], Figs. 7–10 show the relationship between compressive strength, tensile strength, flexural strength, and modulus of elasticity with % replacement of average coarse and fine aggregate with red ceramic as coarse and fine aggregates. Figs. 11–14 show the relation between % replacement and compressive strength, tensile strength, flexural strength, and modulus of elasticity using white ceramic. It should be noted that the excellent increment for modulus of elasticity in by using white ceramic can improve the deflection behavior of the structural element under loading if this type of concrete used in structural members, and the values of deflection can be reduced by using white ceramic in concrete, thus, the white ceramic behavior in concrete is better than red ceramic, but both gave a very good results in the mechanical properties, so that give a more durable low cost concrete and also the use of waste aggregate can give less environmental pollution. The main difference of the replacement dosage of the two types of concretes is that the red ceramic dosage equal to 60 % while the white ceramic dosage of replacement equal to 100 % in this study.

Table 6. Mechanical properties of concrete with waste red ceramic aggregate concrete.

Mix type	Compressive strength, MPa	Tensile strength, MPa	Flexural strength, MPa	Modulus of elasticity, MPa
Reference mix	42.25	2.92	4.34	25665
20 % replacement	43.16	3.08	4.92	26237
40 % replacement	44.29	3.65	5.33	27154
60 % replacement	45.40	3.73	5.47	27813
80 % replacement	44.57	3.60	5.10	26918
100 % replacement	43.84	3.58	4.86	25937

Table 7. Mechanical properties of concrete withwaste white ceramic aggregate concrete.

Mix type	Compressive strength, MPa	Tensile strength, MPa	Flexural strength, MPa	Modulus of elasticity, MPa
Reference mix	42.25	2.92	4.34	25665
20 % replacement	45.61	3.25	5.19	27987
40 % replacement	47.48	3.78	6.36	28588
60 % replacement	50.81	4.26	7.82	30443
80 % replacement	51.64	4.52	8.41	31098
100 % replacement	52.10	4.83	8.72	32824

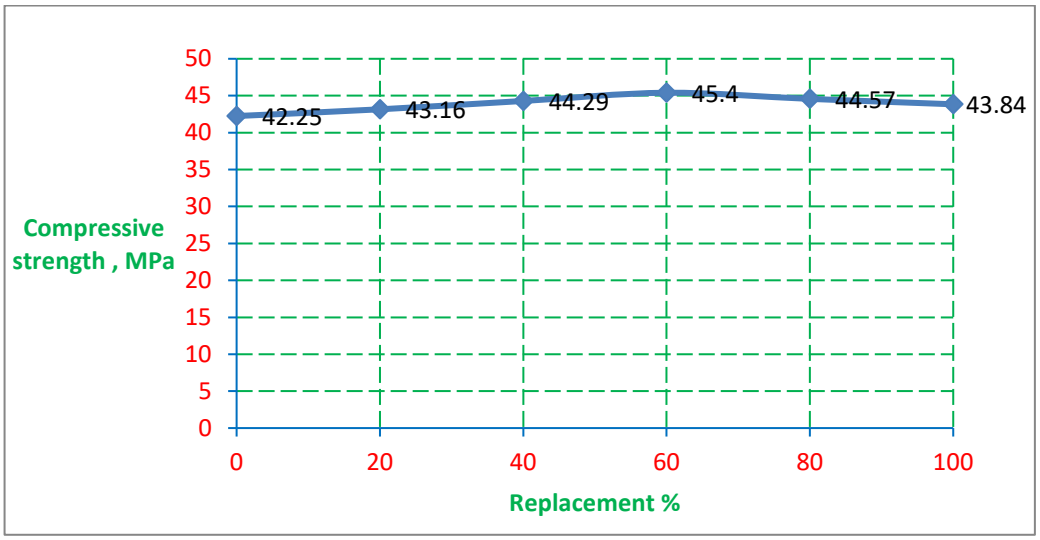

Figure 7. Relationship between replacement and compressive strength by using red ceramic.

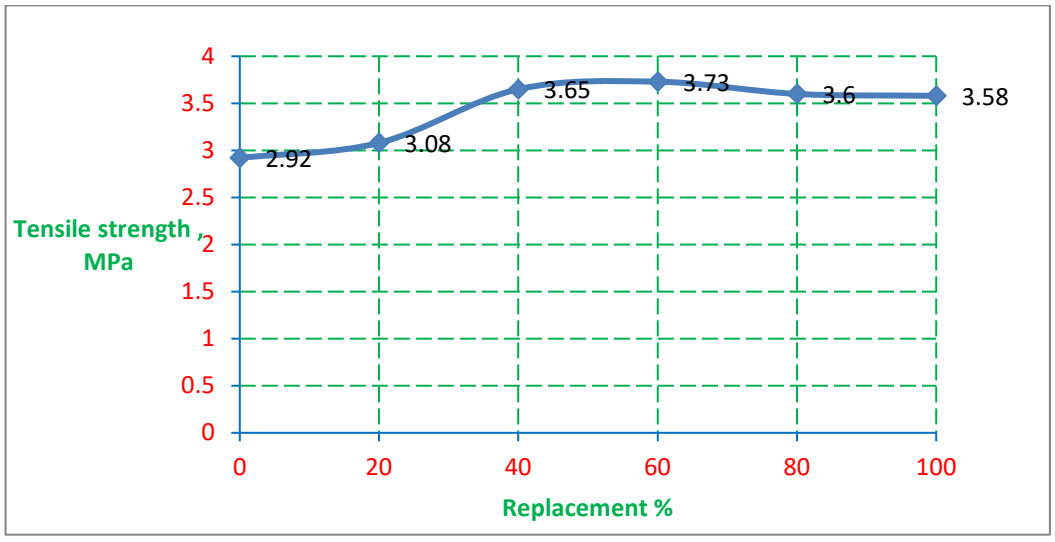

Figure 8. Relationship between replacement and tensile strength by using red ceramic.

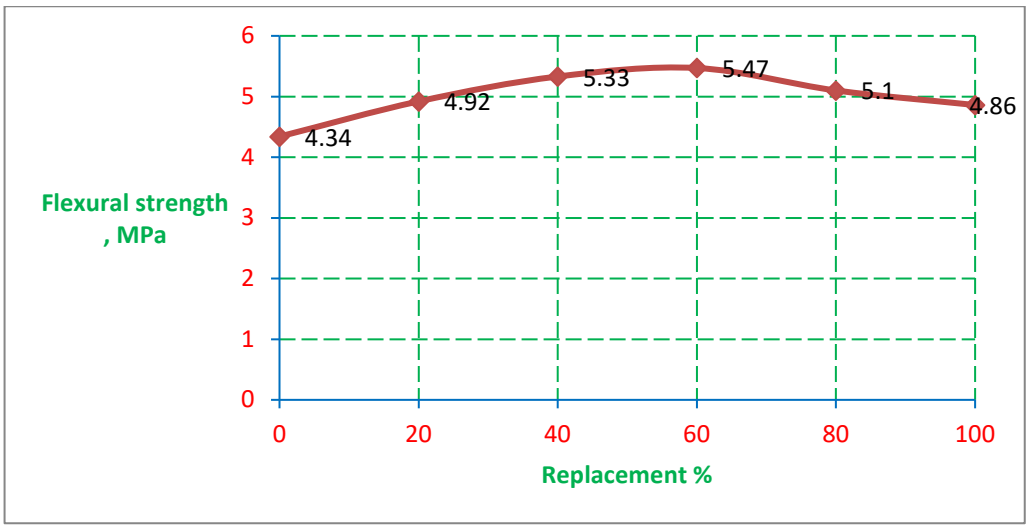

Figure 9.Relationship between replacement and flexural strength by using red ceramic.

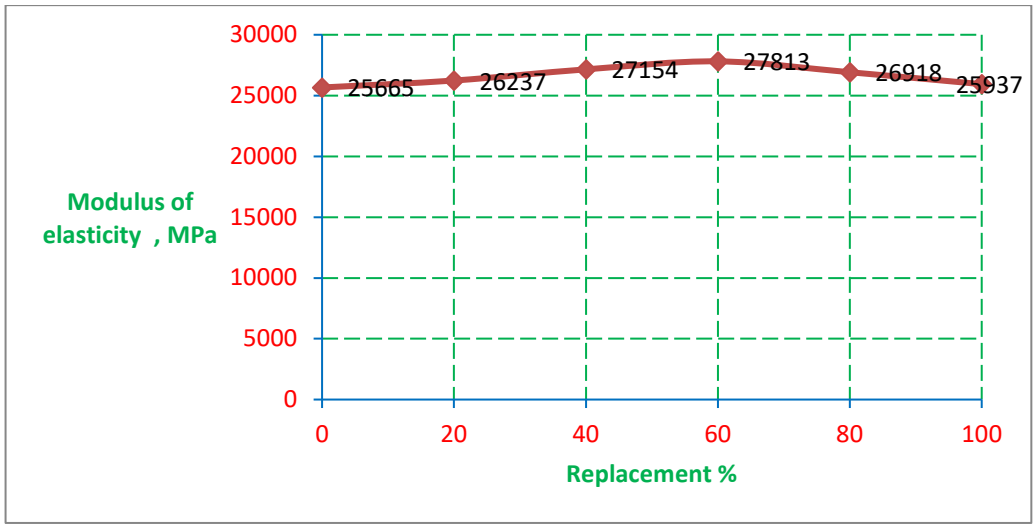

Figure 10. Relationship between replacement and static modulus of elasticityby using red ceramic.

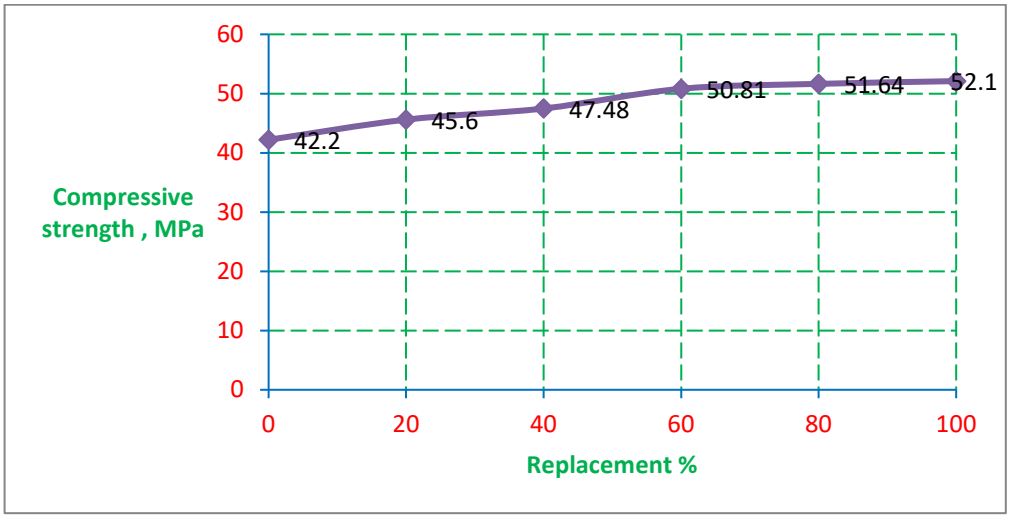

Figure 11. The relationship between % replacement and compressive strength of concrete (white ceramic).

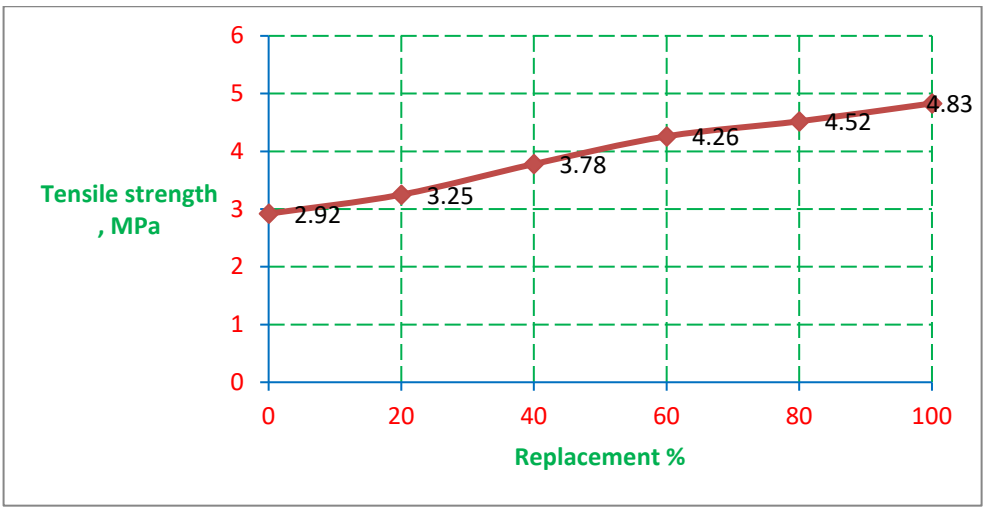

Figure 12. Relationship between % replacement and tensile strength of concrete (white ceramic).

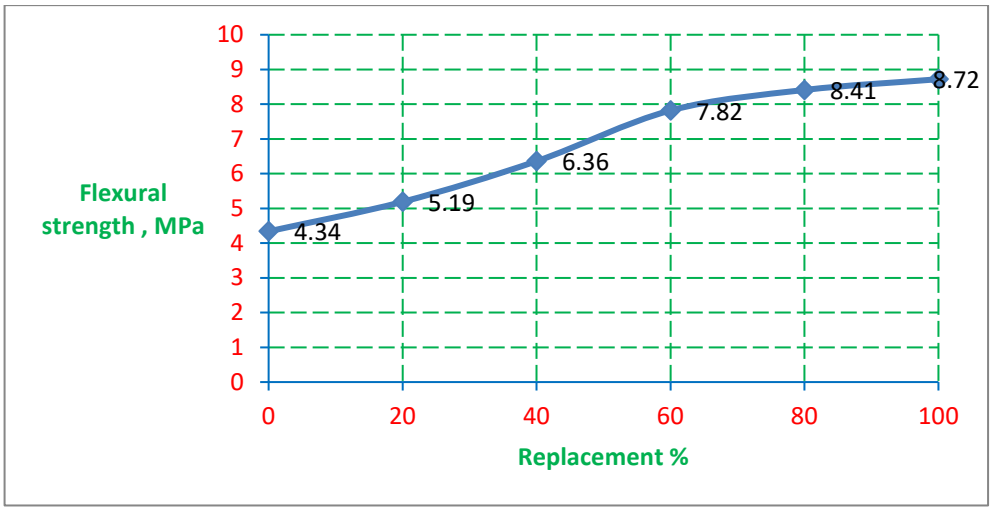

Figure 13. The relationship between % replacement and flexural strength of concrete (white ceramic).

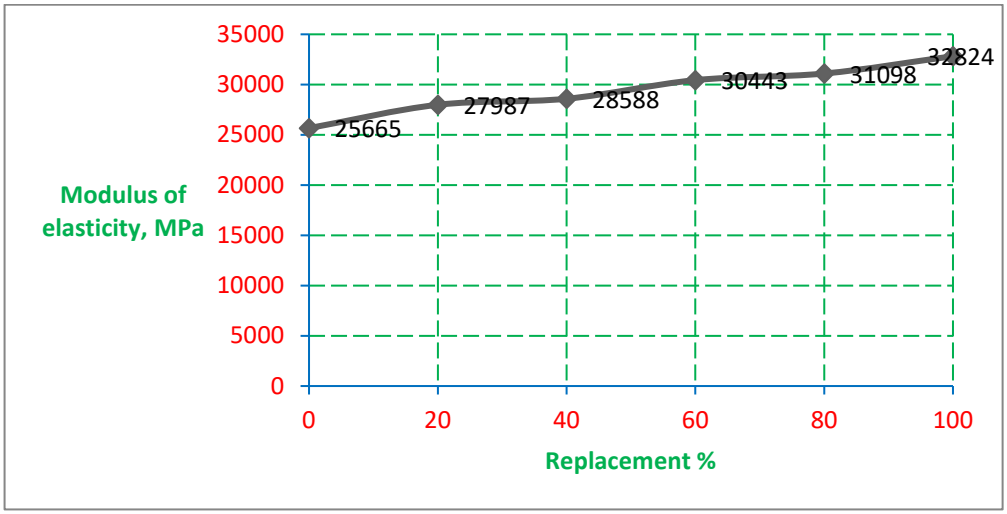

Figure 14. The relationship between % replacement and modulus of elasticity of concrete (white ceramic).

4. Conclusions

The red ceramic, as coarse and fine aggregate, increases mechanical properties, such as compressive strength, tensile strength, flexural strength, and modulus of elasticity until 60 % replacement; additional replacement leads to a slight decrement in mechanical properties.

White ceramic, as fine and coarse aggregate, improves concrete's mechanical properties until 100 % replacement. The use of white ceramic enhance the compressive strength from the value of 42 to 52.1 MPa, tensile strength increased from 2.9 to 4.8 MPa and the flexural strength increased also from 4.3 to 8.7 MPa and that is very good increment. The modulus of elasticity increased from 2.56 GPa to 3.28 GPa by using 100% replacement with white ceramic aggregate and that increment is very important to decrease the deflection of structural elements if this type of concrete used in structural members. For comparison between these two types of ceramic we can also conclude that optimum replacement for red ceramic is 60 % replacement and further replacement can reduce the strength of concrete, while the optimum replacement of white ceramic is 100 % and that can be very useful in construction, because that lowered the total cost of concrete and less environmental pollution.

References

1. Aliabdo, A.A., Abd-Elmoaty, A.E.M., Hassan, H.H. Utilization of crushed clay brick in the concrete industry. Alexandria Engineering Journal. 2014. 53(1). Pp. 151–68. DOI: https://doi.org/10.1016/j.aej.2013.12.003
2. Alwash, A., Al-Khafaji, F. Evaluation of using crushed brick as coarse aggregate in a concrete layer within rigid highway pavement. MATEC Web of Conferences.2018. 162(3). Article no. 01045. DOI: 10.1051/matecconf/201816201045
3. Karthikeyan, M., Balamurali, K., Barath Kumar, V., Manoj Prabakar, S., Janarthanan, R. Utilization of Waste Plastic in Concrete. International Research Journal of Engineering and Technology. 2019. 6(4). Pp. 1400–1405.
4. Alsahaf, N.A., Algharaawyi, A.M., Al Asadi, L.A.R., Jabal, Q.A., Aljumaili, M.A. Improvement of quality of concrete and reducing corrosion of steel reinforcement by using polypropylene fibers, styrene-butadiene rubber, and integral waterproofing admixture. Key Engineering Materials. 2021. 895. Pp. 68–76. DOI: 10.4028/www.scientific.net/KEM.895.68
5. Babafemi, A.J., Šavija, B., Paul, S.C., Anggraini, V. Engineering properties of concrete with waste recycled plastic: A review. Sustainability. 2018. 10(11). Article no. 3875.DOI: 10.3390/su10113875
6. Murali Dharan, Er.A., Mohan, Er.K. Ceramic Waste as Coarse Aggregate in Concrete. International Journal of Engineering Science and Computing. 2016. 6(7). Pp. 8519–8521.
7. Singh, A., Srivastava, V. Ceramic waste in concrete-A Review. Recent Advances on Engineering, Technology and Computational Sciences (RAETCS). Allahabad, 2018. Pp. 1–5.
8. Ramadevi, K. A Study on Properties of Concrete with Ceramic Waste Replaced for Fine Aggregate. International Journal of Civil Engineering and Technology. 2017. 8(8). Pp. 1730–1737.
9. Indian Standards IS-383. Specification for coarse and fine aggregates from natural sources for concrete. Bureau of Indian Standards.New Delhi, 2002.
10. Abdulabbas, Z.H., Alasadi, L.A., Adday, R., Taher, G.H., Farhood, K.T. Evaluation of Suitability of Cement Mortar Including Paper Waste as Construction Materials. Journal of Green Engineering (JGE). 2020. 10(6). Pp. 3206–3223.
11. British Standard 1881. Testing Concrete. Part 118:Method for Determination of Flexural Strength. B.S.I., 1983.
12. Shetty, M.S. Concrete Technology Theory andPractice. 6th (multicolour illustrative) ed. S. Chand & Company Ltd., Ramnagar, New Delhi, 2000.
13. ISO copyright office. INTERNATIONAL STANDARD ISO 9001 Quality management systems—Requirements. ISO 9001:2000(E). Switzerland: International Organization for Standardization; 2000.
14. Neville, A.M. Properties of Concrete. 5th ed.Pearson Education. Harlow, 2011.
15. Falah, M.W., Ghayyib, R.J. Evaluating the Effects of Using Superplasticizer RHEOBUILD® 600 on The Workability and Compressive Strength of Normal Concrete. Journal of University of Babylon, Engineering Sciences. 2018. 26(5). Pp. 95–104.
16. Sadagopan, M., Malaga, K., Nagy, A. RE:Concrete-Study on Recycling of Concrete in Sweden. Nordic Concrete Research. 2017. 56. Pp. 83–99.
17. Topçu, I.B., Şengel, S. Properties of concretes produced with waste concrete aggregate. Cement and Concrete Research. 2004. 34(8). Pp. 1307–1312. DOI: 10.1016/j.cemconres.2003.12.019.
18. El-Gamal, S.M.A., El-hosiny, F.I., Amin, M., Sayed, D.G. Ceramic waste as an efficient material for enhancing the fire resistance and mechanical properties of hardened Portland cement pastes. Construction and Building Materials. 2017. 154. Pp. 1062–1078. DOI: 10.1016/j.conbuildmat.2017.08.040.
19. Assefa, S., Getahun, M.Properties of Brick Waste as Coarse Aggregate Material in Concrete. Applied Journal of Environmental Engineering Science. 2019. 5(2). Pp. 144–152
20. Olutoge, F., Onugba, M., Ocholi, A. Strength Properties of Concrete Produced With Iron Filings as Sand Replacement. British Journal of Applied Science & Technology. 2016. 18(3). Pp. 1–6. DOI: 10.9734/BJAST/2016/29938.
21. Jaafar Kashkool, M., Almadi, W.A., Jabal, Q.A., Alasadi, L.A., Alghurabi, J.K. Some Mechanical Properties of Polymer Modified Concrete by Adding Waste Iron Filings and Chips. Key Engineering Materials. 2021. 895. Pp. 110–120. DOI: 10.4028/www.scientific.net/KEM.895.110.
22. Al-Dikheeli, M.R., Thaib, H.M., Alasadi, L.A.R. Mechanical properties and freeze-thaw resistance of lightweight aggregate concrete using artificial clay aggregate. Open Engineering. 2022. 12(1). Pp. 323–331. DOI: 10.1515/eng-2022-0019.
23. Zaki, H.M., Salih, S.A., Gorgis, I.N. Characteristics of Paper-cement Composite. Journal of Engineering. 2019. 25(4). Pp.122–138. DOI: 10.31026/j.eng.2019.04.09.

Information about the authors:

Afrah Alkraidi,
E-mail: afrraha.alkridy@uokufa.edu.iq

Rasha Aljazaari,
E-mail: rashaa.aljazaari@uokufa.edu.iq

Mohammed Aldikheeli,
E-mail: mohammedr.aldikheeli@uokufa.edu.iq

Layth Alasadi.
ORCID: https://orcid.org/0000-0001-6244-7965
E-mail: laitha.alasadi@uokufa.edu.iq

Thaaer Almusawi,
E-mail: thaaer.almusawi@uokufa.edu.iq

Qusay Alatiya,
E-mail: qusay.alatiya@uokufa.edu.iq

Received 14.02.2023. Approved after reviewing 19.10.2023. Accepted 04.07.2025.

Magazine of Civil Engineering

ISSN 2712-8172

journal homepage: http://engstroy.spbstu.ru/

Research article

UDC 624.012.45:539.376

DOI: 10.34910/MCE.139.2

Stress relaxation behavior of glass and carbon fiber reinforcements in prestressed concrete applications

P.S. Mostovykh , ***A.E. Dontsova*** , ***T.A. Koriakovtseva*** , ***O.N. Stolyarov***

Peter the Great St. Petersburg Polytechnic University, St. Peterburg, Russian Federation

✉ *anne.dontsoova@gmail.com*

Keywords: prestressed concrete, stress relaxation, fiber reinforcement, roving, viscoelasticity, modeling

Abstract. High-performance fibrous materials offer advantages such as high strength and low weight, making them promising for use in prestressed concrete. This work investigates the stress relaxation behavior of glass and carbon fiber reinforcements. Stress relaxation tests were conducted at load levels ranging from 10 % to 40 % of the materials' tensile strength. A mathematical model was developed to describe this behavior, and the model parameters were determined. The stress relaxation of the fiber reinforcements was simulated and the resulting prestress loss was compared with that of traditional steel reinforcement. It was found that stress relaxation is more pronounced in glass and carbon fiber reinforcements than in steel. It was shown that the observed stress loss is primarily caused by the slippage of the fibrous reinforcement. Based on the findings, practical recommendations are provided for the application of these results in prestressed concrete design.

Funding: The research was funded by the Russian Science Foundation (project No. № 25-29-00771).

Citation: Mostovykh, P.S., Dontsova, A.E., Koriakovtseva, T.A., Stolyarov, O.N. Stress relaxation behavior of glass and carbon fiber reinforcements in prestressed concrete applications. Magazine of Civil Engineering. 2025. 18(7). Article no. 13902. DOI: 10.34910/MCE.139.2

1. Introduction

Prestressed concrete structures traditionally offer several advantages compared to conventional reinforced concrete structures [1]. The main advantage is the reduction in the structure's mass and size due to the more efficient use of reinforcement. Prestressed structures with steel reinforcement have been used in the manufacture of concrete products for several decades. Alongside metal reinforcement, composite reinforcement is now being used for reinforcing concrete [2–8]. Various yarns, rovings, straps, sheets, and plates made of high-performance fibers such as glass, basalt, and carbon are used as reinforcement [9]. Its mechanical characteristics are on par with those of steel reinforcement, and due to its corrosion resistance and resilience to aggressive environments, it may even surpass steel reinforcement.

The properties of the fibrous reinforcement vary and depend heavily on the properties of the original fiber. The most common types involve the use of glass (glass fiber reinforced polymer, GFRP) or carbon (carbon fiber reinforced polymer, CFRP) fibers. In the latter case, Young's modulus is comparable to that of the steel reinforcement. Furthermore, if we consider that there is no need to create a concrete protective layer of several centimeters thick, then concrete structures with such reinforcement possess an undeniable advantage. Such structures have found wide application in the building envelopes and other areas over the last two decades. Similar to prestressed steel reinforced concrete, numerous attempts have recently been made to use pre-tensioning in composite concrete structures. The principle of reinforcement is the same as that of steel reinforcement: a carbon mesh is pre-tensioned to a specified stress value, and then the concrete is cast [10, 11]. In [12, 13], the influence of the number of layers and the level of pre-tensioning

on the bending characteristics of textile concrete reinforced with basalt and carbon rovings was investigated. In addition to the undeniable advantages of using composite reinforcement, which include the absence of corrosion, there are several disadvantages inherent primarily to fibrous reinforcement. One of the obvious difficulties in the successful application of composite reinforcement in prestressed structures is the process of loss of internal stress over time, i.e., the instability of the reinforcing mesh properties. A drop in stress in the composite reinforcement can negate all the advantages of a pre-stressed concrete structure [14–19]. Li et al. [14] studied the transverse compression stress relaxation behavior under different stress levels. The relaxation characteristics were analyzed, and the stress-relaxation model was proposed. Under the stress level from 30% to 80%, the long-term stress relaxation ratio was between 19 % and 33 %. Wang et al. [15] showed that the prestress losses of CFRP are due to the anchorage set and the time-dependent behavior. The stress losses are approximately from 12.6 % to 18.2 % and from 2.3 % to 3.9 % of the initial prestress for anchorage and stress relaxation, respectively. Therefore, it is relevant to study the processes of internal stress loss, the so-called stress relaxation, in composite reinforcement.

A drop in stress over time also occurs in traditional steel reinforcement. Therefore, the design of the prestressed reinforcement also accounts for the possible stress loss. This accounting involves adopting various coefficients that consider the effects related to stress relaxation in the reinforcement itself, losses during concrete heating, losses due to concrete shrinkage, and concrete creep. These processes are well studied, and regulatory documents provide various coefficients and formulas that allow for estimating the level of pre-tension loss in steel reinforcement [20].

Unlike steel reinforcement, the nature of these processes in fibrous reinforcement is somewhat different, although some similar aspects can be found. For example, stress relaxation can occur in the reinforcement itself, and there can also be slippage due to the method for anchoring [21–23]. Furthermore, since composite reinforcement consists of high-strength rovings, each composed of several thousand individual filaments that are in contact with each other and with the concrete matrix, interfibrillar friction occurs within the core of the reinforcing component [24]. Also, with an increase in the prestress level, the stress drop in the fibrous reinforcement increases. This is associated with a significant reduction in the cross-sectional dimensions under tension: the fibers group together in the center, migrating from the outside inward, the cross-section reduces sharply, which also affects the stress loss. Similar problems related to stress loss due to anchorage are observed; this process is accompanied by much greater losses because it is very difficult to anchor brittle, high-strength rovings. As mentioned above, carbon rovings are primarily used, which have minimal elongation at break (1–2 %) and are extremely brittle. Therefore, the traditional tensioning methods cannot be applied to these reinforcing meshes. Various materials, such as epoxy resin, must be used to prevent mechanical damage to the ends of the reinforcing mesh. In practice, pre-prepared molds are used to anchor the carbon composite reinforcement, and the ends of the rovings are potted in epoxy resin. After hardening, this allows the reinforcement to be placed in a clamping device and securely fixed.

A literature review revealed a lack of studies specifically focused on investigating stress relaxation processes in prestressed concrete reinforcement. However, there is research related to the study of the creep behavior of high-strength fiber reinforced concrete, which, in principle, provides analogous information and can be considered when developing predictive models for stress relaxation. In [25], the influence of fibers on the creep behavior of fiber-reinforced concrete was studied. It was shown that the creep strain is significantly influenced by the Young's modulus of the fiber and the matrix as well as the fiber length and thickness. The time-dependent behavior of the textile-reinforced concrete was studied via flexural creep [26]. A viscoelastic model was successfully developed to predict the creep deformation of the concrete composite. It can be stated that the processes of stress relaxation in composite reinforcement have been poorly studied. There is only data from testing similar composite materials, but studies specifically concerning pre-stressed composite reinforcement in concrete are practically absent, and no publications by authors on this topic were found. This underscores the relevance of this work. The aim of this work is to study the stress relaxation behavior of glass and carbon fiber reinforcements under different prestress levels and to understand the prestress losses in the fibrous reinforcement applied to the prestressed concrete composites.

The objectives of this work are:

- to conduct experimental studies of the stress relaxation in continuous glass and carbon rovings under different load levels;
- to propose a mathematical model for stress relaxation that accounts for the fiber properties and the initial prestress level;
- to develop a technical approach for measuring stress relaxation in composite reinforcement, comparable to the methods used for traditional steel reinforcement.

2. Materials and Methods

2.1. Test Samples

This study focuses on two fibrous reinforcements made of glass and carbon rovings. Table 1 lists the characteristics of the samples. The ends of the brittle glass and carbon rovings were clamped in a mold, and epoxy resin was poured into the mold to prevent damage to the rovings. Fig. 1a illustrates the setup for testing the roving sample.

Table 1. Characteristics of materials tested.

Sample designation	Raw material	Linear density (tex)	Cross-sectional area (mm^2)	Tensile strength (MPa)	Young's modulus (GPa)
AG	AR-Glass roving	2400	0.896	708	66
CR	Carbon roving, PAN-based, 24K	1600	0.879	2015	173

2.2. Stress Relaxation Testing

Stress relaxation tests were conducted using an Instron universal tensile testing machine (model 5965). The stress relaxation behavior of the glass and carbon rovings was evaluated at various loading levels. The test programs for the stress relaxation and inverse stress relaxation loadings are shown in Table 2. The stress relaxation loadings are shown schematically in Fig. 2b.

The tensile stress of the fabrics (MPa) was calculated by the following formula:

$$\sigma = \frac{F\gamma}{T}, \tag{1}$$

where F is the maximal applied force (N), γ is roving density (kg/m^3), and T is the nominal linear density of the roving (tex).

Table 2. A list of test programs.

No	σ_{rel} (MPa)	as % of σ_{max}	t_{rel} (s)	σ_{3600} (MPa)	σ_{ir} (MPa)	t_{ir} (s)	σ_{7200} (MPa)
Glass roving							
AG-1	70.8	10	3600	62.1	52.1/50.4	3600	50.3
AG-2	140.5	20	3600	124.0	52.1/50.9	3600	52.4
AG-3	211.2	30	3600	183.1	41.6/40.8	3600	57.3
AG-4	280.5	40	3600	247.5	52.1/51.1	3600	59.7
Carbon roving							
CR-1	201.5	10	3600	–	47.3	3600	55.6
CR-2	401.0	20	3600	–	49.3	3600	70.0
CR-3	601.8	30	3600	–	47.3	3600	76.0
CR-4	801.9	40	3600	–	48.1	3600	83.2

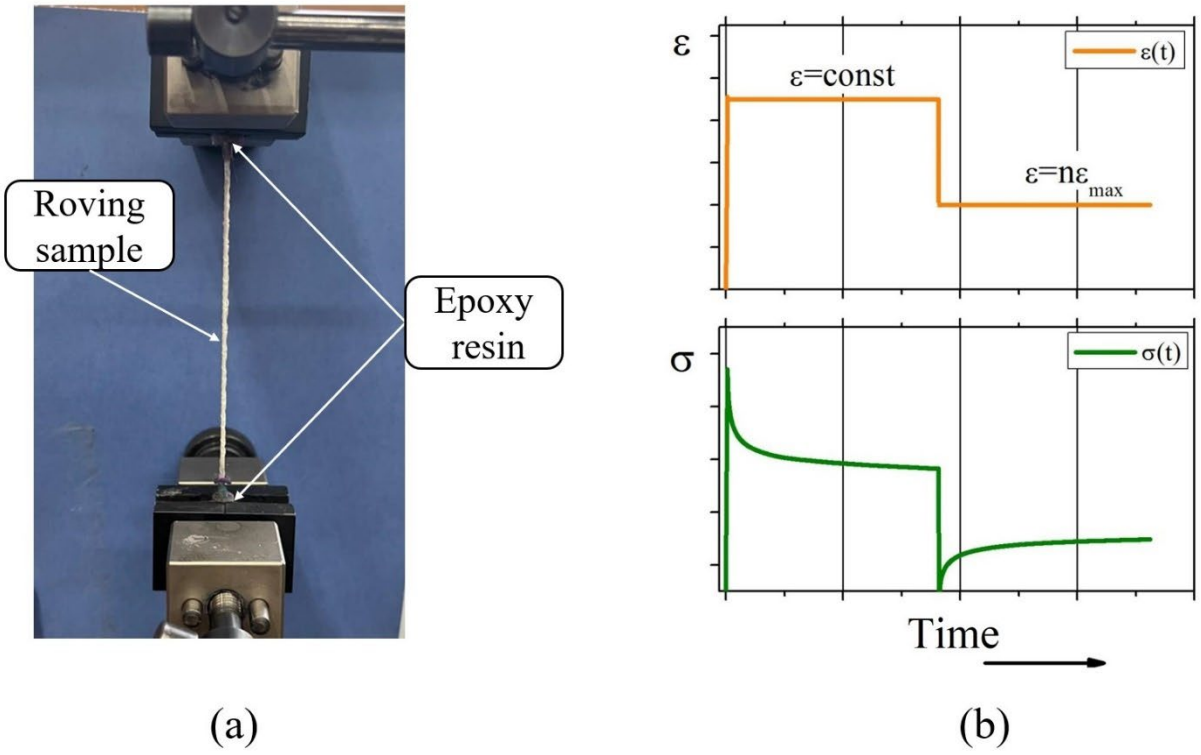

Figure 1. Experimental setup for testing the roving sample (a) and stress relaxation stages examined in this study (b).

3. Results and Discussion

3.1. Stress Relaxation and Inverse Stress Relaxation Tests

Stress relaxation and inverse stress relaxation tests were performed for the glass and carbon roving samples for fixed strain levels that varied from 10 % to 40 % of the tensile strength of the corresponding reinforcing material. Fig. 2 shows the experimentally obtained stress relaxation and inverse stress relaxation for each of the two rovings. Fig. 2a describes the stress relaxation behavior in time for the glass roving, and Fig. 2b describes the stress relaxation behavior in time for the carbon roving.

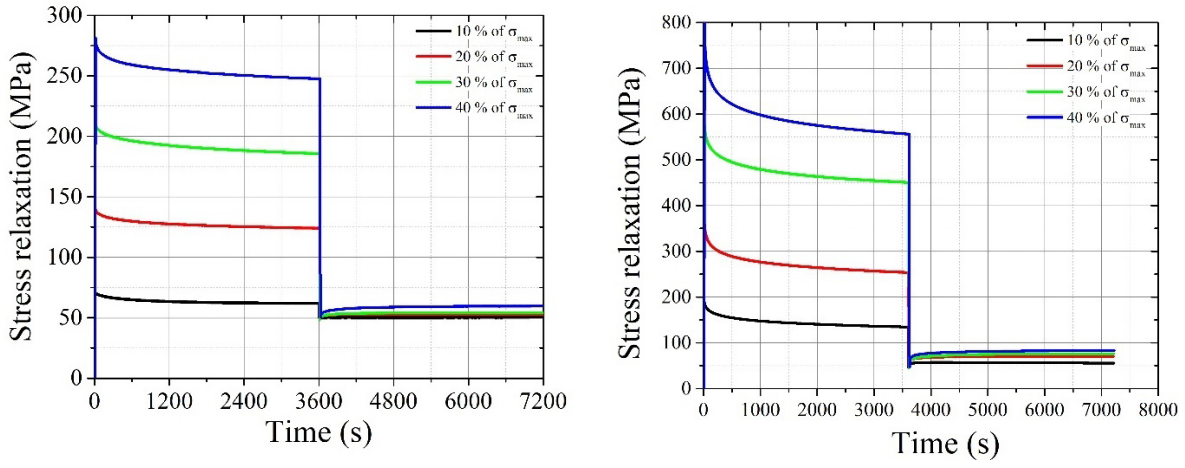

Figure 2. Experimental stress relaxation and inverse stress relaxation curves: glass roving (a), carbon roving (b).

The relaxation modulus curves obtained for the glass and carbon roving samples at various values of tensile stress and strain up to 40 % of the tensile strength were obtained according to the following formula:

$$E_{rel}(t_{rel}) = \frac{\sigma_{rel}}{\varepsilon_0} \quad [MPa], \tag{2}$$

where the relaxation time t_{rel} is calculated from the moment of the beginning of the stress relaxation test (from the moment when the deformation ε_0 is kept constant). In this work, the relative stress is used at relaxation, given by the expression:

$$\xi = \frac{\sigma_{rel}(t_{rel})}{\sigma_{rel}(0)} \quad [MPa / MPa], \tag{3}$$

i.e., the ratio of the stress in the relaxation test to the initially applied stress. Similarly, for inverse stress relaxation, the relative stress during inverse stress relaxation is determined by the following formula:

$$\chi = \frac{\sigma_{ir}(t_{ir}) - \sigma_{ir}(0)}{\sigma_{ir}(0) - \sigma_{rel}(3600)} \quad [MPa / MPa], \tag{4}$$

where the time of reverse relaxation t_{ir} is calculated from the moment of the beginning of the process of inverse stress relaxation, and $\sigma_{rel}(3600)$ represents the stress at the end of the relaxation process and is given in Table 1.

The stress relaxation curves plotted for the dimensionless parameter according to (3) are presented in Fig. 3, and the inverse stress relaxation curves plotted for the dimensionless parameter according to (4) are presented in Fig. 4.

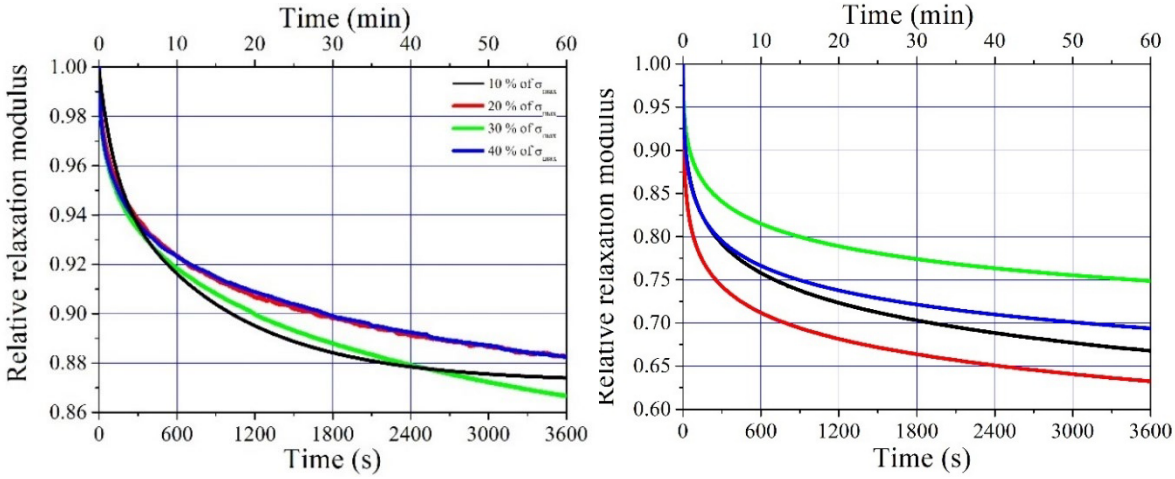

(a) **(b)**

Figure 3. Stress relaxation: glass roving (a), carbon roving (b).

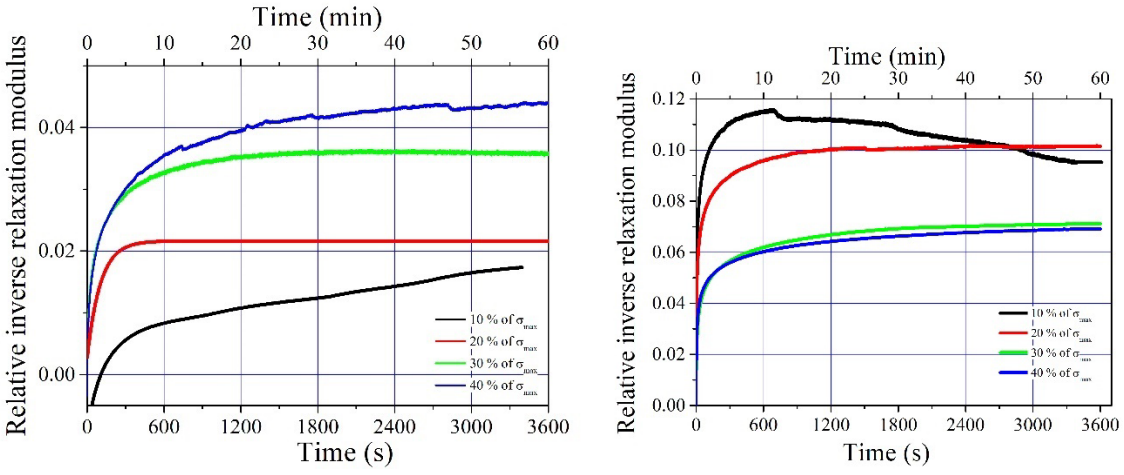

(a) **(b)**

Figure 4. Inverse stress relaxation curves: glass roving (a), carbon roving (b).

As shown in Fig. 3, the stress relaxation curves for the glass roving practically coincide with each other, and the difference in the curves for the carbon roving is not related to the stress, at which the stress relaxation test was carried out. This indicates significant inconsistency of the carbon roving properties when changing from one sample to another. To develop a mathematical model, the average value of the relative relaxation modulus for each value of time was averaged. The best fitting for both the glass and carbon roving was given by the Belehradek formula:

$$1-\frac{\sigma_{rel}(t_{rel})}{\sigma_{rel}(0)}=a\left(\lg t_{rel}\text{-}b\right)^{c}, \tag{5}$$

where the logarithm is calculated from the time measured in seconds, and the values of parameters a, b, c for the tested materials are shown in Table 3.

According to the Belehradek formula, the amount of loss of the applied voltage was calculated for 1 hour, 1 day, 1 week and 1 month (30 days). The corresponding results are also presented in Table 3.

Table 3. Stress relaxation parameters in the glass and carbon rovings as described by the Belehradek formula.

Sample	Belehradek's parameters			Stress decay $\Delta\sigma/\sigma(0)$			
	a	*b*	*c*	1 hour	1 day	1 week	1 month
AG	0.00297	–0.99568	2.472181	12.8	24.2	33.7	42.0
CR	0.02972	–0.99568	1.55988	31.6	47.8	58.8	67.6

3.2. Characterization of Stress Relaxation Behavior

The best fit for the glass fiber was given by the Belehradek formula (5):

$$\sigma_{rel}(t_{rel})=\sigma_{rel}(0)\left(1-0.00297\left(\lg t_{rel}+0.99568\right)^{2.472181}\right),$$

and for the carbon fiber, in addition to the Belehradek formula:

$$\sigma_{rel}(t_{rel})=\sigma_{rel}(0)\left(1-0.00297\left(\lg t_{rel}+0.99568\right)^{1.55988}\right).$$

A good fit was also obtained using a third-degree polynomial fit to the logarithm of time.

$$\sigma_{rel}(t_{rel})=\sigma_{rel}(0)\left(0.97844-0.00397\lg t_{rel}-0.01955\lg^{2} t_{rel}+0.00213\lg^{3} t_{rel}\right).$$

A comparison of the predictions of these three formulas with the experimental data in semilogarithmic coordinates is shown in Fig. 5.

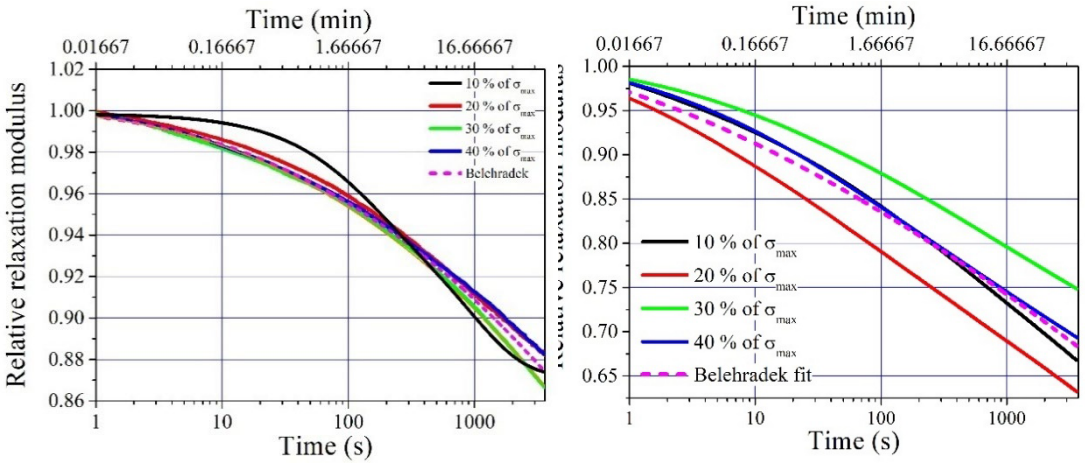

Figure 5. Stress relaxation curves for the glass (a) and carbon (b) rovings and their approximation using Belehradek's formula and a third-degree polynomial in the logarithm of time (for the carbon roving only).

Based on the stress relaxation data, it can be assumed that the material is linearly viscoelastic. This assumption can be tested using the inverse stress relaxation data. Inverse stress relaxation is generally the sum of two processes: the elastic after effect from the unloading process (this part involves the increase in stress over time) and the elastic after effect from the loading process (this part involves the decrease in stress over time). The first of these parts, if the material is linearly viscoelastic, can be determined from the direct stress relaxation data; to estimate the second part, we extrapolate the stress relaxation curve in semi-logarithmic coordinates. Mathematically, then, the stress during inverse relaxation for glass roving will be expressed by the following formula:

$$\sigma_{ir}(t_{ir}) = \sigma_{rel}(0)\left(1 - 0.00297\left(\lg\left(t_{ir} + 3600\right) + 0.99568\right)^{2.472181}\right) -$$

$$-\left[\sigma_{ir}(0) - \sigma_{rel}(3600)\right]\left(1 - 0.00297\left(\lg t_{ir} + 0.99568\right)^{2.472181}\right),$$

and a similar expression can also be written for carbon roving. However, a comparison of the predictions of this formula (which expresses the hypothesis of linearity of the viscoelastic properties of glass and carbon fiber) and actual experimental data shows that the phenomenon of inverse stress relaxation for glass fiber is approximately 2.5 times smaller in magnitude than that predicted by linear theory and more than 3 times smaller for carbon rovings (Fig. 6). In other words, in the studied materials, the relaxation of nonequilibrium processes aimed at increasing the length of the sample occurs faster than the inverse process aimed at decreasing the sample's length.

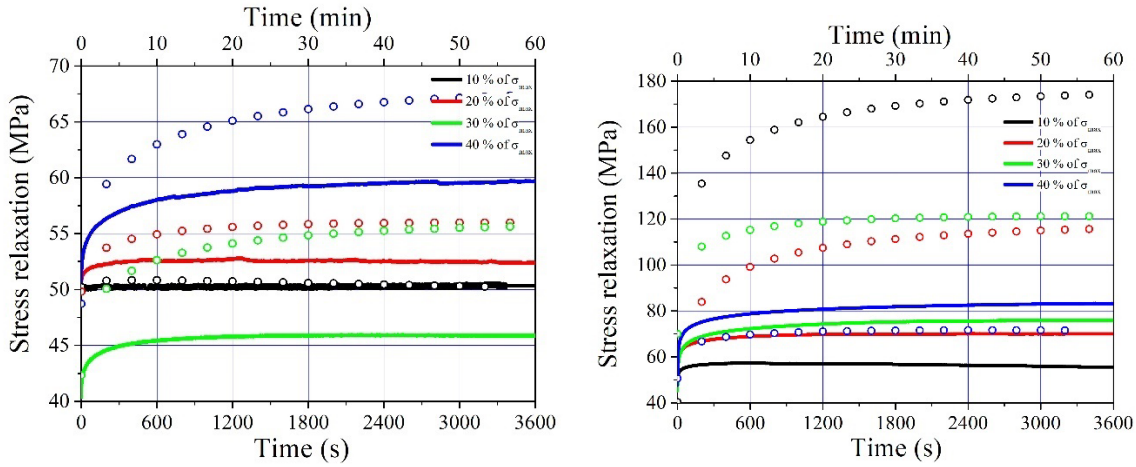

Figure 6. Inverse stress relaxation curves for glass fiber (a) and carbon fiber (b) and their theoretical prediction within the framework of linear viscoelasticity (Belehradek).

3.3. Comparison of the Obtained Data with the Stress Relaxation of Steel Reinforcement

According to [14], there are two types of stress relaxation losses. The first type is due to stress relaxation in the reinforcement, temperature changes during heat treatment of the structure, anchor deformation, and shape distortion. The second type is due to the shrinkage and the creep of the concrete. Let us compare the stress relaxation losses in the traditional steel reinforcement and the composite reinforcement. All data has been taken from the official regulations [14]. The full values of the first and second losses in the steel reinforcement were considered. Fig. 7 presents the theoretical extrapolation of the relaxation curves in glass and carbon compared with [14] for steel reinforcement at the same stress level.

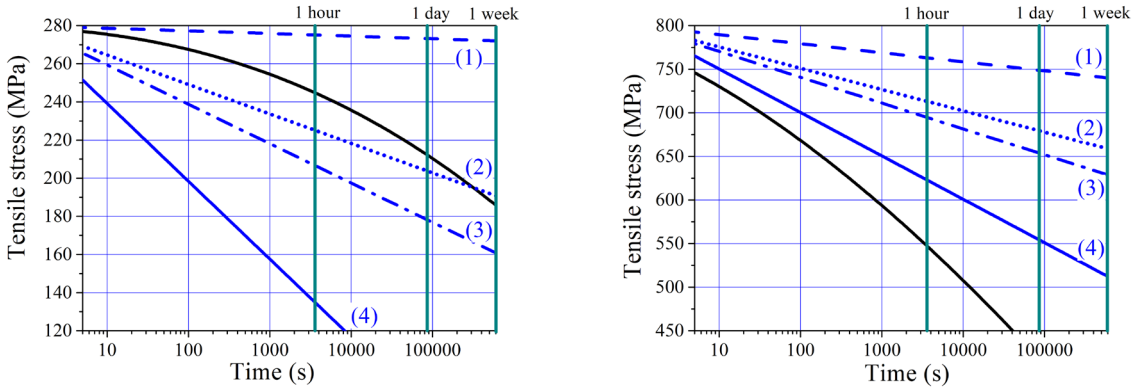

Figure 7. Theoretical extrapolation of the relaxation curves in glass (a) and carbon (b) compared with [12] for steel reinforcement at the same stress level.

The relationships obtained show that different types of losses have varying effects on the decay of internal stresses in the steel reinforcement. The minimum losses are observed when applying the formula for the mechanical losses due to the stress relaxation in the reinforcement (Curve 1). These amounts to no more than a few percent of the initial stress level. A similar trend was noted for carbon sheets in [11], where the reduction was approximately from 2 % to 4 % of the pre-stress level. If, in addition to the relaxation losses, other types of losses are considered (for example, from the temperature difference in the concrete heating), the stress loss becomes more significant (Curve 2). The total value of the immediate losses (from deformation, mechanical relaxation, temperature effects, and deformation of the steel form during non-simultaneous tensioning of the reinforcement) is described by Curve 3. If the time-dependent losses (namely, losses from anchor deformation and concrete shrinkage) are additionally considered and summed with the immediate losses, Curve 4 is obtained, which corresponds to the values of the total immediate and time-dependent losses in the steel reinforcement. Reference [11] also notes that the largest contribution to mechanical losses comes from losses due to insufficient anchorage, amounting to approximately from 12 % to 18 % of the prestress level.

Comparing the losses in the traditional steel reinforcement with the composite reinforcement, the stress relaxation curves for a comparable strain level were additionally plotted on the graphs. An analysis of these curves shows that the results obtained for the composites are close to the range of mechanical losses for the steel reinforcement. It should be considered that not all loss types of steel are inherent to the prestressing process of composites. Therefore, as in the case of glass roving, the total values of the immediate and time-dependent losses may not differ significantly from the stress relaxation curve for GFRP. In the case of glass roving, it is evident that the losses due to stress relaxation are quite large and even exceed the total immediate and time-dependent losses for traditional steel reinforcement. However, as the experiment showed, problems arise with the anchorage of the reinforcement, since pull-out tests demonstrate that a more flattened reinforcement cross-sectional shape improves the mechanical properties of the concrete composites. Hence, it can be concluded that the primary losses in the obtained data are attributable to the clamping device. This conclusion agrees with the findings in reference [11].

Losses due to mechanical relaxation for composite materials are essentially negligible, as glass and carbon rovings are not prone to stress relaxation in the same way as steel. Only a slight relaxation (a few percent) may occur within these rovings due to the interfiber friction in the roving. Accordingly, all major losses are attributed to the clamping device. Unfortunately, in the manufacturing of pre-stressed concrete composites with fibrous reinforcement, this is a primary issue, as the fibers are quite brittle and require the development of special anchoring devices. Such work is already underway, and the authors of this paper have proposed some fundamentally new solutions [15].

4. Conclusions

This study involved testing two types of rovings: glass and carbon, used as composite reinforcement for prestressed concrete structures. Testing was conducted at four levels of pre-stress – from 10 % to 40 % of the ultimate tensile load, in 10 % steps. Both direct and inverse stress relaxation was investigated.

A phenomenological description of the stress relaxation and inverse relaxation curves in glass and carbon rovings is proposed. Two parameters were required to describe the stress relaxation curves; a third was required to describe the inverse relaxation. Within the proposed description, the process of increasing

load and the process of decreasing load are described by different formulas. The results of the mathematical modeling showed satisfactory agreement with the experimental data.

As a practical application, the case of mechanical losses in traditional steel reinforcement was considered, for which curves were plotted according to the relevant regulation for steel reinforcement. A comparison of the stress relaxation results for the investigated materials with the data for the steel reinforcement was carried out. Recommendations are given for the practical application of the obtained data on the stress relaxation of fibrous composite reinforcement in pre-stressed concrete structures.

References

1. Choo, B.S. Reinforced and prestressed concrete. Advanced Concrete Technology. 4: Testing and Quality. Butterworth-Heinemann. Oxford, 2003. Pp. 3–17.
2. El-Hacha, R., Wight, R.G., Green, M.F. Prestressed Carbon Fiber Reinforced Polymer Sheets for Strengthening Concrete Beams at Room and Low Temperatures. Journal of Composites for Construction. 2004. 8(1). Pp. 3–13. DOI: 10.1061/(ASCE)1090-0268(2004)8:1(3)
3. Wang, H.T., Liu, S.S., Zhu, C.Y., Xiong, H., Xu, G.W. Experimental Study on the Flexural Behavior of Large-Scale Reinforced Concrete Beams Strengthened with Prestressed CFRP Plates. Journal of Composites for Construction. 2022. 26(6). Article no. 04022076. DOI: 10.1061/(ASCE)CC.1943-5614.0001246
4. Wang, H.T., Wu, G. Bond-slip models for CFRP plates externally bonded to steel substrates. Composite Structures. 2018. 184. Pp. 1204–1214. DOI: 10.1016/j.compstruct.2017.10.033
5. Lees, J.M., Winistoerfer, A.U. and Meier, U. External Prestressed Carbon Fiber-Reinforced Polymer Straps for Shear Enhancement of Concrete. Journal of Composites for Construction. 2002. 6(4). Pp. 249–257. DOI: 10.1061/(ASCE)1090-0268(2002)6:4(249)
6. Wight, R.G., Green, M.F., Erki, M.A. Prestressed FRP Sheets for Poststrengthening Reinforced Concrete Beams. Journal of Composites for Construction. 2001. 5(4). Pp. 214–220. DOI: 10.1061/(ASCE)1090-0268(2001)5:4(214)
7. Zdanowicz, K., Kotynia, R., Marx, S. Prestressing concrete members with fiber-reinforced polymer reinforcement: State of research. Structural Concrete. 2019. 20. Pp. 872–885. DOI: 10.1002/suco.201800347
8. Kim, Y.J., Green, M.F., Wight, R.G. Prestressed fiber-reinforced polymer (FRP) composites for concrete structures in flexure: fundamentals to applications. Advanced Composites in Bridge Construction and Repair. Woodhead Publishing. Cambridge, 2014. Pp. 30–60. DOI: 10.1533/9780857097019.1.30
9. Peled, A. Pre-tensioning of fabrics in cement-based composites. Cement and Concrete Research. 2007. 37(5). Pp. 805–813. DOI: 10.1016/j.cemconres.2007.02.010
10. Cao, Q., Zhou, J.P., Wu, Z.M., Ma, Z.J. Flexural behavior of prestressed CFRP reinforced concrete beams by two different tensioning methods. Engineering Structures. 2019. 189. Pp. 411–422. DOI: 10.1016/j.engstruct.2019.03.051
11. Haas, R., Quadflieg, T., Stolyarov, O. Analysis of reinforcement efficiency and microscopic characterization of glass and carbon roving geometry in prestressed concrete composites. Journal of Composite Materials. 2021. 55(23). Pp. 3293–3305. DOI: 10.1177/00219983211013382
12. Lou, T., Lopes, S., & Lopes, A. Time-dependent behavior of concrete beams prestressed with bonded AFRP tendons. Composites Part B: Engineering. 2016. 97. Pp. 1–8. DOI: 10.1016/j.compositesb.2016.04.070
13. Du, Y., Zhang, X., Liu, L., Zhou, F., Zhu, D., Pan, W. Flexural Behaviour of Carbon Textile-Reinforced Concrete with Prestress and Steel Fibres. Polymers. 2018. 10(1). Article no. 98. DOI: 10.3390/polym10010098
14. Li, J., Wang, M., Yue, Q., Liu, X. Transverse compressive properties, long-term stress relaxation, and post-relaxation properties of unidirectional CFRP composites. Journal of Building Engineering. 2025. 105. Article no. 112526. DOI: 10.1016/j.jobe.2025.112526
15. Wang, W.W., Dai, J.G., Harries, K.A., Bao, Q.-H. Prestress Losses and Flexural Behavior of Reinforced Concrete Beams Strengthened with Posttensioned CFRP Sheets. Journal of Composites for Construction. 2012. 16(2). Pp. 207–216. DOI: 10.1061/(ASCE)CC.1943-5614.0000255
16. Ornaghi, H.L., Almeida, J.H.S., Monticeli, F.M., Neves, R.M. Stress relaxation, creep, and recovery of carbon fiber non-crimp fabric composites. Composites Part C: Open Access. 2020. 3. Article no. 100051. DOI: 10.1016/j.jcomc.2020.100051
17. Umarov, B.S., Zinnurov, T.A. Studying stress losses in fiberglass reinforcement during relaxation and creep. Vestnik MGSU. 2025. 20(1). Pp. 50–59. DOI: 10.22227/1997-0935.2025.1.50-59
18. Pisani, M.A. Long-term behaviour of beams prestressed with aramid fibre cables: Part 1: a general method. Engineering Structures. 2000. 22(12). Pp. 1641–1650. DOI: 10.1016/S0141-0296(99)00107-8
19. Pisani, M.A. Long-term behaviour of beams prestressed with aramid fibre cables: Part 2: an approximate solution. Engineering Structures. 2000. 22(12). Pp. 1651–1660. DOI: 10.1016/S0141-0296(99)00108-X
20. SP 63.13330.2018. Concrete and reinforced concrete structures. General provisions. Ministry of Construction, Housing and Utilities of the Russian Federation. Moscow, 2019. 119 p.
21. Wang, H.T., Wu, Q., Zhu, C.Y., Mao, Y.H., Guo, C.C. An innovative prestressing system of prestressed carbon fiber sheets for strengthening RC beams under flexure. Construction and Building Materials. 2024. 411. Article no. 134409. DOI: 10.1016/j.conbuildmat.2023.134409
22. Piatek, B., Siwowski, T., Michalowski, J., Blazewicz, S. Flexural Strengthening of RC Beams with Prestressed CFRP Strips: Development of Novel Anchor and Tensioning System. Journal of Composites for Construction. 2020. 24(3). Article no. 04020015. DOI: 10.1061/(ASCE)CC.1943-5614.0001020
23. Yang, J., Johansson, M., Al-Emrani, M., Haghani, R. Innovative flexural strengthening of RC beams using self-anchored prestressed CFRP plates: Experimental and numerical investigations. Engineering Structures. 2021. 243. Article no. 112687. DOI: 10.1016/j.engstruct.2021.112687
24. Stolyarov, O., Quadflieg, T., Gries, T. Effects of fabric structures on the tensile properties of warp-knitted fabrics used as concrete reinforcements. Textile Research Journal. 2015. 85(18). Pp. 1934–1945. DOI: 10.1177/0040517515578334

25. Zhang, J. Modeling of the influence of fibers on creep of fiber reinforced cementitious composite. Composites Science and Technology. 2003. 63(13). Pp. 1877–1884. DOI: 10.1016/S0266-3538(03)00160-X
26. Ghasemi, R., Safarabadi, M., Haghighi-Yazdi, M., Mirdehghan, S.A. Experimental and analytical study of flexural creep of impregnated woven fabric-reinforced concrete. Composite Structures. 2023. 321. Article no. 117192. DOI: 10.1016/j.compstruct.2023.117192

Information about the authors:

Pavel Mostovykh, *PhD in Physics and Mathematics*

ORCID: https://orcid.org/0000-0003-3714-2996

E-mail: mostovykh_ps@spbstu.ru

Anna Dontsova,

ORCID: https://orcid.org/0000-0002-9081-9575

E-mail: anne.dontsoova@gmail.com

Tatiana Koriakovtseva, *PhD in Technical Sciences*

ORCID: https://orcid.org/0000-0002-8380-0067

E-mail: tamusorina@mail.ru

Oleg Stolyarov, *PhD in Technical Sciences*

ORCID: https://orcid.org/0000-0002-2930-5022

E-mail: stolyarov_on@spbstu.ru

Received 13.09.2025. Approved after reviewing 07.11.2025. Accepted 07.11.2025.

Magazine of Civil Engineering

ISSN 2712-8172

journal homepage: http://engstroy.spbstu.ru/

Research article

UDC 69

DOI: 10.34910/MCE.139.3

Behavior of white wood at elevated temperatures: insights from numerical and experimental studies

N. Otmani-Benmehidi[1] ✉ , ***M. Boudjadja***[1] , ***A. Otmani***[2]

[1] *Materials, Geomaterials and Environment Laboratory, Faculty of Technology, Badji Mokhtar-Annaba University, P.O. Box 12, 23000 Annaba, Algeria*

[2] *National Higher School of Technology and Engineering, Department of Process and Energy Engineering, Annaba, Algeria*

✉ *nadia.otmani@univ-annaba.dz*

Keywords: wood, specimen, high temperature, oven, properties, white wood, SAFIR

Abstract. This study investigates the fire behavior of white wood, a commercially dominant softwood in Algerian construction (cf. *Picea abies*). Using a combined experimental and numerical approach, the thermo-mechanical degradation of 8×8×32 cm specimens was analyzed. Experiments involved heating samples in an electric oven at 200 °C and 300 °C, with complementary simulations performed using the SAFIR software. The results confirm that elevated temperatures induce significant mass loss and a pronounced thermal gradient, with the core lagging behind the surface. This thermal degradation directly compromises mechanical properties, notably stiffness. Furthermore, the study establishes a clear link between physical phenomena – charring, smoke emission, mass loss – and the underlying degradation mechanisms. A critical finding was the failure of adhesive bonds at high temperatures, revealing a key vulnerability in assembled wooden structures under fire conditions. These findings provide essential data for modeling the fire performance of a vital local material, thereby informing safer regional construction practices.

Acknowledgements: We sincerely thank the laboratory managers at Annaba Higher School of Industrial Technologies for granting us access to the furnaces for our tests. We also extend our gratitude to Professor J-M. Franssen for providing the 2022 SAFIR software.

Citation: Otmani-Benmehidi, N., Boudjadja, M., Otmani, A. Behavior of white wood at elevated temperatures: insights from numerical and experimental studies. Magazine of Civil Engineering. 2025. 18(7). Article no. 13903. DOI: 10.34910/MCE.139.3

1. Introduction

Wood, a noble material used in construction for millennia, saw a decline in popularity following several major fires and the rise of steel, concrete, and the industrial revolution. Today, however, its unique ecological and aesthetic properties, along with its natural texture, are garnering renewed interest in the era of global environmental consciousness, sustainable development, and the pursuit of a harmonious society. Wood's exceptional natural and environmental performance is capturing attention once more. Notably, the production of concrete and steel is unsustainable and significantly harms our planet [1]. Historically, timber exploitation was challenging due to the difficulty of treating, cutting, and transporting wood. Yet, advances in machinery and factory processes have made these tasks much simpler and more efficient. Growing and harvesting wood has now become a beneficial method, with increasing advantages as large-scale construction with this material expands. Additionally, older trees absorb less CO_2 and produce less oxygen, making it more practical to harvest them and plant new ones in their place [2].

Therefore, the object of this study is to investigate the potential of white wood as a sustainable construction material, particularly in light of its historical use, ecological benefits, and current relevance amid global environmental awareness.

Timber is one of the three primary structural materials used in the construction of large structures, alongside steel and reinforced concrete. When utilized in building types where it is most structurally efficient, harvested timber can significantly reduce the environmental impact of construction [3–6]. Timber's strength parallel to grain is comparable to reinforced concrete: hardwood is slightly stronger, and softwood slightly weaker, although timber cannot match modern high-strength concrete in compression. While timber is less stiff than concrete and both materials are less stiff and strong than steel, timber's low density offers an advantage. This makes it particularly efficient for long-span or tall structures, where a significant portion of the load comes from the structure's own weight [6–9, 13].

Among the many advantages of timber, one of the most significant is that wood is one of the few building materials capable of storing carbon throughout the life of a building [10]. This storage capability helps reduce the carbon emissions released by trees at the end of their life cycle and mitigates the presence of other atmospheric carbon sources. It is generally estimated that 1 m^3 of wood can sequester 1 t of CO_2. Additionally, wood is the only building material sourced from renewable and sustainably managed resources: trees. Unlike materials that originate from non-renewable resources, wood is harvested from forests, making it an eco-responsible and sustainable choice [10, 11].

Wood is often defined as the secondary xylem in the stems of trees, consisting almost entirely of cell wall material. The properties of wood derive from its cell wall structures and the composition of wood polymers [12].

The main hemicelluloses of softwood are galactoglucomannan and arabinoglucuronoxylan, while in hardwood it is glucuronoxylan. Galactoglucomannan from softwood and glucuronoxylan from hardwood are decorated with acetyl groups (Fig. 1). Although it is unknown how different hemicelluloses impart properties to the cell walls, hemicelluloses are proposed to crosslink with cellulose by hydrogen bonds, which may influence the ability of the microfibrils to slip past one another [6]. Wood cell walls (fibers, tracheids, etc.) may be impregnated with lignin, making these walls impervious to water.

Lignin is also often regarded as the cementing agent that provides the cell wall rigidity and compressive strength. Extractives are a collective term for a series of organic compounds present in certain timbers in relatively small amounts, which include coloring matter, phenolics, turpentine, fatty acids, resin, and simple metabolic intermediates. Extractives impart colouration to the wood and give it its natural durability, as most of these compounds are toxic to both fungi and insects [6, 12].

In the secondary cell wall layers, the microfibrils are closely packed and parallel to each other. In addition to the cell lumen, the secondary cell wall is subdivided into three layers: S1, S2, and S3. Wood is highly anisotropic, meaning that its physical properties differ along different axes. The angle between the cellulose microfibrils and the longitudinal cell axis, the microfibril angle, is found to be a critical factor in determining the structural and mechanical properties. The varying fibril orientation in the particular layers (50°–70° in S1, 5–15° in S2, and 60–90° in S3) causes a mechanical locking effect, leading to a very high stiffness of the overall cell [4–6, 12]. Due to its thickness (90 % of the secondary cell wall) and low value of micro fibril angle, the S2 layer is responsible for the high tensile strength and stiffness and low shrinkage of wood in the longitudinal direction. Increased microfibril angle in the S2 layer decreases cell wall tensile strength and stiffness but increases the durability [10–13].

To answer the question why tomorrow's buildings should be made of timber, many studies on wood structures subject to fire have been carried out [14–38].

Hu et al. [15] conducted experimental studies and numerical simulations to investigate the mechanism of the incipient and growth stages of a building fire. The building, constructed in the 1980s with wooden components, has one compartment and one opening. The average fire load density was 1495.3 MJ/m^2, including the wooden columns, beams, furniture, etc. The evolution of indoor temperature, gas concentration, gas flow rate, and burning behaviors were obtained and analyzed in their work. This study helps to learn the characteristics of early and growth stages of building fires with wooden components.

Buchanan [16] has a review paper of the performance of timber buildings exposed to fire. Important distinctions are made between the impacts of pre- and post- flashover fires, and between the performance of light timber framing and heavy timber construction. Recent literature is reviewed.

Dietenberger [17] carried out work on the fire resistance of wood structures, using the ABAQUS software, through simulation, the temperature evolution can be observed in detail in the section and throughout the fire exposure.

Fawaz [18] and Park studied the thermal decomposition of wood. Park & Atreya [19] use 25.4 mm diameter dry wood spheres, both experimentally and theoretically. Pyrolysis of the wood spheres was conducted in a vertical tube furnace at temperatures ranging from 638 K to 879 K. During the pyrolysis process, mass loss and sample temperatures were measured. Center temperature measurements revealed two distinct thermal events, indicating sequential endothermic and exothermic reactions. A numerical study of these reactions, employing various pyrolysis kinetics models, was performed to elucidate the pyrolysis mechanism and the heats of the reactions. The comparison between experimental and numerical results showed that: (1) contrary to suggestions in the literature, the contributions of secondary tar decomposition and lignin decomposition to the center temperature exothermic peak are minimal; (2) the exothermic decomposition of the intermediate solid is responsible for the center temperature peak; (3) the center temperature plateau is due to the endothermic decomposition of cellulose; (4) internal pressure generation is critical as it controls the pyrolyzate mass transfer, thereby affecting both heat transfer and the residence time of the pyrolysis gases for secondary decomposition.

Gernay et al. [20] conducted an experimental study on timber columns, finding that they had a measured fire resistance of 55–58 min (for two specimens). However, when exposed to heating for 15 min, these columns failed during the cooling phase after 98–153 min (for two specimens).

Renard et al. [21] present the findings from six fire tests performed on glue laminated timber columns in a custom-built compartment. Wood cribs are used as fuel. The columns, 3680 mm long with a 280× ×280 mm^2 section, are subjected to constant axial loading during the whole fire duration. Column failure was observed in the six tests, with failure times ranging from 35 min to 71 min.

Elshayeb et al. [22] introduced an advanced methodology using the finite element method (FEM) to analyze square and circular wood columns by developing a virtual temperature history model. A numerical simulation model for the wood column was created using a two-dimensional mathematical framework based on Galerkin's Weighted Residual technique. This model focuses on the regional material properties of the wood column to describe its thermal behavior. By understanding the temperature history within a column and the relevant material properties, the column's strength can be calculated at any point during a fire.

Šulc et al. [23] introduce a heat transport model that incorporates a moving boundary condition, a criterion for finite element deactivation, and an internal heat source. Experimental comparisons using a constant radiative load show that the moving boundary condition becomes significant after approximately 10 min of fire exposure, leading to a consistent charring rate observed in multiple experiments.

Wichman & Atreya [24] developed a simplified model for the pyrolysis of charring materials, excluding the effects of moisture and assuming zero heat of pyrolysis. They identified four stages of pyrolysis: (i) inert heating, (ii) initial pyrolysis, (iii) thin char formation, and (iv) thick char formation. Formulas for the volatile mass efflux, m, are derived for stages (ii), (iii), and (iv), with m = 0 in the first stage. The calculations indicate that during the initial pyrolysis stages (kinetically controlled regime), the surface temperature governs the volatile production rate, whereas during the thick char stage (diffusion-controlled regime), the temperature gradient governs the volatile production rate. Comparisons between the calculated results and numerical computations were made for volatile mass efflux, surface temperature, and density.

Gong et al. [25] initially conducted thermogravimetric analysis (TGA) tests to parameterize the pyrolysis model using the model fitting method. Subsequently, gram-scale autoignition experiments with five power-law heat fluxes (HFs) were performed in a newly designed apparatus. The thermodynamics of oriented strand board (OSB) were determined through inverse modeling, combining an improved numerical model with measured surface temperatures and mass loss rates under a moderate HF. The model's extrapolation capability was verified by simulating additional experimental measurements under different heating scenarios. Critical temperature and critical mass flux were utilized to predict autoignition times. The results demonstrate that the developed pyrolysis model accurately captures the measured mass and mass loss rate from the TGA tests. Additionally, there was good agreement between the simulated and measured surface temperatures and mass loss rates in bench-scale tests, despite minor divergences due to observed cracks in the generated char layer. Other authors have also investigated wood degradation phenomena, such as [26–32].

Majdalani et al. [33] developed a simplified compartment fire model to evaluate the fuel contribution of exposed timber elements. The study concluded that the potential for convective fire spread is positively correlated with the percentage of exposed timber surface area. When exposed to fire, load-bearing mass timber structures, such as cross-laminated timber (CLT), soften and decompose, resulting in significant deformation and weakening, which ultimately leads to structural failure. A combined experimental and modeling analysis is presented to predict the post-fire residual compression properties of CLT. Multiple experimental fire exposure and post-fire mechanical tests were conducted by Loh & Barnett [34] under identical conditions to characterize the internal and external thermal responses of the CLT and evaluate its residual compression properties. An analytical modeling strategy, based on the measured through-the-

thickness temperature profile during fire exposure, is introduced to predict the residual compression properties. X-ray computed tomography analysis revealed a nonconstant charring rate, consistent with current research findings but not with Eurocode design suggestions. The analytical analysis indicated that the transverse (cross) laminae contribute minimally to the axial compression properties but play a critical role in providing thermal protection and maintaining the structural integrity of the longitudinal (load-aligned) laminae during fire exposure.

Khelifa et al. [35] investigated a study to propose a model that accounts for the variation of thermophysical properties, the development of char, and its evolution with temperature. This model integrates a sequential coupling of heat transfer analysis with structural response. The degradation of material properties is considered using the regulatory approach recommended in Eurocode 5. Stress analysis employs an elasto-plastic model with nonlinear isotropic hardening. The model is implemented within the Abaqus finite element software using external subroutines. Its predictions align well with experimental data, accurately reproducing both thermal and structural responses. Specifically, the model accurately predicts temperature profiles, displacements, and the depth of the charred layer, which begins to form above 300 °C.

The behavior of Algerian white wood (AWW) under high temperatures has been rarely considered in the current available literature. This study addresses this significant gap by investigating the phenomena resulting from a fire and determining key properties: the loss of mass and temperature evolution, which are crucial factors for the mechanical behavior of white wood when exposed to fire. Understanding these properties is essential for its application in construction, particularly in Algeria where it is used in individual houses and as structural elements in roof frameworks. By providing new insights into the fire behavior of white wood, this research contributes to safer and more sustainable construction practices, promoting the use of this environmentally friendly material in the building industry.

To analyze the behavior of AWW under various high-temperature conditions, we conducted an experimental study on wooden specimens with dimensions of 8×8×32 cm. The samples were heated in electric ovens at four different temperature levels (150 °C, 200 °C, 300 °C, and 400 °C) for one hour. The physical and mechanical properties of wood at ambient temperature were previously determined through experimental work. Additionally, we performed a numerical study using the SAFIR [36] code on the same type of samples. This approach offers a fairly good understanding of the high temperature behaviour of AWW.

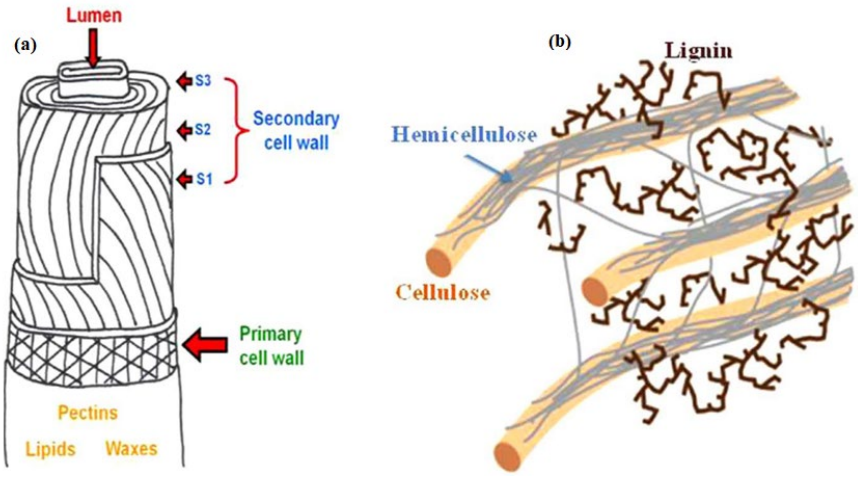

Figure 1. (a) Cell wall structural organization. (b) Cell wall polymer interactions in secondary cell wall of hardwood [6].

2. Materials and Methods

2.1. Materials

This study utilized a commercially prevalent Algerian softwood (AWW), locally known as 'white wood', selected for its direct relevance to regional construction practices. Although a precise botanical classification was unavailable, the timber is characterized as a low-density, light-colored softwood with properties comparable to European spruce (*Picea abies*). This is supported by an average air-dry density of 507.25 kg/m^3, moisture content of 15.35 % and mechanical properties – including a tangent modulus of ≈1779 MPa, tensile strength of ≈100 MPa, and compressive strength of ≈36 MPa – that fall within the expected range for spruce. Full material characterization is provided to guarantee the reproducibility of the experimental work.

2.2. Experimental Study

This study subjected specimens to four heating-cooling cycles from an ambient temperature of 30 °C to target temperatures of 150 °C, 200 °C, 300 °C, and 400 °C in an electric oven (Fig. 2). A heating rate of 12 °C/min was used to simulate severe fire conditions approximating the standard ISO 834 fire curve. The specimens were positioned to ensure even heat distribution. For the 200 °C and 300 °C cycles, a thermocouple placed near the center of the sample sections (Fig. 2b) recorded temperatures at five-minute intervals. As illustrated in Fig. 3 and consistent with the literature [15], the effects of heat were reversible for temperatures below 100 °C (Zone 1).

Figure 2. Type of furnace used: (a) specimen in 300 °C heating, (b) furnace containing a sample with a thermocouple.

Furthermore, prolonged exposure to temperatures exceeding 65 °C leads to persistent alterations in the wood mechanical characteristics. As the temperature approaches 100 °C, the wood rapidly loses its free water, followed by its bound water. The temperature plateaus until all the water has completely evaporated. A rapid temperature increase then results in a slow loss of solid mass up to approximately 240 °C due to pyrolysis (Zone 2). At temperatures around 300 °C (Zone 3), the pyrolysis process releases flammable gases, and the wood is considered carbonized. Consequently, charring layers form and advance through thermal conduction within the material. The combustion of wood, which begins between 150 °C and 200 °C, releases gases including non-combustible carbon dioxide and combustible carbon monoxide [16–18].

2.3. Numerical Study: Thermal and Mechanical Analysis

The numerical study considered the following thermal properties: thermal conductivity, specific heat capacity, density, and emissivity. The convection coefficient ($W/m^2 \cdot K$) and emissivity (–) for both heated and unheated surfaces were also defined. According to Eurocode EN 1991-1-2, the recommended convection coefficient for heated surfaces is 25 $W/m^2 \cdot K$ under standard time–temperature curves, while for unheated surfaces, a value of 4 $W/m^2 \cdot K$ is suggested when radiation heat transfer effects are not taken into account. The recommended emissivity, unless otherwise specified in the material-related fire design parts of the Eurocodes, is 0.8.

The mechanical properties of this type of wood (AWW), determined from previous experiments under normal conditions, are as follows on: tangent modulus = 1779 MPa, tensile strength = 100 MPa, and compressive strength = 36 MPa.

According to Annex B of EN 1995-1-2:2004 [7] for 'WOODEC5', the thermal behavior of wood is considered purely conductive, using modified thermal properties that represent complex phenomena. Two-dimensional numerical models of wood sections were developed in SAFIR, with the grain direction oriented perpendicular to the section.

3. Results and Discussions

3.1. Experimental Results

3.1.1. State of specimens after heating

Table 1. Mass loss of wood specimens.

N°	Level of temperature	Mass before heating (g)	Mass after heating (g)	Mass loss (%)
1	150°C	935	917	1.93
2	200°C	933	850	8.89
3	300°C	984	502	48.98
4	400°C	1034	409	60.44

The mass of the test specimens was measured before and after each heating cycle, revealing a consistent decrease in mass with increasing temperature. The calculated mass loss for each cycle is presented in Table 1.

At 150 °C, the mass loss was negligible (approximately 2 %) and was accompanied by a color change from white to red, indicating the evaporation of free and bound water. As the temperature increased to 200 °C, the mass loss became more substantial, rising to 9 %.

Significant mass loss occurred at 300 °C and 400 °C, exceeding 50 % of the original mass (Fig. 3), a finding consistent with prior studies [23, 24]. These high-temperature cycles were also characterized by copious smoke emission (Figs. 4 and 5), a strong odor, and the blackening of wood due to carbonization.

Furthermore, the adhesive bond between the wood components deteriorated, leading to detachment. This is attributed to the thermal degradation of the glue. The pyrolysis process at these temperatures (200 °C and above) released combustible gases, including carbon monoxide (CO) and carbon dioxide (CO_2), with CO concentration increasing significantly in the high-temperature zone (above 300 °C) [25, 26]. While wood typically contains minimal nitrogen and sulfur, its behavior shares similarities with other biomass materials like coal, though wood generally has a lower aromatic content.

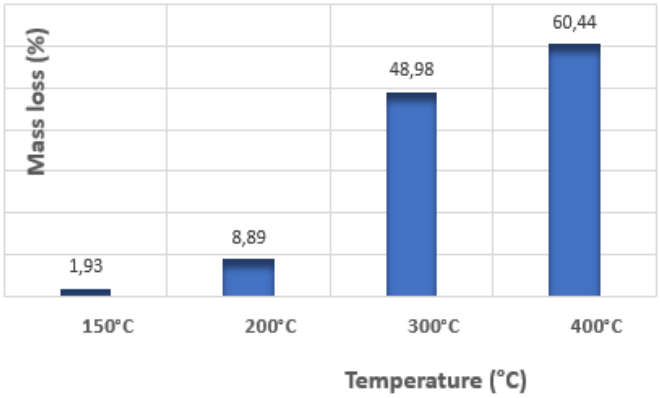

Figure 3. Mass loss of used specimens.

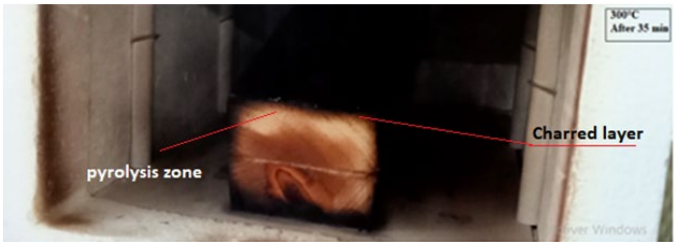

Figure 4. Specimen exposed at 300 °C.

Figure 5. Specimens after exposition to different heating rates, during 60 min.

Fig. 4 shows the cross-section of wood exposed to 300 °C. Different parts are identified: a charred layer, a layer of pyrolysis (about 5 mm) and the core of the intact section.

Smoke emission was observed from 200 °C during the heating phases, indicating the release of volatile gases, including CO and CO_2. This marks the onset of pyrolysis, where wood decomposes into char, non-flammable gases (e.g. water vapour, CO_2), and combustible gases (e.g. CO, H_2, hydrocarbons).

The concentration of combustible gases, particularly CO, increases with temperature [15–18]. The exothermic combustion of these released gases further elevates the system temperature.

When the temperature reached 400 °C, a distinct shift occurred towards dominant char production at the expense of volatile gas release (Zone 4). At this stage, the specimen was cooled outside the oven (Fig. 5).

This thermal degradation behavior is governed by the decomposition of wood primary constituents. Hemicellulose decomposes first (200–260 °C), producing acetic acid. Cellulose degrades between 240–350 °C, forming levoglucosan, while lignin decomposes over a broad range (280–500 °C) and is the primary contributor to char formation [17].

3.1.2. Temperature variation in the cross-section

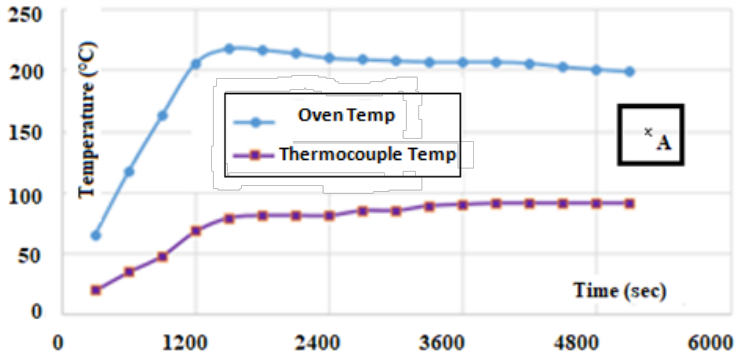

Figure 6. Temperature variation at point in central zone for hating level of 200 °C.

Fig. 6 displays the temperature profiles over time for the furnace air and the center of the wood specimen. The oven temperature rose over 20 min before stabilizing at the target of 200 °C. The temperature at the wood center followed a similar trend in both the 200 °C and 300 °C tests (Fig. 7), consistent with references [19, 20]. However, the wood heated more slowly, creating a thermal lag and a sustained ~100 °C difference from the oven temperature.

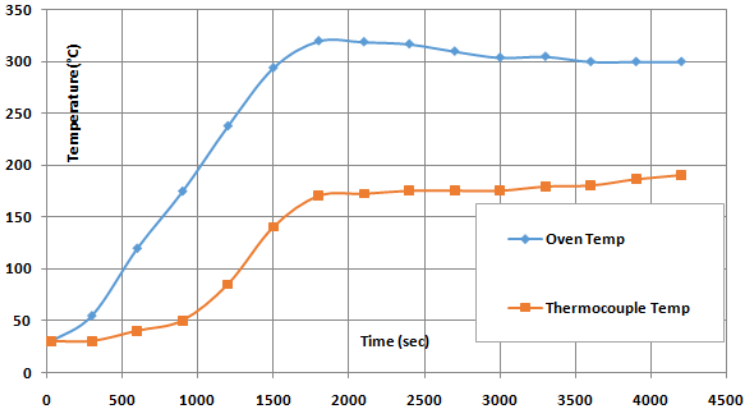

Figure 7. Temperature variation at point in central zone for hating level of 300 °C.

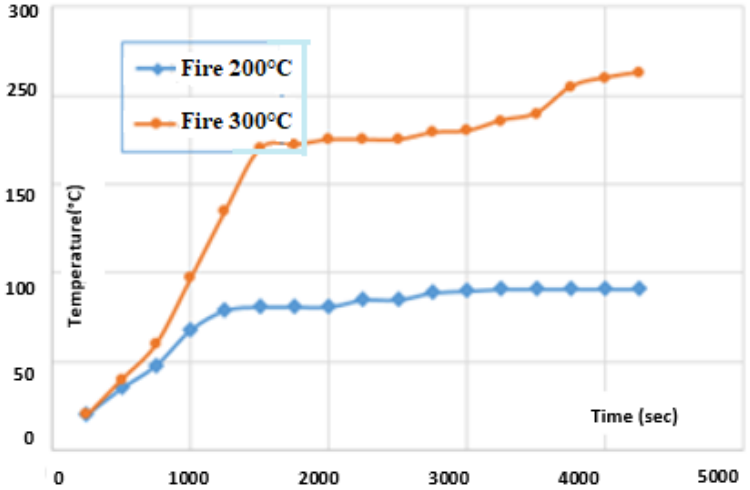

Figure 8. Temperature variation at point in central zone for hating level of 200 °C and 300 °C.

According to Fig. 8, the temperature evolution at a point in the central zone can be observed. At the 200 °C heating level, the temperature curve initially increases with time and then stabilizes at values not exceeding 100 °C. In contrast, at the 300 °C heating level, the temperature at the considered point rises rapidly to approximately 175 °C, remains stable for about 30 min, and then increases again, reaching around 225 °C at the end of the test. This marks the onset of thermal degradation for this type of wood.

It was also observed that during oven cooling (as the furnace temperature decreased to 30 °C), the temperature at the center of the specimen continued to rise, reaching about 270 °C after one hour. After several hours of cooling, the entire sample turned black, indicating significant polymerization of cellulose, which typically occurs in the 300–350 °C range. Chemical reactions occurring at this stage are consistent with findings reported in the literature [21–24].

This study demonstrates that the energy balance at the combustion surface is mainly influenced by the intensity of the heating conditions, which directly affect the evolution of wood mechanical properties [29, 30] (see Fig. 5). These aspects will be analyzed in the future work.

3.2. Numerical Results

3.2.1. Temperature variation in the cross-section

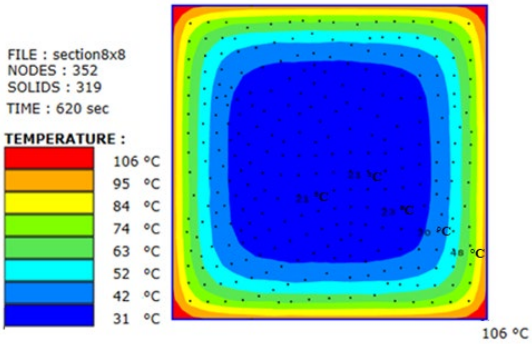

Figure 9. Temperatures distribution within the wood section, considering the heating curve of the furnace during 620 sec (10 min).

Based on the thermal analysis results, the central zone reached a temperature of 21 °C after 10 min of fire exposure (Fig. 9). Moving away from the central zone, the temperature increased; at the corner, it reached 106 °C after 10 min, corresponding to the onset of water evaporation. After 60 min (1 hour), the temperature at this location rose to 299 °C (Fig. 10), which is approximately equal to the furnace temperature corresponding to the 300 °C heating level.

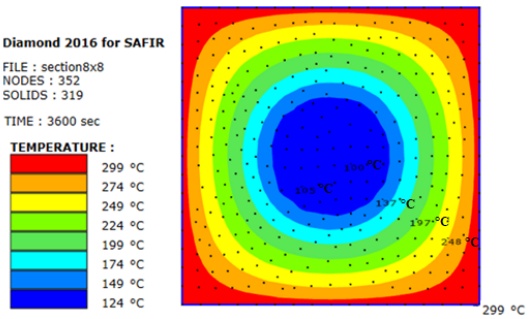

Figure 10. Temperatures distribution within the wood section, considering the heating curve of the furnace during 3600 sec (60 min).

According to Fig. 10, during 60 min of exposure in the furnace, the central zone of the wood section reached a temperature of approximately 100 °C (blue area), corresponding to the release of moisture. The intermediate zone exhibited temperatures in the range of 100–200 °C (light blue and green areas), indicating the onset of the pyrolysis process. Finally, the outermost region, referred to as the charred zone, was represented by yellow, brown, and red colors. The temperature variations at three points within these defined zones are illustrated in Fig. 11.

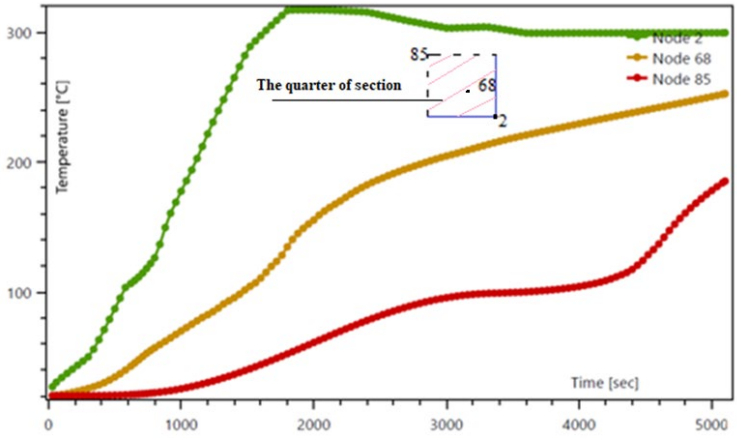

Figure 11. Temperature at the nodes 85, 68, and 2 in the section column heated in the furnace.

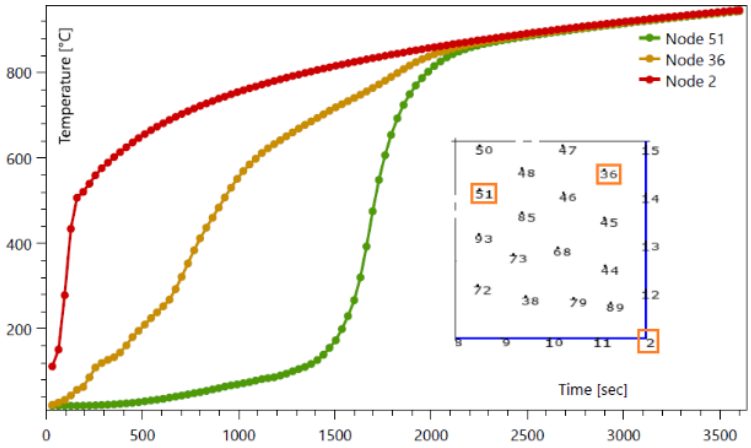

Figure 12. Temperature at the nodes 51, 36, and 2 in the column section exposed to ISO834 fire.

The graphs in Fig. 12 show the temperature variation at three locations on a wood section exposed to the standardized ISO834 fire. Node 2 is at the section corner, and its temperature curve closely follows the ISO834 fire curve. Node 36 is located on the edge of the section, and Node 51 is at the center.

It is clear that the temperature at Node 36 increases more rapidly than at the central Node 51. The standard fire is more severe than the oven fire used in previous tests, which explains why the temperature at the center of the section (Node 51) reaches 900 °C after 60 min in this scenario. These results are in accordance with [19–21].

Fig. 13 shows the progression of carbonization in the section after 25 min of fire exposure. In the normalized fire (Fig. 13a), the charred layer (represented in red) is significant at this stage, a finding

consistent with [19]. Green represents the pyrolysis zone (degrading wood), while blue represents the wood that has lost all its water (dry wood).

As shown in Fig. 13b, the central area (blue) remains quite wide, with a maximum temperature of 55 °C, indicating the fire has not yet reached this wood. Thermal degradation begins around 200 °C to 250 °C (red part), a threshold that aligns with the experimental findings presented in Fig. 5.

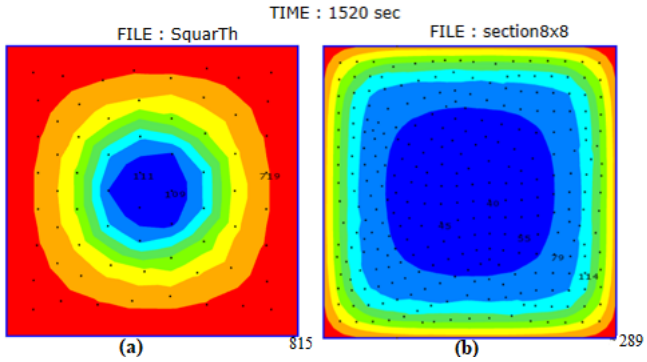

Figure 13. Temperatures distribution within the wood section after 25 min, considering the ISO834 curve fire (a) and heating curve of the furnace (b).

In conclusion, the three distinct zones described in the literature [20–22] – pyrolysis, carbonization, and the core of intact wood – are more clearly observed in the simulation (Fig. 13b) after a 25-minute heating period. This enhanced clarity is due to the specimen's small cross-section, a phenomenon that was also confirmed experimentally (Fig. 4).

According to the model by Khelifa et al. [35], the charred layer begins to form at temperatures above 300 °C. In a rectangular section exposed to fire on all faces, this process causes the residual section to lose its original shape. Furthermore, as the charred layer lacks mechanical strength, the overall load-bearing capacity of the fire-exposed cross-section is reduced [23, 34]. The results of this study are consistent with this model and with the findings of [20, 21].

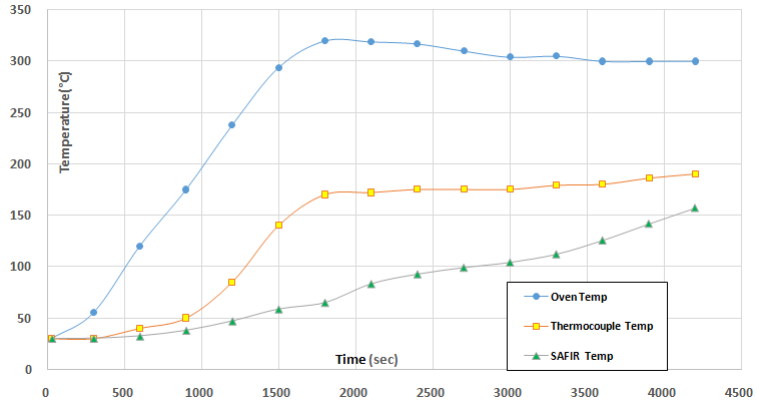

Figure 14. Comparison of numerical and experimental temperature results at a central point, considering a heating level of 300 °C.

Fig. 14 presents two curves illustrating the temperature evolution obtained from the numerical results (blue and brown). The blue curve corresponds to a point located at the corner of the section and closely follows the furnace temperature curve with a heating level of 300 °C. The second curve represents a point at the center of the section. A third curve (gray and green), also corresponding to this central point, is derived from the experimental results. The curves showing the temperature evolution in the central zone display a noticeable deviation. It is important to note that the experimental curve exhibits a rapid increase between 1000 sec and 1750 sec, which can be attributed to the relatively high heating rate applied in this study (12 °C/min).

3.2.2. Residual tangent modulus

At the beginning of heating (30 sec), a slight variation in the tangent modulus is observed, particularly at the corners and along the edges of the element. It can be seen that the tangent modulus of wood decreases due to the rise in temperature (Fig. 15). After 742 sec – the failure time of the wood element – the tangent modulus has significantly decreased. At the upper corners, it reaches a value of zero, while along the edges it is approximately 660 MPa. This value increases toward the center of the section, ranging between 880 MPa and 1540 MPa (Fig. 16).

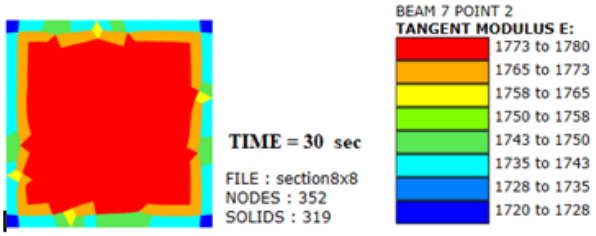

Figure 15. Residual tangent modulus at 30 sec.

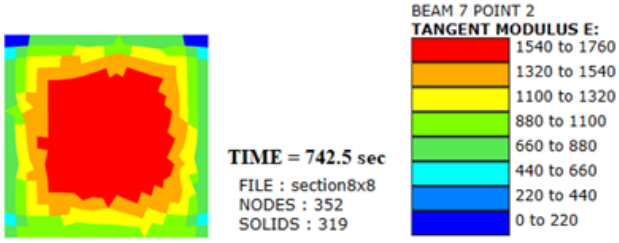

Figure 16. Residual tangent modulus at failed time (742.5 sec).

In SAFIR, the elements of the section considered in the thermal analysis are modeled as fibers when coupling heat transfer with structural behavior. Each fiber possesses mechanical properties that evolve with temperature over time. Fig. 17 presents four curves, each corresponding to a specific fiber within the structural element.

The selected fibers provide insight into the behavior of different regions: the central zone (Fib 117), the edges (Fib 69), and the corners (Fib 205 and Fib 208). The corner and edge fibers generally exhibit similar behavior – their curves decrease over time, indicating a reduction in the tangent modulus to about 600 MPa, approaching failure at approximately 675 sec. For the top-corner fiber (Fib 208), a rapid drop to zero is observed. Fiber 205 initially shows an increase followed by stabilization around 900 MPa, which can be attributed to the anisotropic nature of wood. The edge fiber (Fib 69) also exhibits a decrease in tangent modulus with time and increasing temperature but maintains a difference of about 300 MPa compared to the corner fibers, reaching 700 MPa at failure. In contrast, the central-zone fiber (Fib 117) shows no variation in its tangent modulus.

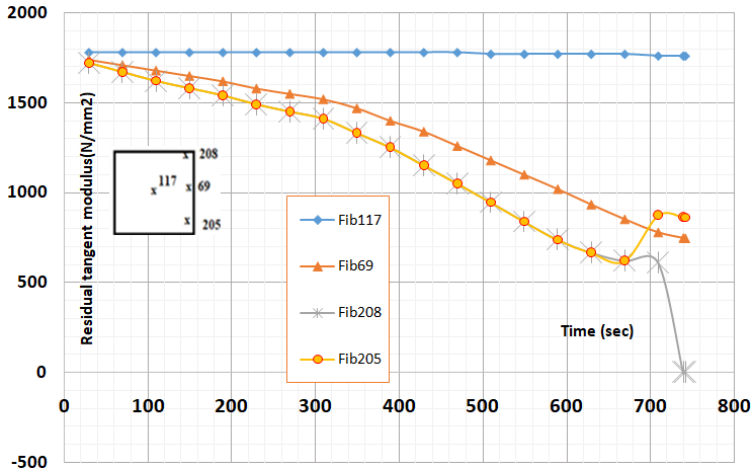

Figure 17. Residual tangent modulus evolution according the time.

This observation is consistent with expectations, as during this period (700 sec), the temperature in this zone remains below 50 °C, as indicated by both the numerical and experimental curves (Fig. 14). Accordingly, the wood in this region retains its integrity and exhibits no signs of thermal degradation.

4. Conclusion

The results of this work lead to the central conclusion that the vulnerability of AWW in fire scenarios stems not only from the degradation of the wood itself but also from the premature failure of its glued connections.

1. This experimental and numerical study delineates the thermal degradation process of wood, revealing a clear sequence of moisture loss, pyrolysis, and charring. The mass loss was negligible at 200 °C but became substantial (exceeding 50 %) at temperatures of 300 °C and above, accompanied by significant smoke and the release of CO and CO_2. A critical finding was the mechanical failure of glued sections at these higher temperatures, highlighting vulnerability in constructed elements. Furthermore, the analysis of individual fibers provided a novel, micromechanical perspective, demonstrating a progressive weakening at the edges and corners while the core remained stable and intact.
2. A key scientific contribution of this work is the successful validation of a thermo-mechanical model using SAFIR software. The simulation results demonstrated a close alignment with experimental data, accurately capturing phenomena such as char layer formation and the preservation of an intact core after a 25-minute heating period. This validates the model as a reliable tool for predicting the behavior of timber sections under fire conditions, which can reduce the reliance on costly and time-consuming experimental testing.
3. Our findings both confirm and supplement prior research. The observed stages of degradation – free and bound water loss followed by pyrolysis and carbonization – are consistent with the established literature on wood combustion [26–32]. Similarly, the formation of a protective char layer and the survival of a cool, intact core align with classical theories of timber fire performance. However, this study supplements this knowledge by quantitatively linking these thermal phenomena to the localized mechanical degradation, specifically the time-and temperature-dependent reduction of the tangent modulus in peripheral fibers. The observed adhesive failure at 300 °C also presents a critical, practical finding that may not be fully accounted for in models focusing solely on solid timber.

5. Implications and Future Work

In conclusion, this research provides a validated framework for analyzing the fire-induced mechanical degradation of wood, with specific insights into the behavior of AWW (cf. *Picea abies*). The demonstrated sensitivity of this timber to the heating source's magnitude and properties underscores the need for material-specific characterization. The central objective of subsequent studies will be to map the progression of residual mechanical properties, thereby refining predictive models to enable safer timber structural design.

References

1. National Lumber Manufacturers Association. Wood Structural Design Data. Vol. 1. 2nd ed. Washington, 1941. 296 p.
2. Hansen, H.J. Timber Engineers Handbook. John Wiley & Sons. New York, 1948. 882 p.
3. CEN. Eurocode 5: Design of timber structures. Part 1-2: General – Structural fire design. EN 1995-1-2. European Committee for Standardization. Brussels, 2004. 71 p.
4. Schweingruber, F.H. Wood Structure and Environment. Springer. Berlin, Heidelberg, 2007. XII + 279 p. DOI: 10.1007/978-3-540-48548-3.
5. Dinwoodie, J.M. Timber: its nature and behaviour. 2nd ed. Taylor and Francis. Abingdon, United Kingdom, 2000. 257 p.
6. Ramage, M.H., Burridge, H., Busse-Wicher, M. The wood from the trees: The use of timber in construction. Renewable and Sustainable Energy Reviews. 2017. 68(1). Pp. 333–359. DOI: 10.1016/j.rser.2016.09.107
7. Cotton, C.M. Ethnobotany: Principles and Applications. John Wiley and Sons. Chichester, 1996. IX + 424 p.
8. Hillis, W.E. Heart Wood and Tree Exudates. Springer. Berlin, Heidelberg, 1987. XIV + 268 p. DOI: 10.1007/978-3-642-72534-0
9. The American Wood Council (AWC). Wood Structural Design Data. 1986 Edition with 1992 Revisions. American Forest & Paper Association. Washington, 2004. 270 p.
10. Švajlenka, J., Pošiváková, T. Innovation potential of wood constructions in the context of sustainability and efficiency of the construction industry. Journal of Cleaner Production. 2023. 411. Article no. 137209. DOI: 10.1016/j.jclepro.2023.137209
11. Budykina, T.A., Anosova, Ye.B. Thermal resistance of fire retardant materials. Magazine of Civil Engineering. 2022. 112(4). Article no. 11213. DOI: 10.34910/MCE.112.13
12. Tsvetkov, N.A., Tolstykh, A.V., Khutornoi, A.N., Boldyryev, S., Kolesnikova, A.V., Tsvetkov, D.N. Thermophysical analysis of heat-insulated glued laminated profiled timber for wooden houses. IOP Conference Series: Earth and Environmental Science. 2021. 866. Article no. 012037. DOI: 10.1088/1755-1315/866/1/012037
13. Zhou, T., Liu, H. Research Progress of Wood Cell Wall Modification and Functional Improvement: A Review. Materials. 2022. 15(4). Article no. 1598. DOI: 10.3390/ma15041598
14. Purkiss, J. Fire Safety Engineering: Design of Structures. 2nd ed. CRC Press. London, 2006. 424 p. DOI: 10.1201/b12845
15. Hu, H., Qi, Zh., Shi, J., Li, H., Ji, J. Experimental and numerical investigations on fire development in a timber-based compartment with identification of characteristic events. Journal of Building Engineering. 2024. 87. Article no. 109033. DOI: 10.1016/j.jobe.2024.109033
16. Buchanan, A.H. Fire performance of timber construction. Progress in Structural Engineering and Materials. 2000. 2(3). Pp. 278–289. DOI: 10.1002/1528-2716(200007/09)2:3<278::AID-PSE33>3.0.CO;2-P
17. Dietenberger, M. Update for combustion properties of wood components. Fire and Materials. 2002. 26(6). Pp. 255–267. DOI: 10.1002/fam.807

18. Fawaz, M., Gollner, M.J., Bond, T.C. A novel representation of time-resolved particle emissions from pyrolyzing wood. Biomass and Bioenergy. 2024. 183. Article no. 107054. DOI: 10.1016/j.biombioe.2024.107054
19. Park, W.C., Atreya, A., Baum, H.R. Experimental and theoretical investigation of heat and mass transfer processes during wood pyrolysis. Combustion and Flame. 2010. 157(3). Pp. 481–494. DOI: 10.1016/j.combustflame.2009.10.006
20. Gernay, Th., Zehfuß, J., Franssen, J.-M., Robert, F., Brunkhorst, S., Felicetti, R., Bamonte, P., Mohaine, S., McNamee, R. Experimental assessment of the burnout resistance of timber and concrete columns. SiF 2022 – The 12th International Conference on Structure in Fire. The Hong Kong Polytechnic University. Hong Kong, 2022.
21. Renard, S., Robert, F., Franssen, J-M., Zehfuß, J., McNamee, R., Bamonte, P., Gernay, Th. Structural behavior of timber columns in wood crib compartment fire tests. Fire Safety Journal. 2025. 155. Article no. 104413. DOI: 10.1016/j.firesaf.2025.104413
22. Elshayeb, M., Ab Malik, A.R., Ideris, F., Hari, Z., Ab Razak, N., Siang, J.E.L., Anuar Z., Utilization of Numerical Techniques to Predict the Thermal Behavior of Wood Column Subjected to Fire. Part A: Using Finite Element Methods to Develop Mathematical Model for Wood Column. Key Engineering Materials. 2006. 306–308. Pp. 577–582. DOI: 10.4028/www.scientific.net/KEM.306-308.577
23. Šulc, S., Šmilauer, V., Wald, F. Thermal Model for Timber Fire Exposure with Moving Boundary. Materials. 2021. 14(3). Article no. 574. DOI: 10.3390/ma14030574
24. Wichman, I.S., Atreya, A. A simplified model for the pyrolysis of charring materials. Combustion and Flame. 1987. 68(3). Pp. 231–247. DOI: 10.1016/0010-2180(87)90002-2
25. Castagna, A., Geng, Y., Rein, G. Historical investigation into the first burning model of a solid fuel and the origin of the Crank–Nicolson numerical method. Applications in Energy and Combustion Science. 2025. 24. Article no. 100404. DOI: 10.1016/j.jaecs.2025.100404
26. Zhang, Y., Lu, J., Yu, J., Wang, W., Zhai, Sh., Yu, Yi., Qi, D. A controllable and fast carbonization strategy under air conditions and its application in electromagnetic interference (EMI) shielding. Composites Part A: Applied Science and Manufacturing. 2025. 192. Article no. 108764. DOI: 10.1016/j.compositesa.2025.108764
27. Gong, J., Zhang, M. Pyrolysis and autoignition behaviors of oriented strand board under power-law radiation. Renewable Energy. 2022. 182. Pp. 946–957. DOI: 10.1016/j.renene.2021.11.032
28. Spearpoint, M.J., Quintiere, J.G. Predicting the burning of wood using an integral model. Combustion and Flame. 2000. 123(3). Pp. 308–325. DOI: 10.1016/S0010-2180(00)00162-0
29. Agarwal, P.K. Transport phenomena in multi-particle systems-IV. Heat transfer to a large freely moving particle in gas fluidized bed of smaller particles. Chemical Engineering Science. 1991. 46(4). Pp. 1115–1127. DOI: 10.1016/0009-2509(91)85104-6
30. Yao, X., Yu, Q. Kinetic and experimental characterizations of biomass pyrolysis in granulated blast furnace slag. International Journal of Hydrogen Energy. 2018. 43(19). Pp. 9246–9253. DOI: 10.1016/j.ijhydene.2018.03.173
31. Di Blasi, C. Modeling chemical and physical processes of wood and biomass pyrolysis. Progress in Energy and Combustion Science. 2008. 34. Pp. 47–90.
32. Colombiano, J., Batiot, B., Dréan, V., Richard, F., Guillaume, E., Rogaume, T. Numerical analysis of the characteristics of the decomposition zone of a burning wood sample under cone calorimeter and evaluation of the limiting process. Journal of Analytical and Applied Pyrolysis. 2022. 168. Article no. 105752.
33. Majdalani, A.H., Calderón, I., Jahn, W., Torero, J.L. Understanding Compartmentation Failure for High-Rise Timber Buildings. Fire. 2024. 7. Article no. 190. DOI: 10.3390/fire7060190
34. Loh, T.W., Barnett, J.R. Fire-induced damage and postfire analysis of the compression properties of cross-laminated timber. Journal of Materials in Civil Engineering. 2024. 36(31). Article no. 04023595. DOI: 10.1061/JMCEE7.MTENG-16285
35. Khelifa, M., Thi, V., Oudjène, M., Khennane, A. Modelling the Response of Timber Beams Under Fire. International Journal of Civil Engineering. 2024. 22. Pp. 1537–1549. DOI: 10.1007/s40999-024-00973-2
36. Franssen, J.-M., Gernay, T. User's Manual for SAFIR (Version 2022) – A Computer Program for Analysis Of Structures Subjected to Fire. Part 5: Material Properties. Liege: University of Liege, 2022.
37. Boudjadja, M., Otmani-Benmehidi, N. Thermomechanical behavior of wooden and steel columns in fire situation. ICCEE2023 – 1st International Conference on Civil and Earthquake Engineering. EDP Sciences. Annaba, 2023.
38. Gravit, M.V., Dmitriev, I.I. Numerical modeling of basalt roll fire-protection for light steel thin-walled structures. Magazine of Civil Engineering. 2022. 112(4). Article no. 11215. DOI: 10.34910/MCE.112.15

Information about the authors:

Nadia Otmani-Benmehidi,
ORCID: https://orcid.org/0000-0002-3565-5942
E-mail: nadia.otmani@univ-annaba.dz

Marwa Boudjadja,
ORCID: https://orcid.org/0009-0000-9772-1194
E-mail: marwa.boudjadja@univ-annaba.dz

Abdessalem Otmani,
ORCID: https://orcid.org/0000-0001-8316-1843
E-mail: a.otmani@ensti-annaba.dz

Received 05.07.2024. Approved after reviewing 17.10.2025. Accepted 18.10.2025.

Magazine of Civil Engineering

ISSN 2712-8172

journal homepage: http://engstroy.spbstu.ru/

Research article

UDC 691.3

DOI: 10.34910/MCE.139.4

Use of fluorohydride as a binder for stabilization of weak soils in road construction

A.M. Alexandrov[1], ***G.I. Yakovlev***[1], ***A.F. Buryanov***[2], ***M.R. Bekmansurov***[1], ***N.V. Martyushev***[3] ✉, ***N.I. Vatin***[4], ***A.I. Karlina***[2]

[1] *Kalashnikov Izhevsk State Technical University, Izhevsk, Russian Federation*

[2] *Moscow State University of Civil Engineering (National Research University), Moscow, Russian Federation*

[3] *National Research Tomsk Polytechnic University, Tomsk, Russian Federation*

[4] *Peter the Great St. Petersburg Polytechnic University, St. Petersburg, Russian Federation*

✉ *martjushev@tpu.ru*

Keywords: soil stabilization, strengthening, fluoroanhydrite, IR spectroscopy, differential thermal analysis, microstructure

Abstract. In the conditions of growing attention to resource saving and environmental safety in road construction, the search for new binding materials for soil stabilisation is topical. This work is devoted to the study of the possibility of using fluoranhydride, a waste product of hydrofluoric acid production, as a binder for road base stabilisation. The object of the study is a composite material based on fluoranhydride, clay, and activator – sodium phosphate solution. The influence of fluorohydride activation on the physical and mechanical characteristics of the composite, including compressive strength, water absorption, and softening coefficient, has been studied. Fluoranhydrite is activated by 3 % sodium phosphate solution, which increases the strength of the obtained material. The physical and mechanical properties of composites consisting of fluorangydrite, loam, and sodium phosphate have been investigated. X-ray phase and IR spectral analyses were carried out, as well as scanning electron microscopy and energy dispersive X-ray spectroscopy. The results show that the optimum ratio of loam to fluorohydrite is 40/60 as it provides the highest economic efficiency. The compressive strength of this composition at the age of 28 days is also favourable: 8.9 MPa in the dry state and 7.3 MPa in the wet state, while the water absorption is 6.82 % and the softening coefficient is 0.82. The study confirms that fluorohydrite can be used as a binder to stabilize weak soils, which helps to reduce the cost of works and reuse waste materials, reducing the environmental load.

Citation: Alexandrov, A.M., Yakovlev, G.I., Buryanov, A.F., Bekmansurov, M.R., Martyushev, N.V., Vatin, N.I., Karlina, A.I. Use of fluorohydride as a binder for stabilization of weak soils in road construction. Magazine of Civil Engineering. 2025. 18(7). Article no. 13904. DOI: 10.34910/MCE.139.4

1. Introduction

A road is a complex structure, and its strength depends directly on the quality of the base on which it is built. The durability and reliability of the entire road depends on the stability of the soil, its strength, and ability to withstand loads. However, the soils is not always suitable for road construction ‘as is’. Often, it is too weak, unstable, easily subsides under the weight of vehicles [1–3]. Soil stabilization (a process of

improving the mechanical and physical properties of soil to increase its strength and durability) is a crucial step for creating reliable roads. This leads to serious problems: the road surface can deform, cracks and potholes can appear, and the whole road surface can subside and lose its shape [4, 5].

Another problem is that the soil is susceptible to various factors that can aggravate the situation, namely, high moisture that makes the soil soft and unable to bear loads or low humidity, which, on the contrary, can cause the soil to shrink, causing cracks and deformations in the road. Besides, the roads are always subjected to variable traffic loads, which can create 'fatigue' in the soil, leading to its gradual deterioration [6].

In the conditions of growing attention to resource saving and environmental safety in road construction, the search for new binding materials for stabilisation of weak soils is relevant. This paper is devoted to the study of the possibility of using fluorohydride, a waste product of hydrofluoric acid production, as a binder for stabilising (rather than strengthening) weak soils in the base of road pavements. The use of fluorohydride will reduce the cost of road construction by utilising industrial waste and reducing the need for traditional, more expensive materials, as well as reducing the environmental burden. It is important to note that materials used in road construction must meet the requirements of the Technical Regulations of the Customs Union TR TS 014/2011 'Safety of Motorways'. In particular, Section 5 'Requirements for earth bed and road pavements' establishes requirements for physical and mechanical characteristics of soils reinforced or stabilised with binding materials.

Thus, before building a road, it is necessary to improve the properties of the soil – this is called 'soil stabilization'. Soil stabilization is an important step to make the road base strong, stable, and less sensitive to various external factors. Soil stabilization is not just a desirable step but a mandatory element in road construction and repair [7, 8]. Imagine a road as a huge 'pie' where each layer fulfils its role, and the base, i.e. soil, plays the role of foundation, which provides the strength and durability of the whole structure. The problem is that the characteristics of the soil can vary dramatically [9]. Sometimes the soil is too weak, unable to withstand traffic loads, easily subsides, or has an uneven structure [10, 11]. Such soil can cause many troubles: the road surface will deform, cracks and potholes will appear, and the whole road may subside and lose its shape [12].

Soil stabilization solves this problem by making the soil stronger, more stable, and able to withstand loads. This increases the durability of the road surface and reduces the number and frequency of repairs needed. The benefits of soil stabilization are not just limited to strength. It also saves money and time in construction as the amount of excavation work is reduced by eliminating the need to replace weak soil with stronger material. Therefore, it allows existing soil to be used with minimal changes, reducing the cost of delivery and purchasing additional materials.

In summary, soil stabilization is not just a technological process but a necessary investment in road quality, durability, and safety. There are many methods of soil stabilization, each suitable for specific conditions. One of the most common methods is mixing soil with various binding materials. The binders help to 'glue' the soil particles together, making the soil stronger and more stable. Portland cement, lime, non-metallic materials (crushed stone, gravel), high calcium ash [13], and other substances are often used as binders. Apart from mixing with binders, other methods are also used to stabilise the soil:

- Mechanical compaction: Compacting the soil with rollers or other mechanisms can remove air from the soil and make it more dense.
- Wetting and drying cycles: The use of wetting and drying cycles can improve the soil structure and make it more resistant to moisture [14].
- Application of geosynthetics: Special geosynthetics can be used to reinforce the soil, which improves its strength and resistance to deformation [15].
- Electrical stabilization: This method can strengthen the soil using electric current.
- Biopolymer treatment: Biopolymers are organic substances that can bind soil particles and improve soil properties.

The choice of soil stabilisation method and materials used should be made taking into account the requirements of regulatory documentation. According to GOST R 58406.1-2020 'Public roads. Crushed stone and gravel-sand mixtures, crushed stone and gravel mixtures treated with inorganic binding materials. Technical requirements', mixtures used for road base construction must meet certain requirements for strength, frost resistance, and water resistance. The use of fluorohydride meets these requirements [16].

In addition, special additives are used to strengthen weak soils, which also improve other soil properties such as environmental resistance and drainage quality. In recent years, resource- and energy-saving technologies have been increasingly emphasised in road construction. Therefore, scientists are looking for new ways of soil stabilization that would be not only effective but also environmentally friendly

and economically viable. One of such promising directions is the use of angydrite as a binding material [17–19].

Anhydrite binder is an air binder consisting mainly of anhydrous calcium sulfate $CaSO_4$, which is a natural material that usually accompanies gypsum deposits. The technology for producing anhydrite binder is quite simple and, unlike cement, does not require heat treatment. Therefore, its production includes the extraction of anhydrite itself, its crushing and drying. Another method to obtain anhydrite is from natural gypsum by firing it at a temperature of 600–700 °C with subsequent grinding. The advantages of anhydrite include its environmental friendliness, non-flammability, the possibility of reprocessing products from it into a binder with the preservation of properties.

A cheap substitute for natural gypsum and anhydrite are wastes from various industries such as phosphogypsum, formed during the sulfuric acid decomposition of phosphate raw materials in the production of mineral fertilizers; red gypsum, formed during the desulfurization of flue gases; fluorogypsum or fluoroanhydrite, formed during the production of hydrofluoric acid; citrogypsum – a waste from the biochemical production of citric acid; hydrolysis gypsum – a waste from the technological processing of cellulose in the production of ethyl alcohol, a waste from the chemical polishing of glass, etc.

The most widely used multi-ton chemical industry waste in the production of building materials, phosphogypsum, requires preliminary preparation – neutralization with lime, and further dehydration at a temperature of 150–170 °C. Sulfogypsum, obtained during gas purification in the non-ferrous metallurgy industry, contains virtually no harmful impurities, being one of the purest gypsum-containing wastes, hovewer, it requires heat treatment to obtain gypsum grade G2–G4.

Fluoranhydrite, a by-product of hydrofluoric acid production after leaving the reactor, does not require additional processing and can be used in construction material industry in its original form. It is also possible to obtain an anhydrite binder from uncooled acidic waste from the production of hydrogen fluoride, including mixing and neutralizing the acidic fluoroanhydrite waste with a lime-containing agent while simultaneously grinding the mixture. In this case, Ilyinsky [20] suggests to add self-disintegrating ferrochrome slags a neutralizing lime-containing agent, and during mixing introduce a setting accelerator and superplasticizer in an amount of 0.7 and 0.5 wt.%, respectively, of the mass of the waste. The compressive strength of the composition after 28 days of hardening reached 27 MPa.

Anikanova et al. [21] developed compositions based on fluoroanhydrite, including structural, thermal insulation, and finishing materials, which can be used in the construction of enclosing and load-bearing structures of low-rise residential buildings.

Another composition [22] for the production of facing slabs, finishing layers of building products, load-bearing structures of buildings, wall stones based on fluoroanhydrite with the addition of slag and fillers – anhydrite crushed stone and carbonate sand has been developed. The characteristics of the binder on the 3rd day of hardening are as follows: strength 48.6 MPa, softening coefficient 0.89–0.91.

A fluoroanhydrite binder can also be used for road base construction. Fedorchuk describes a method for the use of joint soil fluoroanhydrite and substandard ferroalloy slag as a binder [23]. During grinding, acid (sulfuric, orthophosphoric, or their mixtures) is additionally introduced until the mixture pH reaches 1.0–6.5, followed by mixing the grinding product with an alkaline additive (lime, liquid glass, alkali – NaOH or KOH, soda) until pH reaches 7.0–12.0. Processing the mixture with this method promotes the decomposition of CaO, MgO and the formation of insoluble compounds that increase the water resistance of the finished product. The declared strength of the samples on the 28th day reaches 40 MPa.

The use of fluoranhydrite as a binder would provide an opportunity to reduce the cost of road construction. Also this solution allows to reduce the environmental load due to the utilisation of industrial waste. The aim of this work was to evaluate the possibility of using fluorohydrite as a binding material for stabilising weak soils in road construction.

To achieve this goal, the following tasks were solved:

- Optimisation of the mixture composition: Determination of the optimal ratio of fluorangydrite, loam, and activator (sodium phosphate) to achieve the required mechanical characteristics of the material.
- Study of physical and mechanical properties: Study of compressive strength, water absorption, softening coefficient, and other important characteristics of the obtained composite material.

It is important to note that the research presented aims not only to investigate the feasibility of using fluorangydrite but also to find a way to reduce the cost of construction, and to have a positive impact on the environment by utilising the industrial waste product.

2. Methods and Methods

In the course of this work, an attempt is made to use fluorohydrite, a waste product of hydrofluoric acid production, in the construction industry. This material, obtained at the enterprise 'HaloPolymer' in Perm, meets all the necessary technical requirements (TU 5744-132-05807960-98), which makes it potentially suitable for use in construction.

The chemical composition of fluorangidrite is as follows – CaO – 35.0–36.5 %; SO_3 – more than 45 %; Fe_2O_3 – 0.2–0.95 %; SiO_2 – 2.6–3.4 %; CaF_2 – 2.2–5 %; $A1_2O_3$ – 0.5–0.7 %.

The analysis of the X-ray diffraction of fluorohydrite showed the presence of reflections corresponding to soluble anhydrite – $CaSO_4$ (d_a =3.50; 2.85; 2.33; 2.21; 1.87 Å). In addition to these reflections, reflections of gypsum dihydrate $CaSO_4 – 2H_2O$ (d_a =7.55; 4.26; 2.85 Å) are visible in the X-ray spectrum. Reflections of silicon oxide SiO_2 (d_a = 3.35 Å) and calcite $CaCO_3$ (d_a = 3.03 Å) are also present. However, the reflections of gypsum dihydrate, silicon oxide, and calcite are weak, and the intensity of the peaks is not high.

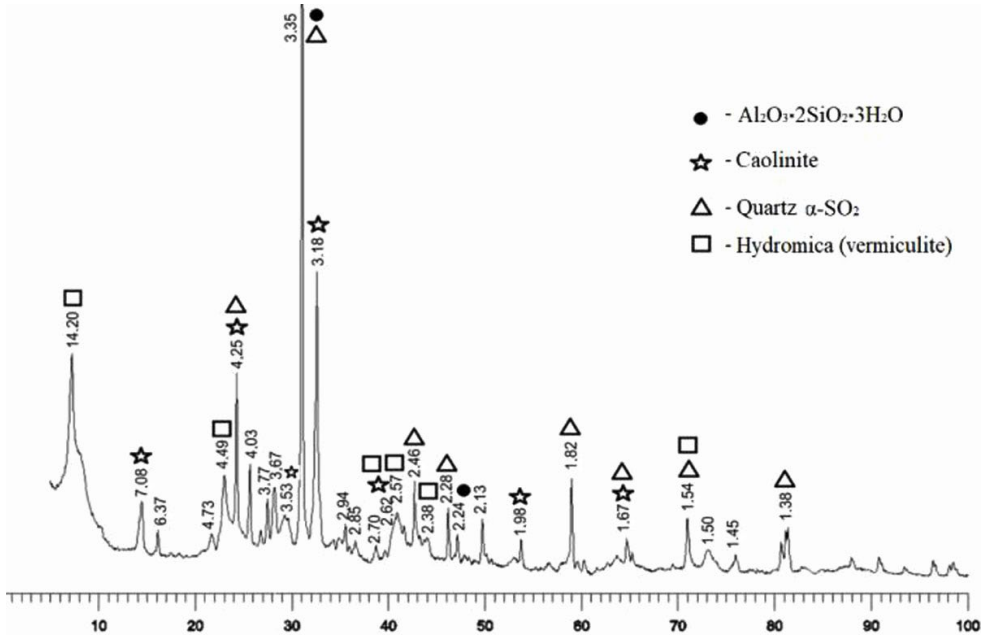

Figure 1. Diffractogram of loam.

The X-ray diffraction pattern of the loam (Fig. 1) shows strong reflections of quartz (d_α = 4.25; 3.35; 2.46; 1.82 Å), which suggests its predominance in the soil. Reflection lines in the range of d_α = 7.08; 4.25; 3.18; 2.55; 1.98 Å correspond to the presence of kaolinite. Strong reflection line d_α = 14.20 Å, corresponding to hydromica (vermiculite), was also noted.

Fluorohydrite, like many other materials, does not simply mix with water and solidify. In order for it to acquire the desired properties and become a strong building material, it is necessary to activate its solidification process. In this study, the authors used sodium phosphate (Na_3PO_4) to activate fluorohydrite. Sodium phosphate 'triggers' the hydration process, that is, the interaction of fluoranhydrite with water. The water reacts with anhydrous calcium sulphate, which is the main component of fluorangydrite, to form calcium sulphate hydrate [24–27]. This process leads to an increase in volume and the formation of a solid structure.

To verify the effectiveness of this method, experimental studies were conducted. The samples of fluorohydrite-based composition were prepared by mixing it with water without the added activator (reference group). These samples were aged for 28 days and then, their compressive strength was measured. As a result, the control samples were found to have a compressive strength of up to 20 MPa. Then, another group of samples was prepared, with a 3 % sodium phosphate solution added to the mixture. After 28 days, it turned out that the compressive strength of these samples reached 40 MPa. Thus, the study confirmed that activation of fluorangydrite with sodium phosphate significantly increases its strength. This makes fluorohydrite a more promising material for use in construction.

In this study, the soil at the experimental site is represented by loams with a moisture content of 15.5 %. The site area is 5 hectares, which is planned to be used for storage of gravel and crushed stone. It was suggested to use fluoroanhydrite as a binder to stabilize the soil. Sodium phosphate was used as an

activator for fluoroanhydrite hardening. The mixing water complied with the requirements of GOST 23732 – 2011 'Water for concrete and mortars'. The water-to-binder ratio was W/B=0.2.

In order to study in detail the properties of the obtained composites based on fluorohydrite and soil, several modern analysis methods were used.

One of such methods is differential scanning calorimetry (DSC). DSC measures the thermal effects that occur in a material when it is heated or cooled. In this study, DSC was used to study the phase transformations occurring in the composite when it was heated. For this purpose, composite samples were placed in a special device, a MettlerToledo TGA/DSC1 Starsystem derivatograph. The samples were heated from 60 to 1100 °C at a rate of 30 °C per minute, which allowed the thermal effects to be recorded and the changes in the material to be analysed.

Another important method of analysis is thermogravimetric analysis (TGA). TGA measures the change in mass of a sample when it is heated. In this work, TGA was used to determine, which components vaporise or decompose when the sample is heated and how the sample composition changes during the heating process. The TGA was also conducted on MettlerToledo TGA/DSC1 Starsystem derivatograph.

In order to determine the mineralogical composition of the composite, X-ray phase analysis was carried out. X-ray phase analysis was carried out on a diffractometer DRON-3 using a cobalt X-ray tube.

IR spectroscopy method was used to study the chemical bonds in the composite and to determine the presence of different chemical groups. The method is based on the fact that different chemical bonds absorb infrared radiation at different frequencies. By analysing the absorption spectrum of infrared radiation, the composition and structure of the substance can be determined. IR spectroscopy was carried out on a Shimadzu IRAffinity-1 spectrometer in the frequency range of 400 to 4000 cm^{-1}.

Scanning electron microscopy (SEM) was used to study the microstructure of the composite. In this study, SEM was performed on a Thermo Fisher Scientific Quattro S scanning electron microscope at the Centre for Collective Use 'Surface and New Materials' of the Ural Branch of the Russian Academy of Sciences (Izhevsk, Russia). Energy dispersive X-ray spectroscopy (EDS) was used to determine the chemical composition of individual regions of the sample.

3. Results and Discussion

To determine the optimal ratio between soil and binder, cube samples with the dimensions of 100×100×100 mm were prepared in metal molds (Fig. 2) and exposed to semi-dry pressing on a hydraulic press under a pressure of 20 MPa.

Figure 2. 100×100×100 mm cube samples with fluoroanhydrite to loam ratio 40:60 by weight.

The compressive strength of the samples at the age of 5 and 28 days is presented in Table 1.

Table 1. Compressive strength of the samples.

No.	Composition	Compressive strength, [MPa] at the age of	
		5 days	28 days
1	Fluoroanhydrite 100 %	6	30.7
2	Fluoroanhydrite + Sodium phosphate	10	40.2
3	80 % Fluoroanhydrite + 20 % Loam	13	17.3
4	60 % Fluoroanhydrite + 40 % Loam	4.3	8.9
5	50 % Fluoroanhydrite + 50 % Loam	2.4	6.3
6	40 % Fluoroanhydrite + 60 % Loam	1	4.6

In the study, samples of pure fluorohydrite were prepared, mixed with water and kept for 28 days to fully harden. The compressive strength of these samples was then measured. The tests showed that it reached 30.7 MPa. This means that fluorohydrite itself already has a fairly good strength. Further studies allowed to reveal the possibility of further strengthening of fluorohydrite. For this purpose, an activator, sodium phosphate, was added. Sodium phosphate is a substance that can accelerate and enhance the hydration process of fluorangydrite. Hydration is the interaction of fluoranhydrite with water, resulting in the formation of calcium sulphate hydrate, which makes the material stronger. New samples of fluorangydrite were mixed it with water, sodium phosphate in the form of 3 % solution was added. These samples were also aged for 28 days. Then, their compressive strength was measured. The result showed that the strength of the samples with sodium phosphate reached 40.2 MPa. Thus, the study showed that activation of fluorangydrite with sodium phosphate significantly increases its strength. This makes fluorangydrite an even more promising material for use in construction because it allows for the creation of stronger and more reliable structures.

As a result of the tests, three optimal compositions were selected (Table 2), which can be used as road bases according to the standards [10]. It is noted that with an increase in the proportion of fluoroanhydrite in the composition, the content of calcium sulfate dihydrate also increases (Fig. 7a), whereas the content of hydroaluminosilicates decreases. Due to the fact that calcium sulfate dihydrate has low water resistance, an increase in its amount in the samples (for example, Sample 3) is accompanied by a decrease in the softening coefficient.

Table 2. Optimal compositions.

No.	Composition	Sample weight, [g]	Sample weight after saturation with water, [g]	Compressive strength of the sample, [MPa]	Compressive strength of a water-saturated sample, [MPa]	Water absorption, W, [%]	Softening coefficient, Kp
1	80 % Fluoroanhydrite + 20 % Loam	1969	2140	17.3	12.3	8.68 %	0.71
2	60 % Fluoroanhydrite + 40 % Loam	1994	2130	8.9	7.3	6.82 %	0.82
3	50 % Fluoroanhydrite + 50 % Loam	1949	2150	6.3	4.1	10.31 %	0.65
4	40 % Fluoroanhydrite + 60 % Loam	1944	2230	4.6	2.6	14.71 %	0.56

In order to study the structure and properties of the composition, physical and chemical analyzes of the samples at the age of 4 months were carried out.

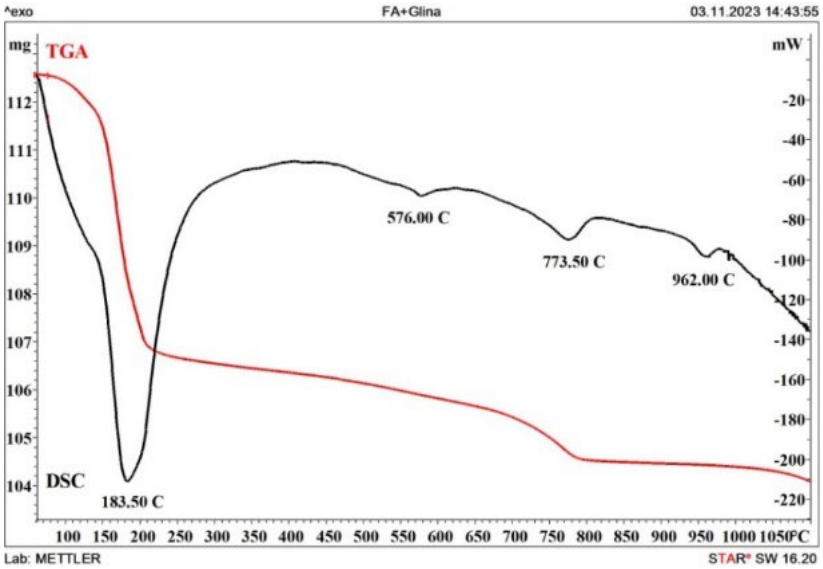

Figure 3. DTC and TGA spectra of a mixture of fluoroanhydrite (40 %) and loam (60 %) mixed with 3 % sodium phosphate solution.

In order to find out the changes occurring in the composite material during heating, two types of analyses were carried out: differential thermal calorimetry (DTC) and TGA. DTC allowed to detect thermal changes in fluorohydrite when it was heated (Fig. 3). This explains how the energy within the material changes and what processes occur within it. TGA focused on the mass change of the sample when heated. It showed which substances vaporise or decompose when heated and how the composition of the material as a whole changes. The results of these analyses revealed a number of interesting thermal effects occurring in the composite when it is heated:

At around 183.5 °C, an endothermic peak is observed. This means that at this point there is heat absorption by the material. This peak is due to dehydration of gypsum dihydrate and hydrosilicate formations such as calcium aluminosilicate hydrates. There was a release of water from the material when it was heated. In the temperature range of 100 to 350 °C, the composite lost about 5.6 % of its mass.

At about 400 °C, a weak exothermic peak was observed. This means that at this point, there is a release of heat by the material. This peak is due to the rearrangement of the calcium sulphate crystal lattice resulting in the formation of insoluble anhydrite.

When the composite was heated to a temperature of about 400 °C, the material started to release heat, an exothermic effect was obtained. This heat release is due to the rearrangement of the internal structure of calcium sulphate. When calcium sulphate is heated, a new mineral, anhydrite, is formed. Anhydrite is a more stable form of calcium sulfate that does not dissolve in water. Thus, when the composite is heated, there is a ‘transition’ of calcium sulfate into anhydrite. This process is accompanied by the release of heat, as recorded in the experiment.

When the composite is heated to a temperature of 576 °C, heat absorption (an endothermic effect) occurs. This heat absorption is due to the rearrangement of the internal structure of silicon oxide. Silicon oxide is a mineral that is present in loams. The silicon oxide is heated to a specified temperature and the recrystallisation process begins. The recrystallisation of silicon oxide causes it to become more resistant to high temperatures. This is an important factor because the composite can be used in a variety of environments, including elevated temperatures.

When the composite is heated to a temperature of about 773.5 °C, it absorbs heat again, the endothermic effect starts again. And this time, the heat absorption is due to dehydration. In the composite at this temperature, there is a release of water from calcium silicate hydrates, potassium aluminosilicate hydrates, and calcium carbonate. These are substances that are part of the loam and as a result of interaction with fluorohydrite have formed hydrates, that is, compounds that contain water. When heated to 773.5 °C, these hydrates lose their water and as a result, the mass of the composite is reduced by 1.8 %. This is similar to how a wet sponge loses weight when dried.

At 962 °C, there is an endothermic peak associated with the breakdown of the crystal lattice and crystallisation of amorphous calcium aluminosilicate products.

These data help scientists better understand the properties of the composite and the processes that happen to it when heated. This is important in order to prevent the material from degrading during application and to ensure its reliability and durability.

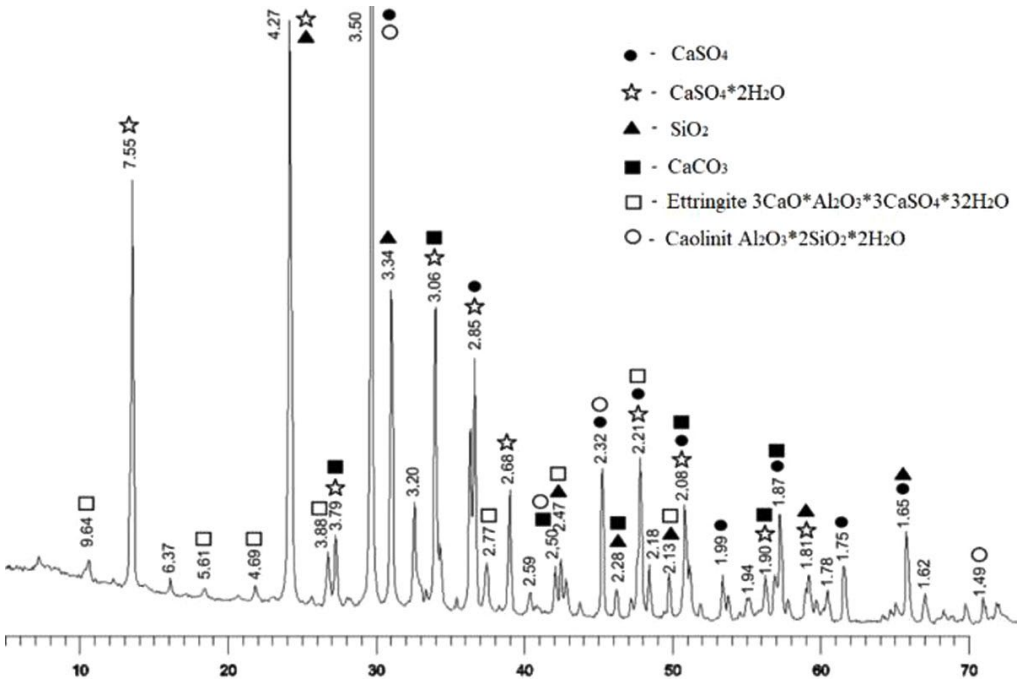

Figure 4. X-ray phase analysis of a mixture of fluoroanhydrite (40 %) and loam (60 %) mixed with a 3 % sodium phosphate solution.

X-ray phase analysis (Fig. 4) of the composition showed the presence of calcium sulfate dihydrate (d_α = 7.55; 4.27; 3.79; 2.68; 2.11; 2.08 Å), which is formed in the process of anhydrite (d_α = 3.50; 2.85; 2.08 Å) activation with sodium phosphate. Reflection lines corresponding to quartz (d_α = 3.34 Å) and calcium carbonate $CaCO_3$ (d_α = 3.88; 3.06; 2.08; 1.87 Å) were also noted. The formation of aluminosilicate (kaolinite) and ettringite $3CaO \cdot Al_2O_3 \cdot 3CaSO_4 \cdot 32H_2O$ is suggested by the presence of reflection lines d_α = = 3.50; 2.50; 2.32; 1.49 Å and d_α = 9.64; 5.61; 4.69; 3.88; 2.77; 2.21 Å, respectively.

IR spectral analysis (Fig. 5) of the composition confirmed the presence of gypsum dihydrate (absorption lines 580.87; 1145.72; 1118.71; 1622.13; 3404.36 and 3545.18 cm^{-1}), anhydrite (1145.72; 611.43; 1400 cm^{-1}) and ettringite (1118.71 cm^{-1}, in the region of 1675 cm^{-1}, 3404.36 cm^{-1}). Absorption lines at 1429.25 cm^{-1} and in the region of 874 cm^{-1} corresponding to calcium carbonate were also noted. The presence of ettringite is associated with the interaction of aluminosilicates in the composition of loam and calcium sulfate in the composition of fluoroanhydrite. The formation of ettringite was later confirmed by the results of energy dispersive analysis (Fig. 10).

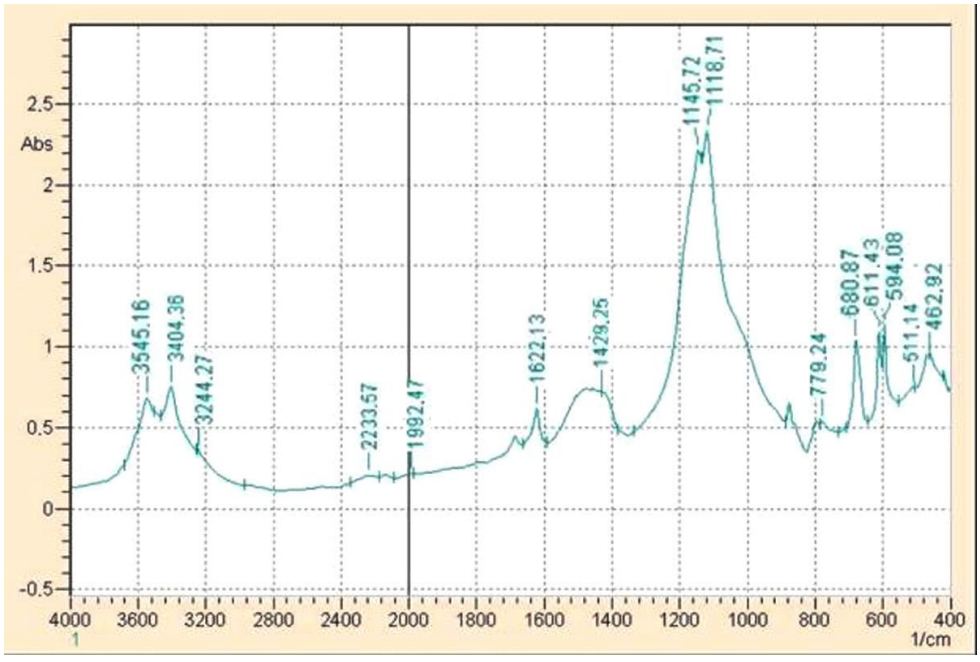

Figure 5. IR spectrum of a composition based on fluoroanhydrite (40 %) and loam (60 %) activated with sodium phosphate.

Microstructure analysis performed on a Thermo Fisher Scientific Quattro S scanning electron microscope showed that the hydration of fluoroanhydrite and the formation of new hydration products based on gypsum dihydrate of prismatic (Fig. 6b) and acicular structure (Fig. 7a) contributed to the compaction of the matrix (Fig. 6a, b).

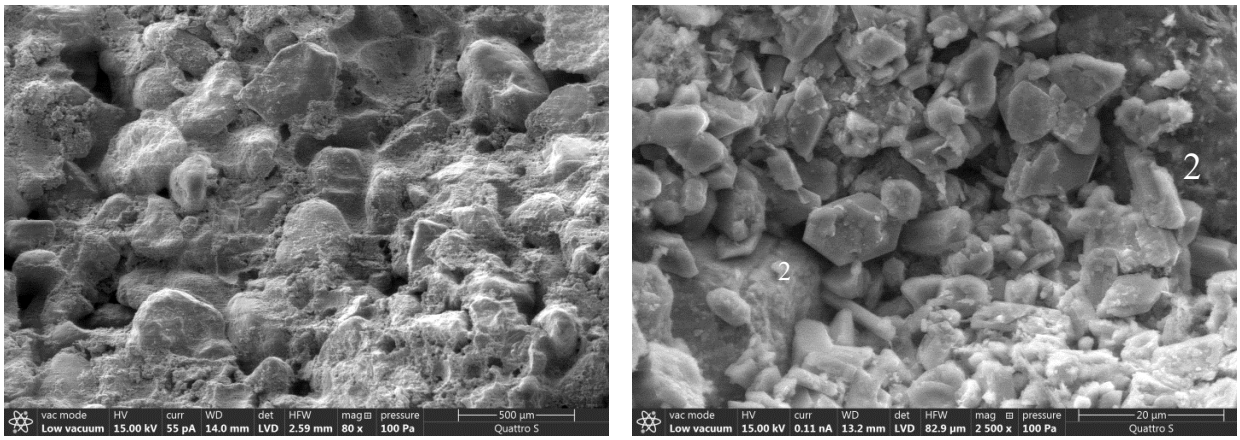

a **b**

Figure 6. Composition of a mixture of fluoroanhydrite (40 %) and loam (60 %), mixed with a 3 % sodium phosphate solution: a) general view at 80-fold magnification, b) formation of prismatic crystals based on gypsum dihydrate (1) between loam particles (2).

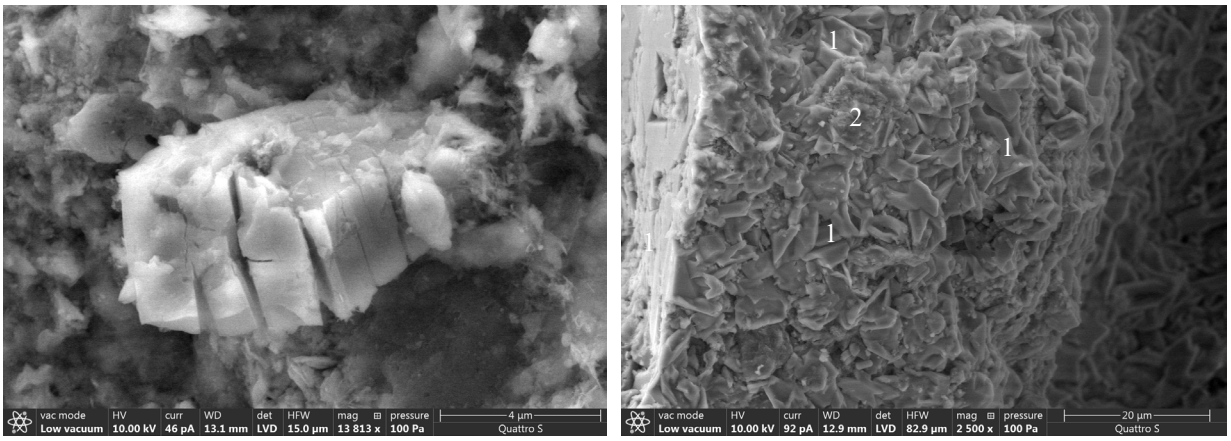

a **b**

Figure 7. Crystal hydrates of gypsum dihydrate with a needle-like structure (a), compaction of gypsum crystals (1) by hydration products (2) when interacting with loam minerals in a composition of a mixture of fluoroanhydrite (40 %) and loam (60 %), mixed with a 3 % sodium phosphate solution (b).

Studying the microstructure of the composite material under the microscope (Figs. 7, 8) showed interesting results. It turned out that the gypsum matrix formed from fluorohydrite was not just mixed with loam minerals, but interacted with them. This interaction led to the formation of new compounds, calcium and potassium hydrosulfoaluminates. These new compounds are located inside the composite and act as a ‘fastener’, additionally strengthening the structure of the material. They seem to ‘bind’ the particles of gypsum and minerals of loam, making the composite more dense and strong (Fig. 8a, b). The formation of hydrosulfoaluminates also gives the composite increased water resistance. This means that the material is less affected by moisture and does not swell or deteriorate when exposed to water. The formation of hydrosulfoaluminates increases the water resistance of the composite, which is an important factor for the durability of the pavement.

Thus, the interaction between fluorangydrite and loam leads to the formation of new compounds that improve the properties of the composite, making it stronger and more resistant to moisture. This means that fluorangydrite can be used as an effective and reliable material for soil stabilization in road construction.

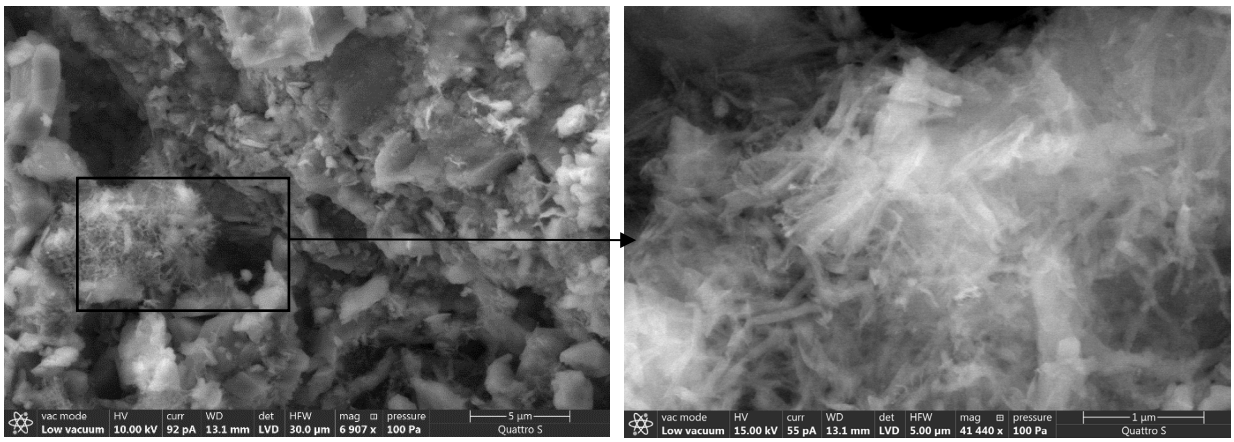

a **b**

Figure 8. Formation of calcium hydrosulfoaluminates in the contact zone between gypsum crystals and clay mineralin the composition of a mixture of fluoroanhydrite (40 %) and loam (60 %), mixed with a 3 % sodium phosphate solution: a) at 6907-fold magnification (G – gypsum crystal), b) at 13813-fold magnification (E – ettringyte).

In the process of fluoroanhydrite hydration, gypsum dihydrate $CaSO_4 \cdot 2H_2O$ is formed, which is partially crystallized on the surface of loam particles in the form of large crystals (Fig. 9). Fig. 10 shows that the influence of an electron beam during microanalysis of gypsum crystals (Fig. 9) results in a partial dehydration of these crystals (Fig. 7a) even despite the presence of a 'shell' containing silicon and aluminum atoms (in the composition of hydroaluminosilicates) around them. As a result, a layered structure (Fig. 7a) is formed due to the removal of water molecules from the internal layers of gypsum dihydrate, which additionally confirms the interaction of fluoroanhydrite and loam in the composition.

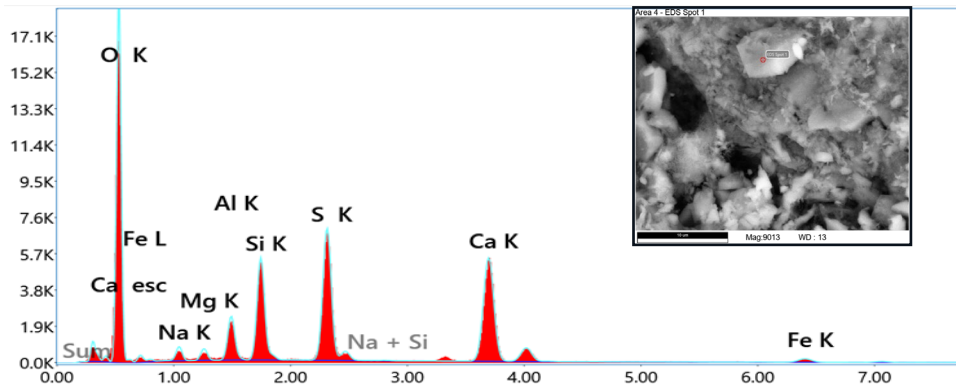

Figure 9. Energy dispersive analysis of a gypsum crystal.

Energy dispersive analysis confirmed the formation of calcium hydrosulfoaluminates in the contact zone between loam minerals and fluoroanhydrite (Fig. 10). Calcium (Ca), sulfur (S), aluminum (Al), and oxygen (O) atoms were noted on the spectrum, which are present in calcium hydrosulfoaluminates $3CaO \cdot Al_2O_3 \cdot 3CaSO_4 \cdot 32H_2O$ (ettringite).

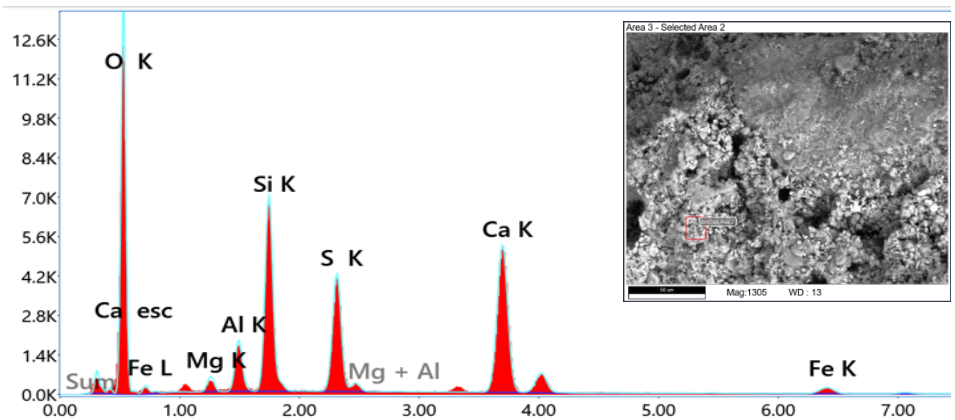

Figure 10. Energy dispersive analysis of hydration products in the contact zone between fluoroanhydrite and loam particles in a composition of a mixture of fluoroanhydrite (40 %) and loam (60 %) mixed with a 3 % sodium phosphate solution.

The study of fluorangydrite and loam composite showed that its strength is not just the result of mechanical mixing of different materials. New chemical bonds are formed between the fluorangydrite particles and the loam minerals. These new bonds bind the particles together and make the material stronger. In addition, the interaction between the fluorangydrite and the loam leads to the formation of new compounds called calcium and potassium hydrosulfoaluminates. These compounds make the composite stronger and more resistant to various influences such as moisture or temperature variations. Thus, the study showed that the strength of the composite is not only due to physical bonding but also due to chemical interactions between its components. This is an important factor that makes fluorohydrite a promising material for use in construction.

4. Conclusions

In this paper, fluoranhydrite composition designed for road base reinforcement was described. This composition consists of fluorangydrite mixed with loam and 3 % sodium phosphate solution. The conducted research has shown:

- Fluorangydrite by itself has sufficient strength, reaching 30.7 MPa at the age of 28 days.
- Activation of fluorangydrite with sodium phosphate significantly increases its strength, reaching 40.2 MPa at the age of 28 days.
- The optimum ratio of fluorangydrite and loam in the composition is 60/40.
- The compressive strength of the composition with this ratio is 8.9 MPa in the dry state and 7.3 MPa in the wet state at the age of 28 days.
- The water absorption of the composition was 6.82 % and the softening coefficient was 0.82.
- Physico-chemical studies have shown that the strength of the composition is provided not only by physical bonding but also by chemical interaction between fluorohydrite and loam.

The conducted research proves that fluorangydrite can be successfully used as a binder for stabilization of weak soils. This allows to reduce the cost of works due to the use of available and inexpensive material – fluorohydrite. It also provides an opportunity to recycle waste products of hydrofluoric acid production, reducing the environmental load. The use of fluorohydride is the most promising for stabilisation of soils for pavement bases on roads of IV–V categories, where there are no increased requirements for strength and frost resistance.

The results of the study can be used in road construction for stabilization of soils, which will allow to create stronger and more durable roads at minimum cost and have a favourable impact on the environment. The use of fluorohydride for soil stabilisation will improve the environmental situation in regions with a developed chemical industry by recycling industrial waste and reducing its disposal in landfills.

References

1. Sherov, K.T., Donenbayev, B.S., Sikhimbayev, M.R., Kuanov, I.S., Tazhenova, G.D. The Research of Circular Saw Blade Stability State for Thermal Frictional Cutting by the Method of Calculation in the Form of a Hingeless Circular Arch. News of the National Academy of Sciences of the Republic of Kazakhstan. Series of Geology and Technical Sciences. 2022. 4(454). Pp. 240–251. DOI: 10.32014/2022.2518-170X.213
2. Tiraturyan, A.N. Dissipation of dynamic deformation energy in pavements of automobile roads. Sustainable Development of Mountain Territories. 2024. 16(3). Pp. 909–920. DOI: 10.21177/1998-4502-2024-16-3-909-920
3. Dyachenko, V.V., Turkin, V.A., Vorobev, A.E., Kukartsev, V.V., Tynchenko, Ya.A. Mechanisms of high hazard landslide formation (rapid and slow). Russian Mining Industry. 2024. 4. Pp. 96–100. DOI: 10.30686/1609-9192-2024-4-96-100
4. Klyuev, R.V., Martyushev, N.V., Kukartsev, V.V., Kukartsev, V.A., Brigida, V. Analysis of geological information toward sustainable performance of geotechnical systems. Mining Informational and Analytical Bulletin. 2024. 5. Pp. 144–157. DOI: 10.25018/0236_1493_2024_5_0_144
5. Zhuravlev, A.G., Cherepanov, V.A., Karpov, V.A., Nevezhin, A.Yu. Recommendations on operation and improvement in the quality of in-pit road maintenance at the Olympiadinsky and Blagodatny mining and processing plants. Russian Mining Industry. 2023. 5. Pp. 88–95. DOI: 10.30686/1609-9192-2023-5-88-95
6. Gorbunov, R.N., Gorbunova, Z.V., Gorbunova, L.N., Kolchin, V.S., Karlina, A.I. Evaluation of the efficiency of the road network functioning. IOP Conference Series: Materials Science and Engineering. 2021. 1061(1). Article no. 012018. DOI: 10.1088/1757-899X/1061/1/012018
7. Badarchi, X.B., Soyan, Sh.Ch., Kylgyday, A.Ch. Economic potential of a border region in connection with the implementation of an integrated transport infrastructure project. Russian Mining Industry. 2023. 2. Pp. 52–55. DOI: 10.30686/1609-9192-2023-2-52-55
8. Maltseva, T.V., Nabokov, A.V., Vatin, N. Consolidation of water-saturated viscoelastic subgrade. Magazine of Civil Engineering. 2024. 17(1). Article no. 12502. DOI: 10.34910/MCE.125.2

9. Sherov, A.K., Myrzakhmet, B., Sherov, K.T., Sikhimbayev, M.R., Absadykov, B.N. Gear pump quality improving by changing the design and size of the support bushings. News of the National Academy of Sciences of the Republic of Kazakhstan. Series of Geology and Technical Sciences. 2021. 6(450). Pp. 155–162. DOI: 10.32014/2021.2518-170X.132
10. Kulikova, E.Yu., Konyukhov, D.S. On the determination of buildings technological deformations in geotechnical construction. Sustainable Development of Mountain Territories. 2022. 14(2). P. 187–197. DOI: 10.21177/1998-4502-2022-14-2-187-197
11. Shevchuk, R.V., Manevich, A.I., Akmatov, D.Zh., Urmanov, D.I., Shakirov, A.I. Modern methods, techniques and technical means of monitoring movements of the Earth crust. Russian Mining Industry. 2022. 5. Pp. 99–104. DOI: 10.30686/1609-9192-2022-5-99-104
12. Sherov, K.T., Alikulov, D.E., Sikhimbayev, M.R., Sherov, A.K., Absadykov, B.N., Imanbaev, E.B., Gabdysalyk, R. The method of selecting the optimal layouts of the size limit deviations during assembly. News of the National Academy of Sciences of the Republic of Kazakhstan. Series of Geology and Technical Sciences. 2021. 1(445). Pp. 144–150. DOI: 10.32014/2021.2518-170X.20
13. Kolesnikova, O., Vasilyeva, N., Kolesnikov, A., Zolkin, A. Optimization of raw mix using technogenic waste to produce cement clinker. Mining Informational and Analytical Bulletin. 2022. 10–1. Pp. 103–115. DOI: 10.25018/0236_1493_2022_101_0_103
14. Salakhov, R.R. Chemical methods for stabilizing clay soils. Transport. Transport facilities. Ecology. 2023. 3. Pp. 59–64. DOI: 10.15593/24111678/2023.03.06
15. Bosikov, I.I., Klyuev, R.V., Martyushev, N.V., Modina, M.A., Khekert, E.V. Analysis of the quality of underground mineral waters of terrigenous deposits of the hauteriv-barremian aquifer of the lower cretaceous. News of the National Academy of Sciences of the Republic of Kazakhstan. Series of Geology and Technical Sciences. 2024. 2. Pp. 36–47. DOI: 10.32014/2024.2518-170X.392
16. Ilyinsky, B.P. Composition for road pavement construction: pat. 1758136 A1 USSR : MPK E01C 7/36, C04B 11/06, C04B 28/16. Ilyinsky, B.P., Ivanchin, N.N., Letskikh, V.A. Applicant [and patentee]. Published on 30.08.1992. Bulletin no. 32.
17. Gordina, A.F., Yakovlev, G.I., Pervushin, G.N., Gumenyuk, A.N., Ukraintseva, V.M., Buryanov, A.F. Non-Autoclaved Aerated Concrete Based on Sulfate-Containing Technogenic Waste. Stroitel'nye Materialy [Construction Materials]. 2023. 10. Pp. 42–46. DOI: 10.31659/0585-430X-2023-818-10-42-46
18. Lindh, P., Lemenkova, P. Impact of Strength-Enhancing Admixtures on Stabilization of Expansive Soil by Addition of Alternative Binders. Civil and Environmental Engineering. 2022. 18(2). Pp. 726–735. DOI: 10.2478/cee-2022-0067
19. Jeremiah, J.J., Abbey, S.J., Booth, C.A., Eyo, E.U. Viability of calcinated wastepaper sludge ash geopolymer in the treatment of road pavement subgrade materials. Transportation Geotechnics. 2023. 40. Article no. 101165. DOI: 10.1016/j.trgeo.2023.101165
20. Golik, V.I., Klyuev, R.V., Martyushev, N.V., Zyukin, D.A., Karlina, A.I. Technology for Nonwaste Recovery of Tailings of the Mizur Mining and Processing Plant. Metallurgist. 2023. 66(11–12). Pp. 1476–1480. DOI: 10.1007/s11015-023-01462-y
21. Kurmangalieva, A.I., Anikanova, L.A., Kudyakov, A.I., Steshenko, A.B., Buryanov, A.F., Lukyanova, N.A., Inozemtsev, A.S., Inozemtsev, S.S. Formation of porous structures in production technology of construction materials based on building gypsum plaster. Nanotechnologies in Construction. 2023. 15(4). Pp. 319–327. DOI: 10.15828/2075-8545-2023-15-4-319-327
22. Kulikova, E.Yu., Balovtsev, S.V., Skopintseva, O.V. Geoecological monitoring during mining operations. Sustainable Development of Mountain Territories. 2024. 16(2). Pp. 580–588. DOI: 10.21177/1998-4502-2024-16-2-580-588
23. Dabiev, D.F., Chupikova, S.A., Chuldum, A.F. Assessment of various scenarios for the development of mineral deposits in the region (as exemplified by the Republic of Tuva). Russian Mining Industry. 2021. 6. Pp. 9–102. DOI: 10.30686/1609-9192-2021-6-99-102
24. Malyukova, L.S., Martyushev, N.V., Tynchenko, V.V., Kondratiev, V.V., Bukhtoyarov, V.V., Konyukhov, V.Yu., Bashmur, K.A., Panfilova, T.A., Brigida, V. Circular Mining Wastes Management for Sustainable Production of Camellia sinensis (L.) O. Kuntze. Sustainability (Switzerland). 2023. 15(15). Article no. 11671. DOI: 10.3390/su151511671
25. Mouli, K.C., Raghavendran, C.V., Mallikarjuna Rao, C., Ushasree, D., Indupriva, B., Vatin, N.I., Negi, A.S. Performance analysis of linear and non-linear machine learning models for forecasting compressive strength of concrete. Cogent Engineering. 2024. 11(1). Article no. 2368101. DOI: 10.1080/23311916.2024.2368101
26. Rassokhin, A.S., Ponomarev, A.N., Karlina, A.I. High-performance fine-grained nanostructured concrete based on low strength aggregates. Magazine of Civil Engineering. 2022. 114(6). Article no. 11413. DOI: 10.34910/MCE.114.13
27. Wang, X., Wang, X., Fu, P., Lei, B., Shi, J., Xu, M. Synergetic Mechanism of Multiple Industrial Solid Waste-Based Geopolymer Binder for Soil Stabilization: Optimization Using D-Optimal Mixture Design. Processes. 2024. 12(3). Article no. 436. DOI: 10.3390/pr12030436

Information about the autthors:

Alexandr Alexandrov,
E-mail: aleksandrov2332@yandex.ru

Grogory Yakovlev, *Doctor of Technical Sciences*
ORCID: https://orcid.org/0000-0002-2754-3967
E-mail: gyakov@istu.ru

Aleksandr Buryanov, *Doctor of Technical Sciences*
ORCID: https://orcid.org/0000-0002-3331-9443
E-mail: rga-service@mail.ru

Marat Bekmansurov,
E-mail: bekmansurov2@mail.ru

Nikita Martyushev, *PhD in Technical Sciences*
E-mail: martjushev@tpu.ru

Nikolai Vatin, *Doctor of Technical Sciences*
ORCID: https://orcid.org/0000-0002-1196-8004
E-mail: vatin@mail.ru

Antonina Karlina, *PhD in Technical Sciences*
ORCID: https://orcid.org/0000-0003-3287-3298
E-mail: karlinat@mail.ru

Received 07.11.2024. Approved after reviewing 24.10.2025. Accepted 24.10.2025.

Magazine of Civil Engineering

ISSN 2712-8172

journal homepage: http://engstroy.spbstu.ru/

Research article

UDC 624.12

DOI: 10.34910/MCE.139.5

Flow turbulence conditions and sensitivity of bucket-type spillway geometry parameters in energy dissipation

S. Mohammadalizadeh[1] ✉ , ***A. Yasaei***[2], ***A. Mardookhpour***[2]

[1] *Islamic Azad University, Lahijan Branch, Lahijan, Iran*

[2] *Islamic Azad University, Lahijan Branch, Department of Civil Engineering, Lahijan, Iran*

✉ *saeidmhmdalizadeh74@gmail.com*

Keywords: bucket spillway, energy dissipation, throw length, throw height, throw angle, RNG turbulence model, (k-ε) turbulence model, Flow-3D software

Abstract. Energy dissipation downstream of dams is considered one of the important issues in these structures. Various structures have been employed to perform this function. Among them, bucket-type spillways are of great importance, where the outflow jet from these structures faces complex issues, including jet diffusion and downstream erosion. With the hardware and software advancement of numerical simulation systems, the evaluation of this phenomenon is possible at a lower cost compared to laboratory conditions. In this research, using FLOW-3D software and the RNG turbulence model, the effects of various geometric and hydraulic parameters related to the bucket-type spillway on the outflow jet have been investigated. The results of the RNG turbulence model show better agreement with laboratory results compared to the (k-ε) turbulence model. The relative error in energy reduction between laboratory results and numerical model results is less than 5%, and the error related to maximum jump length is less than 7%. The changes in spillway geometry include changes in the spillway angle from 52° to 32° and changes in the spillway arc radius from 12-19 cm.

Citation: Mohammadalizadeh, S., Yasaei, A., Mardookhpour, A. Flow Turbulence conditions and sensitivity of bucket-type spillway geometry parameters in energy dissipation. Magazine of Civil Engineering. 2026. 18(7). Article no. 13905. DOI: 10.34910/MCE.139.5

1. Introduction

Energy dissipation downstream of high dams constitutes a serious problem. When high flow velocities exist, stilling basins present problems of cavitation and erosion, so they are used as ski jump spillways. Therefore, this energy dissipation system is widely used and seemingly is the only structure that is both technically and hydraulically suitable and safe for excess flow energy control. Although numerous ski-jump spillways have been constructed to date, most have been designed based on physical models and regional studies, and no standard design guidelines exist in this field. In recent years, numerical methods, including three-dimensional Computational Fluid Dynamics (CFD), have rapidly developed due to advances in computer technology and numerical methods. CFD models are more flexible than physical models and require less time and cost; furthermore, due to the use of actual prototype dimensions in these models, scale effects are eliminated. CFD analyses are extensively used in fluid mechanics applications such as multiphase flows and free surface flows. When CFD analysis results, numerical validations, and prototype observations demonstrate appropriate correlation with one another, the results of numerical modeling may be utilized. In this research, through numerical investigation of flow over ogee spillways with flat ski-jump buckets using FLOW 3D software, models with different geometries in ski-jump buckets have

been examined, and various parameters, including Froude numbers, different discharge rates, geometries with different launch angles, and different arc radii have been investigated.

With the increasing trend in constructing high dams and rising dam safety standards, hydraulic engineers have shown a growing interest in designing reliable and economical energy dissipation systems at the terminals of main flood discharge channels in high dams. Energy dissipation structures are facilities placed at the end of dam spillways to dissipate water flow energy. Among various types of energy dissipation structures, three types (stilling basins with hydraulic jump, roller dissipators, and bucket-type dissipators) are widely used in dams [1].

The use of free-falling jets in bucket-type spillways (along with associated plunge pools), given suitable geological and topographical conditions, offers significant economic and safety advantages compared to other types of energy dissipation structures. In high dams, bucket spillways, utilizing the high velocity of inflow to the bucket, can deflect the flood discharge from the spillway as a free-falling jet in such a way that it falls at a safe distance from the spillway and dam into the plunge pool or river bed. The optimal design of a bucket-type spillway, in addition to proper positioning, geometric shape, and appropriate dimensions, requires extensive study of scour and analysis of excess flow energy dissipation efficiency. This necessitates calculation and analysis of flow variables and geometric parameters related to the spillway, as improper design without proper analysis of these parameters could damage the structure and ultimately lead to irreparable damage to the chute the dam itself and cause adverse effects on the stilling basin and downstream areas [1].

Olsen et al. (1998) examined the performance of FLOW-3D simulation in analyzing pressure values and discharge over an ogee spillway. The results obtained from numerical simulation showed acceptable agreement when compared with physical simulation values [2]. Meilan et al. (2000) conducted studies on bed erosion caused by vertical and oblique water jet impact in submerged conditions. The results showed that at low velocities, scour volume changes with jet velocity, such that increasing the jet angle also increases scour volume. However, at high velocities, the effect of jet angle is not significant [3].

Savage and Johnson (2001) studied a standard ogee spillway through FLOW-3D software. The numerical analysis results matched well with experimental findings according to the study [4]. Ho et al. (2003) utilized computational fluid dynamics to model spillway behaviors across two-dimensional and three-dimensional domains at different water height levels which yielded results that matched field data measurements [5]. Free-flow spillway modeling with an S-shaped plan was performed by Sarker and Rhodes (2002) using FLUENT software. The standard turbulence model accompanied the VOF multiphase flow model for performing simulations. The RNG model demonstrated the most accurate correlation between numerical and physical results regarding average velocity according to the research in [6].

The research conducted by Weilin et al. (2004) investigated how jet velocity influences the main dimensions of flat jet scour holes. The authors established that higher velocity at all tailwater depths along with various bed particle types, results in deeper and longer scour holes. The length and depth of scour holes decrease when tailwater depth increases with constant velocity and particle size [7]. Heller et al. (2005) conducted experiments on circular bucket spillway outflow to study jet pressure parameters together with jet trajectory and downstream wave formation. The experimental results indicated that both Froude numbers and surface curvature and surface angle proved to be significant factors in this study. The use of these parameters proved essential for ski jump design because they directly affected the overall functionality [8].

Pagliara et al. (2006) conducted approximately 60 experiments studying the effect of upstream flow velocity at jet impact location in the tailwater on scour hole dimensions. They presented an equation for scour depth as a function of upstream Froude number. They concluded that with increasing the Froude number, suspended sediments in the scour hole are transported downstream, the scour hole deepens, and the downstream mound gradually decreases due to erosion [9]. Dargahi (2006) performed a three-dimensional numerical simulation of an ogee spillway in his study, comparing the water surface profile and discharge coefficient with experimental results, which fell within an accuracy range of 5.1 to 9.2% [10].

Steiner et al. (2008) conducted research on pressure distribution in ski jump energy dissipators with triangular buckets by using experimental models. The researchers evaluated how the spillway's hydraulic performance worked in this particular configuration by studying pressure distribution on the bucket along with angle effects on downstream motion. The circular bucket design proved to be the most optimal among all tested shapes, according to their findings [11]. Kavianpour Esfahani et al. (2011) performed experimental research that studied the impact of discharge rates and tailwater depths on bucket-type spillway jet flow scour patterns. The hydraulic model study conducted at the Azad Dam flood discharge system revealed that variations in discharge rate and tailwater depth substantially affect the maximum scour depth [12].

Arefpour et al. (2012) studied hydrodynamic pressure distribution and instantaneous pressure fluctuations along a bucket-type spillway using the Balaroud Dam experimental model, testing six different

return period discharges. Results from measuring minimum and maximum dynamic pressure fluctuations indicated that these fluctuations do not have a destructive effect on the structure [13].

Mousavi Jahromi and Omidvarinia (2012) studied ski jumps in triangular-type spillways with geometry different from bucket-type spillways. The researchers conducted a hydraulic performance study that compared triangular bucket spillways against circular bucket spillways with specific emphasis on outflow trajectory effects. A physical prototype of the ogee spillway underwent testing by changing both the discharge rates and the flow angles. An increase in flip bucket angle resulted in thinner outflow jet thickness while changing Froude numbers between 41.6 and 44.4, which extended the travel length [14].

Askari and Ghomeshi (2013) demonstrated through experimental modeling of an ogee spillway with a bucket-type flip bucket, using various discharges and angles, that different angles result in varying energy dissipation rates. Energy loss percentage increases with higher Froude numbers [15]. Nikpour et al. (2014) analyzed flow over an ogee spillway using the k-ε turbulence model, employing finite element and finite volume methods in two dimensions with FLUENT software. The model accuracy in determining water surface profile and flow velocity assessment was conducted by comparing simulation results against measured values. The numerical models showed effective performance in determining free water surface profiles according to the study results [16].

Eshrati et al. (2015) created a physical model of a free ogee-type spillway with a curved plan to conduct tests. The researchers analyzed spillway efficiency results that compared normal and submerged conditions at equal discharges. The researchers determined that axial curve spillways produce a 21% increase in discharge coefficient when compared to straight-crested spillways at equivalent hydraulic and geometric conditions [17].

Kakeshpour et al. (2016) utilized FLOW-3D software for numerical modeling derived from the Balaroud Dam spillway physical model research. The analysts utilized the VOF method with the RNG turbulence model to evaluate flip bucket designs that used circular and triangular shapes. Numerical and experimental models produced results that differed by 15%. The researchers analyzed how the Froude number related to the cavitation number within the chute end zone and flip bucket space while identifying that maximum erosion potential emerges at a specific critical point that might not match the peak Froude number [18].

Fazlollahnejad et al. (2016) modeled and studied hydraulic flow characteristics over a converging chute and bucket-type spillway with a negative slope at Gotvand Neka Dam using FLOW-3D software. Comparing results from modified spillway geometry to the original model, they found that changing the circular arc radius did not significantly affect hydraulic characteristics, with only a 5m increase in throw length observed with increased radius [19].

Zhenwei et al. (2012) modeled spillway flow using the VOF model in FLUENT computational fluid dynamics software. The modeling results agreed with the experimental model regarding pressure, free surface fluid level, and flow velocity along the spillway [20]. Sharifi and Rostami Ravori (2013) conducted experiments and modeling on various geometries, including flat chute with a 40° flip bucket angle and a compound chute with two different angle combinations (20 and 40°) and (40 and 80°). They modeled results using FLOW-3D and compared depth and energy curves, finding that compound flip buckets with lower angles demonstrated greater energy dissipation capability [21].

Fadaei Kermani and Barani (2014) conducted a numerical analysis of bucket-type flip buckets through the implementation of the RNG turbulence model to study pressure and velocity variations. The numerical calculations performed for piezometric pressure and velocity near the spillway showed maximum differences between experimental and calculated results of 47.5% for average velocity values and 79.7% for pressure values [22].

Parsaie et al. (2016) studied numerical modeling of cavitation phenomena on Balaroud Dam spillway bucket surfaces. This research compared numerical modeling performance with a physical model built for this purpose. During numerical modeling, they found the RNG turbulence model suitable for cavitation modeling. Physical modeling showed a minimum cavitation index of around 0.85, while FLOW-3D results yielded approximately 0.1665, with the main difference between numerical and physical modeling related to velocity. Numerical simulation results indicated that cavitation does not occur along the spillway based on a cavitation index of 0.25 [23].

Regarding the necessity and importance of this research, it can be stated that given the significance of energy dissipation in high dams, their spillways with ski-jump buckets are of particular importance. Energy dissipation in such spillways is related to various hydraulic and geometric factors of the structure, requiring appropriate investigation to achieve the highest dissipation efficiency. To date, comprehensive efforts have not been made to obtain the complete set of parameters used in designing such structures with ski-jump buckets. Obtaining these optimal geometric and hydraulic conditions for the structure and its

outlet jet is of paramount importance and must be investigated, considering its impact on downstream scour and erosion. Geometric and hydraulic parameters are examined and modeled with software so that conditions that give maximum dissipation with minimal downstream effects can be approached.

The objective of this research is to investigate flow turbulence conditions and the sensitivity of ski-jump bucket geometric parameters and flow hydraulics relative to energy dissipation. The general objectives are itemized as follows:

1. Evaluation of turbulence models and selection of appropriate models for use in ski-jump spillways
2. Investigation of geometric parameters related to ski-jump buckets
3. Investigation of hydraulic parameters related to flow
4. Assessment of the sensitivity of bucket geometric parameters and flow hydraulics relative to energy dissipation

2. Materials and Methods

The section begins with presentations of continuity and momentum equations before explaining turbulence models active in software programs including the K-ε model. The research software FLOW-3D receives further description in this section.

2.1. Computational Fluid Dynamics

Theoretical methods begin with observing physical phenomena, expressing the relevant differential equations, and then addressing the algebraic equations governing the problem. The challenge is that, unlike phenomena for which appropriate mathematical models have been developed (such as laminar flow), there are phenomena for which suitable mathematical models have not yet been found (such as two-phase flows). Numerical methods function as the third approach for solving fluid flow problems because of their known limitations. Three categories make up the entire field of fluid dynamics according to [24].

- Experimental Fluid Dynamics
- Theoretical Fluid Dynamics
- Computational Fluid Dynamics

The CFD method serves as a fluid mechanics branch dedicated to analyzing fluid flow problems through numerical analysis paired with numerical algorithms. Computers operate simulations which model the interaction between liquids and gases with boundary condition surfaces. This fluid mechanics branch connects classical mechanics with the modern computational capabilities of computer science during the new millennium [24].

The CFD method is the structure of numerical programs, and numerical algorithms include the following steps [24]:

- Integration of fluid flow governing equations over all control volumes related to the solution field
- Discretization, including substitution of finite difference approximations for terms within the integral equation, which represents flow processes such as convection, diffusion, and sources. This process converts integral equations into a system of algebraic equations
- Solving algebraic equations using an iterative method. CFD in fluid system design has several unique advantages over experimental methods
- Substantial reduction in time and cost of new designs
- Ability to study systems where experiments are difficult or impossible
- Ability to study systems under random conditions and beyond their normal limits

Discretization methods for differential equations in computational dynamics [24]:

- Finite Element Method
- Finite Volume Method
- Finite Difference Method
- Spectral Methods

The finite volume method provides superior application in modeling incompressible flow systems. Computational fluid dynamics commercial software companies have primarily developed their products through this method [24].

2.2. Flow Equations

Fluid dynamics function through flow equations, which result from three fundamental physical conservation laws for mass, momentum, and energy. The governing equations of fluid flow represent mathematical expressions of physical conservation laws according to [24].

- The principle of mass conservation leads to flow continuity equations
- The principle of momentum conservation leads to momentum equations
- The principle of energy conservation leads to flow energy equations

2.3. Continuity Equation

Mass conservation of a small fluid element proves that the total mass flux into the element equals the element's mass growth rate through the relation below:

$$\frac{\partial \rho}{\partial t}+\frac{\partial(\rho u)}{\partial x}+\frac{\partial(\rho v)}{\partial y}+\frac{\partial(\rho \omega)}{\partial z}=0. \tag{1}$$

The relationship for incompressible fluids reduces to this form:

$$\mathrm{div}U=\frac{\partial u}{\partial x}+\frac{\partial v}{\partial y}+\frac{\partial \omega}{\partial z}=0. \tag{2}$$

The equations include spatial coordinates $x,\ y,\ z$ along with velocity components $u,\ v,\ w$ that operate in the directions of $x,\ y,\ z$. The fluid velocity takes vector form through U and combines with fluid density which is represented by ρ [24].

2.4. Momentum Equation

When applying the principle of conservation of momentum to a designated fluid element, you find that acting forces balance the rate at which fluid momentum increases within that element. The fluid particle experiences two types of forces which include pressure forces acting on the surface and gravitational forces acting as body forces. This principle has a mathematical expression that works in different directions (x, y and z) as follows [24]:

$$\begin{cases} \rho\dfrac{Du}{Dt}=\dfrac{\partial(-P+\tau_{xx})}{\partial x}+\dfrac{\partial \tau_{xy}}{\partial y}+\dfrac{\partial \tau_{zx}}{\partial z}+S_{MX} \\ \rho\dfrac{Dv}{Dt}=\dfrac{\partial \tau_{xy}}{\partial x}+\dfrac{\partial(-P+\tau_{yy})}{\partial y}+\dfrac{\partial \tau_{zy}}{\partial z}+S_{MY} \\ \rho\dfrac{Dw}{Dt}=\dfrac{\partial \tau_{xz}}{\partial x}+\dfrac{\partial \tau_{yz}}{\partial y}+\dfrac{\partial(-P+\tau_{zz})}{\partial z}+S_{MZ} \end{cases}. \tag{3}$$

In fact, the above body forces are:

$$S_{MX}=S_{MY}=0; \tag{4}$$

$$S_{MZ}=-\rho g. \tag{5}$$

In a Newtonian fluid, viscous stresses are proportional to strain rates. The three-dimensional form of Newton's viscosity for compressible flows contains two constants: dynamic viscosity (μ) and secondary viscosity (λ). Considering these, the surface stresses will be:

$$\begin{cases} \tau_{xx} = 2\mu\dfrac{\partial u}{\partial x} + \lambda \mathrm{div}U \rightarrow \tau_{yx} = \tau_{xy} = \mu\left(\dfrac{\partial u}{\partial y} + \dfrac{\partial v}{\partial x}\right) \\ \tau_{yy} = 2\mu\dfrac{\partial v}{\partial y} + \lambda \mathrm{div}U \rightarrow \tau_{xz} = \tau_{zx} = \mu\left(\dfrac{\partial u}{\partial z} + \dfrac{\partial w}{\partial x}\right) \\ \tau_{zz} = 2\mu\dfrac{\partial w}{\partial z} + \lambda \mathrm{div}U \rightarrow \tau_{zy} = \tau_{yz} = \mu\left(\dfrac{\partial v}{\partial z} + \dfrac{\partial w}{\partial y}\right) \end{cases}. \quad (6)$$

Given that liquids are incompressible and have no volumetric deformation (ε = 0), and according to the continuity relation $\mathrm{div}U$ = 0, substituting the above relations into equations (3) and performing necessary simplifications yields [25]:

$$\begin{cases} \rho\dfrac{Du}{Dt} = -\dfrac{\partial p}{\partial x} + \mathrm{div}\left(\mu \mathrm{grad}u\right) + S_{MX} \\ \rho\dfrac{Dv}{Dt} = -\dfrac{\partial p}{\partial y} + \mathrm{div}\left(\mu \mathrm{grad}v\right) + S_{MY} \\ \rho\dfrac{Dw}{Dt} = -\dfrac{\partial p}{\partial z} + \mathrm{div}\left(\mu \mathrm{grad}w\right) + S_{MZ} \end{cases}. \quad (7)$$

The following relations represent fluid mechanics equations where x, y, z denote spatial directions while u, v, w represent their velocity portions and U indicates velocity vector and ρ stands for fluid density with μ representing fluid dynamic viscosity and p indicating fluid pressure at any point and s representing the source term. The Navier-Stokes equations represent these relations [24].

The governing equations require turbulence models to determine the connection between Reynolds stresses and mean flow velocity components.

2.5. Turbulent Flows

Turbulence occurs frequently in engineering problems as well as hydraulic engineering structures. Turbulence presents diverse applications that make its study a complex multifaceted field. The flow remains smooth when the Reynolds number stays below the critical limit because different fluid layers glide past one another while steady flow occurs when boundary conditions remain constant with time. The laminar flow area exists within this region. The flow behavior alters because conditions change when the Reynolds number exceeds its critical value. A high wall shear rate triggers an instability in laminar flow to cause increased momentum transfer. The establishment of turbulent points at local regions leads to flow turbulence which generates random flow patterns. The turbulence grows into a system that no longer depends on either initial or random fluctuations or irregularities. Turbulent flow exists in this region as per [25].

Various turbulent flow analysis methods are as follows [25]:

- Experimental methods
- Direct solutions of the governing dynamic equations of turbulent flow fields
- Dimensional analysis methods
- Statistical equation simplification methods

The experimental method primarily relies on constructing laboratory models. In dimensional analysis, equations are compared, and terms of lower order are neglected. Given the random and stochastic nature of turbulent flow, turbulent flow field quantities can be decomposed into two components: a permanent mean value and a fluctuating value. When applied to governing equations and time-averaged, this decomposition introduces new unknowns into the governing equations. The random and irregular motion of fluid masses in turbulent flows can also generate another type of stress; consequently, the additional terms in the equations have become known as apparent stresses or Reynolds stresses. Considering the above factors, statistical methods for equation simplification are most commonly employed in the study and analysis of turbulent flows [25].

2.6. Turbulent Flow Equations

The computational method used for solving diverse flow problems through the closure of the continuity equations and Reynolds equations together with scalar transport equations defines a turbulence model. One needs to use simplified equations representing complicated turbulent behavior to determine Reynolds stresses for time-averaged equations [26].

In 1885, Reynolds decomposed a field quantity into two components: one related to the mean flow and another related to its fluctuations [26].

$$\varphi = \overline{\varphi} + \varphi'. \tag{8}$$

The pressure and velocity components in turbulent flow take the following form:

$$V = \overline{V} + \hat{V}; \tag{9}$$

$$P = \overline{P} + P. \tag{10}$$

The substitution of relationships (9) and (10) followed by time average calculation leads to mean turbulent flow equations for continuity and momentum. The instantaneous continuity equation is:

$$\frac{\partial \rho}{\partial t} + \operatorname{div}\left(\rho V\right) = 0. \tag{11}$$

The time average of this expression results in:

$$\frac{\partial \rho}{\partial t} + \operatorname{div}\left(\rho V\right) = 0. \tag{12}$$

The time-averaged momentum equation follows a similar procedure in all directions x, y and z and yields:

$$\begin{cases} \dfrac{\partial u}{\partial t} + \operatorname{div}\left(u\overline{V}\right) = -\dfrac{1}{\rho}\dfrac{\partial P}{\partial x} + V\operatorname{div}\left(\operatorname{grad} u\right) + \left[\dfrac{-\partial\overline{u^2}}{\partial x} - \dfrac{-\partial\overline{\dot{u}\dot{v}}}{\partial y} - \dfrac{-\partial\overline{\dot{u}\dot{w}}}{\partial z}\right] \\ \dfrac{\partial v}{\partial t} + \operatorname{div}\left(v\overline{V}\right) = -\dfrac{1}{\rho}\dfrac{\partial P}{\partial y} + V\operatorname{div}\left(\operatorname{grad} v\right) + \left[\dfrac{-\partial\overline{\dot{u}\dot{u}}}{\partial x} - \dfrac{-\partial\overline{v^2}}{\partial y} - \dfrac{-\partial\overline{\dot{v}\dot{w}}}{\partial z}\right] \\ \dfrac{\partial w}{\partial t} + \operatorname{div}\left(w\overline{V}\right) = -\dfrac{1}{\rho}\dfrac{\partial P}{\partial z} + V\operatorname{div}\left(\operatorname{grad} w\right) + \left[\dfrac{-\partial\overline{\dot{u}\dot{w}}}{\partial x} - \dfrac{-\partial\overline{\dot{w}\dot{v}}}{\partial y} - \dfrac{-\partial\overline{w^2}}{\partial z}\right] \end{cases}. \tag{13}$$

The random and irregular motion of molecules causes molecular viscosity and stress. Similarly, the random and irregular motion of fluid masses in turbulent flows can generate another type of stress. Consequently, the additional terms in equations (13) are known as apparent stresses or Reynolds stresses. Due to their significant magnitude relative to molecular viscosity stresses throughout most of the flow domain, apparent stresses are of paramount importance and constitute the primary factor distinguishing between mean quantity behavior in turbulent versus laminar flow. The additional stresses appearing in the above expressions, termed Reynolds stresses, are [26]:

$$\begin{cases} \tau_{xx} = -\rho\overline{u^2} \quad \tau_{yy} = -\rho\overline{v^2} \quad \tau_{zz} = -\rho\overline{\dot{w}^2} \\ \tau_{xy} = \tau_{yx} = -\rho\overline{u'v} \quad \tau_{yz} = \tau_{zy} = -\rho\overline{\dot{v}w} \quad \tau_{xz} = \tau_{zx} = -\rho\overline{u'w} \end{cases}. \tag{14}$$

2.7. Various Turbulence Model Types

The classification of Turbulent models depends on their method of implementation in the transport equation. A single transport equation approach applies to velocity scale V for fluctuating velocity and another approach uses length scale L. More complex models also exist.

Turbulence transport model classifications rely on the methods used to determine eddy viscosity, although it may be identified as a characteristic of velocity and length. Different models fitting this context include those listed below in [26].

2.8. Zero-Equation Models (Algebraic)

Differential Models

One-equation Models

Two-equation Models

Multi-equation Models

2.9. Zero-Equation or Algebraic Model

Prandtl's mixing length theory (1925) forms the basis of the algebraic models. This is his theory through which he proposed that the turbulent viscosity is proportional to fluid density, a characteristic velocity, and a characteristic length. This model has a significant limitation in its predetermined distribution of l-meter near the wall, resulting in a large difference between the experimental results and the theoretical results. If a distribution of l-meter of width is indeed reasonably accurate, these models produce satisfactory results for velocity and shear stress (but not mean velocity or mean shear stress). The mixing length model is simple, and it is economical because the solution of differential equations is not required. Yet experimental data is very flow-dependent, and the mixing length model could no longer be used for the turbulent transport (convection and conduction (diffusion)) processes. Since transport and turbulence history is neglected in the mixing length hypothesis, unlike in point equilibrium, it cannot be applied to complex flows [26].

2.10. One-Equation Model

In order to associate the characteristic flow velocity with the root mean square of the turbulent kinetic energy, differential equations, rather than algebraic equations, were used to include the effects of turbulence diffusion and convection on the characteristic velocity. From this, one differential model equation was developed wherein the characteristic velocity is the turbulent kinetic energy, which is calculated via a differential equation. The turbulent flow velocity scale is used in combination with transport, diffusion, convection, and turbulence history in one-equation model. It is found that these transport phenomena are significant, and these models also have a distinct advantage over zero-equation models. One of the main reasons to study such models is that they are simple; however, such models are not suited to study highly complex flows [26].

2.11. Two-Equation Model

Complex flow conditions require precise assessment of transport and diffusion impacts from characteristic dimensions. The development of two-equation differential models of turbulent viscosity became necessary. All these models determine turbulent viscosity through the relation Vt=lk^0.5. The models develop a variable z=k^m L^n composed of m and n constants and use Navier-Stokes equations to derive Z exactly. The research study declines to use L as a variable because it approaches the problem by treating Z together with turbulent kinetic energy k and characteristic length as the unresolved aspect. The development of diverse two-equation models proceeds from different m and n values according to Table 1, found in [26].

Table 1. Various Two-Equation turbulence models

m	n	Z	Dimension	Model
0	1	L	M	k − L
1	1	KL	M^3/T	k − kL
2/3	–1	$K^3/2/L$	M^2/T^3	k − ε
1	–2	k/L^2	$1/T^2$	k − w
1/3	–1	K1/3/L	1/T	k − f

All models, in practice, yield equivalent results that can be arranged in a single mathematical expression. The standard $k-\varepsilon$ model represents the most popular choice from two-equation models for turbulent flow analysis, according to reports [26].

2.12. The Standard $k-\varepsilon$ Model

The model considers $z=\frac{k^{\frac{2}{3}}}{l}$ and designates it as ε to denote the turbulent energy dissipation rate [26].

$$\varepsilon = \nu\overline{\frac{\partial u_1'}{\partial x_J}\frac{\partial u_1'}{\partial x_J}}. \tag{15}$$

Through Navier–Stokes equations, the transport equations for k and ε quantities appear as (16) and (17):

$$\frac{\partial k}{\partial t}+\bar{u}_i\frac{\partial k}{\partial x_i}=\frac{\partial}{\partial x_i}\left[\left(\nu+\frac{\nu_t}{\partial k}\right)\frac{\partial k}{\partial x_i}\right]+p-\varepsilon; \tag{16}$$

$$\frac{\partial \varepsilon}{\partial t}+\bar{u}_i\frac{\partial \varepsilon}{\partial x_i}=\frac{\partial}{\partial x_i}\left[\left(\nu+\frac{\nu_t}{\partial \varepsilon}\right)\frac{\partial \varepsilon}{\partial x_i}\right]+c_{1\varepsilon}\frac{\varepsilon}{k}p-c_{2\varepsilon}\frac{\varepsilon^2}{k}; \tag{17}$$

$$\nu_t=c_\mu\frac{k^2}{\varepsilon}; \tag{18}$$

$$p=\nu_t g=\nu_t\left[\frac{\partial\overline{u_t}}{\partial x_j}+\frac{\partial\overline{u_j}}{\partial x_i}\right]\frac{\partial\overline{u_t}}{\partial x_j}. \tag{19}$$

In the $k-\varepsilon$ model, the production and dissipation of turbulent kinetic energy are consistently assumed proportional to each other, such that the transport equations for k and ε quantities presume their production and dissipation are proportional. The standard $k-\varepsilon$ model is applicable for fully turbulent regions of a flow field; however, near walls, the local Reynolds number is consistently small, such that molecular viscosity effects dominate flow turbulence, consequently preventing the use of the standard $k-\varepsilon$ model in these regions [26].

Two solutions exist to overcome this limitation [26]:

2.13. Implementation of the Wall Function Method

Utilization of modified forms of the standard $k-\varepsilon$ model that account for molecular viscosity effects near walls, known as low-Reynolds $k-\varepsilon$ models.

2.14. Multi-Equation Models

Reynolds Stress Model (RSM) and Algebraic Stress Model (ASM) represent significant examples of multi-equation models. RSM represents one of the most advanced classical turbulence models that effectively tackles multiple limitations of the k model when predicting complex strain fields and significant body force conditions. Multi-equation models offer both realistic physical turbulence process representation and successful performance for free-stream flow together with near-wall flow as well as two-dimensional internal flows [24].

2.15. Introduction to Computational Software (FLOW 3D)

Computational fluid dynamics features FLOW 3D as one of its important commercial software solutions. Flow Science in the United States develops and supports this software program as it serves multiple engineering fields such as mechanical and fluid dynamics, metallurgy and chemical engineering, environmental engineering, water engineering hydraulics, and marine applications. The distinct element of this software enables free-surface flow simulation that proves crucial for hydraulic and hydrodynamic engineering applications.

FLOW 3D's capabilities in hydraulic engineering include modeling cavitation phenomena, air entrainment and dispersion in fluid flow, wall stresses, porous media, sediment scour, shallow flows,

turbulent and laminar flows, and floating object movement. FLOW 3D offers five turbulence models: zero-equation, one-equation, two-equation ($k-\varepsilon$ and RNG), and Large Eddy Simulation.

FLOW 3D serves as an appropriate model for complex CFD problems with broad applications. The program is applicable to three-dimensional unsteady flows with free surfaces and complex geometries. FLOW 3D employs two numerical techniques for geometric simulation [27]:

- Volume of Fluid (VOF) method, applied to represent fluid behavior at free surfaces
- Fractional Area/Volume Obstacle Representation (FAVOR) method, utilized for simulating solid surfaces and volumes such as geometric boundaries [27]

The modeling utilized results from experiments conducted by Babak Navaee et al. (2016) on standard ogee spillways with flip buckets at 32 and 52° takeoff angles, as well as without buckets. In the laboratory model, energy dissipation in this type of spillway was examined through 21 experiments with flow rates ranging from 330 to 864 L/min. The physical laboratory spillway model was constructed according to USBR standards with the height of 27.2 cm, length of 40 cm, and width of 30 cm, including a rectangular block (height of 6.6 cm, length of 10 cm, and width of 30 cm) and two flip buckets (length of 10 cm, width of 30 cm, and radii of 12 and 19 cm) made of polyethylene using CNC machinery. The experiments were conducted by placing the rectangular block and buckets at the end of the ogee spillway [1].

The practical and laboratory phases of this research were conducted in the Hydraulics Laboratory of Maragheh University, Maragheh, Iran, using a flume with a length of 6 m, width of 0.3 m, and height of 0.45 m. Fig. 1 shows the laboratory flume cross-section (a) and ogee spillway (b), while Fig. 2 displays the flip buckets and rectangular blocks with their dimensions [1].

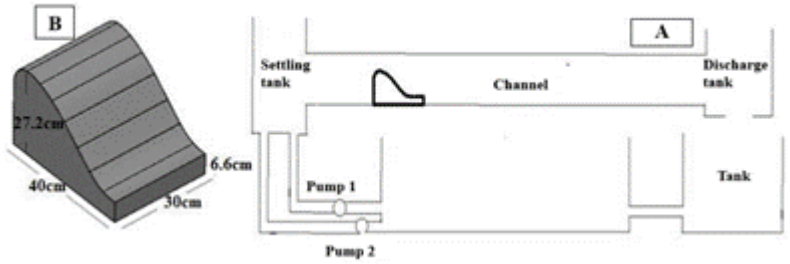

Figure 1. Laboratory flume cross-section (a) and ogee spillway (b).

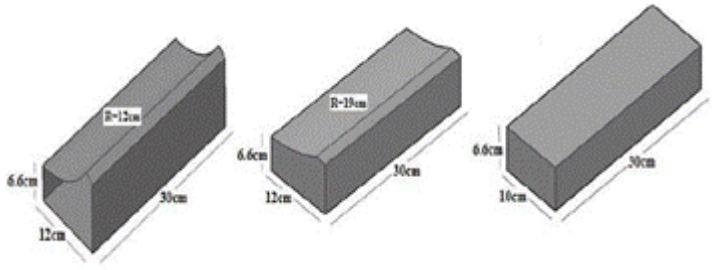

Figure 2. Flip buckets and rectangular block.

Flow rate was measured with 0.001 accuracy using two tachometers installed at the end of the pumps before entering the stilling basin [1].

Selection of Turbulence Model between k-ε and RNG in Modeling

For validation and selection of the turbulence model, numerical modeling was performed using FLOW 3D software with identical geometry hydraulic conditions but different turbulence models. The results comparing the maximum fluid throw length are shown in Table 2.

Table 2. Comparison of different turbulence models' results for fluid jump length with reference laboratory results

	RNG		**$k-\varepsilon$**		**Experimental results [15]**
Q (L/min)	Max L (cm)	Error (%)	Max L (cm)	Error (%)	Max L (cm)
508	20/2	5/2	20/4	6/25	19/2
597	26/6	5/97	26/8	6/77	25/1
659	33/1	6/78	33/3	7/4	31

The RNG turbulence model provides better accuracy with a reduced error percentage as compared to the $k-\varepsilon$ model. The RNG turbulence model became the selected choice for modeling purposes in this research. The largest error in jump length measurement took place at a flow rate of 659 L/min, with an error amounting to 6.8%.

3. Results and Discussion

3.1. Numerical Model Sensitivity to Meshing

Numerical modeling of projected flow requires meshing as an essential factor which can be implemented through different methods beyond geometry.

Multiple blocks can be created for meshing in FLOW 3D numerical software, defining each numerical model as single-block or multi-block. Each block can be specified with different dimensions and mesh numbers to achieve acceptable sensitivity and obtain various results. Higher mesh numbers and smaller sizes create appropriate sensitivity and acceptable results with lower errors in modeling. Several numerical modeling approaches were implemented:

- Single-block model with 5 mm mesh cells for 5 sec
- Set for analysis with 0.01-time steps, total computational cells amount to (total active cells 1,262,320)

  Additionally, the total number of cells (active and inactive) are 1,451,298, with total active cells at 1,262,320.

Active cells include:

- Real cells used for flow equation solving (1,185,330)
- Real open cells (1,181,212)
- Fully blocked real cells (4,118)
- External boundary cells (76,990)
- Inter-block boundary cells (0)

Fig. 3 below shows the single-block numerical model with specified 5 mm meshes.

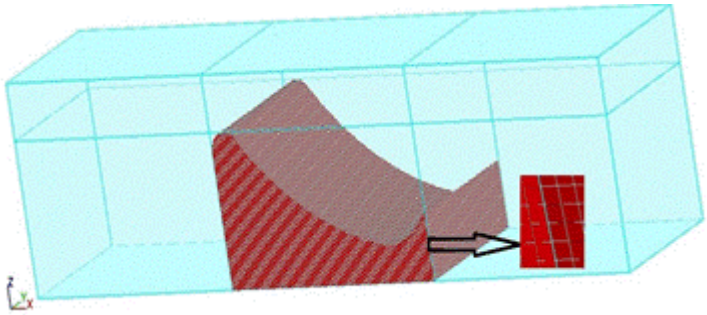

Figure 3. The numerical model meshes with one block.

The growth rate in the laboratory with a flow rate of 597 L/min is 0.715, whereas in the numerical model, the ΔEr value at different points around the projectile is mentioned in Table 3. In this Table, the sample numbers are designated such that sample (11) indicates the first point in zone zero, which is the area before the spillway, and sample (12) indicates the first point in zone one, which is the area after the spillway. For each zone, the x, y and z coordinates of the point of interest are specified in the Table.

Table 3. Hydraulic energy levels at points with 597 L/min flow rate and 5 mm mesh

Sample	X(m)	Y(m)	Z(m)	E(m)	ΔE_r = = $(E_0 - E_1) / E_0$	Error(%)
01	1.2157e+01	7.3610e+0	2.5378e-03	3.3194e-01	0.0759	6.15
11	1.3397e+01	7.3610e+0	2.5378e-03	0.79897e-02		
02	1.2072e+01	7.3611e+0	2.5379e-03	3.3189e-01	0.758	6
12	1.3412e+01	7.3660e+0	2.5379e-03	0.80140e-02		
03	1.2102e+01	7.3612e+0	2.5380e-03	0.33179e-01	0.726	1.4
13	1.3417e+01	7.3661e+0	2.5380e-03	9.0723e-02		

The ΔEr value obtained in the numerical model differs from the laboratory model, with an average error of 4.4% across these points, which is acceptable and suitable.

3.2. The Single-block Model with 5 mm and 4 mm Cells for 5 Sec

Five mm cells were used to create the front and back sections of the block because these areas lack a spillway while four millimeter cells were used for the middle section containing the spillway. This configuration allows the numerical model to operate as a single block through analysis of 5 sec with 0.01 time steps. There are 1,952,778 computational cells in relation to the active cells within the model.

The analysis shows that the study contains 2,314,622 cells which includes both active and inactive cells while the total active cells number reaches 1,952,778.

Active cells consist of:

- The total number of real cells that participated in flow equation calculations reached 1,850,578
- Real open cells (1,844,081)
- Completely blocked real cells (6,497)
- External boundary cells (102,200)
- Inter-block boundary cells (0)

The laboratory ΔEr at 597 L/min flow rate is compared with the numerical model, and the error rates at various points around the projectile are listed in Table 4.

Table 4. Hydraulic energy levels at points with 5 mm and 4 mm mesh in single-block configuration

Sample	X(m)	Y(m)	Z(m)	E(m)	$\Delta E_r = (E_0 - E_1) / E_0$	Error(%)
01	1.2057e+01	7.3635e+0	2.0012e-03	3.3195e-01	0.716	0.13
11	1.3374e+01	7.3635e+0	2.0012e-03	9.4099e-02		
02	1.2063e+01	7.3635e+0	2.0012e-03	3.3192e-01	0.710	0.069
12	1.3379e+01	7.3635e+0	2.0012e-03	9.5984e-02		
03	1.2069e+01	7.3635e+0	2.0012e-03	3.3190e-01	0.704	0.15
13	1.3385e+01	7.3635e+0	2.0012e-03	9.7984e-02		

The computed ΔEr shows acceptable deviation from the laboratory model to the extent of less than 0.7% due to denser mesh structure.

3.3. The Three-block Model with 5 mm and 4mm Cells for 5 Sec

A numerical model consisting of three blocks uses 5 mm cells for blocks one and three with no spillway and 4 mm cells for block two with the spillway and operates for 5 sec with a time step of 0.01. The computational system has 1,603,195 cells for numerical processing and also includes 1,603,195 active cells that demonstrate an adequate and appropriate level of responsiveness and maintain acceptable levels of error.

The analysis shows that the total quantity of cells reached 1,973,208, of which 1,603,195 cells were categorized as active.

Active cells consist of:

- The enumeration of real cells which executed flow equation calculations amounted to (1,479,328)
- Real open cells (1,472,831)
- Completely blocked real cells (6,497)
- External boundary cells (88,640)
- Inter-block boundary cells (35,227)

Fig. 4 below illustrates the numerical model meshes with three blocks.

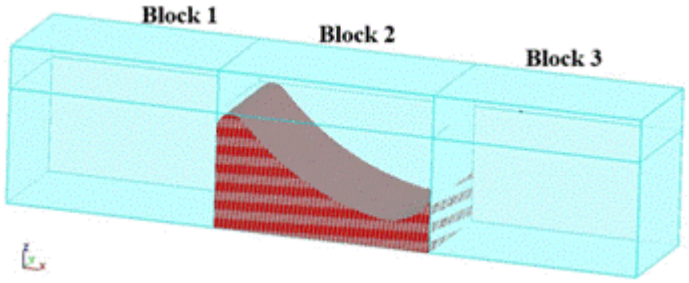

Figure 4. Numerical model meshes with three blocks.

The laboratory ΔEr value is 0.715 at a flow rate of 597 L/min, which has been compared with the numerical model at various points around the projectile, and the error rates are shown in Table 5.

Table 5. Hydraulic energy levels at points with 5 mm and 4 mm mesh in a three-block configuration

Sample	X(m)	Y(m)	Z(m)	E(m)	ΔE_r = = $(E_0 - E_1) / E_0$	Error(%)
01	1.2057e+01	7.3560e+0	0.24739e-03	3.3197e-01	0.705	1.4
11	1.3397e+01	7.3560e+0	0.24739e-03	0.97683e-02		
02	1.2062e+01	7.3560e+0	.24739e-03	3.3197e-01	0.721	0.084
12	1.3407e+01	7.3560e+0	7.4199e-03	0.92570e-02		

The measurements of ΔEr deviate from laboratory values at a 1.12% average discrepancy.

The numerical models in single-block and three-block configurations show acceptable error rates for both simulation types. The number of active cells used to solve flow equations decreased when the model evolved from a single-block to a three-block configuration. When assessing the results between single-block and three-block numerical models with their distinct ΔEr error rates, one can determine that complex geometries benefit from three-block modeling yet simple geometries benefit from more blocks, reducing the cell count but increasing the error margin. The single-block numerical model with two different mesh sizes of 4mm and 5mm demonstrates suitability for analytical purposes.

3.4. Impact of Froude Number at the Flip Bucket Edge on Maximum Jump Length and Height

According to this study, the Froude number at the flip bucket edge determines the greatest length of fluid jumps. Studies within the numerical model evaluated Fr = 3.9, 4.21, 4.45 using identical geometry to determine maximum jump length in centimeter as shown in Fig. 5.

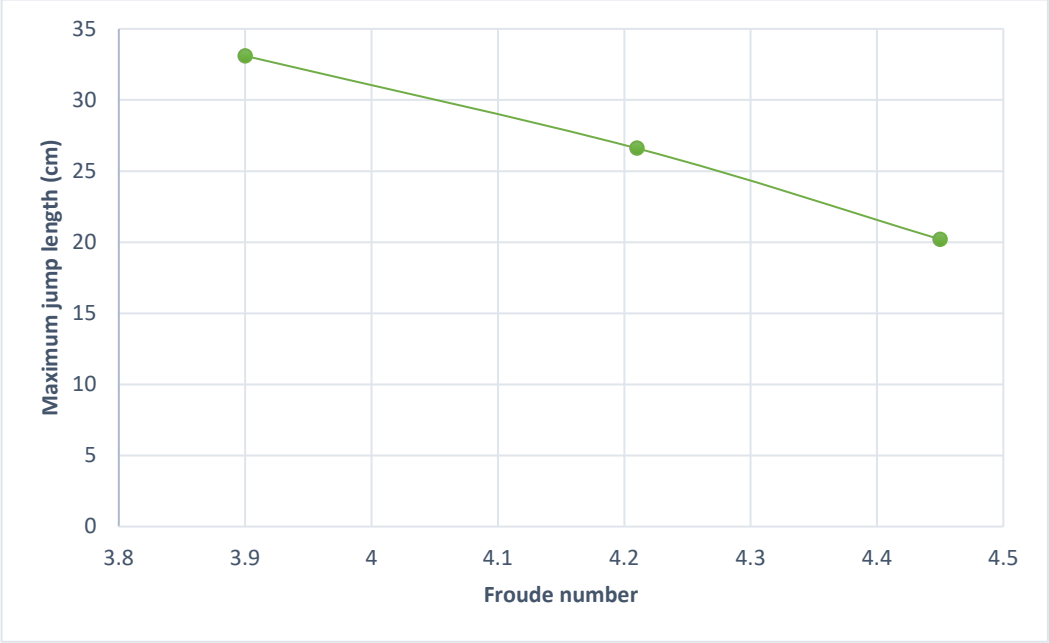

Figure 5. Changes in maximum jump length relative to Froude number at the flip bucket edge.

According to Fig. 5, it is clear that as the Froude number increases, the maximum jump length decreases, which aligns with the results of Navai et al. [28] and Mousavi Jahromi and Omidvarinia [14] experiments.

The analysis of Froude number at the flip bucket edge relative to maximum jump height was also conducted with different Froude numbers (Fr = 3.9, 4.21, 4.45), and the results are expressed in centimeters, shown in Fig. 6.

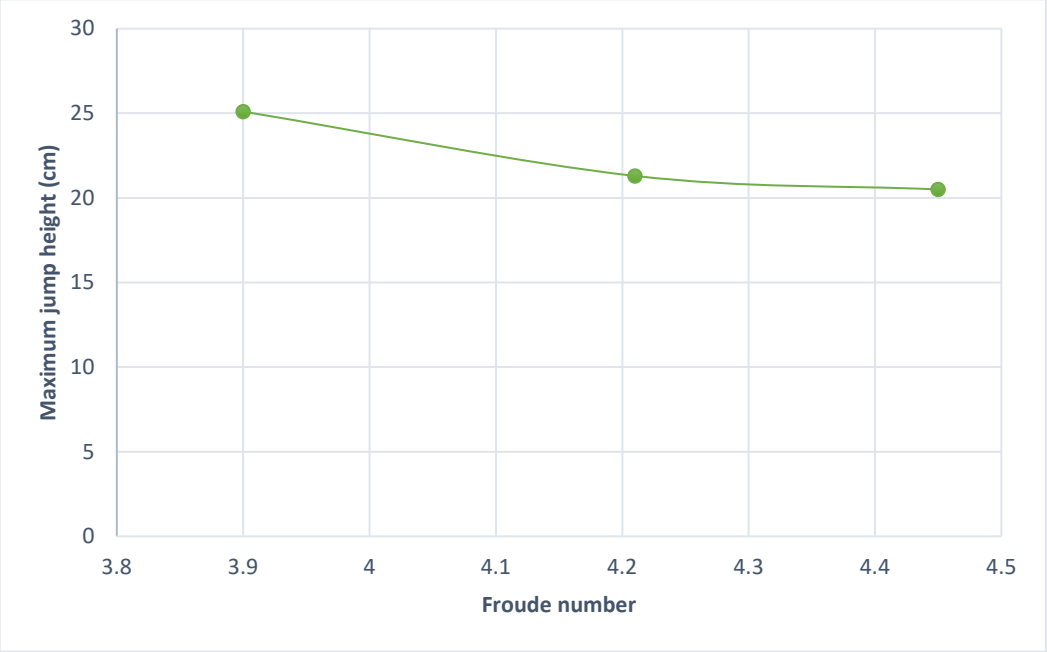

Figure 6. Changes in maximum jump height relative to Froude number at the flip bucket edge.

The results of Heller et al. [8] showed that jump height decreases with increasing Froude number, which is consistent with the modeling results shown in Fig. 6.

3.5. The Impact of Flow Rate on Maximum Jump Length and Height

The analysis of flow rate relative to maximum jump length was conducted with flow rates of 508, 597, and 659 L/min, and the results are expressed in centimeters, shown in Fig. 7.

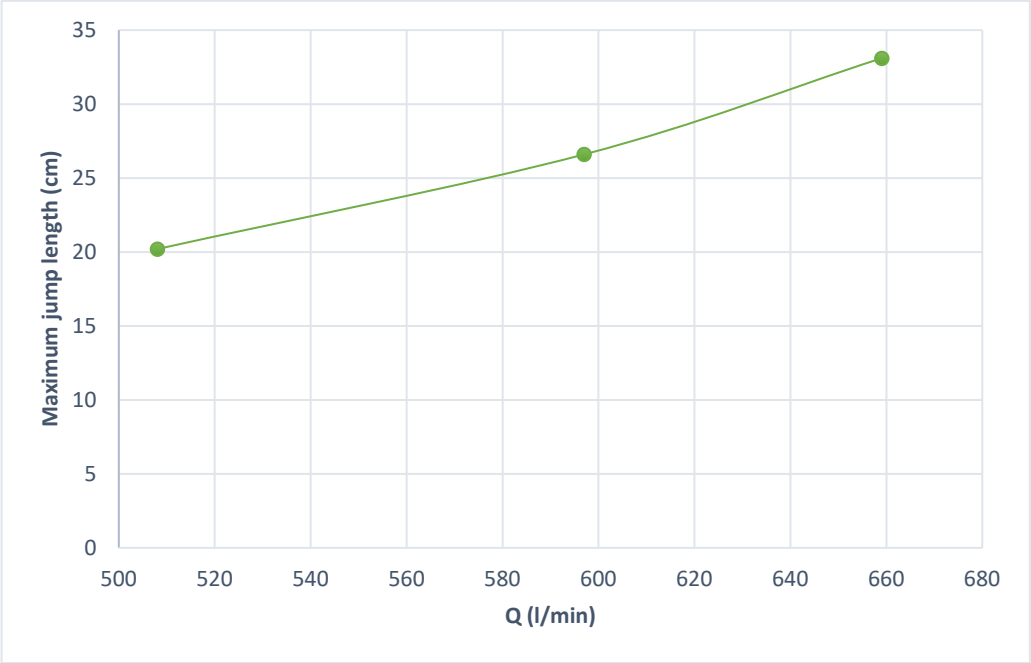

Figure 7. Changes in maximum jump length relative to flow rate.

According to the results and Fig. 7, with increasing flow rate, the maximum jump length increases, which aligns with the laboratory model results of Navai et al. [28].

The analysis of flow rate relative to maximum jump height was also conducted with flow rates of 508, 597, and 659 L/min, with results expressed in centimeters and shown in Fig. 8.

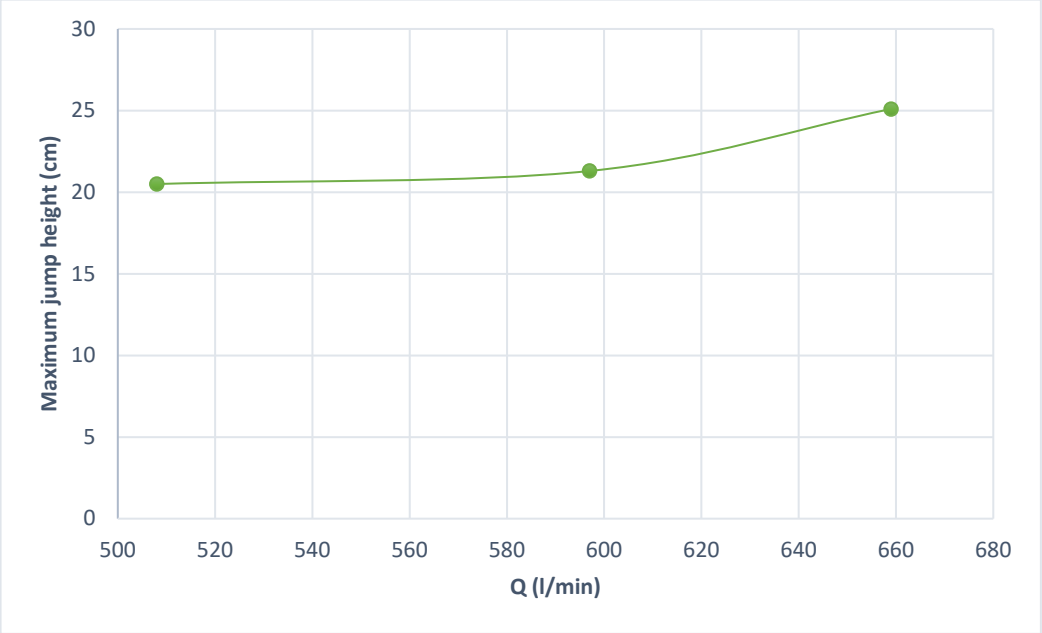

Figure 8. Changes in maximum jump height relative to flow rate.

Based on the results and Fig. 8, it is evident that with increasing flow rate, the maximum jump height increases, which aligns with the laboratory results of Mousavi Jahromi and Omidvarinia [14].

3.6. Impact of Flip Bucket Angle on Maximum Jump Length and Height

Numerical modeling of the bowl-shaped flip bucket generated maximum projectile length and maximum fluid projectile height results using an analysis flow rate of 508, 597, and 659 L/min under identical geometric conditions at a 52° angle with a 12 cm radius of curvature.

The same flow conditions (508, 597, and 659 L/min) were used for running the numerical model after changing the flip bucket geometry to a 32° angle with a 19 cm radius of curvature. Results were analyzed on this configuration.

Results from the numerical model appear in Table 6 following alterations to flip bucket angle and curvature.

Table 6. Maximum jump length, jump height, and Froude number for different flip bucket geometries

Turbulence Model RNG	**Projectile Angle: 52° Arc Radius: 19 cm**			**Projectile Angle: 32° Arc Radius: 12 cm**		
Q (L/min)	508	597	659	508	597	659
Max L (cm)	20.2	26.6	33.1	31.3	34.8	39.6
Fr	4.45	4.21	3.9	4.35	4.1	3.78
Max h (cm)	20.5	21.3	25.1	12.2	13.8	15.6

Based on Table 6 results, graphs of maximum jump length, maximum jump height, and Froude number with different launch angles relative to flow rate have been specified. Fig. 9 shows the maximum jump length relative to different flow rates of 508, 597, and 659 L/min.

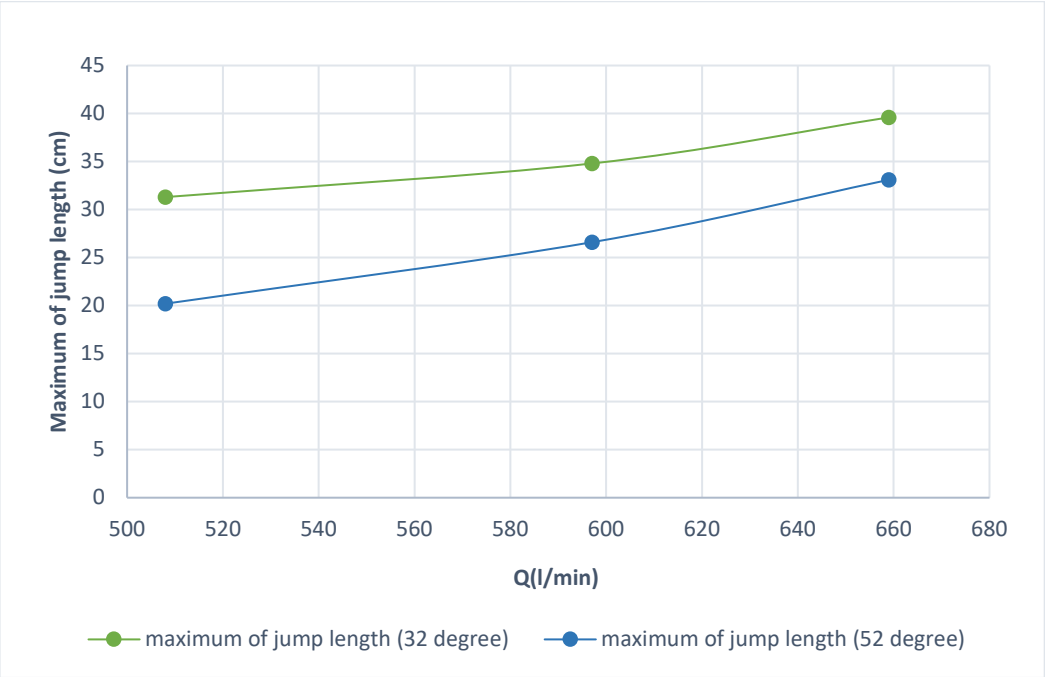

Figure 9. Changes in maximum jump length with jump angles of 52 and 32° relative to flow rate.

The results and Fig. 9 show that changing the flip bucket angle from 52 to 32° increases the maximum fluid jump length, which aligns with the laboratory results of Heller et al. [8].

Fig. 10 shows the maximum fluid jump height relative to different flow rates of 508, 597, and 659 L/min.

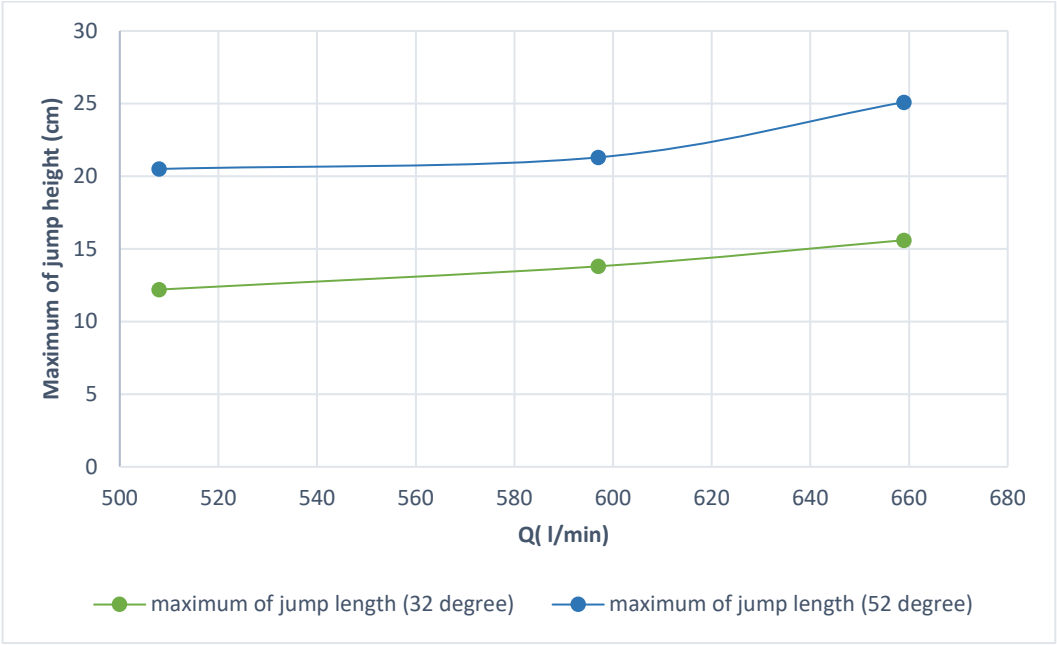

Figure 10. Changes in maximum jump height with jump angles of 52 and 32° relative to flow rate.

The results and Fig. 10 show that changing the flip bucket angle from 52 to 32° decreases the maximum fluid jump height, which aligns with the laboratory results of Mousavi Jahromi and Omidvarinia [14] and Navai et al. [28].

Fig. 11 shows the maximum Froude number at the flip bucket edge relative to different flow rates of 508, 597, and 659 L/min.

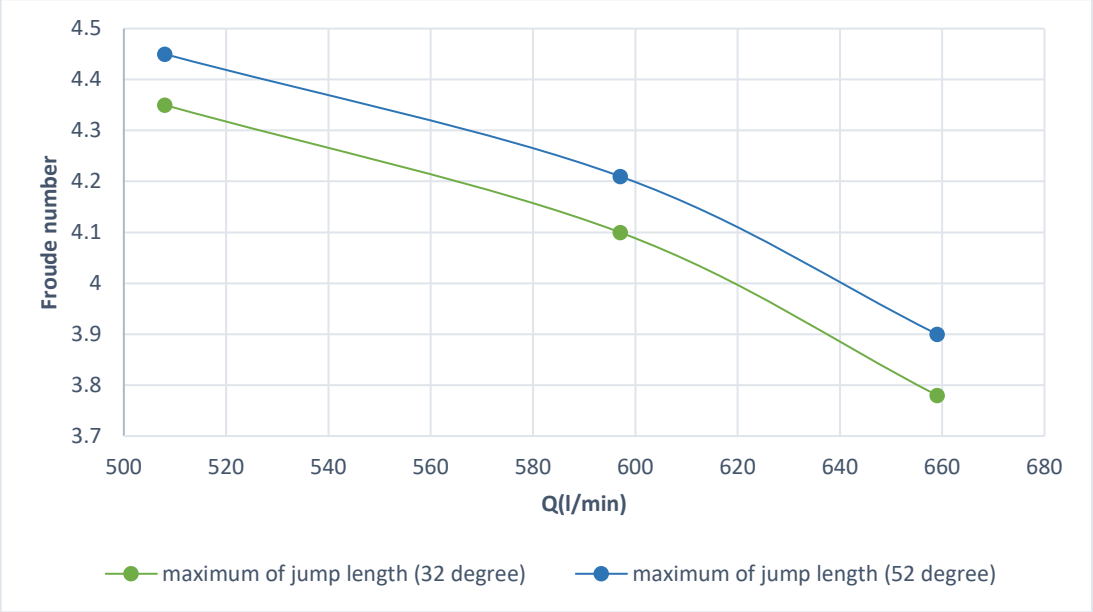

Figure 11. Changes in Froude number at the flip bucket edge with jump angles of 52 and 32° relative to flow rate.

Fig. 11 shows that changing the flip bucket angle from 52 to 32 degrees decreases the Froude number at the flip bucket edge, which aligns with Mousavi Jahromi's [14] results.

Energy Dissipation

Analysis of results shows that the energy loss ratio (output to input energy) decreases with increasing flow rate from 508 to 659 L/min, and changing the flip bucket angle from 52 to 32° reduces energy dissipation in the bowl-shaped flip bucket. Table 7 shows the energy loss relative to flow rate and flip bucket angle.

Table 7. Energy loss relative to flow rate and flip bucket angle

Flow Rate (L/min)	Energy Loss at 52° Projectile Angle	Energy Loss at 32° Projectile Angle
508	0.766	0.727
597	0.737	0.702
659	0.728	0.696

In Fig. 12, changes in energy loss relative to flow rate and projectile angle are shown.

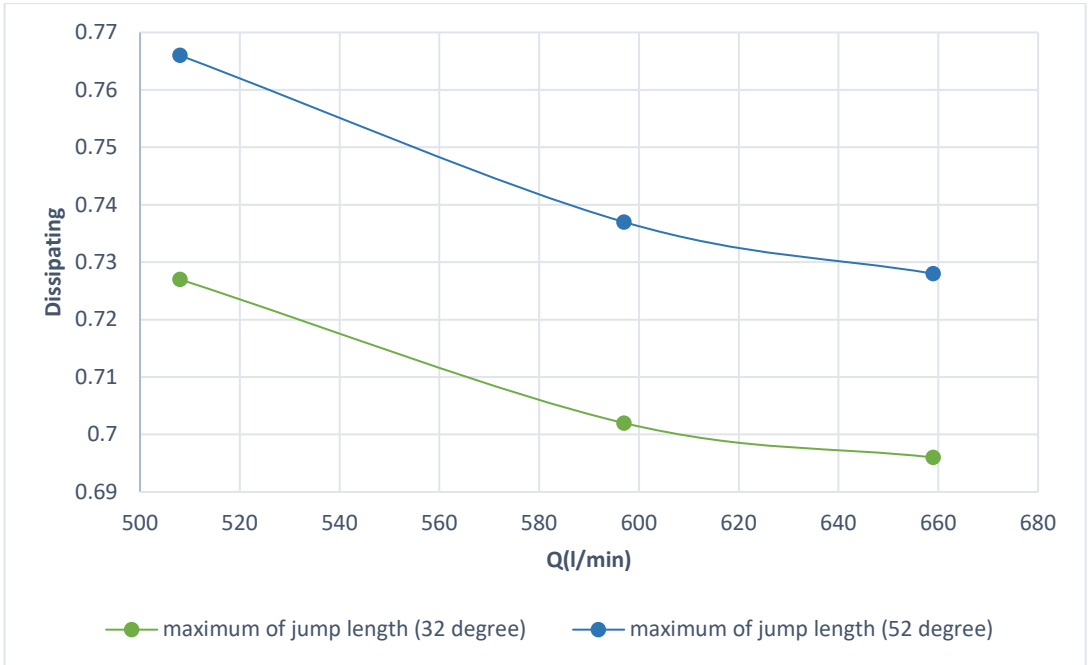

Figure 12. Changes in energy loss relative to flow rate and projectile angle.

Based on comparing the numbers in Fig. 12, the effect of angle changes on energy loss is greater than flow rate changes.

4. Conclusion

The procedure through which dams release energy stands among the critical matters regarding their design. Energy dissipation through dams requires the implementation of multiple systems that perform this function. Ski-jump spillways stand out as critical among these structures, while the exit jet of these structures experiences multiple difficulties, including jet diffusion and downstream erosion. More affordable evaluations of challenging topics become possible through the combination of developed software and hardware systems for numerical simulation. Using meshing and the FAVOR method for simulating the mesh generation process has made modeling complex geometries easier for users. In this research, square meshing with dimensions of 4 mm and 5 mm was used.

This research used CFD methods to investigate and numerically model the effects of various geometric and hydraulic parameters related to ski-jump spillways on the exit jet. The RNG turbulence model was used to examine parameters affecting the exit jet from the spillway, and numerical results were compared and validated with existing experimental studies and measurements. Changes related to maximum jump length and maximum jump height were also examined. The results obtained from this study are presented in this chapter.

The specific results of this research are as follows:

1. In this research, using FLOW 3D software and the RNG turbulence model, the effects of various geometric and hydraulic parameters related to ski-jump spillways on the exit jet were investigated. Given the alignment obtained between the software and experimental results, it can be stated that this software is suitable and highly capable of analyzing various issues related to energy dissipation, ski-jump spillways, and open channel flows. The RNG turbulence model results show better agreement with experimental results than the $(k-\varepsilon)$ turbulence model.

2. In this research, the relative error in energy reduction between experimental results and numerical model results was less than 5%, and the error related to maximum jump length was less than 7%.

3. In this research, the flow rate range was considered between 508 and 659 L/min. With increasing flow rate in a specific and fixed geometry, the maximum jump length and maximum jump height increased, and consequently, the Froude number decreased. The design process should account for the increased maximum length and height that occurs at lower Froude numbers. The reduction of the Froude number to achieve maximum height and maximum jump length becomes possible through increased flow rates. The acceptable flow rate increase needs to maintain a safe operating zone for spillway capacity during this process.

4. Changes in ski-jump spillway geometry were also investigated in this research. Geometric changes included varying the spillway angle from 52 to 32° and changing the arc radius from 12 cm to 19 cm. These geometric changes had a direct and significant impact on the maximum spillway length, maximum spillway height, and Froude number at the spillway lip.

5. Analysis of the numbers showed that with decreasing spillway angle, the maximum jump length increased while the maximum jump height decreased. The effect of angle change on reducing maximum jump height was more noticeable compared to the maximum jump length. With changes in spillway geometry and a reduction in spillway angle, the Froude number decreased, although this decrease was not significant. If the angle reduction becomes greater, this change in the Froude number will consequently increase as well.

References

1. Santorok, F. Hydraulics of Dams and Reservoirs. Noavar Publication, Tehran, 2012. Pp. 86–102.
2. Olsen, N., Kjellesvig, H.M. Three-dimensional numerical flow modeling for estimation of spillway capacity. Journal of Hydraulic Research, 1998, 36(5), pp. 775–784. DOI: 10.1080/00221689809498602
3. Meilan, Q.L., Fujisak, K., Tanaka, K. Sediment re-suspension by turbulent jet in an intake pond. Journal of Hydraulic Research, 2000, 38(5), pp. 323–330. DOI: 10.1080/00221680009498313
4. Savage, B., Johnson, M. Flow over ogee spillway: Physical and numerical model case study. Journal of Hydraulic Engineering, 2001, 127(8), pp. 640–649. DOI: 10.1061/(asce)0733-9429(2001)127:8(640)
5. Ho, H., Boyes, K., Donohoo, S., Cooper, B. Numerical flow analysis for spillways. Proceedings of 43rd ANCOLD Conference, Hobart, Tasmania, 2003, pp. 24–29.
6. Sarker, M.A., Rhodes, D.G. Physical modeling and CFD applied to hydraulic jumps. Cranfield University Report, Institute of Technology, Bangladesh, 2002. Pp 552–563.

7. Weilin, X., et al. Experimental investigation on the influence of aeration on plane jet scour. Journal of Hydraulic Engineering, 2004. 130(2), DOI: 10.1061/(asce)0733-9429(2004)130:2(160)
8. Heller, V. Ski Jump Hydraulics. Journal of Hydraulic Engineering, 2005. 131, pp. 347–355. DOI: 10.1061/(asce)0733-9429(2005)131:5(347)
9. Pagliara, S., Hager, W.H., Minor, H.-E. Hydraulics of plane plunge pool scour. Journal of Hydraulic Engineering, 2006, 132(5), DOI: 10.1061/(asce)0733-9429(2006)132:5(450)
10. Dargahi, B. Experimental study and 3D numerical simulations for a free-overflow spillway. Journal of Hydraulic Engineering, 2006, pp. 899–907. DOI: 10.1061/(asce)0733-9429(2006)132:9(899)
11. Steiner, R., Heller, V., Hager, W.H., Minor, H.-E. Deflector ski jump hydraulics. Journal of Hydraulic Engineering, 2008, 134, pp. 562–574. DOI: 10.1061/(asce)0733-9429(2008)134:5(562)
12. Kavianpour Esfahani, M.R., Ajdari Moghadam, M., Goodarzi, M. Experimental study of flow rate and tailwater depth effects on maximum scour depth downstream of ski jump spillways, Proceedings of 10th Hydraulic Conference, 2011. Pp. 128–136.
13. Arefpour, M., Fathi Moghadam, M., Douraghi, A., Hosseini, A., Tajaran, A. Investigation of hydrodynamic pressure distribution and instantaneous pressure fluctuations along the ski jump spillway of Balaroud Dam, Proceedings of 9th International Seminar on River Engineering, 2012. Pp. 246–255.
14. Mousavi Jahromi, S.H., Omidvarinia, M. Effect of threshold length and angle in triangular deflectors on overall exit jet trajectory, Water and Soil Resources Protection, 2012, 1(4), pp. 1–17.
15. Askari, M., Ghomeshi, M. Energy losses due to deflector in simple ski jump spillway and ski jump spillway with approaching channel, Journal of Water and Soil Knowledge, 2013. 23. Pp. 340–349.
16. Nikpour, M.R., Salmani Jelodar, Z., Hosseinzadeh Dalir, A., Sani Khani, H., Shoja, F. Application of finite element and finite volume methods in water flow analysis over ogee spillway (case study: Damghan Dam), Iranian Water Research Journal, 2014, 8(14), pp. 55–63.
17. Eshrati, T., Fazloli, R., Sanei, M., Emadi, A. Experimental investigation of hydraulic performance of ogee spillway and downstream channel in axial curve conditions, Journal of Water and Soil Knowledge, 2015. 29(4). Pp. 98–110.
18. Kakeshpour, M., Pirestani, M.R., Zakeri Niri, M. Investigation of ski jump deflector shape effect in chute spillway using numerical model, Journal of Water and Soil Knowledge, 2016, 23(5). Pp 841–857.
19. Fazlollahnejad, M., Hosseini, K., Karami, H., Farzin, S. Investigation of flow characteristics in Golvard Neka Dam chute spillway using computational fluid dynamics, Environment and Water Engineering, 2016. 3. Pp. 411–423.
20. Zhenweia, M., Zhiyan, Z., Tao, Z. Numerical simulation of 3D flow field of spillway based on VOF method, Proceedings of International Conference on Modern Hydraulic Engineering, 2012, 28. Pp. 808–812. DOI: 10.1016/j.proeng.2012.01.814
21. Sharif, N., Rostami Ravori, A. Experimental and numerical study of the effect of flow separation on dissipating energy in compound bucket, APCBEE Procedia, 2014, 9. Pp. 334–338. DOI: 10.1016/j.apcbee.2014.01.059
22. Fadaei-Kermani, E., Barani, G.A. Numerical simulation of flow over a spillway based on the CFD method, Scientia Iranica A, 2014, 21(1). Pp. 91–97.
23. Parsaie, A., Dehdar-behbahani, S., Hamzeh haghiabi, A. Numerical modeling of cavitation on spillway's flip bucket, Frontiers of Structural and Civil Engineering, 2016, 10(4). Pp. 438–444. DOI: 10.1007/s11709-016-0337-y
24. Barani, G.A., Yousef Abbasi, P. Energy dissipation in hydraulic structures (field study of energy dissipating structures), Amirkabir University of Technology, Jahad Daneshgahi Publications, 2009.
25. Pope, S.B. Turbulent Flows, Cambridge: Cambridge University Press, 2000, p. 771 DOI: 10.1017/cbo9780511840531
26. Flow Science, Flow-3D User Manual, [Online], URL: http://www.flow3d.com/ (reference date: 10.02.2026).
27. Goodarzi, M. Study of erosion downstream of ski jump spillways using CFD method. Master's Thesis, University of Sistan and Baluchestan, 2011.
28. Navaei, B., et al. Experimental study of the effect of ski jump bucket at the end of ogee spillway on energy dissipation and throw length, Journal of Water and Soil Knowledge, 2016, 26(3-2). Pp. 133–142.

Information about the authors:

***Saeid Mohammadalizadeh**,*
ORCID: https://orcid.org/0009-0000-7574-9313
E-mail: saeidmhmdalizadeh74@gmail.com

***Ali Yasaei**,*
E-mail: aliyasaei5@gmail.com

***Alireza Mardookhpour**,*
ORCID: https://orcid.org/0000-0001-8054-8209
E-mail: AR.mardookhpour@iau.ac.ir

Received 31.03.2025. Approved after reviewing 18.10.2025. Accepted 20.10.2025.

Magazine of Civil Engineering

ISSN 2712-8172

journal homepage: http://engstroy.spbstu.ru/

Research article

UDC 626.01

DOI: 10.34910/MCE.139.6

Variation of stress-strain state of rockfill dam affected by creeping

M.P. Sainov[1] ✉ , ***A.A. Zuzov***[2]

[1] *Moscow State University of Civil Engineering (National Research University), Moscow, Russian Federation*
[2] *National Research University "Moscow Power Engineering Institute", Moscow, Russian Federation*

✉ *mp_sainov@mail.ru*

Keywords: concrete faced rockfill dam, stress-strain state, creep, numerical analysis, rheological model, long-term deformation, settlement, displacement

Abstract. Rockfill is subject to creeping and this phenomenon has negative consequences for rockfill dam stress-strain state (SSS). Recently, rockfill creeping attracts more and more attention in China where a great number of embankment dams are constructed. Chinese scientists fulfilled tests of rockfill in stabilometers. However, for SSS numerical modeling, there are used other empirical rheological models whose parameters are determined by the method of SSS back analysis of existing rockfill dams. For studying the effect of creeping on rockfill dam SSS, the authors fulfilled back analysis for Tianshengqiao-I dam in China. Modeling the dam SSS was carried out with the aid of software package MIDAS. Two analyses were performed: without consideration of creeping and with consideration of it. Mohr–Coulomb model was used for description of rockfill deformation. For consideration of creeping, it was added by Maxwell–Kelvin rheological model. Reliability of SSS modeling was provided by selection of soil model parameters from condition of approximate correspondence between design and field displacements. Comparison of two design alternatives of analysis permitted making conclusions on the role of rockfill creeping in formation of the dam SSS. There was determined the share of displacements reached during construction due to time-dependent component of rockfill deformation. For settlements, it was amounted to approximately 20–30 %, and for horizontal displacements, it was higher. Creeping affects the character of settlement distribution in a complicated way. This is related to the fact that it causes growth of deformation of two types: shear deformations toward the downstream side and deformations of lateral expansion. In the lower part of the dam, deformations of lateral expansion prevail and in the upper part – share deformations. Such character of displacements may affect reinforced concrete face. Effect of creeping on rockfill stress state is not great and it is mainly related to rather small increase of tangent stresses.

Citation: Sainov, M.P., Zuzov, A.A. Variation of stress-strain state of rockfill dam affected by creeping. Magazine of Civil Engineering. 2025. 18(7). Article no. 13906. DOI: 10.34910/MCE.139.6

1. Introduction

Subject of research

Soil deformation occurs not instantly but during a long period of time. Slow increase of soil deformations in the course of time at the action of constant external load is called creeping. Creeping is a characteristic feature of coarse soils (rockfill) used for construction of rockfill and rock-earthfill dams.

Formulation of relevance of research

Rockfill creeping causes constant increment of the dam deformations both during construction and operation periods; these deformations may have negative consequences for the dam safety.

Due to additional settlements, the dam crest elevation may become sufficiently lower than the design value. At the existing rock-earthfill and rockfill dams, which were constructed before 1960s with use of methodology without rockfill compaction by rollers, the crest settlement during operation period could exceed 1 % of the dam height [1]. There are cases of high settlements also at modern dams. For example, the crest settlement of ultra-high Atatürk rock-earthfill dam (Turkey, H = 184 m high, 1990) over the 7 years of operation exceeded 2.5 m [2]. Constant settlements of the embankment dam of Boguchany HPP (Russia, H = 77 m, 2012) cause permanent problems in operation of its conjugation with the concrete dam.

Creep deformations may be also dangerous for integrity for the rockfill dam concrete face. There are well-known cases of emergency situations related to formation of large structural cracks in the face [3].

At present, more and more high dams are constructed. By 2023 in China, there had been constructed 406 concrete faced rockfill dams, including 94 dams with height exceeding 100 m [4]. With growth of the dam height, the danger of creep deformations increases. Russian norms envisage that the design validation of high dam structures should be carried out with consideration of creeping.

All this conditions urgency of study and prediction of rockfill creep deformations.

Literature review

Creep of materials has been studied from the 19th century. Studies of creeping are directed on development of rheological models of materials, which permit making predictions of deformations.

The simple theoretical models of viscoelastic behavior of materials are J.C. Maxwell model and W.T. Kelvin – W. Voigt model. Mechanical scheme of Maxwell model presents sequential relations of the elastic element (spring) and the viscous damper: total deformation is composed of deformations of these two elements. In Kelvin–Voigt model, the spring and the damper are connected in parallel (Fig. 1a); at perception of load, they are deformed jointly. However, experiments are required for determination of parameters of rheological models.

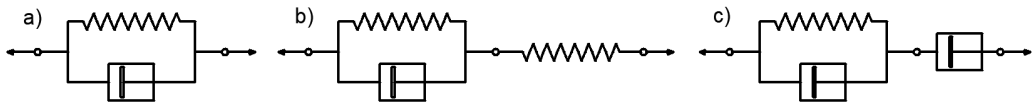

Figure 1. Mechanical schemes of rheological models:
a – Kelvin–Voigt model; b – Merchant model; c – Maxwell–Kelvin model.

Up to the middle of the 20th century, rockfill creeping had been studied only based on the experience in operation of the constructed rockfill dams. Later, due to appearance of large-scale instruments allowing development of great forces, study of rockfill creeping in laboratory conditions became possible.

In 1960–1970s, for the constructed Mica dam (Canada, H = 243 m, 1973), tests of coarse soils were carried out. R.J. Marsal during studies marked two characteristic stages of soil deformation in odometer [5]. These stages differ by the form of the diagram of relationship between deformations and time. The first stage is characterized by active growth of deformations; at the diagram plotted in semilogarithmic scale (time logarithm is put on the horizontal axis), this stage is presented in the form of “S-shaped” curve. The second stage is characterized by damping of creep deformations. In semilogarithmic system of coordinates, it may be presented in the form of a straight line, therefore, at this stage, the logarithmic relationship between deformations and time may be assumed. In [6], it is shown that, based on the results of in-kind measurements, the dam settlements change over time according to a logarithmic curve.

Fuller understanding of soil deformation mechanisms is obtained from the tests in stabilometer in conditions of triaxial compression. Large volume of such experimental studies was performed by the Chinese scientists [7–14] as a great number of high and ultra-high dams were constructed in this country. Experimental studies of rockfill were carried out using large-scale instruments. [12] describes the results of tests in a compression instrument with a diameter of 502 mm and a height of 252 mm. [10] describes the results of tests of granite rock mass in a triaxial compression device with a diameter of 150 mm and a height of 300 mm. [7–9, 13–14] describe tests in triaxial compression devices with a diameter of 300 mm and a height of 600–700 mm under high compression pressures (up to 2 MPa). These tests show that rockfill deformations are durable in time. The less is the ratio between axial and lateral stresses, the more share of deformations will be revealed in the form of creeping.

The authors of experimental studies [7–9, 12, 14] recommended to use exponential function for description of time dependent variation of deformations. In the function of this type, the rate of deformation also varies by exponential law. In [8], it is substantiated that logarithmic and exponential functions cannot be used for description of the creeping process.

However, laboratory tests do not give full understanding of rockfill creeping because they cover only the first day after load application.

Experimental data cannot provide thorough information on damping of rockfill in the dam body because it may take place in a more complicated way. Growth of creep deformations may have damping, stable (at constant rate), or progressive character.

Therefore, starting from the end of the 20th century the other method of rockfill creeping study, i.e., "back analysis," began to be used. It envisages selection of such soil mathematical model, which can properly describe deformation of the existing dam.

In [11], a linear model supplemented with a creep model was used for stress-strain state (SSS) modeling. In China, the Duncan–Chang hyperbolic model, supplemented with a creep model, is used to model SSS dams. Several creeping models are applied.

In 1998, the Chinese scientists Z. Shen and K. Zhao proposed [15] use of the creep model (Shen-Zhujiang model) whose mechanical scheme corresponds to W. Merchant model. In it, Kelvin–Voigt model is sequentially joined with the elastic element (Fig. 1b). In Shen-Zhujiang model, there was adopted exponential relationship between deformations and time. During refinement, the number of this model parameters increased from 3 to 7. Different alternatives of this model were used in [3, 16–20] for modeling SSS of a number of dams. It should be noted that in the study in [3], use of the model alternative with 4 parameters did not permit reaching good agreement of the design data with the field measurements.

In 2004, Chinese researches Z. Cheng and H. Ding based on experiments proposed a similar model of creeping, but with exponential function [7]. This model with 9 parameters was used for modeling behavior of Shuibuya dam (China, H = 233 m, 2008) [21–23]. In [24], a different soil model was used to calculate the Shuibuya dam, but also with an exponential creep function.

Later, the Chinese researches also began to use more complicated rheological models (for example, Burgers model). Composite models not only contain a greater number of parameters but are also based on more complicated mechanical scheme, with more complicated structure and greater number of elements. At that, different functional relationships may be adopted for the elements of one type.

In [25, 26], there was applied the model with J.M. Burgers mechanical scheme. In [27–30], the model was used whose mechanical scheme contains 3 elastic elements, 3 dampers, and 1 element of dry friction.

Variety of rheological models evidences that rockfill creeping was insufficiently studied. Therefore, effect of creeping on rockfill dam workability also remains unstudied.

Aims and tasks of study

The aim of our study consists of investigating the effect rockfill creeping on the dam SSS.

However, there are several obstacles in reaching this aim. One of them is in the fact that in Russia, there are no suitable software permitting use of complicated rheological models. Therefore, one of the tasks of studies was selection of a rheological model, which, on the one hand, could be available, and on the other hand, could rather accurately represent creep deformations of a rockfill dam.

2. Materials and Method

Soil model

Software package MIDAS permits to carry out creep modeling. In it at use of Mohr–Coulomb elastic-plastic model, there is a possibility to apply integrated empirical model of creeping. This creep empirical model corresponds to mechanical scheme of Maxwell–Kelvin. As Merchant model, the model of Maxwell–Kelvin also presents a sophisticated Kelvin–Voigt model. But in its mechanical scheme, to the model of Kelvin–Voigt there sequentially connected not an elastic element but one more damper (Fig. 1c). At such a scheme, Kelvin–Voigt model is intended for simulation of damping creep, and the second damper – for representation of continuous deformations.

Maxwell–Kelvin model is simpler than the other models (for example, Burgers model), but composition of its elements may be quite sufficient for designing.

Mathematical model of Maxwell–Kelvin in software package MIDAS is written in the form of the following formula:

$$\varepsilon = a \cdot \sigma^b \left[1 - \exp\left(-c \cdot \sigma^d \cdot t\right)\right] + e \cdot \exp\left(f \cdot \sigma\right) \cdot t, \quad (1)$$

where ε – relative deformation; σ – stress; a, b, c, d – empirical parameters for description of damping creep; e, f – empirical parameters for description of constant creeping.

As we can see, the empirical model of creep (1) contains 6 parameters. However, as compared to Shen-Zhujiang model, it includes not a single but two components. The first component represents the damping character of creeping and the second one – the undamped character.

In formula (1), the rate of deformation variation depends not only on time but also on stresses, i.e., it considers the effect, which was found in laboratory experiments.

Subject of study

As a subject of study, there was selected Tianshengqiao-I concrete faced rockfill dam (China, H = 178 m, 1999) because the results of field measurements during construction and operation periods were published for this dam [3].

Tianshengqiao-I dam was constructed of sedimentary rocks and has a heterogeneous structure (Fig. 2). In the dam upstream zone (IIIB), there was placed limestone rock mass from the quarry (maximum size 800 mm), and in the downstream zone (IIIC) – rock mass of mudstone with size up to 1600 mm (zone IIID).

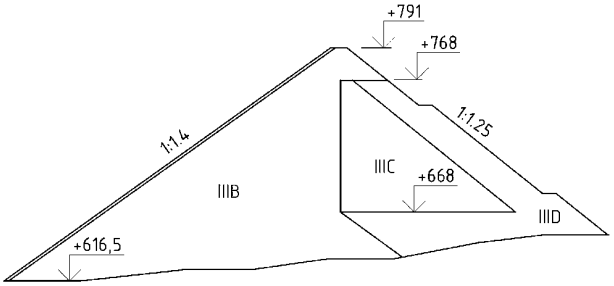

Figure 2. Scheme of the structure of the Tianshengqiao-I dam profile (China): IIIB – limestone fill up to 800 mm in size, IIIC – argillite and sandstone fill from useful excavations, IIID – limestone fill up to 1600 mm in size.

The dam was constructed in the period of 1996–1999. In September 1999, the reservoir was impounded to the level of 768 m. The diagram of the dam height growth and the reservoir level is shown in Fig. 3; it was plotted in compliance with [3].

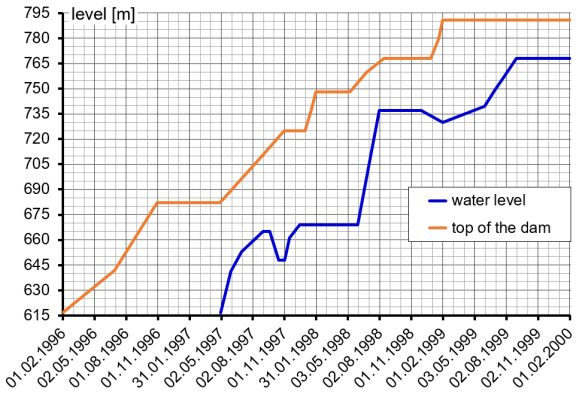

Figure 3. Graph of changes in dam crest and reservoir level.

A number of sensors was located in the dam for measuring displacements (Fig. 4). Analysis of natural displacements show that the dam had high deformations during the construction period. Maximum construction settlement (in 1999) amounted to 3.2 m (Fig. 4), i.e., 1.8 % of the dam height. The crest horizontal displacement after the reservoir impoundment comprised about 0.4 m.

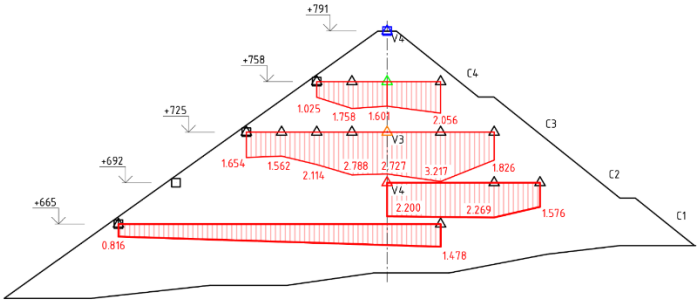

Figure 4. Settlement (m) of Tianshengqiao-I Dam points in August 1999.

High deformation of rock mass became the cause of emergency situations related to break of integrity of the reinforced concrete face. In the zones of conjugation of different construction stages, horizontal cracks appeared in the face [3].

Finite element model was performed for maximum by height cross section of the dam. It included only the rockfill shell; the reinforced concrete face was not taken into account. Dividing the section into finite elements considers the presence in the structure of soils of various quality, as well as sequence of the dam filling. The finite element model consists of 2562 finite elements of solid type (Fig. 5).

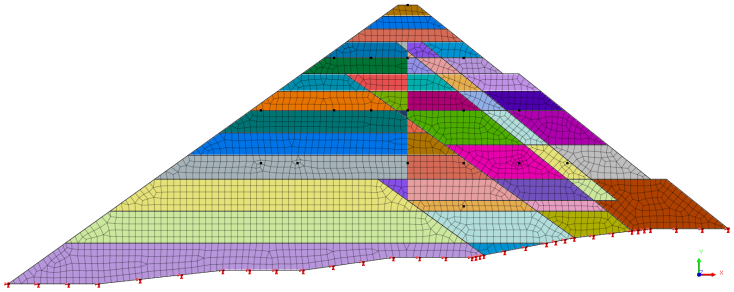

Figure 5. Finite element model of a dam cross-section.

Design procedure

The study was conducted by "back analysis;" the aim of analysis was selection of parameters for Mohr–Coulomb and Maxwell–Kelvin models. They were selected in such a way to obtain proper conformance of the design and natural displacements of the dam body.

Analysis was performed for loads from the dead weight and hydrostatic pressure on the dam upstream face; at each stage, the load was applied instantly. The construction period included 23 stages of the dam body filling and 13 stages of the reservoir level variation. Non-stationary problem was solved: there were sequentially considered SSS variation during several thousands of time intervals; the time interval was 1 day.

Density (specific weight) of the dam body soils was taken by data [3]. Selected as a result of studies, parameters of Mohr–Coulomb and Maxwell–Kelvin models are given in Tables 1 and 2.

Table1. Design physical and mechanical properties of rockfill.

Profile zones	Specific weight, κN/m^3	Elastic modulus, MPa	Poisson's ratio
Upstream zone	21.2	50	0.27
Downstream zone	21.5	40	0.27
Downstream slope cover	20.5	40	0.27

Table 2. Design parameters of creep model.

Parameter	a	b	c	d	e	f
Value	$2\cdot10^{-5}$	0.5	$1.5\cdot10^{-8}$	0.015	$1\cdot10^{-11}$	$1.5\cdot10^{-15}$

Of interest is the fact that the parameter is not equal to 1, which evidences that the selected empirical model provides non-linear relationship between stresses and deformations.

The indicated model parameters correspond to the design alternative 1. For evaluation of creeping effect, there was accomplished the design alternative 2, where the creeping model is not used and calculation is carried out by initial Mohr–Coulomb model.

3. Results and Discussion

As a result of studies, for each design alternative, there was obtained the dam SSS at all the design stages.

Checking adequacy of the dam numerical model

For checking adequacy of the obtained results, the comparison was made of design displacements of the dam points with the measured ones at the existing dam. Fig. 6 shows comparison of settlements for four points located along the dam axis at different heights; Fig. 7 shows comparison of the crest horizontal

displacements. Data of field measurements are given for these points in [3]. From the diagrams of Fig. 6 and 7, it is seen that on the whole the numerical model satisfactorily represents both displacement values of the existing dam points and their variation in time.

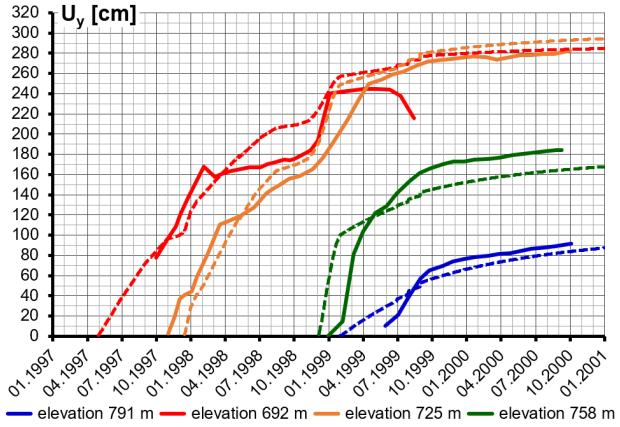

Figure 6. Change in time of settlement of dam points.
The solid line indicates measured settlement, the dotted line indicates calculated settlement.

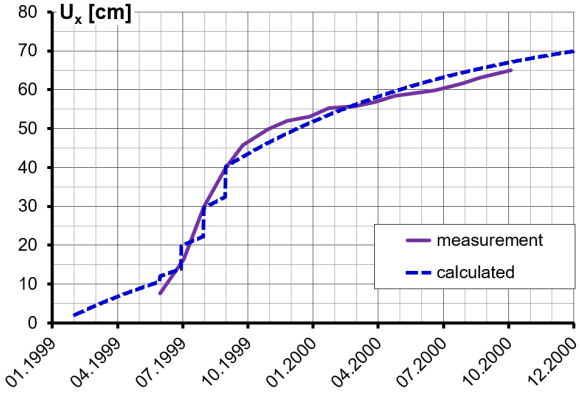

Figure 7. Time evolution of horizontal displacements of the dam crest.

Reliability of the numerical model permitted analyzing time-dependent variation of the dam SSS and effect of rockfill creeping on this process.

Analysis of dam SSS

Figures present SSS for three moments of time. The first moment corresponds to completion of the dam filling in January 1999, the second – to the time of the reservoir level elevation in August 1999. These two moments of time correspond to the completion stage of the construction period. The third moment of time corresponds to November 2006, i.e., 7 years of operation.

Analysis showed that at the completion stage of the dam construction, considerable SSS variations took place. They were caused by increase of hydrostatic pressure on the upstream face and rockfill creeping. Maximum settlements of fill increased from 270 cm (Fig. 8a) to 280 cm (Fig. 8b), and horizontal displacements towards the downstream side increased from 125 cm (Fig. 9a) to 145 cm (Fig. 9b).

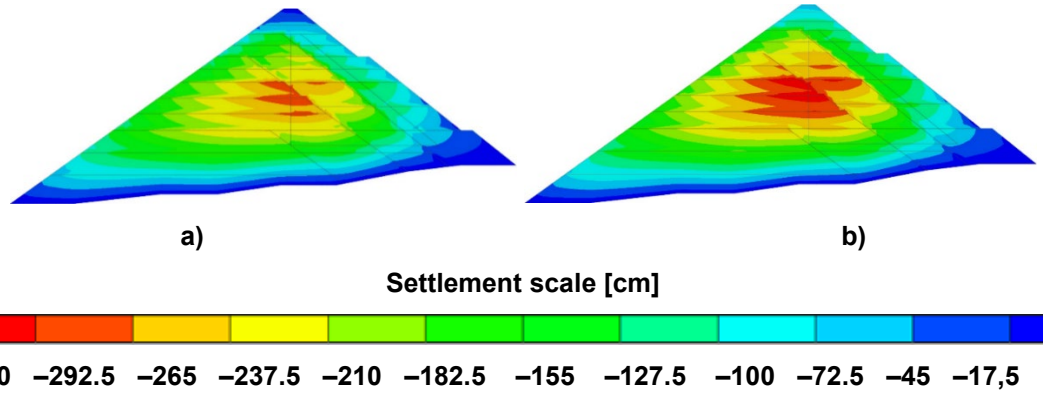

Figure 8. Dam settlements based on numerical modeling results taking into account creep: a – January 1999, b – August 1999.

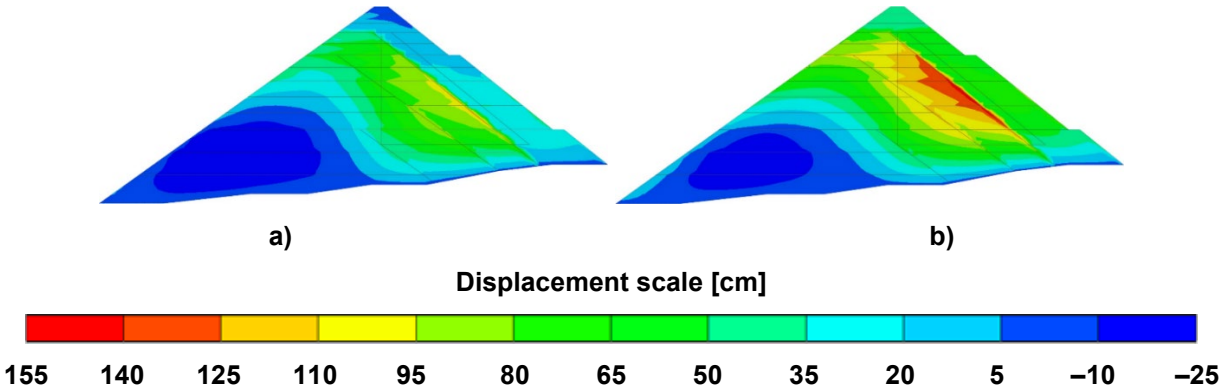

Figure 9. Horizontal displacements of the dam based on the results of numerical modeling taking into account creep: a – January 1999, b – August 1999.

During operation, creeping causes further growth of the dam displacements (Fig. 10). In the first 3 years of operation, it is rather intensive. By November 2006, maximum settlements U_y increased to 320 cm (Fig. 10a), and maximum displacements to 155 cm (Fig. 10b). In percentage terms, maximum settlement increased by 14 %, and maximum displacement by 7 %.

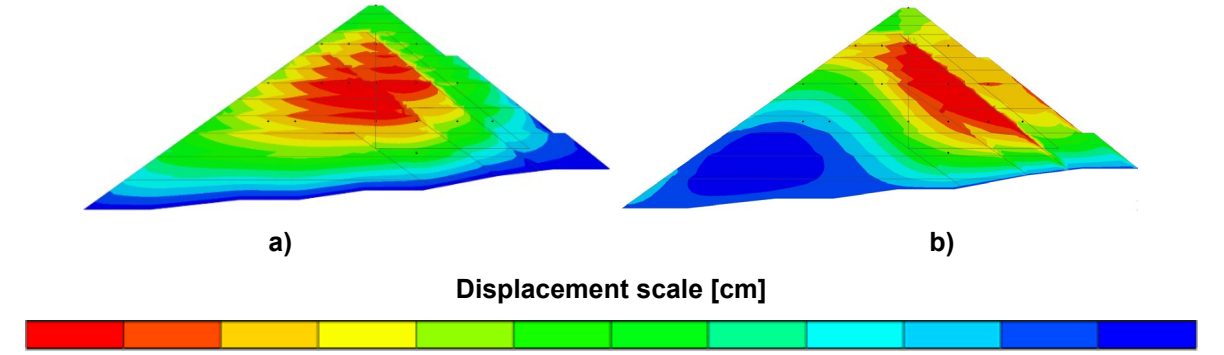

Figure 10. Dam displacements based on numerical simulation results (November 2006) taking into account creep: a – horizontal displacements, b – vertical settlements.

Evaluation of creeping effect on dam displacements and deformations

In order to evaluate the effect of creeping on the dam displacements during construction period, there were compared the displacements calculated with use and without use of the creeping model. The displacements obtained from Mohr–Coulomb model without use of the creeping model are shown in Figs. 11 and 12. It is well noticed that settlements (Fig. 11) and horizontal displacements (Fig. 12) of the dam in this case are much less than at consideration of development of creeping deformations.

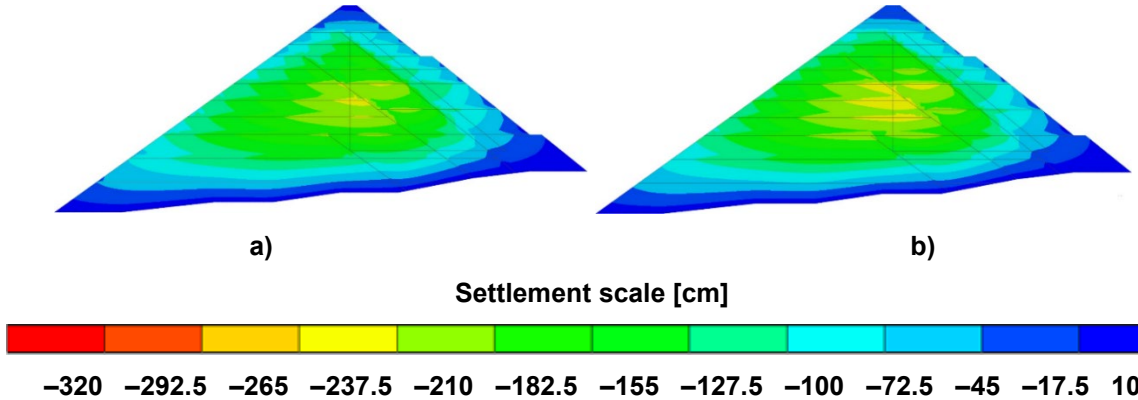

Figure 11. Dam settlements based on numerical modeling results without taking into account creep: a – January 1999, b – August 1999.

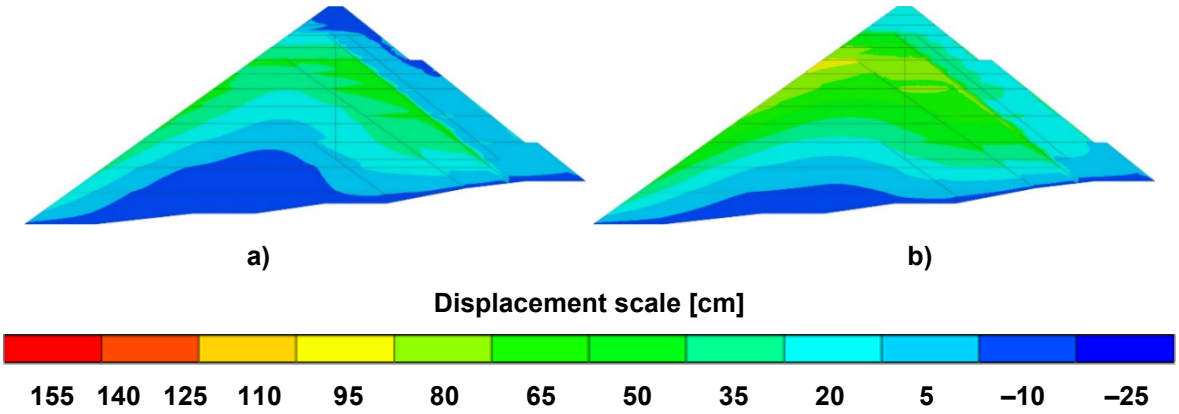

Figure 12. Horizontal displacements of the dam based on the results of numerical modeling without taking into account creep: a – January 1999, b – August 1999.

Difference in displacements obtained for two indicated design diagrams reflects the effect of creep deformations. However, these displacements correspond not to total creep deformations (which are developed from the moment of load application) but only to their part for which durable time was required (more than design step for time of 1 day). The durable part of creep deformations represented by the empirical model creeping will be called cumulative (with time) deformations.

Comparison showed that in settlement values, the share of cumulative deformations is not large. For the moment of the dam filling completion (January 1999), it does not exceed 33 %; its maximum is a characteristic feature for the dam upstream part in the middle of the height. In the other dam zones, this share decreases to 15 %. With time, the share of cumulative deformations increases mainly in the upper part of the dam. In the crest settlement, this share amounts to: for the moment of dam filling completion (January 1999), it is about 20 %, and at the start of operation (August 1999), it is already 70 %.

In formation of horizontal displacements, the role of cumulative deformations is much greater; it is revealed both in the values of displacements and in the pattern of distribution along the dam profile. This is related to the fact that the dam is subject to two types of loads: the dead weight and hydrostatic pressure on the upstream slope. Under the action of the dead weight, deformations of lateral expansion take place and under the action of hydrostatic pressure, it displaces towards the downstream side. Complicated character of horizontal displacements is the result of these two types of deformations.

Two zones may be distinguished in the dam: the near-crest zone (approximately higher than ∇745 m) and the lower zone. In the near-crest zone, shear deformations prevail; here with time, the displacements increase towards the downstream side. For example, for the moment of start of operation period (August 1999), the crest displacement by Mohr–Coulomb model amounts to 23 cm, and by calculation with consideration of creeping, it is 40 cm.

In the lower part of the dam, deformations of lateral expansion prevail. With time, increase of the dam upper part displacements towards the upstream side takes place and in the lower part – towards the downstream side. The more is the distance from the dam axis, the higher are increments of accumulated displacements. Increments of displacements are comparable by value with displacements by Mohr–Coulomb model (without consideration of creeping) or even exceed them.

With time, the described character of displacements is remained, but in view of cumulative deformations in values of displacements. For example, over the first 3 years of operation, the crest displacement increased from 40 cm to 83 cm.

Of special interest is the effect of cumulative deformations on the values and distribution of displacements of the upstream face because the reinforced concrete face is located there. In the lower part, accumulation of creep deformations leads to decrease of displacements of the upstream face towards the downstream side and in the upper part – to their increase (Fig. 13). This result is indirectly confirmed by the data of field measurements at the dam. By [3], maximum face displacements were observed in the dam upper part and amounted to 70 cm. Such pattern of the face displacements has adverse effect on the face strength because it increases its bend.

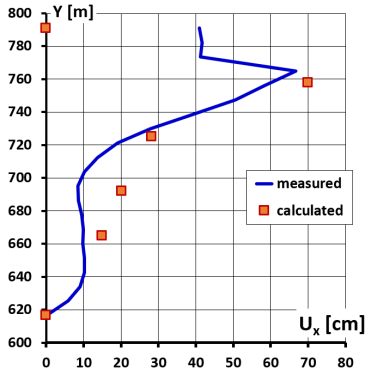

Figure 13. Horizontal displacements of the upstream face of the dam.

Evaluation of the effect of accumulated with time deformations on the dam stress state

For evaluation of the creeping effect on stresses, comparison of stresses was made for two moments of time: for start of operation (August 1999) and after 7 years of operation (November 2006).

Analysis showed that in spite of the existing growth of displacements due to creeping, stresses in the dam body vary to a small extent. Variations in distribution and values of normal stresses (horizontal σ_x and vertical σ_y) during operation are actually unnoticed. For distribution of stresses σ_y, the characteristic feature is weak hanging-up of the dam downstream part over its upstream part (Fig. 14b). For distribution of stresses σ_x, the typical feature is development of the zone of concentration of compressive stresses at the contact with the rock foundation (Fig. 14a).

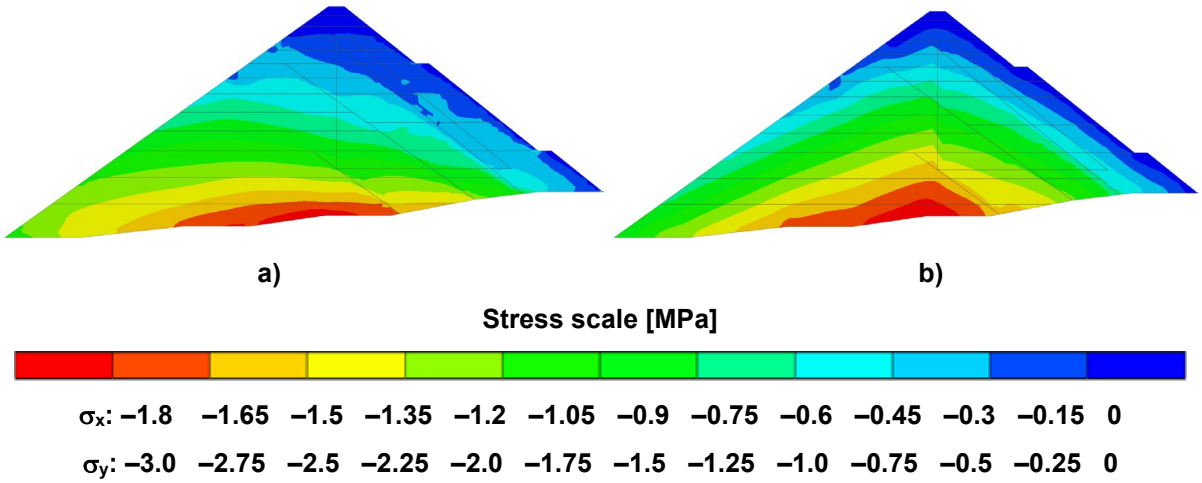

Figure 14. Normal stresses in the dam body based on the results of numerical modeling (August 1999) taking into account creep: a – stresses σ_x, b – stresses σ_y.

According to the shear stresses τ, some increase in values is noted in the first 3 years of operation (Fig. 15), which is explained by the increase in shear deformations due to creep.

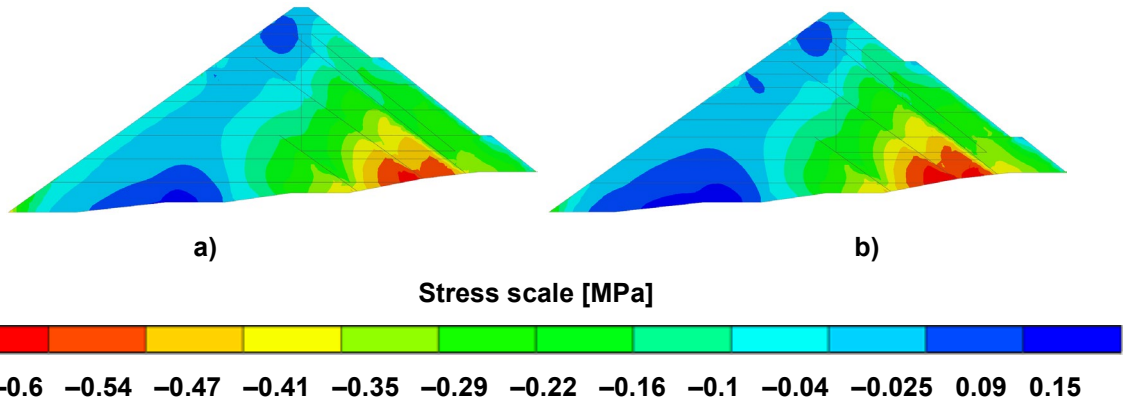

Figure 15. Shear stresses in the dam body based on the results of numerical modeling: a – August 1999, b – November 2006.

4. Conclusion

1. Maxwell–Kelvin rheological model with sufficient accuracy permits simulation of time-dependent character of growth of rockfill dam deformations due to rockfill creeping. Its adding to linear Mohr–Coulomb model allows solving the problem on dam SSS formation with consideration of non-linear character of rockfill deformation.
2. By the results of analysis, a large share of the dam displacements during construction period was accumulated with time due to creeping. In settlements, the share of cumulative with time deformations reaches 33 % of the total ones. The indicated deformations consider the part of creep deformations, which accumulated over durable time after application of load.
3. Rockfill creep deformations affect accumulation of horizontal displacements in a complicated way. The character of the dam deformation due to creeping is the result of summation of two processes. On the one hand, creeping contributes to further dam displacement (shear) towards the downstream side under the action of hydrostatic pressure. On the other hand, it leads to increase of the dam expansion to both sides under the action of the dead weight. In the dam lower part, the deformations of lateral expansion prevail while in the upper part, shear deformations prevail. Such character of the dam deformation may affect the SSS of the reinforced concrete face located on the dam upstream slope because it increases its bend deformations.
4. For the considered dam, the increment of maximum displacements over the first 3 years of operation (from displacements of construction period) amounted to: settlements – 15 %, horizontal displacements – 7 %.
5. Creep deformations have small effect on the stress state of the rockfill dam body; growth of shear deformations results in some increase of tangent stresses in the first 3 years of operation.

References

1. Oldecop, L.A., Alonso, E.E. Theoretical investigation of the time-dependent behavior of rockfill. Géotechnique. 2007. 57(3). Pp. 289–301. DOI: 10.1680/geot.2007.57.3.289
2. Cetin, H., Laman, M., Ertunç, A. Settlement and slaking problems in the world's fourth largest rock-fill dam, the Ataturk Dam in Turkey. Engineering Geology. 2000. 56(3–4). Pp. 225–242. DOI: 10.1016/S0013-7952(99)00049-6
3. Zhang, B., Wang, J.G., Shi, R. Time-dependent deformation in high concrete-faced rockfill dam and separation between concrete face slab and cushion layer. Computers and Geotechnics. 2004. 31(7). Pp. 559–573. DOI: 10.1016/j.compgeo.2004.07.004
4. Liao, W., Zhang, Z., Liu, B., Lu, X., Liu, D., Liu, Q., Duan, Z., Liu, C. Intelligent zoning design of concrete-faced rockfill dams using image-parameter fusion enhanced generative adversarial networks. Engineering Structures. 2025. 339. Article no. 120662. DOI: 10.1016/j.engstruct.2025.120662
5. Marsal, R.J. Mechanical Properties of Rockfill. Embankment Dam Engineering. Casagrande Volume. John Wiley and Sons. New York, 1973. Pp. 109–200.
6. Wu, E., Zhu, J., Wang, J., Guo, W., Wang, L., Wang, W. Investigation on the incremental creep model of rockfill material for dam building. Computers and Geotechnics. 2024. 174. Article no. 106636. DOI: 10.1016/j.compgeo.2024.106636
7. Cheng, Z., Ding, H. Creep test for rockfill. Chinese Journal of Geotechnical Engineering. 2004. 26(4). Pp. 473–476.
8. Li, H., Zhang, Y. Creep Rate and Creep Model of Rockfill. Procedia Engineering. 2012. 28. Pp. 796–802. DOI: 10.1016/j.proeng.2012.01.812
9. Wang, C., Zhang, J., He, P. Creep Properties of Rockfill Materials with Fractal Structure in Mass. Electronic Journal of Geotechnical Engineering. 2014. 19. Pp. 2713–2722.
10. Zhang, B.Y., Chen, T., Peng, C., Qian, X.X., Jie, Y.X. Experimental study on loading-creep coupling effect in rockfill material. International Journal of Geomechanics. 2017. 17(9). Article no. 04017059. DOI: 10.1061/(ASCE)GM.1943-5622.0000938
11. Raposo, R.S.P., Hernández, Y.Z., Assis, A.P. Simplified model for dam rockfill creep and influence of constructive delay of concrete face. Soils and Rocks. 2022. 45(3). Article no. e2022074221. DOI: 10.28927/SR.2022.074221
12. Chen, X., Chen, Q., Zhou, C., Li, J. Creep behavior of rockfill with soft rock under different relative densities. Chinese Journal of Geotechnical Engineering. 2020. 42(2). Pp. 118–122. DOI: 10.11779/CJGE2020S2021
13. Chen, Z., Li, G., Mi, Z., Wei, K. Creep model for rockfill materials based on particle breakage energy consumption. Chinese Journal of Geotechnical Engineering. 2024. 46(6). Pp. 1155–1165. DOI: 10.11779/CJGE20230202
14. Sun, X., Liu, L., Deng, S., Zuo, Y., Pan, J. Experimental Study on Creep Characteristics of Rockfill Material of Lianghekou Hydropower Station on High Stress State. Journal of Changjiang River Scientific Research Institute. 2024. 41(3). Pp. 88–101. DOI: 10.11988/ckyyb.20221305
15. Shen, Z., Zhao, K. Back analysis of creep deformation of rockfill dams. Journal of Hydraulic Engineering. 1998. 6. Pp. 1–6.
16. Wang, G., Yu, T., Li, Y., Li, G. Creep deformation of 300 m-high earth core rockfill dam. Chinese Journal of Geotechnical Engineering. 2014. 36(1). Pp. 140–145. DOI: 10.11779/CJGE201401013
17. Zhou, M., Zhang, B., Jie, Y. Numerical simulation of soft longitudinal joints in concrete-faced rockfill dam. Soils and Foundations. 2016. 56(3). Pp. 379–390. DOI: 10.1016/j.sandf.2016.04.005
18. Guo, Q., Pei, L., Zhou, Z., Chen, J., Yao, F. Response surface and genetic method of deformation back analysis for high core rockfill dams. Computers and Geotechnics. 2016. 74. Pp. 132–140. DOI: 10.1016/j.compgeo.2016.01.001

19. Zhou, X., Sun, X., Zheng, J., Jiang, H., Li, Y., Li, Z., Ma, Z., Cao, P., Zhan, Q., Zhao, Y. Long-Term Settlement of High Concrete-Face Rockfill Dam by Field Monitoring and Numerical Simulation. Advances in Civil Engineering. 2020. 2020. Article no. 8898433. DOI: 10.1155/2020/8898433
20. Chen, H., Zhang, Y. Simulation of creep deformation of faced rockfill dam based on secondary development of ABAQUS. IOP Conference Series: Earth and Environmental Science. 2021. 831. Article no. 012024. DOI: 10.1088/1755-1315/831/1/012024
21. Zhou, W., Chang, X. Three dimension FEM numerical simulating of the rockfill creep of high concrete face rockfill dam. Rock and Soil Mechanics. 2006. 27(8). Pp. 1389–1393.
22. Zhou, W., Hua, J., Chang, X., Zhou, C. Settlement analysis of the Shuibuya concrete-face rockfill dam. Computers and Geotechnics. 2011. 38(2). Pp. 269–280. DOI: 10.1016/j.compgeo.2010.10.004
23. Zhu, Y., Chi, S. The Application of MsPSO in the Rockfill Parameter Inversion of CFRD. Mathematical Problems in Engineering. 2016. 2016. Article no. 1096967. DOI: 10.1155/2016/1096967
24. Fu, Z., Chen S., Wei, K. A generalized plasticity model for the stress-strain and creep behavior of rockfill materials. Science China Technological Sciences. 2019. 62(4). Pp. 649–664. DOI: 10.1007/s11431-018-9362-3
25. Qin, X., Gu, C., Shao, C., Chen, Y., Vallejo, L., Zhao, E. Safety evaluation with observational data and numerical analysis of Langyashan reinforced concrete face rockfill dam. Bulletin of Engineering Geology and the Environment. 2020. 79. Pp. 3497–3515. DOI: 10.1007/s10064-020-01790-2
26. Raggi, F., Altarejos-García, L. A Visco-Elasto-Plastic Constitutive Law for Deformation Prediction of High Concrete Face Rockfill Dams. Applied Sciences. 2024. 14(22). Article no. 10535. DOI: 10.3390/app142210535
27. Gan, L., Shen, Z., Xu, L. Long-Term Deformation Analysis of the Jiudianxia Concrete-Faced Rockfill Dam. Arabian Journal for Science and Engineering. 2014. 39. Pp. 1589–1598. DOI: 10.1007/s13369-013-0788-6
28. Gan, L., Shen, X., Zhang, H. New deformation back analysis method for the creep model parameters using finite element nonlinear method. Cluster Computing. 2017. 20(4). Pp. 3225–3236. DOI: 10.1007/s10586-017-1049-3
29. Deng, C., Xu, C., Li, X., Zheng, M. Rheology Test and Finite Element Analysis: A Case Study of a Rockfill Dam in China. IOP Conference Series: Earth and Environmental Science. 2021. 643. Article no. 012074. DOI: 10.1088/1755-1315/643/1/012074
30. Li, J., Lu, X., Chen, J., Yang, S., Kuang, C., Yong, Y., Hu, K. Reliability-monitoring data coupled model for concrete slab safety evaluation of CFRD and its engineering application. Structures. 2022. 35. Pp. 520–530. DOI: 10.1016/j.istruc.2021.11.004

Information about authors:

***Mikhail Sainov**, Doctor in Technical Sciences*
ORCID: https://orcid.org/0000-0003-1139-3164
E-mail: mp_sainov@mail.ru

***Alexey Zuzov**,*
E-mail: zuzuv3@yandex.ru

Received 28.07.2025. Approved after reviewing 18.10.2025. Accepted 02.11.2025.

Magazine of Civil Engineering

ISSN 2712-8172

journal homepage: http://engstroy.spbstu.ru/

Research article

UDC 624

DOI: 10.34910/MCE.139.7

Advancing geotechnical engineering via sustainable biomass-based soil stabilization

N.J. Shen[1], ***M. Hasan***[1]✉, ***Y.W. Er***[1], ***Md. I. Hoque***[2]

[1] *Universiti Malaysia Pahang Al-Sultan Abdullah, Pahang, Malaysia*

[2] *Khulna University of Engineering & Technology, Khulna, Bangladesh*

✉ *muzamir@umpsa.edu.my*

Keywords: cow bone, soil stabilization, sustainability, soil-bearing capacity, kaolin clay

Abstract. This research investigates the potential influence of mixing biomass resources, cow bone ash, in various percentages into the untreated kaolinitic soil in altering the geotechnical parameters. The nature of clayey soil frequently triggers the prevailing issues, such as uneven settlement, insufficient soil-bearing capacity, and abnormal compressibility coefficient. Several fundamental laboratory approaches were deployed to obtain information on grain size distribution, consistency limits, proctor behaviors, and specific gravity. The optimum moisture content of kaolin stabilized with cow bone ash was discovered at 6 %, and this value was utilized for the assessment of unconfined compression data. The examination of shear strength parameters was implemented via the fabrication of a cylindrical sample, dimensioned at 38 mm in diameter and 76 mm in height. The kaolin samples were altered using 3 %, 6 %, 9 %, and 12 % of cow bone ash content, and cured for periods of 7 and 14 days, respectively. The discoveries revealed that associating all portions of cow bone ash enhanced the kaolin shear strength significantly, ranging from 81.15 % to 578.10 %. The accuracy was verified by the utilization of the correlation technique, where all the curing periods of the samples possess a coefficient of determination greater than 0.9. Furthermore, the establishment of cost-analysis calculation generates a thorough framework for optimizing the total cost of stabilization, with the efficiency reaching 49.56 %. In short, using cow bone ash in soil stabilization resulted in positive implications that advance the technology of the geotechnical industry, proposing a promising development practice via the application of sustainable material.

Funding: Universiti Malaysia Pahang Al-Sultan Abdullah (UMPSA), International Matching Grant RDU252702. Hokoku Engineering Co. Ltd. (Japan), Grant UIC251503. The Ministry of Higher Education Malaysia, MYBRAIN 2.0 Scholarship.

Citation: Shen, N.J., Hasan, M., Wan, E.Y., Hoque Md, I. Advancing geotechnical engineering via sustainable biomass-based soil stabilization. Magazine of Civil Engineering. 2025. 18(7). Article no. 13907. DOI: 10.34910/MCE.139.7

1. Introduction

From the ancient to modern era, the responsibility of civil engineering has been enormous for the quality of life of people, being a catalyst in fostering the global civilization. Previous research data have proven that the significance of modernization is coherent with the advancement of building technology, which links to sustainable [1]. Possessing an excellent infrastructure system that complies with the Environment, Social, and Governance (ESG) is a huge challenge for a country, as it costs a huge amount of money to overcome myriad challenges. Correspondingly, Mochida et al. [2] and Li et al. [3] reported the association of the ESG concept in construction activities is crucial, which is consistent with the 17

Sustainable Development Goals (SDGs). Historically, Leknoi and Likitlersuang [4] emphasized the significance of ideas in handling soil erosion and slope stabilization that aligns with Goal 11, sustainable cities and communities. Abundant data from previous studies have verified the possibility of advancing the construction projects while practicing the SDGs, whereby utilizing recycling waste, industrial by-products, and disposal items has become evidence [5], [6]. In completing an infrastructure project, the soil condition is the fundamental consideration for the parties involved, such as engineers, developers, and contractors. The physicochemical behaviors of soil, particularly clayey minerals are always complex, dealing with the evolution of architecture beneath the ground [7]. Naturally, clayey soil is categorized as a low-performing soil, as compared to other soils like gravel [9]. The reported problems include soil particle dispersion, abnormal coefficient of compressibility, insufficient soil-bearing capacity, Plasticity Index (PI) exhibited higher values, excessive pore water pressure, and sensitivity to moisture content. Analyzing its grain size, the clay soil has an overall grain size (>50 %) of less than 2×10^{-6} mm, which makes the entrapped water not easily to escape via its adjacent drainage boundaries [10]. The research data of clay properties provided by Hasan et al. [11] and Hoque et al. [12] confirmed the results, in which the authors classified kaolin clay as a less permeable soil via the determination of its coefficient of hydraulic conductivity. Chemically, the formula of kaolin clay is $Al_2Si_2O_5(OH)_4$, composed of the elements of aluminium, silicon, oxygen, and hydroxide. The hydrophobic behavior of kaolin is due to the hydroxyl group (–OH) of kaolin, connected by a hydrogen bond that makes it attractive to water mode [13]. The authors summarized that the polarity of partial positive (H+) and negative (OH^-) from oxygen and hydrogen elements elaborates the excellence of water retention capability. Based on a report published by Abbaslou et al. [14], at least 75 countries around the world, like Malaysia, Thailand, Iran, South Africa, etc., have expressed their concerns about the dispersive clayey minerals discovered, along with the detected issues. It implies that the problematic clay soil is a worldwide problem, not restricted to respective regions only. Corresponding to that, there are a lot of studies being implemented to alter the weak clay soil properties by discharging the additional water retained in the soil mass. Through chemical approach, Karkush and Ali [15] reported that changes in soil pH via electroosmosis in pore water, combined with chemical grouting in the electrokinetic method, can improve the shear strength of soil. This finding is supported by Al-Ani et al. [16] who observed that altering the magnetic field from 500 to 2000 Gauss reduced the plasticity of soil, particularly its Liquid Limit (LL) and Plastic Limit (PL). Similarly, Jawad and Karkush [17] obtained comparable results to those reported in the literature, demonstrating that the use of magnetized water is an effective technique for treating soft clay soil. Other than these approaches, Jun Shen et al. [18] enhanced the soil through bottom ash, and Baldin et al. [19] mixed the soil with rich husk and proved to raise the strength. Concerning the mentioned statements and data, the ground remediation works are continuously improved by the parties involved around the work, and they should vigorously participate in the development of sustainable buildings.

Conventionally, there are many existing ground amelioration techniques that are applied to treat the soft soil. Regardless of the type of techniques, Vakili et al. [20] discovered that the purpose of the soil stabilization method is to reduce the potential of magnesium and calcium particles to detach from each other, and decrease the magnitude of repulsive inter-particle forces that resulted in the instability of particles. Azimi et al. [21] reported that the chemical stabilization is an effective approach, provided in a controlled condition, specifically in the supervision of environmental impact. Referring to Herrmann and Bucksch [22], the adoption of a technique should be based on the type of soil (cohesive or non-cohesive soil) and the cost of the foundation. In this case, the choices of cohesive soil are vertical drains, vacuum dewatering, stone columns, and the in-situ mixing method. From the perspective of the economy and laboratory scale, the in-situ mixing method is mostly practiced by researchers due to its convenience of application. However, traditional soil stabilization approaches mostly involve the use of chemical admixture and mechanical modification, which can be substantially detrimental to the environment. Almuaythir et al. [23] summarized the effective materials but harmful substances for conventional stabilization are cement and lime, which have remarkably high carbon dioxide emissions due to the huge energy demand. In contrast, the authors implemented the cost analysis on the usage of clamshell ash as the source of lime silica-fume stabilized kaolin for the source of silicon and aluminium, which can optimize the cost of stabilization up to 10.06 %. It is deduced that the association of clamshell ash raises the pH condition of soil swiftly via the hydration process when contacted with moisture content, and generates the calcium hydroxide compound. It yields an identical effect as compared to quicklime (CaO), which accelerates the dissolution of amorphous compounds such as Si^{4+} and Al^{3+} ion. This statement is supported by Hashim Mohammed et al. [24], the production of Calcium Silicate Hydrate (CSH) and Calcium Aluminate Hydrate (CAH) is a significant product. Other products, such as nano-silica, are also widely applied and recognized for activating and accelerating pozzolanic activity to produce the aforementioned hydrated compounds [25]. The refinement of the properties of clay, persistently manifesting in pore refinement, particle bonding, and water mobility due to pozzolanic reaction. As the curing period extends, the CSH is gradually undergoing densification, which fills the capillary pores of soil through the procedure of sluggish polymerization. However, the CAH exists in a better crystallized state, which only contributes to the early strength development, and presents insignificant improvement of shear strength corresponding to the curing factor.

Therefore, all the above-mentioned studies have accentuated that traditional stabilizers or materials such as cement and sand are appropriate in altering clay properties, but also that greenery substituents can be utilized for improvement purposes, which aligns with the real-world construction industry.

Cow bone, being a source of biomass is appropriate to extract the calcium compound for various purposes [26]. The primary content of cow bone is Hydroxyapatite (HPA) or $Ca_{10}(PO_4)_6(OH)_2$, a type of stabilized crystalline structure that is held strongly by the three-dimensional lattice. Baroutkoob et al. [27] verified the effectiveness of cow bone as it is a sustainable source of nano-phosphorus in the increase of tomato yield by amending the biochemical and physiological properties of clayey soil. Norrahim et al. [28] utilized the advantage of cost-effective, renewable, and high stiffness in the polymer composites, acting as a reinforcement filler. Awotemi et al. [29] discovered the ideal proportion of Cow Bone Ash (CBA) is approximately 10 % of the total weight of concrete, where the maximum flexural strength was observed. The authors concluded that the rise of concrete strength is attributed to the high-water demand by CBA, which increases the Optimum Moisture Content (OMC). It stimulates the mobilization of ions and, therefore, the period of hydration is shortened. Coherently, the formation of CBA is done through the calcination process with the purposes of (1) removing impurities and organic matter, (2) transition of complex compounds to reactive minerals such as calcium oxide, (3) initiating the pozzolanic potential, and (4) transformation of biomass into a stabilizing agent. However, the temperature of calcination influences the productivity of calcium oxide, in which the factor of temperature and its yield is in a directly proportional relationship. Oluniyi et al. [30] reported that heating within the range of 800–900 °C yields calcium oxide contents of 87–99%. Due to its calcium-based biominerals, they are efficient in the absorption of contaminants, or catalyzing the decomposition of heavy metals, dyes, fluorides, surfactants, etc [31]. With the prior references of applying CBA, Yilmazoğlu [32] reported the curing period of 7 days, 14 days, and 28 days presented a significant alteration of unconfined compressive strength (UCS) as compared to the raw kaolin soil. The authors recorded the fluctuation of UCS was from 4.47 % to 23.34 %, and the negative results were due to the procrastination of pozzolanic reaction, transition of pore fluid, and the breakdown of kaolin fabric. The above data are verified by Parihar and Gupta [33] as the authors obtained a similar condition when using CBA as a substituent. The result of shear strength was raised drastically from 27 kPa to 257 kPa or 851.85 % after 28 days of curing, which densified and interlocked the soil matrix productively.

In today's engineering landscape, there has been a surge in research interest focused on the interaction of sustainable materials or the combination of other greenery materials in the application of soil stabilization. CBA, a biomass material sourced from the restaurants and poultry industry, has gained prominence as an origin of calcium replacement, such as quicklime and limestone. The major component of CBA, calcium carbonate ($CaCO_3$), occupies almost the entire volume of its component, with at least 90 % of occupancy depending on the calcination procedure. Resultantly, there are myriad potentials, benefits, values, and promises that can be explored in the construction industry. Without ambiguity, it can be stated that the replacement proportion must be in a commanded condition, refraining from obtaining unnecessary negative results. Established literature has confirmed the association of cow bone-derived substituents, suggested that further tailored materials are robust, and reduces the volume of disposal from the respective industries. Highlighting the civil-geotechnical area, the mixture of CBA into clayey soil has gained a huge momentum from the related parties, particularly the researchers. Previous investigations have tested and verified the suitability of CBA in altering the properties of soil, cement, and so on [29]–[31]; but there is no exact focus on the direct substitution of CBA with percentage in stabilizing the kaolinitic clay, along with the cost-analysis framework.

The current study emphasizes and carries out the association of CBA with the increment of 3% and 9 % by referring to previous analyses [21], [34]. It analyzes the engineering properties of kaolin, CBA, and refined kaolin with CBA through geotechnical approaches. These properties are significant in generating the relationship between kaolin and CBA, and provide new insight to readers regarding the soil stabilization effect corresponding to the curing periods of 7 days and 14 days. According to the experimental framework, several hypotheses can be drawn: (1) The mixture of CBA as a foreign material can react effectively with kaolin soil through the pozzolanic reaction, producing cementitious-behaved products; (2) regardless of the percentage of CBA used, the shear strength parameters of refined kaolin can be modified; (3) a comprehensive cost-analysis system can be established based on the comparison between conventional soil stabilizers and CBA materials. To highlight the advancement of this study relative to the literature data, the objectives are established to provide new knowledge to readers: (1) determine the geotechnical properties of the research materials (kaolin and CBA) utilized in this study; (2) obtain the shear strength parameters of kaolin and refined kaolin with CBA in various percentages; (3) establish the cost-analysis framework to verify the effectiveness of sustainable refined kaolin in actual construction sites via a prediction model.

2. Materials and Methods

The study (soil stabilization) is conducted on the scale of laboratory scale with the aim of modifying the shear strength properties of soil, which suits the common practice of research. The preparation of relevant materials is purely carried out in a controlled environment, complying with the BS and ASTM standards.

2.1. Materials

This section reveals the interaction of the investigated materials between the soft soil and the substitute. For the structurally deficient candidate, the kaolin soil with grade S300 is chosen, as depicted in Fig. 1. The selection of this grade material is due to several reasons: (1) homogeneous property, (2) cost-effectiveness, and (3) empirically validated material. The general formula of kaolin is $Al_2Si_2O_5(OH)_4$, and the geotechnical characteristics is tabulated in Table 1. Remarkably, the coefficient of permeability of kaolin is explored at 4.0×10^{-8} m/s, which fulfills the criteria of treatment-required material [5]. This material is sourced from Kaolin (M) Sdn. Bhd, a Malaysian clay leading company that specializes in supplying silica sand, China clay, mica powder, and sericite. The chemical composition of kaolin and CBA is listed in Table 2. Located in Puchong, Selangor, the company is approximately 19 km from Kuala Lumpur, the capital of Malaysia. The price of consideration for the above-mentioned kaolin is purchased at RM1.20 per kg (≈0.28USD), and the total usage of kaolin in this study is around 3.5 kg, which encompasses the potential wastage that occurred during the execution of the experiment.

Figure 1. Kaolin clay type S300.

Table 1. Geotechnical characteristics of kaolin

Characteristic	Unit	Data
LL	41	%
PL	33	%
PI	8	%
Gravel	0	%
Sand	39	%
Silt and clay	61	%
Specific gravity	2.64	NA
Optimum moisture content	19.77	%
Maximum dry density (MDD)	1.53	Mg/m^3
Permeability coefficient	4.0×10^{-8}	m/s

Table 2. Compound percentage of research materials

Sample	Composition (%)					
	SiO_2	CaO	Al_2O_3	K_2O	MgO	Fe_2O_3
Kaolin	66.1	0.1	20.2	2.9	1.2	0.7
CBA	12.6	61.0	16.8	0.6	1.5	1.2

Furthermore, the integrated reinforcement to the weak soil is the cow bone member, acting as a soil stabilizer to facilitate the pozzolanic reaction. The raw cow bone is collected from the local restaurants in Kuantan. It is washed with tap water to remove the impurities present on the surface, and air-dried for 7 days. As shown in Fig. 2, the clean cow bone is crushed into smaller pieces via a jaw crusher, ensuring an effective calcination process due to a higher surface-to-volume ratio. Afterwards, the crushed cow bone

was heated under a chamber furnace at 900 °C for 10 hours, following the standard procedure of calcination. The white color product is obtained, signifying the complete conversion of calcium carbonate into calcium oxide. The CBA is left in a desiccator for 24 hours, which avoids unnecessary reactions such as hydration due to the atmospheric moisture.

Figure 2. Preparation of CBA

2.2. Methods

This section discusses the entire flow of research work, beginning from the preparation of unrefined and refined kaolin, followed by the setup of experiments. The flow of preparation of unrefined and refined kaolin is shown in Fig. 3. The preparation of unrefined kaolin signifies the use of air-dried kaolin soil, weighing 110 g. The volume of water is set at 20.00 % of its total soil mass, determined from the OMC value as stated in Table 1. The dimension of the steel mold is measured at 38 mm in diameter and 76 mm in height for the sample fabrication process. As demonstrated in Fig. 3(a), the prepared kaolin mixture is transferred into the mold and undergoes compaction. The compaction effort varies accordingly, depending on the stiffness of the materials. Afterwards, an extruder (see Fig. 3(b) is used to extrude out the sample before storing it in a suitable container for stabilization purposes. Referring to the literature, the refined kaolin presents the unrefined kaolin mixed with the respective percentage of CBA, including 3 %, 6 %, 9 %, and 12 % [34]. Regarding the CBA material, it was selected for several reasons, including its proven effectiveness in rectifying the shear strength parameters of various types of soil with only a mild amount substituted under specific curing periods [33]. Previous studies highlighted that the CBA substitution has great potential to act as a supplementary material for cementitious and pozzolanic applications, such as concrete and soil enhancement [29]. The authors mentioned that the replacement of a certain portion of soil (not more than 20 %) with CBA accelerates this reaction mechanism for the production of cement hydration products. In addition, the utilization of CBA material is considered sustainable. Correspondingly, this material was obtained from disposed food waste from a local restaurant in Kuantan, Malaysia, and hence it did not incur additional cost.

The sample coding of refined kaolin is tabulated in Table 3. Correspondingly, the curing day of kaolin is chosen at 7 and 14 days, and measuring the rate of change of shear strength within this timeframe is significant to notice the reactivity of amorphous contents. The selection of these respective curing periods is attributed to literature remarks and results. The 7-day and 14-day curing periods are the common practice in soil stabilization methods, during which the reaction mechanism between kaolin soil and CBA has already demonstrated early to mid-term strength development through the formation of gel calcium compounds. In terms of practicability, timeline, and construction practice, the data acquired from the optimum curing periods of 7 days and 14 days are sufficient to evaluate the pozzolanic reaction, while subsequent curing periods record only mild improvement in engineering properties. A longer curing period (for example, 28 days) was not deployed in this study because it is more appropriate for cement-based materials, such as Ordinary Portland Concrete.

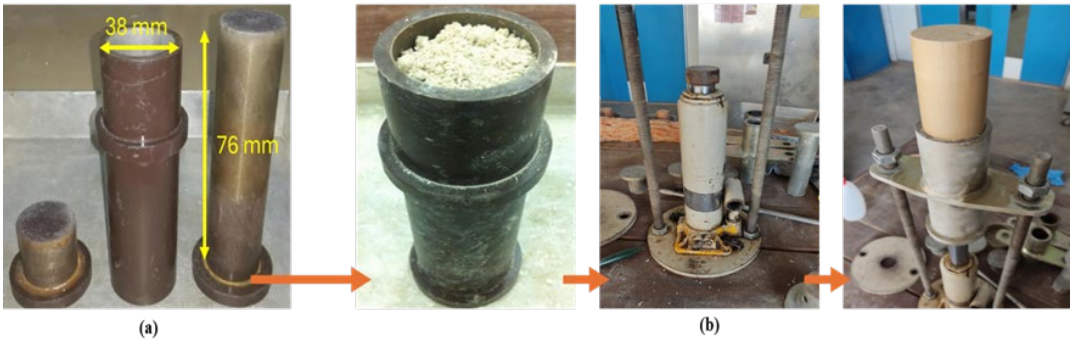

Figure 3. Procedure of kaolin preparation.

Table 3. Design of kaolin mixture with CBA

Sample coding	Percentage of association (%)		
	Kaolin	CBA	Total
7K	100	0	100
7K3CBA	97	3	100
7K6CBA	94	6	100
7K9CBA	91	9	100
7K12CBA	88	12	100
14K	100	0	100
14K3CBA	97	3	100
14K6CBA	94	6	100
14K9CBA	91	9	100
14K12CBA	100	12	100

*7K3CBA – 7 days of curing kaolin sample with 3 % of CBA mixture

Afterwards, the research process proceeds to the introduction of physical and mechanical investigations, as shown in Fig. 4 and Fig. 5. As demonstrated in Fig. 4(a), the dry sieving process begins with the selection of the relevant sieve size, including 5 mm, 3.35 mm, 1.18 mm, 0.6 mm, 0.3 mm, 0.15 mm, 0.063 mm, and a pan. The CBA is mechanically shaken for 15 minutes, and the percentage passing through its sieve size is plotted algorithmically. The subsequent analysis of grain size distribution (GSD) involves the use of hydrometer test, testing for the particle size of kaolin. This wet sieving process utilizes the same technique of data interpretation, as shown in Fig. 4(b) and the significant amount of kaolin particles retained is referred to as the final value. The execution of Atterberg limit is categorized into 2 sections: the LL and PL determination. Referring to Fig. 4(c), the LL value is obtained via the assistance of Casagrande device, and the PL value is yielded through the rolling method and oven drying at 100 °C. Last but not least, the small pycnometer is applied for the evaluation of the specific gravity of kaolin and CBA confined in the pycnometer. This technique subtracts the loss of water vapor, the change in mass between the material, soil, and pycnometer, to determine the average specific gravity.

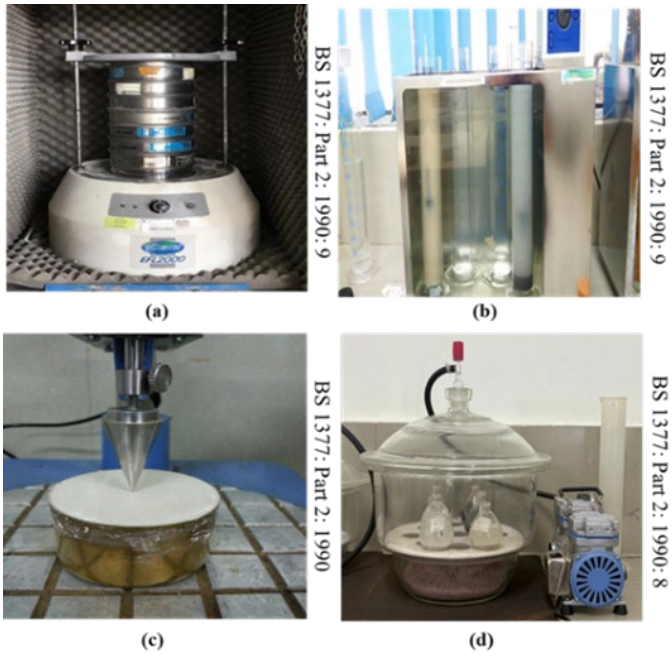

Figure 4. Physical experiments (a) Sieve analysis (b) hydrometer (c) cone penetrometer (d) small pycnometer.

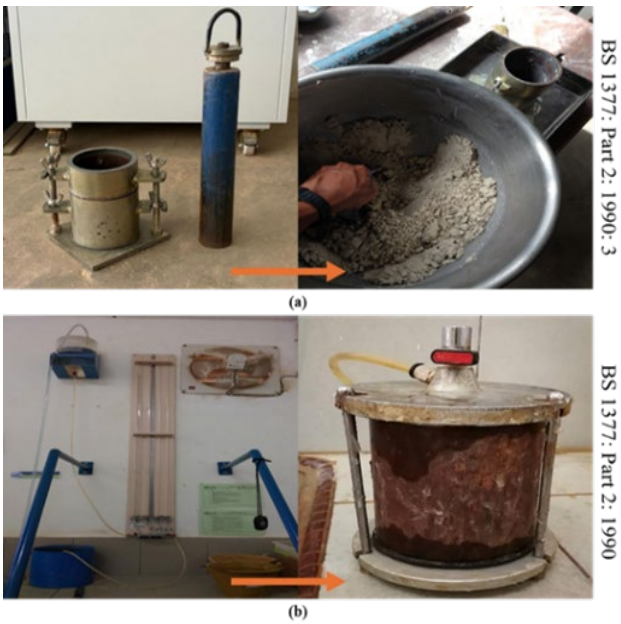

Figure 5. Mechanical experiments (a) Standard compaction (b) falling head test.

As shown in Fig. 5(a), the mechanical characterization of unrefined and refined kaolin is acquired through the execution of standard compaction test. The raw kaolin soil is first analyzed to obtain the OMC and MDD values, followed by the mixture of relevant percentage of CBA as tabulated in Table 3. It ensures the homogeneity, accuracy, and reliability of data upon executing the UCT. For all designs, the range of moisture content addition is from 5 % to 30 %, with the 5 % of increment for the subsequent analysis. For calibration purposes, the hammer used for compaction is weighted at 2.5 kg, and the height and diameter of the compaction mold are measured for accurate dry density calculation, following the BS standard. Besides, the oven temperature was calibrated between 100 °C and 105 °C during the drying process. The compaction hammer is used to reduce the air voids of soil, measured from a distance of 15 cm from the steel mold. The turning point of graph is marked as the reference for OMC and MDD determination. In addition, the rate of water flow across the kaolin particle is expressed via the coefficient of hydraulic conductivity. As depicted in Fig. 5(b), the falling head approach is implemented to acquire the data. This method computes the flowrate of water within a stipulated timeframe, assisted by a burette. After obtaining the significant geotechnical properties, the samples of unrefined and refined kaolin are investigated under the approach of UCT (see Fig. 6). Before beginning the test, the load frame is calibrated to zero indication which shows no load being applied. Referring to the dimension of specimen, the constant strain rate is fixed at 1 %, following the ASTM standard. Thus, the specimen undergoes 1 mm/min. This machine shears the specimen at a constant rate of deformation, with the calibration ring factor of 0.00167 kN/div. The axial stress strain, unconfined compression stress, and undrained shear strength are calculated concerning this value. This method complies with the ASTM D 2166, in which the examination is halted when column failure is observed, for instance, column bulging. For the purpose of accuracy, each specimen from Table 3 is examined for 3 times, and the average value is picked up as the final value.

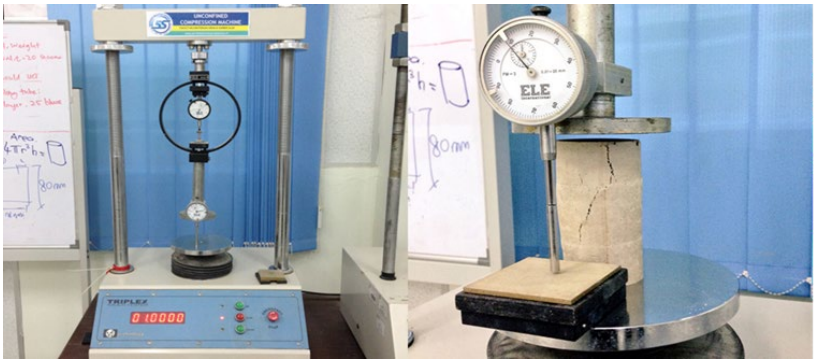

Figure 6. Determination of shear strength parameters through the execution of UCT.

3. Results and Discussion

This chapter demonstrates thoroughly the geotechnical engineering properties of kaolin clay and CBA, and the alteration of their characteristics when kaolin mixes with CBA at 3 %, 6 %, 9 %, and 12 %,

respectively. These samples are tested without curing, by approximating real-world soil behavior under the experimental settings. Their performance under the fixed rate of deformation is also evaluated. The use of statistical analysis presents entirely their relationship, correlation, and strength align to all the involved variables.

3.1. Effect of CBA on the Modification of Kaolin Particle Size

Fig. 7 demonstrates the graph of kaolin, CBA, and kaolin + 6 % CBA, corresponding to their percentage passing and particle size. It is noticed that without the addition of CBA, the curvature of graph is positioning outwards, indicating a bigger variation in terms of particle size. From the results, there are only 3 types of grain size detected from this category, which are 0.15 mm, 0.063 mm, and less than 0.063 mm. The largest occupancy of particle size is from 0.063 mm, which represents 62.82 %. The above discovery is coherent with the findings by Shen and Hasan [35], in which 50 % or more 0.063 mm kaolin particle is anticipated to obtain. In contrast, the graph of cow bone is curved inwards, as compared to kaolin soil. It is predicted to occur due to its calcined properties, where the bone microstructure is naturally dense, attributed to HPA component [26]. The largest portion of particle size discovered is at 0.3 mm, followed by 0.6 mm which holds 32.34 % and 26.73 %, respectively. However, Norrahim et al. [28] emphasized the moderate size of CBA can enhance the mechanical properties of soft clay soil effectively, due to its larger surface area exposure to undergo cementitious and pozzolanic reaction.

Due to the acquisition of optimum shear strength parameters result from the inclusion of 6 % CBA in kaolin, this specific design is only selected to quantify the degree of dispersion across the dataset. Interestingly, the 6% substitution yields particle sizes ranging from 0.15 mm to 0.3 mm at 93.08%, which validates the literature data. According to Abdulwahab et al. [36] mentioned surpass the optimum addition percentage of CBA, it induces the chemical saturation condition, where the calcium oxide has no longer demanded by the amorphous oxide. The current findings deduce that 6 % CBA mixture is effective and the occurrence is due to physical mixing influence as well as vigorous flocculation and agglomeration. The calcium oxide extracted from CBA is adequate to facilitate the cation exchange in kaolin particle efficiently.

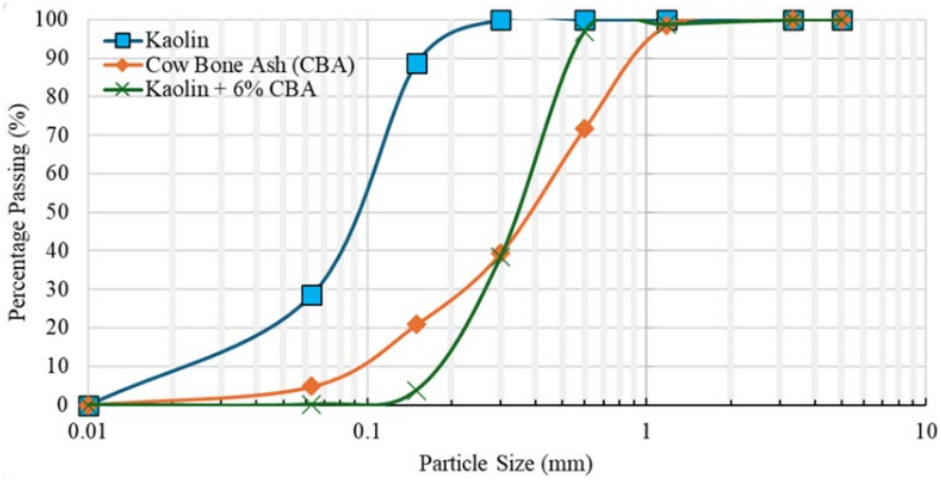

Figure 7. Modification of particle size of kaolin and kaolin with CBA.

3.2. Effect of CBA on the Modification of the Consistency Limit of Kaolin

Fig. 8 displays the data generated by Atterberg limit, presenting the value of LL, PL, and PI. From the dataset, the total change of LL, PL, and PI is recorded at 16.62 %, 24.96 %, and 157.39 %, respectively. Without the inclusion of CBA content, the raw kaolin has the value of LL and PL at 41 % and 33 %, which is not favorable for construction activities [39]. It proves that the raw kaolin is subjected to high compressibility and sensitive to moisture content, aligning to its LL value. Furthermore, the undisturbed kaolin is potentially to lose its plasticity when exposing to continuous water supply. Nonetheless, the utilization of CBA does not guarantee a continuous improvement of consistency limits, where the LL, PL, and PI magnitude demonstrate a fluctuating condition. For 3 % and 9% CBA embracement, the magnitude of consistency limits rectifies moderately, in which the improved LL and PL value compromise each other.

Notably, both the maximum LL and PL values were recorded at 12% CBA inclusion, which yielded the smallest PI value across the study. The above condition is similar to the experiment conducted by Jamhuri et al. [34], in which the authors mentioned the dissolution process of cow bone into cations and anions, comprising of calcium ion (Ca^{2+}) and hydroxide ion (OH^{-}) displace hydrogen ion (H^{+}) to accelerate the process of kaolin flocculation. This condition is explained by the overdose of CBA substituent, which produces an insignificant effect on reducing water affinity but worsens the surface roughness of the soil matrix. Consequently, the modified soil mass with 12 % CBA content tends to trap more moisture content

on the kaolin particle lining wall. The calcium compounds are also potentially to interrupt the original soil matrix structure, transforming the state of soil into a mixture of kaolin-silt. Hence, as proven by the result from UCT, the optimum inclusion percentage fells to 6 % CBA, in which the demonstration of LL, PL, and PI figures are in ideal status.

The validation of accuracy of consistency limits is carried out by the deployment of correlation technique, and the cubic function is chosen to establish the equation for LL, PL, and PI as shown in Eq. 1, Eq. 2, and Eq. 3. According to the R^2 parameter, the values are 0.986, 0.975, and 0.9938, respectively, as recorded in Eq.1, Eq.2, and Eq.3. This signifies that more than 95 % of the variables can be explained by these models. In addition, the regression analysis on LL, PL, and PI generated p-values of 0.2485, 0.1634, and 0.5972. Hence, the findings verify that CBA content is effective in the development of shear strength while showing insignificant modification of plasticity.

$$LL = -0.0283(CBA)^3 + 0.5794(CBA)^2 - 2.7064(CBA) + 40.831; \quad (1)$$

$$PL = -0.0076(CBA)^3 - 0.0163(CBA)^2 - 0.3841(CBA) + 33.173; \quad (2)$$

$$PI = -0.036(CBA)^3 + 0.5953(CBA)^2 - 2.3069(CBA) + 7.6507. \quad (3)$$

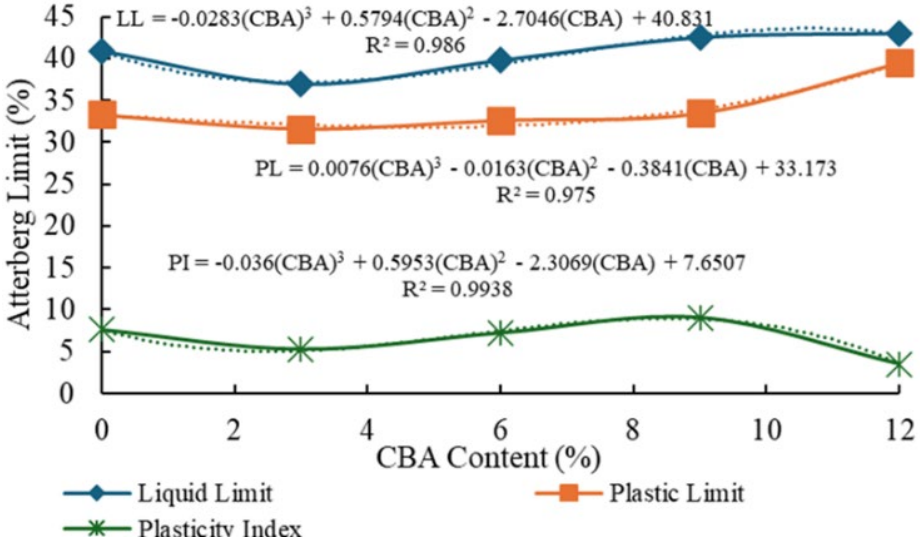

Figure 8. Consistency limits of kaolin altered with varying content of CBA.

3.3. Effect of CBA on the Proctor Test Properties of Kaolin

The association of CBA content in varying content modifies the proctor characteristic of kaolin soil, causing the inconsistent movement of OMC and MDD across the proportion. As displayed in Fig. 9 and Fig. 10, all the designs show decreasing trend after achieving its ideal proctor parameters. Referring to the data, the highest OMC and MDD value recorded is at 19.97 % and 2.53 Mg/m^3, extracted from the refined kaolin at 3 % and 6 % CBA content, respectively. Table 4 summarizes the ideal value of OMC and MDD concerning the unrefined and refined kaolin sample. Remarkably, it is discovered that there is a sharp reduction of OMC at 6 % of CBA content used, dropped from 19.77 % to 9.42 %. In contrast, the MDD value is increased drastically from 0.79 Mg/m^3 to 2.53 Mg/m^3. Therefore, this study concludes that the optimum content of CBA is fixed at 6 %, corresponding to the reported data. Previous experiment data discovered that the optimum value of lime-based stabilized material inclusion should not exceed 10 % of its total soil volume, as the unreacted CBA content introduces micro-voids to the soil particles [37]. It explains the reason of obtaining the MDD at 2.53 Mg/m^3 when the 6 % of CBA is utilized. The effective densification process by the calcined CBA stimulates the volume occupant of voids which then requires a better compaction effort to attain the respective MDD value. A greater value of MDD is favorable for mega infrastructure project, which caters for a better load bearing capacity [9], [38].

Table 4. Summary of the compaction features from distinct samples

Sample	OMC (%)	MDD (Mg/m³)
K	19.77	1.53
K3CBA	19.97	0.79
K6CBA	9.42	2.53
K9CBA	14.49	1.61
K12CBA	15.44	1.59

Observing from 9 % CBA content onwards, the recovery of OMC value from its trough signifies the subside of MDD value from its crest. It is deduced that the OMC and MDD possess an inverse proportional relationship, regardless the inclusion of CBA content. As explained by Hasan et al. [39], the rise of OMC indicates the increase of degree of water molecule mobilization and therefore, pore pressure volume increases. This causes the decrease of compaction effort to achieve the MDD value under the identical soil matrix. Therefore, the generation of R^2 are at 0.9551, 0.8893, 0.987, 0.8168, 0.8168, and the functions are presented in Eq. 4, Eq. 5, Eq. 6, Eq. 7, and Eq. 8. Coherent with this, the modification of Proctor properties by CBA leads to higher accuracy in variability explanation, increasing from 81.68 % to 98.70 % according to the R^2 values. Furthermore, the p-values for each function are recorded at 0.613, 0.2187, 0.1609, 0.4622, and 0.3241, respectively. These data support the rejection of the alternative hypothesis, indicating an insignificant relationship between MDD and OMC, although the regression model fits the variables properly. The current results confirm that the Proctor properties of soil and refined soil are governed by their size distribution and texture.

$$MDD = -0.0007\left(OMC\right)^2 + 0.0274\left(OMC\right) + 1.2538; \tag{4}$$

$$MDD = -0.014\left(OMC\right)^2 + 0.0466\left(OMC\right) + 0.3728; \tag{5}$$

$$MDD = -0.014\left(OMC\right)^2 + 0.0312\left(OMC\right) + 2.3660; \tag{6}$$

$$MDD = -0.0009\left(OMC\right)^2 + 0.0254\left(OMC\right) + 1.4119; \tag{7}$$

$$MDD = -0.0007\left(OMC\right)^2 + 0.0158\left(OMC\right) + 1.4785. \tag{8}$$

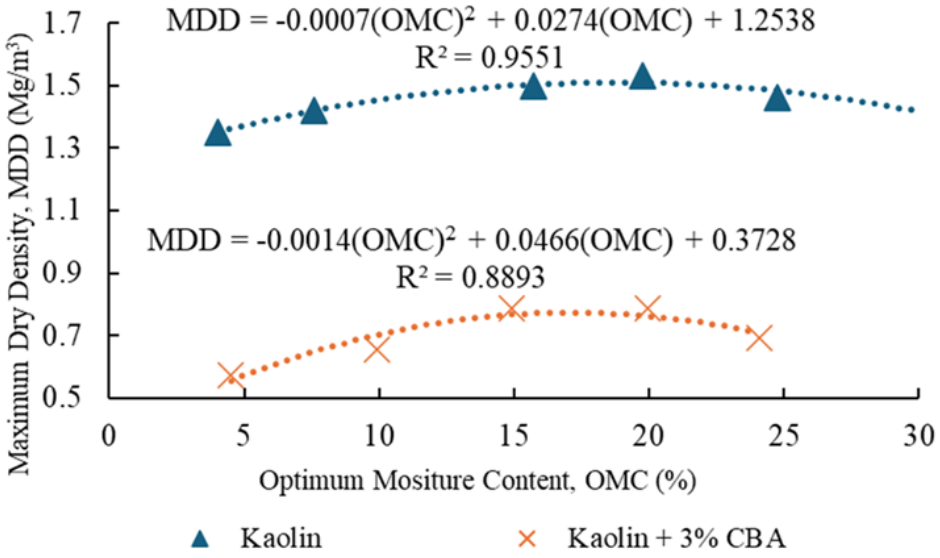

Figure 9. Proctor characteristics of kaolin and refined kaolin at 3% CBA content.

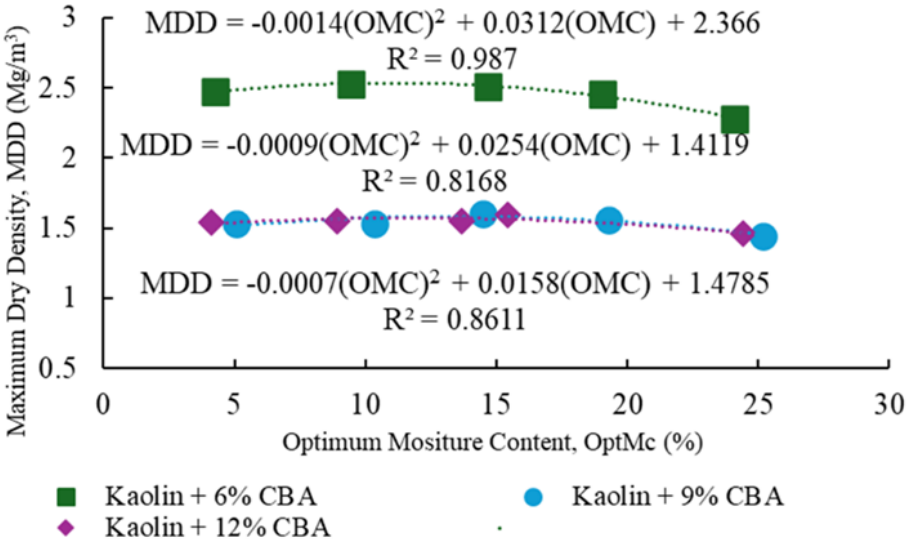

Figure 10. Proctor characteristics of refined kaolin at 6 %, 9 %, and 12 % CBA content.

3.4. Effect of CBA on Kaolin Specific Gravity

This section expresses specifically the details of specific gravity, referring to its raw value of kaolin soil and CBA. From the study, the specific gravity of kaolin and CBA is obtained at 2.64 and 0.89, respectively. Bozyigit et al.[40] reported the value at 2.62, Hoque et al. [12] discovered at 2.68, and Hasan and Yee [8] mentioned 2.64. Thus, it is concluded that the undisturbed kaolin soil has a small variation, and can be attributed to the impurities found on the pycnometer surface. Furthermore, the CBA specific gravity is influenced by its calcination process, and exert a greater fluctuation value corresponding to the temperature control in the furnace [41]. Based on the results, it interprets that the kaolin soil is 2.64 times heavier than the water, while CBA is lighter than the water due to its value less than 1.

The addition of varying CBA contents rectifies the specific gravity of undisturbed kaolin, as shown in Fig. 12. As referred to the initial value of specific gravity of kaolin, the variation of specific gravity value ranges from 2.67–14.78%, smaller undulation as compared to other geotechnical characteristics. From the graph, it is noticed the gradual increment of CBA content (up to 6 %) produces the lowest value of specific gravity of refined kaolin. This situation confirms that the refined kaolin has become a porous and lightweight structure, which is ready to absorb more moisture content due to its enlargement of volume tolerance. In addition, at 6 % CBA content, the refined kaolin possesses a better dispersion behavior or an ideal blend density, where it can react more vigorously with the calcium compounds, such as calcium oxide.

This trend is reversed when the CBA content increases to 9 %, causing the specific gravity to rise 2.17 %. It shows that the refined kaolin begins to densify, where the unreacted calcined CBA has predominantly occupied the pore of kaolin particles. Furthermore, the above condition also signifies the density gradient is restored, in which the ideal dosage of CBA has been surpassed. Similarly, the kaolin mixes with 9 % CBA content onwards got a better capability in modifying the moisture content, as the pore water being entrapped in the soil mass can be eliminated more effectively. The subsequently increment of CBA content to 12 % has expected to rise the specific gravity to the highest among this research, recorded at 2.67. It is possible to hinder and reduce the efficiency of pozzolanic reaction, because of the deceleration of ion exchange during hydration process. Besides, it expresses the refined kaolin has a heavier weight, which has limited usage and not practical in actual construction industry. Thus, the current findings propose 6 % CBA content is the appropriate proportion for kaolin soil substitution. The R^2 is calculated at 0.9306, and its function is displayed in Eq. 9. Correspondingly, the p-value of this function is calculated at 0.9275, suggesting the acceptance of the null hypothesis. This result indicates that the research is consistent with findings in the literature, where substituents such as CBA and cementitious materials act chemically rather than physically altering particle density. On the other hand, the variation in specific gravity depends on its mineral composition relative to the water ratio.

$$SG = 0.0095\left(CBA\right)^2 - 0.1163\left(OMC\right) + 2.6694. \quad (9)$$

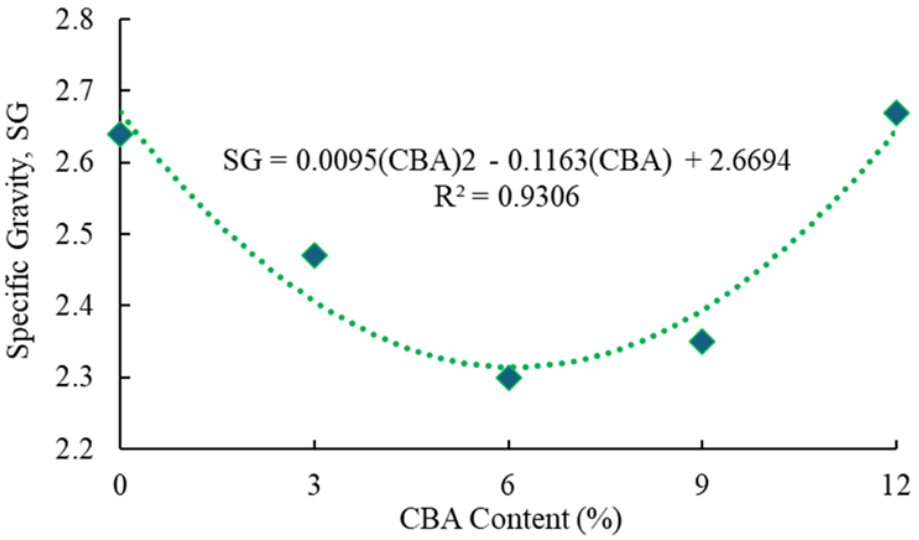

Figure 11. Specific gravity of kaolin and refined kaolin at 6 %, 9 %, and 12 % CBA content.

3.5. Effect of CBA on the Kaolin Shear Strength

Via the execution of UCT, the average value of kaolin shear strength (KSS) is obtained from 3 identical samples, and the improvement rate is calculated according to the unrefined kaolin sample, as displayed in Fig. 12. Based on the data, all the refined kaolin specimens with 3 %, 6 %, 9 %, and 12 % CBA content produce shear strength enhancement, ranging from 81.15 % to 578.10 %. Notably, the significant rise in shear strength is attributed to the extremely low baseline strength of unrefined kaolin, whose soil matrix is primarily comprised of pore water, contributing to higher compressibility. The complete formation of CSH and CAH compounds within the soil structure results in a denser matrix, thereby providing better resistance against axial force. It is also observed that this value occurs at the highest CBA content, 12 %, which supports the statement regarding the complete formation of hydrated calcium compounds. The potential sources of error in this value include material handling issues, material variability, and the preparation process. The refined kaolin sample is categorized into 2 categories, 7 days and 14 days curing samples. Remarkably, the highest KSS value is generated from 7K6CBA, which yielded a KSS value at 57.36 kPa. In contrast, the smallest KSS value is produced from 14K3CBA, recorded at 20.09 kPa. The numerical difference is calculated at 37.27 kPa, which translates into 64.98 %. The huge gap of difference is predominantly attributed to the curing process, in which the rapid strength development is noticed at 7 days. Furthermore, the optimum amount of CBA substitution accelerates the surge of shear strength, where the calcium compound has been fully mobilized to form the gel substance, mainly the silicate and aluminate hydrate. This in turns produce the environment which has no excessive calcium compounds that can possibly disturb the soil matrix which leads to the over-densified condition.

Notably, the 14K sample has a bigger value of KSS as compared to the value of KSS produced by 7K. The difference of KSS value is recorded at 2.63 kPa, or 23.72 %. It signifies that without the interruption of foreign material, the strength of kaolin is gradually built up corresponding to the curing period. However, when the introduction of calcium source is carried out, a guarantee of certain period of curing is necessary, regardless the type of lime introduction [42]. The authors deduced that the emerging of cementitious compounds require a longer time for the treated materials to stabilize, for the purpose of interlocking the particles in an undrained condition. The variation observed in the current research data arises from two factors, namely the curing period and the column dimension. According to Jamhuri et al. [34], the column diameter generates a substantial influence to the reinforcement member, in which a rise of column dimension leads to the surge of reinforcement magnitude, in a vice versa condition. Nonetheless, Shen and Hasan [35] reported the above-mentioned relationship is only applicable when the substituent possesses the following criterions, including identical or similar particle size, bulk density, proctor properties, and coefficient of hydraulic conductivity. Hence, the current result concludes that a 6 % CBA replacement into the kaolin soil sample which has a 38 mm diameter and 76 mm height is ideal, practical, and sustainable for the rectification of soil-bearing capacity. The comparison of CBA with other biomass materials is summarized in Table 5, corresponding to varying curing periods and its maximum improvement in shear strength (SSI) value.

Table 5. Different type of biomass in soil stabilization corresponding to its curing periods

Biomass substituent	Curing periods (0, 7, 14, and 28 days)				
	Max $SSI_{0\ day}$ (%)	Max $SSI_{7\ days}$ (%)	Max $SSI_{14\ days}$ (%)	Max $SSI_{28\ days}$ (%)	Reference
CBA	NA	278.10	296.92	NA	Current
Rice husk	35.46	NA	NA	NA	[19]
Grinded coconut shell	28.51	NA	NA	NA	[43]
BA + rice husk ash	NA	16.77	NA	80.22	[32]
Cockle shell ash	NA	90.52	91.35	NA	[44]

The correlation equation is outlined in Eq. 10 and Eq. 11 according to the UCT result in 7 and 14 days of curing. The corresponding R^2 values were 0.9794 and 0.9464, respectively, based on Fig. 13. Using the same approach, the p-values for both curing periods were obtained at 0.005 and 0.008, which reject the null hypothesis. This validates the previous data and literature findings regarding curing periods, substitution percentage, cementitious reactions, and pozzolanic mechanisms. It also suggests to readers the formation of hydrated compounds over time, binding the dispersive particles together and leading to an increase in shear strength magnitude.

$$SSI = 0.3772(CBA)^3 - 15.438(CBA)^2 - 168.91(CBA) - 7.7924; \quad (10)$$

$$SSI = 0.7357(CBA)^3 - 8.2163(CBA)^2 + 20.79(CBA) - 7.0607. \quad (11)$$

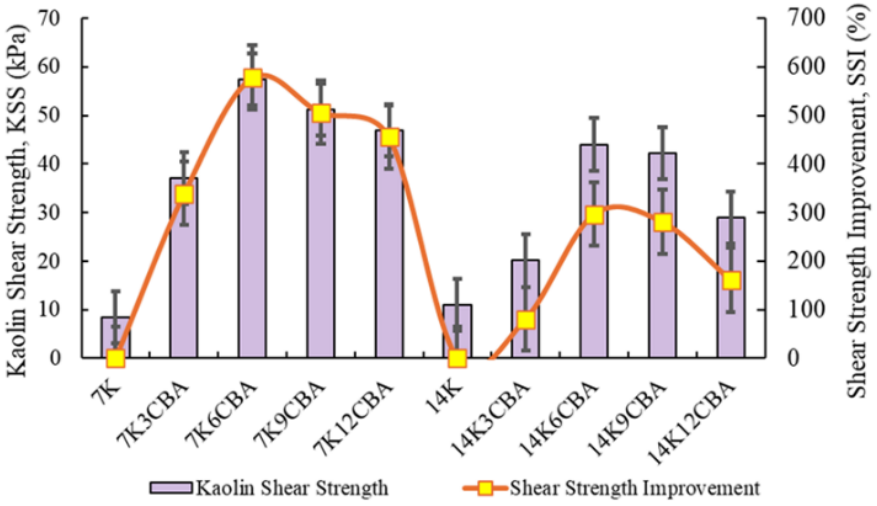

Figure 12. ***Relationship between KSS and SSI rate.***

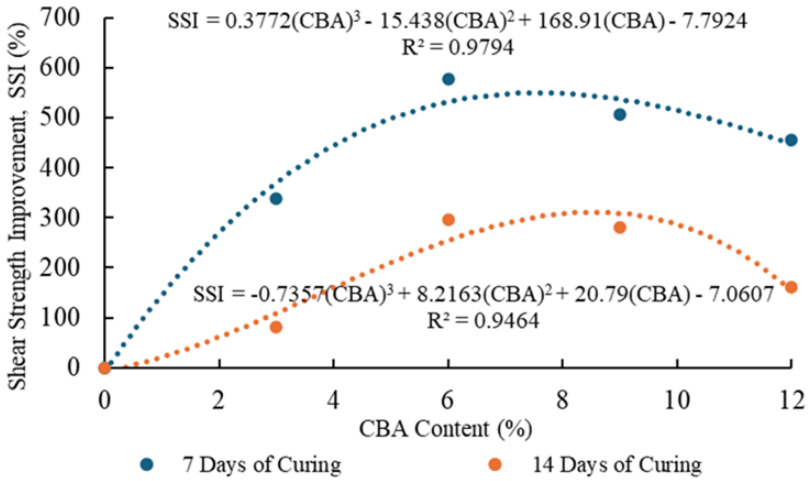

Figure 13. The correlation of SSI and its CBA content.

3.6. Effect of CBA on the Kaolin Stress-Strain Relationship

This section discusses the stress-strain relationship of raw kaolin and refined kaolin soil, which examines their ductility, brittleness, and the peak strength across the pre-determined curing periods, 7 days and 14 days, respectively. Fig. 14 demonstrates the stress-strain relationship of raw kaolin and refined kaolin across all the CBA content, at 3 %, 6 %, 9 %, and 12 %, respectively. The maximum stress produced by 7K sample yielded at 17.29 kPa, corresponding to the strain value at 2.17 %. These data provide a comprehensive understanding that after 17.29 kPa or its peak strength, the soil failure occurs but deformation continues. It is noticed by the condition of column, and at this case, bulging of 7K sample is observed. As explained by Hasan and Yee [8], other common column failure observation under the UCT includes shear failure, buckling failure, and compression failure. With the addition of CBA content, the stress value from 7K3CBA, 7K6CBA, 7K9CBA, and 7K12CBA rise significantly. The recorded magnitude of its peak value are 61.38 kPa, 113.1 kPa, 99.28 kPa, and 68.45 kPa, aligning with the strain value of 6.32 %, 4.58 %, 6.36 %, and 8.85 %, respectively. Coherently, the optimum value of CBA content is at 6 % for the acquisition of peak stress magnitude, and the ideal substitution CBA content for obtaining strain value is at 12 %. It validates that at 6 % CBA content, the cementitious compounds, CSH and CAH have an optimum ratio, which densifies the particles evenly. In addition, the gel produces a stiffer kaolin specimen but brittle in catering shear force. Interestingly, the 12 % CBA content leads to a deformable behavior of kaolin, absorbing slowly the pressure imposed by the axial loading. On the other hands, 7K12CBA specimen possesses a systematic soil particle configuration due to the mild cementitious behavior exist on the soil mass. According to literature, the overdose CBA content causes the unreacted calcium compounds remain within the soil matrix.

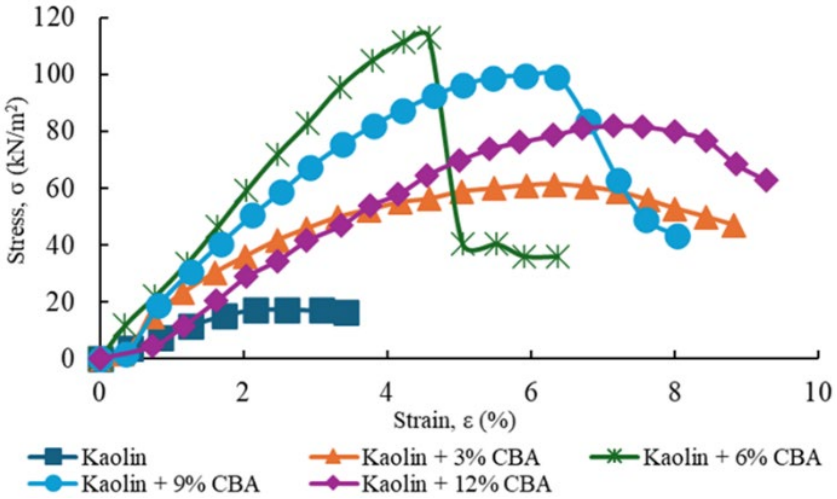

Figure 14. Stress-strain relationship of 7 days curing kaolin and refined kaolin at 3 %, 6 %, 9 %, and 12 % CBA content.

Correspondingly, the stress-strain relationship of 14 days curing specimen is displayed in Fig. 15. The 14 days of curing generates the similar data as compared to 7 days of curing. Aligning to that, the gradient of all designs (includes 14K, 14K3CBA, 14K6CBA, 14K9CBA, and 14K12CBA) are less steep than the gradients of 7 days cured kaolin samples. It expresses the 14 days of curing samples possess the behavior of low stiffness and rigidity, or a lower value of Young's modulus. The peak stress from these specimens were generated at 20.21 kPa, 48.45 kPa, 81.86 kPa, 92.53 kPa, and 57.06 kPa, with the strain value of 1.97 %, 6.00 %, 4.15 %, 7.59 %, and 5.49 %, respectively. It proves that the 14 days curing is an intermediate duration for the reaction of calcium compounds and the kaolin particles to enhance its cementitious properties. Soyemi and Soretire [45] mentioned sufficient curing process leads to the value surge of rectifying parameters, however, it decreases over time because the cementitious reaction is getting completed. Although the previous data validate that the 6 % CBA content is the optimum ratio, but 14 days of curing data present the optimum percentage is at 9 % CBA content. The data discrepancy above has yielded a different of 3 % CBA content, which is minor to quantify. The mild variation of CBA proportion also provides a better understanding that curing duration has indeed imposed a substantial effect to the enhancement of stress-strain value. Conspicuously, the stress magnitude of 7K6CBA and 7K9CBA are higher than 14K7CBA and 14K9CBA, with the difference of 31.24 kPa and 6.75 kPa, respectively. Therefore, the interpretation of stress-strain relationship data deduce that 6 % CBA content association is optimum under 7 days of curing, and beyond this percentage, a longer curing period is required to stabilize the substituent and the soil.

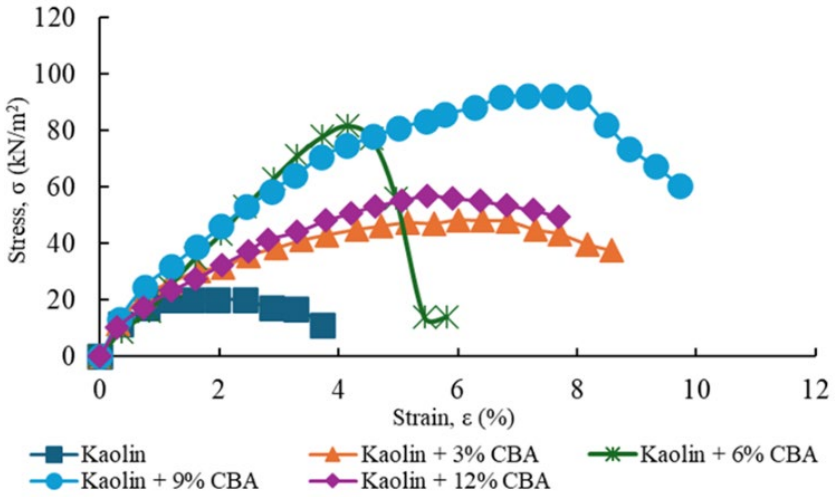

Figure 15. Stress-strain relationship of 14 days curing kaolin and refined kaolin at 3 %, 6 %, 9 %, and 12 % CBA content.

3.7. Effect of CBA on the Kaolin Stabilization Mechanism

The generation of the greater KSS difference is attributed to the curing process, CBA association percentage, and the preparation process. However, the percentage used depends on the type of lime introduction, and the preparation procedure exerts insignificant influence if it is not mixed with reactive chemicals. Analyzing from the perspective of CBA mixture, it facilitates the cation exchange, flocculation, and pozzolanic reaction. These reactions exert a significant role in the evolution of strength via the necessary chemical and physical transformation [36]. Cation exchange is a displacement process where the introduction of CBA provides Ca^{2+} ion to displace other cation like Na^{+} ion and K^{+} ion which has a lower charge density. The addition of CBA has effectively raised the pH to appropriate alkaline condition, proceeding through the hydration of calcium oxide to form calcium hydroxide [46], as shown in Eq. 10. Simultaneously, the flocculation process occurs due to the electrostatic interactions between the kaolin surface and Ca^{2+} ion which clumps the dispersive kaolin particles together. The production of sufficient amount of this compound is important to source the quantity of CSH and CAH, which is CBA amount dependent variable.

Hydration reaction:

$$CaO + H_2O \rightarrow Ca(OH)_2 . \quad (10)$$

Parihar and Gupta[33] emphasized the sufficient curing day can lead to a surge of rectified parameter. However, the authors also mentioned the design of curing day should correspond to the use of soil stabilizer, due to the influence of compaction efforts required to achieve the ideal proctor properties. The above statement is coherent with the current findings, where the 14 days of curing does not project a continuous rice of KSS magnitude. As reported by Jamhuri et al. [34], the sudden rise of KSS value can be due to the unacknowledged behavior of CSH, which fills the capillary pores of kaolin soil gradually. The establishment of silica link by the CSH requires a longer period to achieve a completed densified condition [32]. The rectification of soil-bearing capacity of kaolin expresses the effective pozzolanic reaction has taken place after 7 and 14 days of curing, regardless the design. The production of cementitious material accelerates the initial build-up of KSS value, causing the continuous increment at the period of 7 days. However, the 14 days of curing has somewhere probably led to the microcrack on the refined kaolin samples, which impair the soil matrix currently. The detection of microcrack can lead to the delayed pozzolanic reaction which undermines the effectiveness of CSH gel densification. Nonetheless, during the stipulated curing periods, the silicon oxide and aluminium oxide react efficiently with the calcium hydroxide, yielding sufficient concentration of CSH and CAH for the growth of kaolin strength. The chemical equations for the reactions involving calcium, hydroxide, and silicon oxide, which produce hydrated calcium compounds (CSH and CAH), are outcomes of the soil-stabilizing agent [46] and are presented in Eq. 11 and Eq. 12.

Pozzolanic reaction:

$$Ca^{2+} + 2[OH]^{-} + SiO_2 \rightarrow CSH; \quad (11)$$

$$Ca^{2+} + 2[OH]^{-} + Al_2O_3 \rightarrow CAH. \quad (12)$$

3.8. Cost Analysis of Kaolin Stabilization Mechanism

In the focus of applying the cost-effective material, CBA in civil engineering world, developing a comprehensive data within the constraint budget is essential for the construction, development, and maintenance activities. To examine the efficiency of CBA in the technique of soil stabilization as a replacement of calcium source, it is compared with the conventional treatment which has similar characteristics, mainly the cement material. A financial viability occurs as a crucial factor that governs the decision makers across diverse alternatives. Table 5 summarizes the cost of each required materials, aligning to the relevant sources and data. The price of water and excavation are determined according to the rate set by the Malaysian government, all the prices may vary according from time to time, currency exchange, and across countries. Because of the collection method of CBA was from the local restaurants (disposal site) and was complementary, the price of CBA was considered RM0.00. However, the price of biomass varies according to collection methods, national policies, global commodity price movements, and environmental factors. Changes in any of these factors may result in additional costs for relevant parties, such as engineers seeking to replicate the current experimental program and its findings. Thus, as compared to the traditional stabilizing agent, cement, the price difference is RM0.45/kg. Table 6 is significant to outline the budget for stabilizing the clayey soil, with the details of portion and amount of soil stabilizer. Referring to the data, the amount of stabilizer required is corresponding to the portion of stabilizer, varying across the design. Therefore, Table 7 presents the total stabilization cost for cement and CBA, relative to the assumed soil quantity. As discussed by previous studies, the total amount of soil that requires to be stabilized in the current research was 10 m^3 or equivalent to 10,000kg [47].

Table 6. The data of soil stabilization framework, corresponding to its materials and prices

Material & process	Unit price (RM/kg)	Reference
Clay	0.00	[46]
Cement	0.45	[48]
CBA	0.00	NA
In-place stabilization	0.02	[47]
Water	0.00286	Suruhanjaya Perkhidmatan Air Negara (SPAN)
Excavation	0.032	Jabatan Kerja Raya (JKR)

Table 7. Details assumption of stabilizer portion and its amount based on the soil quantity at 10m^3 Volume = 10,000 kg. Cement (Ce); clay soil (K); CBA

Design	Portion of stabilizer (%)		Amount of stabilizer (kg)	
	Ce	CBA	Ce	CBA
K3CBA	N/A	3	N/A	300
K3Ce	3	N/A	300	N/A
K6CBA	N/A	6	N/A	600
K6Ce	6	N/A	600	N/A
K9CBA	N/A	9	N/A	900
K9Ce	9	N/A	900	N/A
K12CBA	N/A	12	N/A	1200
K12Ce	12	N/A	1200	N/A

Table 8. Tabulation of cost analysis based on the designs, in comparing with the cement and CBA material. Total cost = (Stabilizer quantity × unit price of materials) + (In-place stabilization × soil quantity) + (Water times [OMC × stabilizer quantity] + Soil quantity) + (Excavation × soil quantity)

Design	Amount of stabilizer (kg)		Total cost (RM)
	Ce	CBA	
K3CBA	N/A	300	548.77
K3Ce	300	N/A	683.64
K6CBA	N/A	600	548.76
K6Ce	600	N/A	818.69
K9CBA	N/A	900	548.97
K9Ce	900	N/A	953.73
K12CBA	N/A	1200	549.13
K12Ce	1200	N/A	1088.77

Based on the calculated cost obtained, the price of stabilization is ranging from RM548.77 to RM1088.77, or a difference of RM540 between the type of soil stabilizer, cement and CBA across the percentage of 3 %, 6 %, 9 %, and 12 %. For stabilizing the quantity of 10 m^3 of clay soil, the difference in total cost for all designs are discovered at RM134.87, RM269.93, RM404.76, and RM539.64, respectively. This in turns translates to an additional cost at 19.73 %, 32.97 %, 42.44 %, and 49.56 %. Fig. 16 depicts the cost comparison between both materials, represented by CBA stabilized-soil (red color) and cement stabilized-soil (grey color). It is deduced that when the percentage of cement increases, the total cost for soil stabilization increases more than 10 %. In contrast, the rise of CBA content does not subject to double digit cost increment, attributing to the cost-effective factor of CBA. Analyzing from the optimum portion of CBA, the total cost of stabilization is found at RM548.76. Comparing with the identical percentage of traditional soil stabilizer, cement, the total cost is calculated at RM818.69, which is equivalent to approximately 33 % of the work efficiency. The OMC of ordinary concrete is selected at five %, according to the research implemented by Pongsivasathit et al. [49]. Therefore, because of the cost-effectiveness of CBA and its lime-identical properties, it is an ideal alternative to act as a soil stabilizer in rectifying the expansive clay soil.

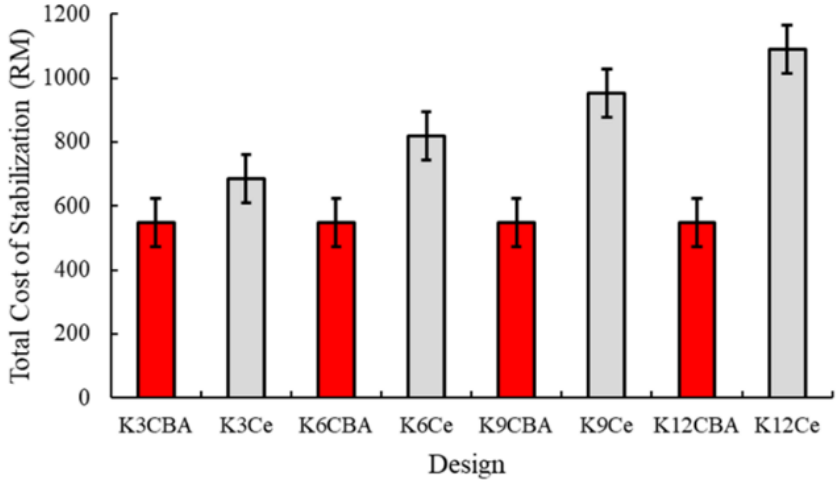

Figure 16. Cost comparison between cement and CBA for each design in this research.

4. Conclusions

A spectrum of laboratory approaches had been implemented to confirm the geotechnical properties of kaolin, CBA, and refined kaolin with different CBA content. The investigation has involved the determination of particle size gradation, consistency limits, proctor behaviors, specific gravity, rate of shear strength improvement of kaolin and kaolin-stabilized CBA soil. According to the data, there are several conclusions and recommendations can be deduced.

1. The kaolin soil particles are dispersive, with a larger proportion of grain size variation, specifically in a smaller size, for instance, 0.063 mm. With the addition of CBA at 6 % to its total mass, the grain size of kaolin has improved significantly, with more than 90 % of particle size detected at 0.15 to 0.3 mm. In addition, the consistency limits of raw kaolin proved to be unfavorable for construction activitie because of its high compressibility behavior. By adding the CBA content from 3 –12 %, the ideal substitution content is deduced at 6 %, validated by its improvement percentage of consistency limit. The LL, PL, and PI values have enhanced 2.76 %, 2.28 %, and 5.00 %, respectively. Analyzing from the standard compaction test, the promising proctor behaviors exhibited by the refined kaolin is also discovered at 6 %, provided by its OMC and MDD value at 9.42 % and 2.53 Mg/m^3. It verifies that at 6 % CBA content, the pozzolanic reaction is effective to occur due to the lower value of OMC or low consumption of water. In addition, a high MDD shows that this refined kaolin has a stabilized soil matrix, even under constant compaction force. The specific gravity of kaolin is improved from 2.64 to 2.30, which yields a difference of 0.3 % or 12.88 %. It expresses a sign of dead load reduction and reinforced compaction characteristic.
2. With the assistance of UCT machine, the influence of constant rate of deformation on the soil specimen is evaluated. For 7 days of cured refined kaolin, the SSI value is recorded from 339.00–578.10 %. Similarly, the 14 days of cured refined kaolin samples present a SSI value ranges from 81.15–296.92 %. Interestingly, the largest SSI is yielded from 7 days cured samples, 7K6CBA while the smallest SSI is produced from 14 days cured samples, 14K3CBA. The above condition is attributed to the rapid grain of shear strength provided by the CAH, which leads to a sudden surge of KSS value when the CBA content is at 6 %. Coherently, the identical design of refined kaolin at

14 days reduces the KSS value drastically to 20.09kPa or a loss of 64.98%. At 14 days of curing, the moisture content inside the soil particle is still in the balancing and drying stage, which restraints certain degree of pozzolanic reaction. Therefore, the strength contributed by the expansion of silica chains link is not sufficient to compromise this situation. Combining all the above-mentioned factors and the reduction of 50 % of CBA content, the 14K3CBA specimen contributes a mild improvement in terms of shear strength. Thus, it is concluded that 6 % CBA content cured at 7 days produces an optimum value of shear strength.

3. The establishment of cost-analysis framework provides a comprehensive set of data by comparing the utilization of conventional material and sustainable substituent. For the sake of aligning experimental program with industry-scale execution, the materials and processes applied in the fieldwork are extracted based on the actual costing in the market. By replicating the current designs, the total cost of stabilization for cement ranges from RM683.63–RM1088.77 for a quantity of 10,000 kg clayey soil. Notably, the total cost of stabilization using CBA is from RM548.77–RM549.13 for the same volume of soil stabilization. Based on this system, it optimizes the cost from 19.73–49.56 %, concerning the replacement ratio of 3 %, 6 %, 9 %, and 12 %, respectively.

4.1. Limitations and Recommendations for Future Research

1. The study assumes that all kaolin and refined kaolin specimens with CBA were prepared homogeneously, with no impurities contained within the specimens. The specimen dimensions were fabricated at 50 mm and 100 mm; therefore, any insignificant variations were disregarded during the execution of the UCT.
2. The entire experiment was conducted at laboratory scale, and the procedures can be conveniently replicated using other types of biomass and industrial materials to verify their effectiveness in soil stabilization.
3. Similarly, incorporating advanced geotechnical approaches, such as triaxial testing, may provide a more comprehensive understanding of the engineering behavior of kaolin, CBA, and refined kaolin with varying proportions of CBA content.
4. A detailed analysis of market price fluctuations, including acquisition costs, transportation costs, currency variations, and international trade policies should be undertaken before replicating the cost analysis results derived from this research.

References

1. Jun Shen, N., Hasan, M., Yong Ler, L. Influence of Crushed Brick Columns on Geotechnical Properties of Expansive Soil. Jurnal Teknologi. 2024. 86(4). DOI: 10.11113/jurnalteknologi.v86.21191.
2. Mochida, Y., Olabamiji, O.J., Kasahara, K. Study on Development of Soil Improvement Pile Method Using Recycled Soil. International Journal of GEOMATE. 2021. 20(82). Pp. 28–33. DOI: 10.21660/2021.82.Gx249.
3. Li, T.T., Wang, K., Sueyoshi, T., Wang, D.D. Esg: Research progress and future prospects. Sustainability (Switzerland). 2021. 13(21). DOI: 10.3390/su132111663.
4. Leknoi, U., Likitlersuang, S. Good practice and lesson learned in promoting vetiver as solution for slope stabilisation and erosion control in Thailand. Land Use Policy. 2020. 99. DOI: 10.1016/j.landusepol.2020.105008.
5. Shen, N.J., Hasan, M. Installation of polyethylene terephthalate (PET) columns to promote the soil-bearing capacity of soft kaolin clay. Journal of King Saud University – Engineering Sciences. 2025. 37(4). Pp. 14. DOI: 10.1007/s44444-025-00011-z. URL: https://link.springer.com/10.1007/s44444-025-00011-z.
6. Sarioğlu, E., Kaynak, H.K. PET Bottle Recycling for Sustainable Textiles. Polyester - Production, Characterization and Innovative Applications. InTech, 2018.
7. Shen, N.J., Hasan, M., Amina, N., Hashim, A. The Influence of Bottom Ash Column in the Geotechnical Properties Enhancement of Soft Clay Soil. 5(5). Pp. 1–13.
8. Shen, N.J., Hasan, M. Sustainable Modification of Stone Column Technique with Polyethylene Terephthalate (PET) Plastic for Strengthening the Expansive Clay. Journal of Sustainable Construction Materials and Technologies. 2025. 10(2). DOI: 10.29187/2458-973X.1186.
9. de Almeida, M. de S.S., Marques, M.E.S., Riccio, M., Fagundes, D. de F., Lima, B.T., Polido, U.F., Cirone, A., Hosseinpour, I. Ground improvement techniques applied to very soft clays: state of knowledge and recent advances. 46(1). Associacao Brasileira de Mecanica dos Solos, 01-01-2023.
10. Hasan, M., Husaini, N.A., Pangee, N. Shear strength of clay reinforced with square and triangular arrangement of group encapsulated bottom ash columns. International Journal of GEOMATE. 2017. 12(33). Pp. 127–133. DOI: 10.21660/2017.33.2608.
11. Hoque, M.I., Hasan, M., Mim, N.J. Shear Strength of Soft Clay Reinforced With Single Encased Stone Dust Columns. Jurnal Teknologi. 2023. 85(5). Pp. 27–34. DOI: 10.11113/jurnalteknologi.v85.19879.
12. Mousavi, S., Wong, L.S. Mechanical behavior of compacted and stabilized clay with kaolin and cement. Jordan Journal of Civil Engineering. 2015. 9(4). Pp. 477–486. DOI: 10.14525/jjce.9.4.3120.
13. Abbaslou, H., Abbaslou, H. Characterization of dispersive problematic soils and engineering improvements: A review Characterization of Dispersive Problematic Soils2016.

14. Karkush, M., Ali, N.A. Electrokinetic enhancement of microbial induced calcite precipitation used in improving the shear strength of soft clay. Smart Geotechnics for Smart Societies. CRC Press, 2023. Pp. 155–163.
15. AL-Ani, S.M.A., Karkush, M.O., Zhussupbekov, A., Al-Hity, A.A. Influence of Magnetized Water on the Geotechnical Properties of Expansive Soil. Lecture Notes in Civil Engineering. 112. Springer Science and Business Media Deutschland GmbH, 2021. Pp. 39–50.
16. Jawad, S., Karkush, M. Shear strength and chemical properties of soft clayey soil treated with magnetized water. Magazine of Civil Engineering. 2023. 124(8). DOI: 10.34910/MCE.124.6.
17. Jun Shen, N., Hasan, M., Md Mashod Fakeh, N. Effect of the waste bottom ash strengthened the problematic clay soil: The use of by-product material. Engineering and Applied Science Research. 2025. 52(2). Pp. 229–239. DOI: 10.14456/easr.2025.20.
18. Baldin, C.R.B., Kawanami, M.Y., Costa, W.G.S., Bordignon, V.R., Luz, C.C. da, Izzo, R.L. dos S. Mechanical properties of a clay soil reinforced with rice husk under drained and undrained conditions. Journal of Rock Mechanics and Geotechnical Engineering. 2023. 15(10). Pp. 2676–2686. DOI: 10.1016/j.jrmge.2023.02.022.
19. Vakili, A.H., Salimi, M., Keskin, İ., Jamalimoghadam, M. A systematic review of strategies for identifying and stabilizing dispersive clay soils for sustainable infrastructure. 239. Elsevier B.V., 01-06-2024.
20. Azimi, M., Soltani, A., Mirzababaei, M., Jaksa, M.B., Ashwath, N. Biopolymer stabilization of clayey soil. Journal of Rock Mechanics and Geotechnical Engineering. 2024. 16(7). Pp. 2801–2812. DOI: 10.1016/j.jrmge.2023.12.020.
21. Herrmann, H., Bucksch, H. Ground Improvement Technique. Dictionary Geotechnical Engineering/Wörterbuch GeoTechnik. 2014. (2). Pp. 638–638. DOI: 10.1007/978-3-642-41714-6_72392.
22. Almuaythir, S., Zaini, M.S.I., Hasan, M., Hoque, M.I. Stabilization of expansive clay soil using shells based agricultural waste ash. Scientific Reports. 2025. 15(1). DOI: 10.1038/s41598-025-94980-5.
23. Hashim Mohammed, S., Saeed, K.A., Ibrahim Al Shaikhli, H. Evaluation of the strength and microstructural characteristics of stabilized organic clay soil. Case Studies in Chemical and Environmental Engineering. 2024. 9. DOI: 10.1016/j.cscee.2024.100647.
24. Karkush, M., Ali, S.D. Durability of Gypseous Soil Stabilized with Nano-silica under Environmental Conditions. Jordan Journal of Civil Engineering. 2025. 19(1). Pp. 164–178. DOI: 10.14525/JJCE.v19i1.12.
25. Azeem, M., Arockiam Jeyasundar, P.G.S., Ali, A., Riaz, L., Khan, K.S., Hussain, Q., Kareem, H.A., Abbas, F., Latif, A., Majrashi, A., Ali, E.F., Li, R., Shaheen, S.M., Li, G., Zhang, Z., Zhu, Y.G. Cow bone-derived biochar enhances microbial biomass and alters bacterial community composition and diversity in a smelter contaminated soil. Environmental Research. 2023. 216. DOI: 10.1016/j.envres.2022.114278.
26. Baroutkoob, A., Haghighi, M., Hajabbasi, M.A. Amending clayey and sandy soils with nano - bio phosphorous for regulating tomato growth, biochemical, and physiological characteristics. Scientific Reports. 2024. 14(1). DOI: 10.1038/s41598-024-76389-8.
27. Norrrahim, M.N.F., Nurazzi, N.M., Knight, V.F., Farid, M.A.A., Andou, Y., Jenol, M.A., Naveen, J., Asyraf, M.R.M., Rani, M.S.A. Cow bone as reinforcement fillers in polymer composites for structural applications. Polymer Composites Derived from Animal Sources. Elsevier, 2024. Pp. 277–293.
28. Awoyemi, T.J., Ibedu, K.E., Kaura, J.M., Lawan, A. Strength-Durability Properties and Microstructural Analysis of Concrete Containing Cow Bone Ash and Bentonite. Fudma Journal of Sciences. 2023. 7(5). Pp. 39–49. DOI: 10.33003/fjs-2023-0705-1900.
29. Oluniyi, P., Kayode, O., Kabiru, Y. Effects of Cow Bone Ash on Chemical and Geotechnical Properties of Lateritic Soil. World Journal of Engineering Research and Technologies. 2023. 9(1). Pp. 84–92.
30. Khalid, Z., Sun, L., Lv, G., Lin, S., Wei, B., Duan, Y., Liu, X., Jiang, X. Utilization of cow bone waste and calcium oxide for the solidification and stabilization of MSWI fly ash: Towards sustainable practices. Process Safety and Environmental Protection. 2024. 190. Pp. 829–841. DOI: 10.1016/j.psep.2024.08.095.
31. Yilmazoğlu, M.U. Effect of bone ash and rice husk ash on the unconfined compressive strength of silt soil. Kastamonu University Journal of Engineering and Sciences. 2024. DOI:10.55385/kastamonujes.1470525.
32. Parihar, N.S., Gupta, A.K. Stabilization of Expansive Soils Using Non-conventional Waste Stabilizers: A Review. Indian Geotechnical Journal. 2024. 54(3). Pp. 971–997. DOI: 10.1007/s40098-024-00923-8.
33. Jamhuri, S.S., Hasan, M., Nik Aziz, N.N.A. Utilization of Silica Fume and Clamshell Ash as Stabilization Materials for Kaolin Clay. Jurnal Teknologi (Sciences & Engineering). 2025. 87(3). Pp. 587–594. DOI: 10.11113/jurnalteknologi.v87.23100.
34. Shen, N.J., Hasan, M. Transforming waste into stability: improving the soft clay soil with polyethylene terephthalate (PET) column as a sustainable solution. Journal of Engineering and Applied Science. 2025. 72(1). Pp. 52. DOI: 10.1186/s44147-025-00620-0.
35. Abdulwahab, R., Ikotun, B.D., Raheem, A.A., Adetoro, E.A., Salihu, R., Oribamise, O.A. Effects of cow bone ash as a partial replacement of cement in the production of concrete. Journal of Building Pathology and Rehabilitation. 2025. 10(2). DOI: 10.1007/s41024-025-00627-3.
36. Ayoola, A., Philip, A. Stabilization of Lateritic Soil for Road Application Using Lime and Cow Bone Ash. Journal of Engineering Research and Reports. 2023. 25(6). Pp. 109–121. DOI: 10.9734/jerr/2023/v25i6927.
37. Hasan, M., Samadhiya, N.K. Ground Improvement by Using Floating Granular Piles: Experimental Studies and Numerical Investigations. 187(January). Springer Singapore, 2022. 465–475 p. ISBN: 9789811656682.
38. Hasan, M. Bin, Marto, A.B., Hyodo, M. Strength of Soft Clay Reinforced with Single and Group Bottom Ash Columns. The 2014 World Congress on Civil, Environmental & Materials Research (ACEM 2014). 2014.
39. Bozyigit, I., Bulbul, F., Alp, C., Altun, S. Engineering Science and Technology , an International Journal Effect of randomly distributed pet bottle strips on mechanical properties of cement stabilized kaolin clay. Engineering Science and Technology, an International Journal. 2021. 24(5). Pp. 1090–1101. DOI: 10.1016/j.jestch.2021.02.012.
40. Hasan, N.M., Yee, M. Stabilization of Soft Clay Soil by the Reinforcement of Single Bottom Ash Silica Fume (BASF) Column. Journal of Rehabilitation in Civil Engineering. 2024. 12(3). Pp. 117–131. DOI: 10.22075/jrce.2024.32181.1925.
41. Okeyinka, O.M., Olutoge, F.A., Okunlola, L.O. Durability Performance of Cow-Bone Ash (CBA) Blended Cement Concrete in Aggressive Environment. International Journal of Scientific and Research Publications (IJSRP). 2018. 8(12). DOI: 10.29322/ijsrp.8.12.2018.p8408.

42. Adetayo, O.A., Umego, O.M., Faluyi, F., Odetoye, A.O., Bucknor, A.O., Busari, A.A., Sanni, A. Evaluation of Pulverized Cow Bone Ash and Waste Glass Powder on the Geotechnical Properties of Tropical Laterite. DOI: 10.1007/s12633-021-00999-4/Published.
43. Shen, N.J., Hasan, M., Anuar, N.N. Construction of coconut shell column for the enhancement of expansive soil. Magazine of Civil Engineering. 2024. (8). Pp. 17. DOI: 10.34910/MCE.132.4.
44. Noor, N., Nik Aziz, A., Hasan, M., Syamsul, M., Zaini, I., Nor, S., Mohamed, A., Winter, M.J., Pahang, M., Abdullah, A.-S., Tun, P., Yaakob, K. Hydrated Lime and Cockle Shell Ash: A Sustainable Approach to Soft Kaolin Clay Improvement. Journal of Advanced Research in Applied Mechanics Journal homepage. 2026. 138. Pp. 27–45. DOI: 10.37934/aram.138.1.2745.
45. Soyemi, O.B., Soretire, A. Assessment of the Performance of Crushed Cow Bones as a Partial Replacement for Coarse Aggregate for Concrete. Saudi Journal of Civil Engineering. 2024. 8(03). Pp. 49–57. DOI: 10.36348/sjce.2024.v08i03.001.
46. Ghavami, S., Jahanbakhsh, H., Saeedi Azizkandi, A., Moghadas Nejad, F. Influence of sodium chloride on cement kiln dust-treated clayey soil: strength properties, cost analysis, and environmental impact. Environment, Development and Sustainability. 2021. 23(1). Pp. 683–702. DOI: 10.1007/s10668-020-00603-6.
47. Tripathi, A., Saraf, S.S., Bijwe, A.R. Analysis and Comparision of Cost of Stabilized Soil Using E-Waste and Cement. International Research Journal of Engineering and Technology. 2021. 8(8). Pp. 1557–1562.
48. Assi, L., Carter, K., Deaver, E. (Eddie), Anay, R., Ziehl, P. Sustainable Concrete: Building a Greener Future. Journal of Cleaner Production. 2018. 198. Pp. 1641–1651. DOI: 10.1016/j.jclepro.2018.07.123.
49. Pongsivasathit, S., Horpibulsuk, S., Piyaphipat, S. Assessment of Mechanical Properties of Cement Stabilized Soils. Case Studies in Construction Materials. 2019. 11. DOI: 10.1016/j.cscm.2019.e00301.

Information about the authors:

Ng Jun Shen,
ORCID: https://orcid.org/0000-0002-6113-1237
E-mail: jshenng98@gmail.com

Muzamir Hasan,
ORCID: https://orcid.org/0000-0002-2700-236X
E-mail: muzamir@umpsa.edu.my

Yap Wan Er,
E-mail: muzamir@umpsa.edu.my

Md. Ikramul Hoque,
ORCID: https://orcid.org/0000-0002-7160-3015
E-mail: ikramul3300@becm.kuet.ac.bd

Received 02.08.2025. Approved after reviewing 17.10.2025. Accepted 18.10.2025.

Magazine of Civil Engineering

ISSN 2712-8172

journal homepage: http://engstroy.spbstu.ru/

Research article

UDC 69.07

DOI: 10.34910/MCE.139.8

Structural behavior of ultra-high performance concrete beams with different rebar and fiber reinforcement ratios

Y.Q.Y. Abuizeih , ***M.M. Tamov*** ✉

Kuban State Technological University, Krasnodar, Russian Federation

✉ *murat.tamov@gmail.com*

Keywords: ultra-high performance concrete, steel fibers, flexural behavior, crack control, hybrid reinforcement

Abstract. This experimental study comprehensively analyzes the flexural performance of ultra-high performance concrete (UHPC) beams with combined rebar and fiber reinforcement. The study examines the synergistic effects of longitudinal reinforcement ratio μ_s (varying from 0.31 to 5.13 %), steel fiber content (0–2 % by volume), and fiber geometry (comparing straight and wavy shapes) through testing of seventeen beam specimens under four-point bending conditions. Results demonstrate that steel fiber incorporation significantly enhances structural performance by improving crack control, with maximum crack widths remaining below 0.25 mm at service load levels (65–70 % of ultimate capacity). The benefits of fiber reinforcement show strong dependence on longitudinal rebar reinforcement ratio, with maximum strength improvements reaching 47 % for beams containing 2 % fibers at the lowest reinforcement ratio (0.31 %). Comparative analysis reveals the superior performance of wavy fibers, which provide up to 25 % greater strength enhancement compared to straight fibers in lightly reinforced specimens. The study identifies two distinct failure modes: abrupt failure after crack localization in lightly reinforced beams (μ_s ≤ ≤ 0.87 %) versus gradual strength gain at post-localization stage in highly reinforced specimens (μ_s ≥ ≥ 2.56 %). Fiber effectiveness diminishes significantly in highly reinforced beams due to rebar dominance and fiber distribution challenges in congested tensile zones. These findings provide quantitative evidence for optimizing fiber-rebar combinations in UHPC design, particularly highlighting the importance of fiber geometry selection and dispersion quality. The research establishes clear relationships between reinforcement parameters and structural performance, offering practical guidance for engineers while identifying key areas for future investigation, including advanced fiber dispersion techniques and hybrid reinforcement strategies for improved structural efficiency.

Citation: Abuizeih, Y.Q.Y., Tamov, M.M. Structural behavior of ultra-high performance concrete beams with different rebar and fiber reinforcement ratios. Magazine of Civil Engineering. 2025. 18(7). Article no. 13908. DOI: 10.34910/MCE.139.8

1. Introduction

Ultra-high-performance concrete (UHPC) is an advanced cementitious composite known for its exceptionally high strength, ductility, and durability [1]. The addition of steel fibers to the UHPC matrix further enhances its tensile properties and enables ductile behavior. Over the past two decades, UHPC has emerged as a significant innovation in concrete technology, offering outstanding mechanical performance and strong resistance to environmental deterioration [2]. To enable broader implementation, it is essential to thoroughly investigate and understand the structural performance of UHPC elements under various loading and environmental conditions.

The fibers bridge developing cracks in UHPC and limit their width, leading to the formation of numerous closely spaced, fine cracks, a phenomenon often referred to as multiple cracking [3, 4]. This behavior enhances stress redistribution across the beam, improves ductility, and contributes to greater overall durability by limiting the ingress of aggressive agents. As the applied load approaches the ultimate level, one or more cracks begin to open significantly more than the rest, marking the onset of crack localization [5, 6]. This occurs due to intensive fiber pull-out from the concrete matrix in the affected sections. At this stage, the longitudinal reinforcement typically yields at the locations where it intersects these dominant cracks. Thus, the reinforcement parameters are a key factor determining the behavior of UHPC beams under loading. Investigation of beam behavior under different combinations of bar and fiber reinforcement ratios is essential for developing more efficient and structurally reliable UHPC beam designs [7].

The influence of longitudinal reinforcement on the behavior of UHPC beams has been examined in several experimental studies [5, 8–15]. In the tests conducted by Li [8], the ductility index f_p/f_y as well as the strength and stiffness of UHPC beams, increased with the reinforcement ratio μ_s up to 5 %, which significantly exceeds the maximum permissible value specified by design codes. Somewhat different results were obtained by Chen et al. [13], who observed that, within a similar range of μ_s, ductility was highest in beams with intermediate reinforcement ratios. In the experiments by Zhang et al. [16], at a constant fiber volume fraction μ_{fv} = 2 %, the ductility of a beam with μ_s = 2.83 % was 27.6 % less than that of a beam with μ_s = 1.48 %.

The addition of steel fibers leads to a significant increase in the bearing capacity of UHPC beams. In the study by Yoo & Yoon [10], fiber reinforcement μ_{fv} = 2 % increased the beam strength by 27–54 % and reduced the ductility index by 13–73 %. Khalil & Tayfur [17] observed up to a 27 % increase in capacity for beams reinforced with crimped and hooked steel fibers at μ_{fv} = 2 %. The strength gain from fibers tends to be more pronounced in beams with a lower amount of longitudinal rebar reinforcement [18]. In the work of El-Din et al. [19], the inclusion of fibers at μ_{fv} = 3 % resulted in a 32.9 % increase of strength for beams with μ_s = 1.33 %, and only 8.1 % for beams with μ_s = 5.36 %.

However, varying the fiber volume fraction μ_{fv} does not always have a significant effect on the strength of UHPC beams [20–22]. For example, in [16], when μ_{fv} was increased from 1.5 to 3.0 %, the maximum load increased by 11.87 % for the beams with the reinforcement ratio of 2.33 %. In the experiments by Feng et al. [23], an increase in μ_{fv} from 2 to 3 % had a noticeable positive effect on the strength of the beams only when μ_s = 1 и 2.9 %, whereas at μ_s = 4.8 and 7.1 %, the beams with different fiber contents failed under nearly identical loads. This is explained by the fact that the contribution of the fibers to the strength of the beam becomes insignificant compared to the contribution of the reinforcing bars [21]. In addition, in the case of beams with high μ_{fv}, it is likely that the researchers were unable to achieve uniform fiber distribution. From this, it can be concluded that using an effective fiber dispersion technology is a crucial condition for ensuring their contribution in the bending strength of UHPC beams. In addition, stirrups can prevent the proper fiber distribution during casting of beams [3].

Several studies have focused on evaluating the effectiveness of various fiber types used as dispersed reinforcement of UHPC beams. The study of Khalil et al. [17] showed that using twisted fibers and increasing the length of straight fibers had little effect on the strength and stiffness of the beams. In the experimental study of Yoo & Yoon [10], the variable parameter in the series of UHPC beams was the fiber length, while the fiber volume fraction was kept constant at μ_{fv} = 2 %. Strength, stiffness, and the energy absorption capacity of beams increased with fiber length up to 19.5 mm. Further increasing the fiber length to 30 mm reduced its effectiveness, which is attributed to the decreased number of fibers bridging the cracks. The authors [17, 10] note that neither the presence of fibers in the concrete mix nor their shape or concentration has a significant impact on the cracking load of beams or the corresponding deflections.

The experimental database of flexural tests on UHPC beams requires both qualitative and quantitative expansion. Currently, it does not allow for a clear understanding of the influence of fiber and rebar reinforcement parameters behavior of beams. Conclusions drawn by different researchers in this area are often contradictory. This is due to the complex nature of the stress-strain state in the tensile zone of

UHPC beams, as well as the variability in UHPC strength characteristics, which depend not only on the mix composition but also on the quality of fiber distribution. In most existing studies, UHPC beams were reinforced with straight fibers. Meanwhile, dispersed reinforcement of UHPC beams with wavy fibers – widely used in Russia and Belarus and known for significantly enhancing the tensile strength of UHPC [24, 25] – is of particular interest. In most studies, the effects of μ_{fv} and μ_s on beam performance are considered separately. However, in the few studies where both parameters were varied, it was clear that the influence of one depended on the value of the other [16, 22, 26]. Tests on beams with low μ_s are rare, yet it is precisely under low reinforcement conditions that the properties of UHPC have the most influence. The aim of this study was to experimentally assess the influence of bar and fiber reinforcement ratios varying in wide ranges, as well as fiber type, on the flexural behavior of UHPC beams.

2. Methods

According to the experimental plan, seventeen UHPC beams were tested, divided into four series based on the value of μ_s (Table 1). Within each series, μ_{fv} and fiber type were varied. Each series included specimens without fiber reinforcement (specimens F0-…). Beams in Group 4, with a high reinforcement ratio, were tested to investigate the behavior under load and failure characteristics of UHPC beams at μ_s values close to or exceeding the limits of balanced sections $\left(\xi \geq \xi_R\right)$.

Beams No. 1–15 had a rectangular cross-section of 100 × 200 mm (Fig. 1b). Beams No. 16 and 17 were designed with a flange in the tensile zone due to the need to enable placement of a large amount of longitudinal reinforcement (Fig. 1c).

The longitudinal reinforcement of the beams consisted of 2 to 6 bars of A500 reinforcement with diameters ranging from 6 to 14 mm (Fig. 1b, 1c). Dispersed reinforcement of UHPC beams in most of previous studies consisted of straight fibers (SFs), with hooked and twisted fibers used only in rare cases. At the same time, dispersed reinforcement of UHPC beams with wavy fibers (WFs), which have become widely used in Russia and Belarus, is of particular interest. Therefore, samples with WFs produced by JSC “BMZ” (Zhlobin, Belarus) were included in the experimental plan.

Table 1. The experimental program for flexural testing of UHPC beams

Group	Beam ID	μ_s (%)	μ_{fv} (%)	Fiber shape	R_b (MPa)	R_{fel} (MPa)	M_p (kNm)
1	F0-030	0.31	0	–	115	–	7.6
	SF1-030		1	SF	130.5	4.25	11
	SF2-030		2	SF	133.2	9.5	16.6
	WF1-030		1	WF	135	6.94	14
	WF 2-030		2	WF	140.4	12	20.1
2	Ф0-085	0.87	0	–	115	–	18.3
	SF1-085		1	SF	130.5	4.25	20.16
	SF2-085		2	SF	133.2	9.5	26.22
	WF1-085		1	WF	135	6.94	22.75
	WF2-085		2	WF	140.4	12	30.8
3	F0-250	2.56	0	–	115	–	41.1
	SF1-250		1	SF	130.5	4.25	46.4
	SF2-250		2	SF	133.2	9.5	45.9
	WF1-250		1	WF	135	6.94	47.4
	WF2-250		2	WF	140.4	12	50.14
4	F0-500	5.13	0	–	115	–	66.2
	WF1.5-500		1.5	WF	137	9.4	74.5

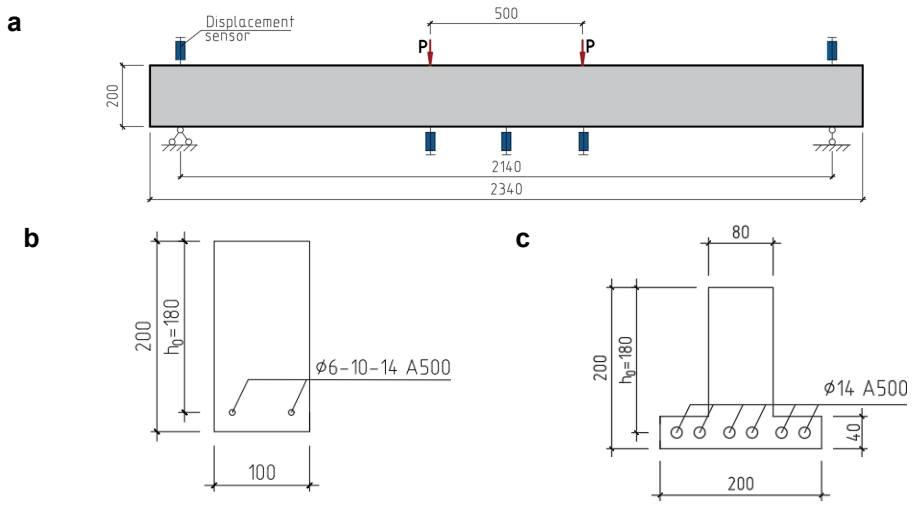

Figure 1. Side view of the beams, their loading scheme (a), cross-sections of rectangular (b), and T-shaped beams (c).

The UHPC mixtures included Portland cement 600-DO (CEM I 52.5 N), condensed silica fume MK-85, a blend of coarse (fineness modulus 2.56) and fine (fineness modulus 0.78) sand, and a polycarboxylate-based superplasticizer [24]. Steel brass-coated straight and WFs with a diameter of 0.4 mm and length of 14 mm, and a tensile strength of 2800 MPa were used as dispersed reinforcement. During casting of the beams, the concrete was placed sequentially along the length of the formwork and consolidated using mechanical vibration to ensure adequate compaction and a uniform distribution of the steel fibers throughout the cross-section. The compressive strength of UHPC was determined by testing cubes (70 × 70 × 70 mm) and prisms (100 × 100 × 400 mm). For UHPC containing fibers, the tensile strength values R_{Fel} were evaluated following the SP 360.13330 procedure through three-point bending tests on notched prisms with dimensions 150 × 150 × 550 mm. The obtained concrete strength characteristics of the beams are given in Table 1.

The beams were subjected to two point loads, spaced 500 mm apart and symmetrically positioned about the midpoint (Fig. 1a). The applied load was controlled by a gauge installed under one support of the beam. Deflections were measured using strain gauge displacement sensors positioned at five points – at the beam midpoint, at the load application points, and at the supports (Fig. 1a). Local concrete strains were measured with strain gauges, and average strains in the tensile zone were recorded using LVDT sensors (Fig. 2).

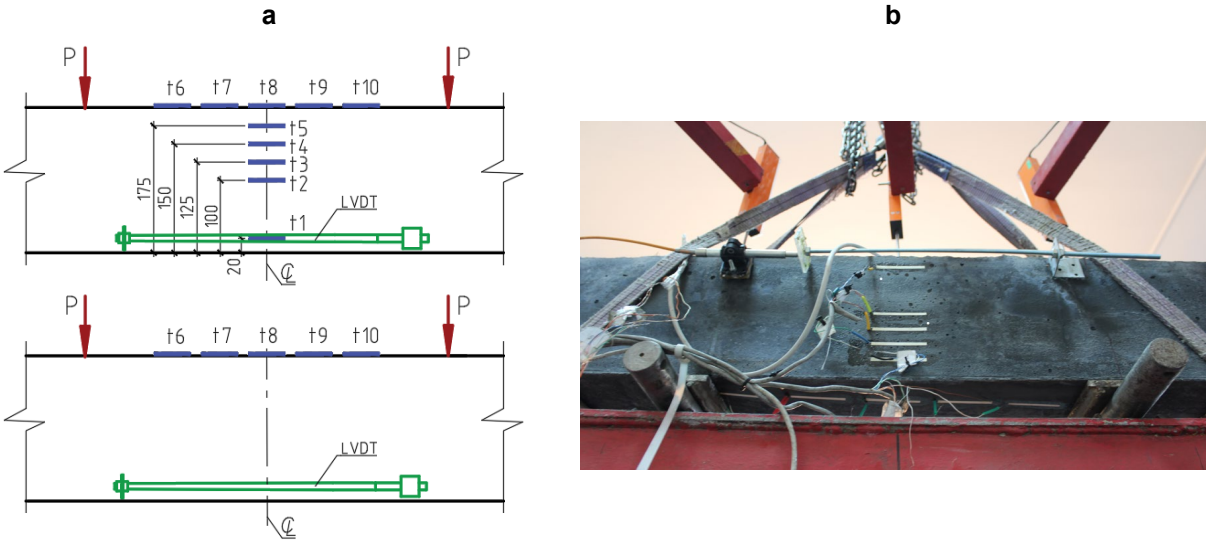

Figure 2. Investigated zone of pure bending (the test load is applied upwards): sensor layout diagram (a) and its actual implementation (b)

3. Results and Discussion

Strain gauge readings recorded during the tests indicate that the failure of beams in Groups 1–3 occurred due to crushing of the concrete in the compressed zone after yielding of the longitudinal

reinforcement. In fiber-reinforced UHPC beams from Groups 1 (μ_s = 0.31 %) and 2 (μ_s = 0.87 %), one or several of the flexural cracks began to open more intensively than the others at later loading stages – this marked the onset of the previously described strain localization in the tensile zone, caused by progressive fiber pull-out. Near failure, the critical crack in these beams extended to a depth of up to 0.9 *h*. In fiber-reinforced UHPC beams of Group 3 (μ_s = 2.56 %), failure also occurred in a sections with localized cracks; however, its depth did not exceed 0.7 *h*. In both beams from Group 4 (with and without fibers), as expected, the reinforcement did not reach yielding stress.

From the analysis of the moment–deflection curves (Fig. 3), the following conclusions can be drawn:

1. The presence of fiber reinforcement influences the performance of the beams for all the studied values of μ_s. A consistent effect observed across all four groups is that the addition of fibers increases both the strength and stiffness of the beams.

2. The most pronounced impact of fiber addition was observed in beams with a low μ_s (Group 1). The deflections of the fiber-reinforced concrete beams at the point of failure were approximately 3–4 times smaller than that of the beam F0-030 without fibers.

3. In Groups 1 (μ_s = 0.31 %) and 2 (μ_s = 0.85 %), increasing μ_{fv} and/or replacing straight fibers with wavy ones led to an upward shift of the curves – i.e., an increase in strength and stiffness. In contrast, in Group 3 (μ_s = 2.56 %), the deformation curves for beams reinforced with different quantities and types of fibers nearly coincided.

4. In Group 3 (μ_s = 2.56 %), beams with fibers exhibited continued growth in moment capacity beyond crack localization. In Group 2 (μ_s = 0.87 %), this post-cracking capacity gain was minimal, and in Group 1 (μ_s = 0.31 %), strength of beams dropped immediately after crack localization. Thus, for beams with μ_s = 0.31 % and 0.87 %, the load at which crack localization occurred was the failure load. In these beams, the tensile force carried by the fiber-reinforced concrete exceeded the capacity of the rebar reinforcement in its strain-hardening stage.

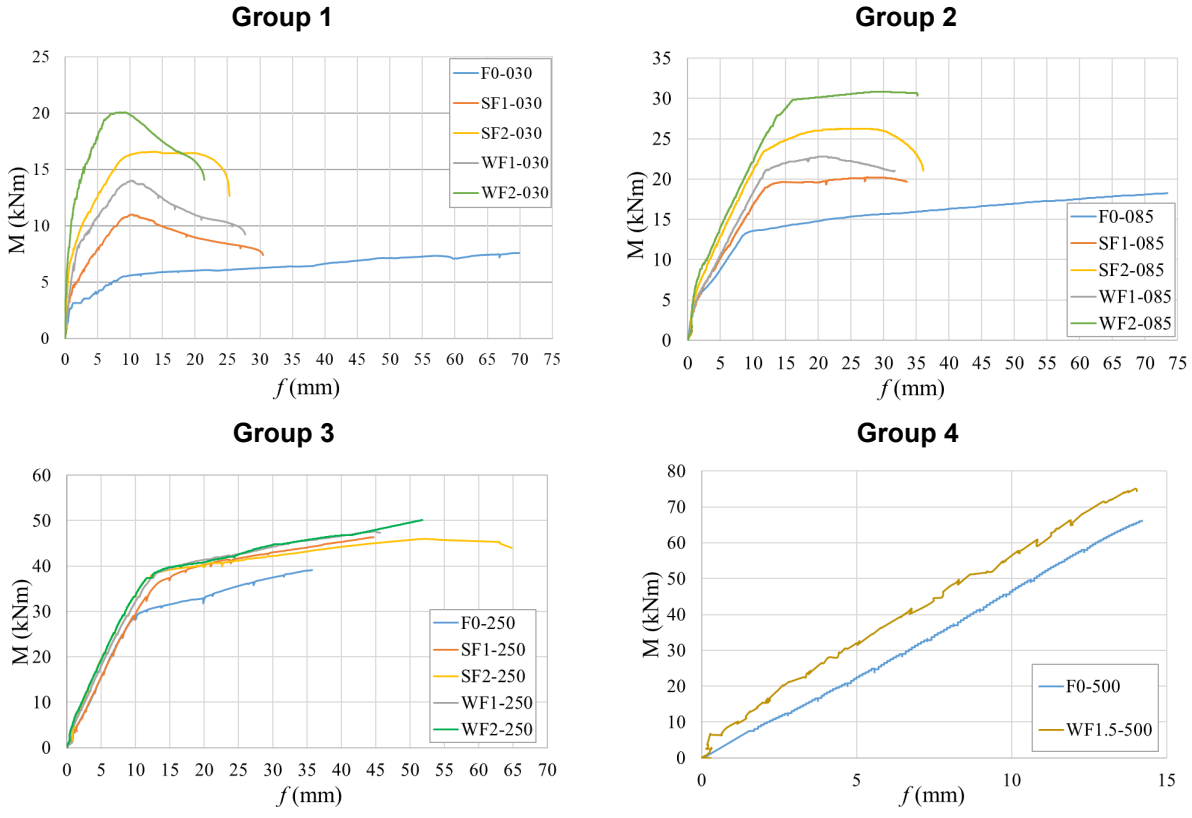

Figure 3. Moment-deflection diagram of beams.

Within Groups 1 (μ_s = 0.31 %), 2 (μ_s = 0.87 %), and 4 (μ_s = 5.1 %), the cracking moment M_{crc} increased with the fiber volume fraction μ_{fv}. In Group 3, however, no such trend was observed based on the obtained M_{crc} values. It should be noted that the beams were inspected only during the constant-load holding phase, which may have led to inaccuracies in identifying the exact moment of crack initiation. The most significant influence of fibers on the cracking load was observed in Group 4 (over-reinforced beams), where the difference in M_{crc} values between beams with and without fibers reached a factor of four.

The width of critical (localized) cracks increased at the same rate as that of other cracks prior to the onset of rapid widening (see Fig. 4). In other words, until the ultimate stage was reached, the critical cracks did not stand out from the rest. In many cases, the formation of the critical crack occurred during the final stages of loading.

Up to the localization of critical cracks, i.e., practically until the ultimate load capacity was reached, crack openings remained small – no more than 0.25 mm. Thus, the results of our tests indicate that under service loads of about 65–70 % of the ultimate loads, the crack width in UHPC beams will not exceed the permissible limits of 0.3–0.4 mm adopted in design codes.

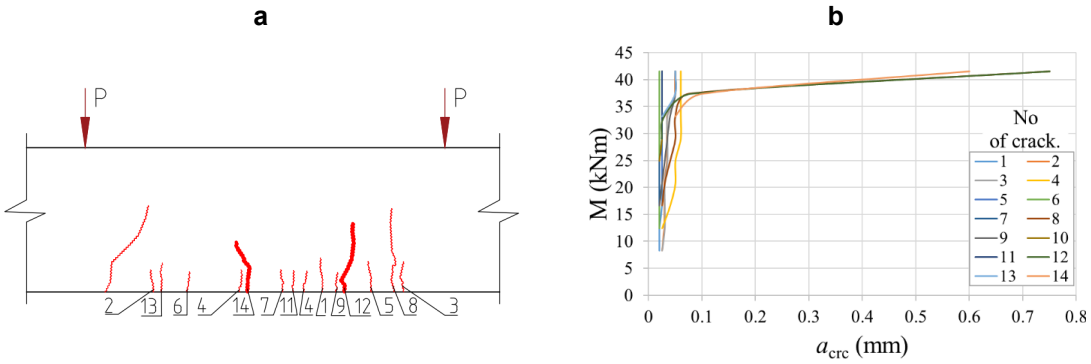

Figure 4. Crack pattern (a) and crack opening diagram (b) for beam SF2-250.

Concrete strains on the compressed side of the beams were measured at five points uniformly distributed within the pure bending zone over a distance of 300 mm. In beams from Groups 3 and 4, as well as in plain UHPC specimens from Groups 1 and 2, concrete strains at failure, $\varepsilon_{b,\max}^{ult}$ were about (260–370) 10^{-5} and mostly significantly exceeded the ultimate compressive strain ε_0 of UHPC determined from prism tests. Moreover, the difference between the average strain ε_b^{-ult} and the maximum strain $\varepsilon_{b,\max}^{ult}$ did not exceed 20 %, which is consistent with results reported by other researchers for beams made of conventional normal strength concrete. In fiber-reinforced UHPC beams from Groups 1 and 2, which failed immediately after the formation and opening of a localized crack, the measured compression strains showed greater variability $\varepsilon_{b,\max}^{ult}$ ranged from (60–310)·10^{-5}, and the difference between ε_b^{-ult} and $\varepsilon_{b,\max}^{ult}$ varied between 5 and 100 %. This scatter is due to the significant influence of the critical crack on the compressed concrete strain in the section. Higher strain values were recorded when the critical crack was located in the same section as the strain gauge (see Fig. 5). In other sections, compressive strains were significantly lower.

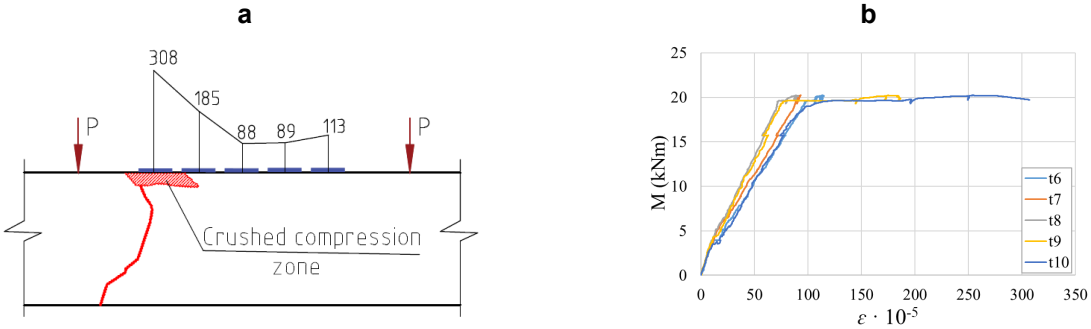

Figure 5. Ultimate values (a) and diagram of the strains on the compressed face (b) of beam SF1-085.

Fig. 6 shows examples of strain profiles of the cross-sections constructed for different loading stages based on readings from strain gauges and LVDT sensors. As can be seen, for beams from all groups, the strains correspond to the assumption of plane sections, including at the ultimate stage. During the test of beam SF1-030, the critical crack formed in the area covered by both LVDT sensors and strain gauges. This made it possible to obtain the strain profile in the section with the critical crack at all stages of the beam behavior. The strain profile at the maximum moment of 11 kNm (development of the critical crack) is shown by the gray line in Fig. 6 SF1-030, while the dashed blue line represents the strain profile at the moment of failure. As loading progresses, the depth of the compressed zone in all beams decreases, with a significantly higher rate observed after the reinforcement yields.

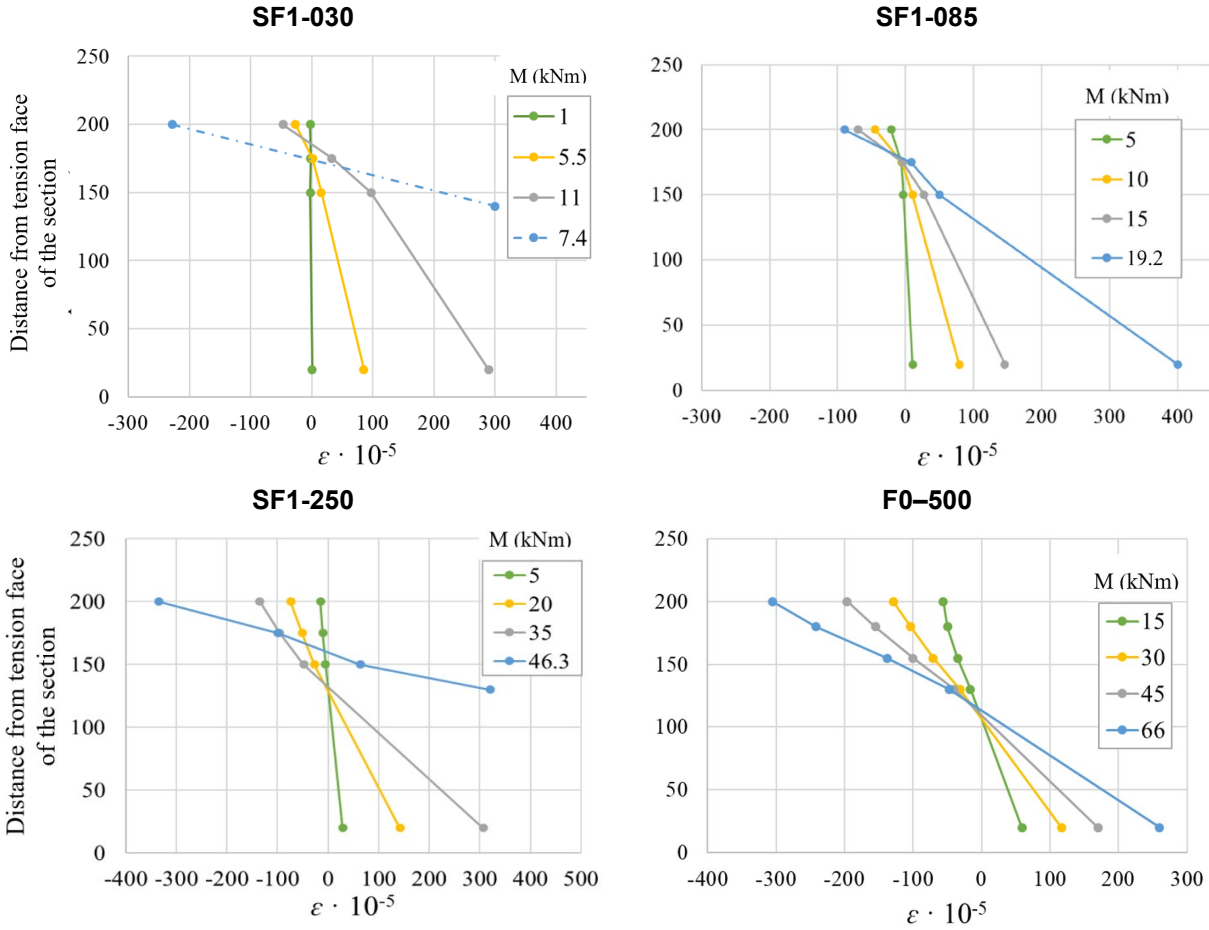

Figure 6. Strain profiles in cross-sections of the beams SF1-030, SF1-085, SF1-250, F0-500.

The beam flexural strength M_p is defined as the value of the bending moment corresponding to the peak point on the moment–deflection diagrams (Table 1, Fig. 3). For clarity, the beam strength values are presented in a summarized bar chart in Fig. 7.

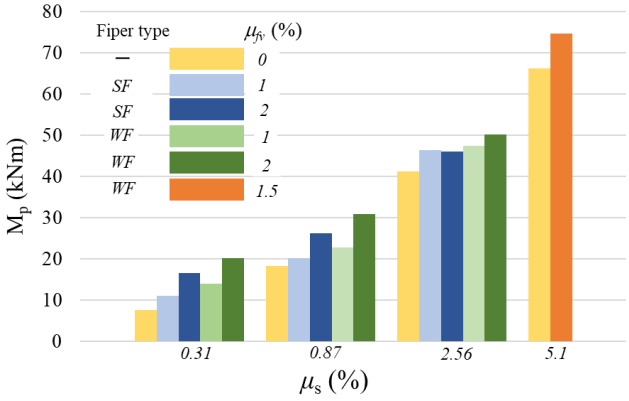

Figure 7. Relationship between beam flexural strength and fiber content and longitudinal reinforcement ratio.

The addition of fibers to the UHPC mix increased the flexural strength of beams across all groups. However, the strength gain from increasing fiber content decreases as the longitudinal reinforcement ratio increases. In Group 1 (μ_s = 0.31 %), the difference in beam strength between fiber volume fractions μ_{fv} = 1 и 2 % was approximately 47 %. At μ_s = 0.87 %, increasing μ_{fv} led to a strength increase of up to 32 %, while at μ_s = 2.56 %, the effect was negligible. The lack of influence of μ_{fv} on the strength of beams with high reinforcement content has also been reported in several other studies. For example, in experiments by Feng et al. [23], increasing the content of straight fibers from 2 до 3 % did not result in any significant effect on beams with μ_s ≥ 2.9 %. Researchers attribute this to the possibility that at high reinforcement ratios, the uniform distribution of fibers in the tensile zone may be hindered due to congestion caused by the reinforcing bars.

WFs enhance the flexural strength of UHPC beams more effectively than SFs. In Groups 1 (μ_s = 0.31 %) and 2 (μ_s = 0.87 %), replacing SFs with WFs resulted in a 12–25 % increase in beam strength. In contrast, in Group 3 (μ_s = 2.56 %), the influence of fiber shape on beam strength was almost negligible. As with the effect of increasing μ_{fv} in this group, the potential gain due to using WFs might have been reduced by poor distribution in the tensile region, where the high reinforcement ratio limited available space.

4. Conclusions

This study experimentally evaluated the influence of longitudinal reinforcement ratio, fiber content, and fiber shape on the flexural performance of UHPC beams. Based on the results, the following conclusions can be drawn:

1. Crack localization was the governing failure mechanism in under-reinforced beams, while in over-reinforced beams, failure occurred by concrete crushing without yielding of steel rebars. Beams with low reinforcement ratios failed abruptly after crack localization, while highly reinforced beams exhibited post-localization strength gains.
2. Width of cracks in fiber-reinforced UHPC beams remained small (≤ 0.25 mm), ensuring serviceability under typical working loads (65–70 % of ultimate capacity).
3. The addition of steel fibers enhanced the flexural strength and stiffness of UHPC beams across all reinforcement levels. In beams with low reinforcement ratios, increasing fiber content from 1 to 2 % resulted in up to a 47 % strength increase. In highly- and over-reinforced beams, the contribution of fibers was reduced due to rebar dominance and potential non-uniform fiber distribution in congested tensile zones.
4. WFs outperform SFs in enhancing beam strength, especially at low reinforcement levels, with gains of up to 25 %.

The results highlight the need to optimize the balance between rebar and fiber reinforcement to achieve desired performance in UHPC beams. Future research should address fiber dispersion techniques and hybrid reinforcement strategies to maximize synergies between these components.

References

1. Khaleel, B.A., Dawood, E.T. Evolution of ultra high performance concrete using hybrid fibers: a review. Discover Concrete and Cement. 2025. 1. Article no. 2. DOI: 10.1007/s44416-025-00001-z
2. Graybeal, B.A. Behavior of Field-Cast Ultra-High Performance Concrete Bridge Deck Connections under Cyclic and Static Structural Loading. FHWA Report no. FHWAHRT-11-023. Washington, 2010. URL: https://rosap.ntl.bts.gov/view/ dot/ 957/dot_957_DS1.pdf (date of application: 21.01.2026).
3. Cai, Z., Duan, X., Liu, L., Lu, Z., Ye, J. Reinforced ultra-high performance concrete beam under flexure and shear: Experiment and theoretical model. Case Studies in Construction Materials. 2024. 20. Article no. e02647. DOI: 10.1016/j.cscm.2023.e02647
4. Zhu, Y., Zhang, Y., Yuan, X., Hou, C. An Adaptive Crack Width Prediction for Flexural Steel Reinforced UHPC Beams. I International Journal of Concrete Structures and Materials. 2023. 17. Article no. 73. DOI: 10.1186/s40069-023-00628-x
5. Shao, Y., Billington, S.L. Utilizing full UHPC compressive strength in steel reinforced UHPC beams. International Interactive Symposium on Ultra-High Performance Concrete Papers. 2019. 2(1). Pp. 1–9. DOI: 10.21838/uhpc.9699
6. Helou, R.G., Graybeal, B.A. Flexural Behavior and Design of Ultrahigh-Performance Concrete Beams. Journal of Structural Engineering. 2022. 148(4). Pp. 1–20. DOI: 10.1061/(ASCE)ST.1943541X.0003246
7. Tamov, M.M., Abuizeih, Y.Q.Y. The Effect of the Longitudinal Reinforcement Ratio on the Behavior of Ultra-High Performance Fibre-Reinforced Concrete Beams. Scientific Works of the Kuban State Technological University. 2025. 2. Pp. 56–71. DOI: 10.26297/2312-9409.2025.2.6

8. Li, H.S. Tension stiffening behavior and structural flexural behavior of steel reinforced UHPFRC members. Master thesis. National Cheng Kung Univ. Dept. of Civil Engineering, 2016.
9. Yang, I.H., Joh, C., Kim, B.S. Structural behavior of ultra high performance concrete beams subjected to bending. Engineering Structures. 2010. 32(11). Pp. 3478–3487. DOI: 10.1016/j.engstruct.2010.07.017
10. Yoo, D.Y., Yoon, Y.S. Structural performance of ultra-high performance concrete beams with different steel fibers. Engineering Structures. 2015. 102. Pp. 409–423. DOI: 10.1016/j.engstruct.2015.08.029
11. Yoo, D.Y., Kang, S.T., Yoon, Y.S. Enhancing the flexural performance of ultra-high-performance concrete using long steel fibers. Composite Structures. 2016. 147. Pp. 220–230. DOI: 10.1016/j.compstruct.2016.03.032
12. Hung, C.C., Chueh, C.Y. Cyclic behavior of UHPFRC flexural members reinforced with high-strength steel rebar. Engineering Structures. 2016. 122(6). Pp. 108–120. DOI: 10.1016/j.engstruct.2016.05.008
13. Chen, S., Zhang, R., Jia, L.J., Wang, J.Y. Flexural behaviour of rebar-reinforced ultra-high-performance concrete beams. Magazine of Concrete Research. 2017. 70(19). Pp. 997–1015. DOI: 10.1680/jmacr.17.00283
14. Hasgul, U., Turker, K., Birol, T., Yavas, A. Flexural behavior of ultra-high-performance fiber reinforced concrete beams with low andhigh reinforcement ratios. Structural Concrete. 2018. 19(6). Pp. 1577–1590. DOI: 10.1002/suco.201700089
15. Turker, K., Hasgul, U., Birol, T., Yavas, A., Yazici, H. Hybrid fiber use on flexural behavior of ultra high performance fiber reinforced concrete beams. Composite Structures. 2019. 229. Article no. 111400. DOI: 10.1016/j.compstruct.2019.111400
16. Zhang, Y., Zhu, Y., Qiu, J., Hou, C., Huang, J. Impact of reinforcing ratio and fiber volume on flexural hardening behavior of steel reinforced UHPC beams. Engineering Structures. 2023. 285. Article no. 116067. DOI: 10.1016/j.engstruct.2023.116067
17. Khalil, W.I., Tayfur, Y.R. Flexural strength of fibrous ultra high performance reinforced concrete beams. ARPN Journal of Engineering and Applied Sciences. 2013. 8(3). Pp. 200–214. URL: https://www.researchgate.net/publication/287399660 (date of application: 21.01.2026).
18. Kodsy, A., Morcous, G. Flexural strength prediction models of non-prestressed Ultra-High Performance Concrete (UHPC) components. Structures. 2021. 34. Pp. 4532–4547. DOI: 10.1016/j.istruc.2021.10.047
19. El-Din, H.S., Husain, M., Khater, M. Effect of steel fibers on flexural behavior of ultra high performance r.c. beams. Egyptian Journal for Engineering Sciences and Technology. 2013. 16(1). Pp. 35–45. DOI: 10.21608/eijest.2013.96788
20. Kahanji, C., Ali, F., Nadjai, A. Structural Performance of Ultra-High Performance Fibre Reinforced Concrete Beams. Structural Concrete. 2017. 18(2). Pp. 249–258. DOI: 10.1002/suco.201600006
21. Randl, N., Meszoly, T. The effect of fibres in UHPFRC beams with longitudinal steel reinforcement. fib Bulletin 79. Fibre-reinforced concrete: From design to structural applications – FRC 2014: ACI-fib International Workshop. 2016. Pp. 181–192. DOI: 10.35789/fib.BULL.0079.Ch18
22. Yang, I.H., Park, J., Bui, T.Q., Kim, K.C., Joh, C., Lee, H. An Experimental Study on the Ductility and Flexural Toughness of Ultrahigh-Performance Concrete Beams Subjected to Bending. Materials. 2020. 13(10). Article no. 2225. DOI: 10.3390/ma13102225
23. Feng, Z., Li, C., Yoo, D., Pan, R., He, J., Ke, L. Flexural and cracking behaviors of reinforced UHPC beams with various reinforcement ratios and fiber contents. Engineering Structures. 2021. 248. Article no. 113266. DOI: 10.1016/j.engstruct.2021.113266
24. Tamov M.M., Salib M.I.F., Abuizeh Y.Q.Y., Sofianikov O.D. Mix design and study of strength properties of self-compacting ultra high-performance fiber-reinforced concrete. News of Higher Educational Institutions. Construction. 2022. 4(760). Pp. 25–39. DOI: 10.32683/0536-1052-2022-760-4-25-39
25. Solhmirzaei, R., Kodur, V.K.R. Modeling the response of ultra high performance fiber reinforced concrete beams. Procedia Engineering. 2017. 210. Pp. 211–219. DOI: 10.1016/j.proeng.2017.11.068
26. Alsomiri, M., Liu, Z. Experimental Study on the Structural Ductility of UHPC Beams under Flexure. International Interactive Symposium on Ultra-High Performance Concrete Papers. 2023. 3(1). Pp. 1–8. DOI: 10.21838/uhpc.16653

Contacts:

Yousef Abuizeih,
ORCID: https://orcid.org/0009-0000-0813-8133
E-mail: yousef.qasem1993@gmail.com

Murat Tamov, *PhD in Technical Sciences*
ORCID: https://orcid.org/0000-0001-8235-2314
E-mail: murat.tamov@gmail.com

Received 01.08.2025. Approved after reviewing 13.10.2025. Accepted 17.10.2025.

Magazine of Civil Engineering

ISSN 2712-8172

journal homepage: http://engstroy.spbstu.ru/

Research article

UDC 691

DOI: 10.34910/MCE.139.9

Durability prediction method for building materials

A.V. Erofeev ✉

Tambov State Technical University, Tambov, Russian Federation

✉ *AV.Erofeev@yandex.ru*

Keywords: building materials, durability, efficiency, forecasting, generalized Zhurkov equation, thermal fluctuation constants, thermal fluctuation

Abstract. The prediction of durability can be approached from the perspective of the thermal fluctuation concept of fracture and deformation of solids. One of the drawbacks of this concept is the high labor intensity involved in determining the thermal fluctuation constants of the generalized Zhurkov equation, as well as the significant errors that may occur in their determination. The aim of this study is to develop methodologies that address and mitigate these shortcomings. The main scientific approaches employed are the hypothetical method and experimental studies (determining the durability of solids under non-destructive stress conditions). A description is provided of a developed methodology for determining thermal fluctuation constants based on a single straight line and one control point. The advantage of this approach is that it reduces the number of required experimental investigations by almost a factor of three. In the classical case, 15 points must be determined, whereas the proposed method requires only six. The main disadvantage of the method is the reduction in the accuracy of determining thermal fluctuation constants. Therefore, it is recommended for cases where approximate values are sufficient and minimal labor costs are desired. A description is also provided of the so-called “reference beam” method. This methodology is based on bringing the obtained fan-shaped family of straight lines converging at a single point (pole) to a selected reference family and determining thermal fluctuation constants using a system of conversion coefficients. Another proposed methodology makes it possible to determine the durability of solids without explicitly determining the thermal fluctuation constants. This method is based on a theoretically derived formula from the generalized Zhurkov equation for direct durability evaluation. The latter two methodologies increase the reliability of durability prediction for solids from the standpoint of the thermal fluctuation concept of fracture and deformation. The first of these methodologies significantly reduces the labor intensity of determining the thermal fluctuation constants of the generalized Zhurkov equation.

Citation: Erofeev, A.V. Durability prediction method for building materials. Magazine of Civil Engineering. 2025. 18(7). Article no. 13909. DOI: 10.34910/MCE.139.9

1. Introduction

The object of this study is the prediction of the durability of building materials and products within the framework of the thermal fluctuation concept of fracture and deformation of solids.

The prediction of building material properties, including durability, is among the most challenging issues in modern construction science. There are several approaches to predicting the durability of building materials [1–3]. In a number of studies, durability forecasting is considered from the standpoint of assessing the remaining service life [4–6], which serves as the basis for predicting the possible future service period. As a rule, this approach is used to estimate the durability of reinforced concrete structures. The initial components of construction materials have a strong influence on their durability [7–9]. One such approach is based on the thermal fluctuation nature of fracture and deformation of solids. This approach is considered within the framework of the thermal fluctuation concept of fracture and deformation, whose founder is rightfully considered to be Serafim Nikolaevich Zhurkov.

Zhurkov proposed that the fracture of a solid body should not be regarded as a critical event occurring when the stresses in the body reach a certain critical value, but rather as a probabilistic process that develops over time. In this context, mechanical loading is not the decisive factor in fracture; instead, thermal oscillations of kinetic particles are considered to be the primary driving force [10–12].

The thermal fluctuation concept of fracture and deformation of solids was further developed in the works of Solomon Borisovich Ratner, Georgy Mikhailovich Bartnev, Vadim Robertovich Regel, Valentin Evgenievich Gul, Engel Evgenievich Tomashevsky, Alexander Ilyich Slutsker, Viktor Petrovich Yartsev, and other researchers [13–15]. However, over the past two decades, the development of the thermal fluctuation concept of fracture and deformation of solids has practically come to a standstill. At the same time, with the advancement of science and technology, questions regarding the possibility and feasibility of applying the thermal fluctuation concept to the prediction of the durability of building materials and products have been increasingly raised [16, 17].

In the past decade, the Russian Federation has been facing increasingly significant challenges. One of the instruments for effectively addressing these challenges is the Fundamental Scientific Research Program for the Long-Term Period 2021–2030, adopted by the Government of the Russian Federation (Decree No. 3684-r of December 31, 2020). The adoption of this Program was based on the Federal Law "On the Russian Academy of Sciences, the Reorganization of State Academies of Sciences, and Amendments to Certain Legislative Acts of the Russian Federation."

One of the research tasks included in the construction sector research plan is to ensure "reliability, safety, and durability"[1]. To address the task of ensuring durability, it is essential to have at one's disposal tools and methodologies that allow for the accurate and adequate determination of the durability of building materials and products.

One of the main drawbacks of the thermal fluctuation concept of fracture and deformation of solids is the high labor intensity involved in determining the thermal fluctuation constants of the generalized Zhurkov equation, as well as the large errors in their determination. Experimental studies have shown that, when working with the same set of initial experimental data, two different specialists with the same level of expertise, applying the same methodology for determining the thermal fluctuation constants of the generalized Zhurkov equation, may obtain values that differ by up to 70 % [18]. This significant discrepancy is attributed to the use of the graph-analytical method for determining thermal fluctuation constants, combined with the need to work in semi-logarithmic coordinates of durability. Another drawback of the concept, also related to the high labor intensity of determining thermal fluctuation constants, stems from the fact that, according to the classical methodology, it is necessary to experimentally determine 15 data points of the durability–stress relationship (five points for each of three different temperatures), with each point being the result of testing no fewer than six specimens under identical conditions.

The outlined problems necessitate the development, within the framework of the thermal fluctuation concept of fracture and deformation of solids, of methodologies that are free from these shortcomings.

Thus, the aim of the present study is to advance methods for assessing the reliability and predicting the performance of building materials and products within the framework of the thermal fluctuation concept of fracture and deformation of solids.

To achieve this goal, it is necessary to develop a methodological basis for conducting the research, including the justification of the materials used, experimental procedures, and methods for processing the obtained experimental data. Furthermore, within the framework of the thermal fluctuation concept of fracture and deformation of solids and based on its further development, alternative methods for determining the strength and durability of solids should be developed. These methods should be characterized by increased reliability and reduced labor intensity in determining the thermal fluctuation constants of the generalized Zhurkov equation.

2. Methods

The primary scientific method used to obtain the initial data on the relationship between the durability of the material and the applied stresses and ambient temperature, necessary for the development of durability prediction methodologies within the framework of the thermal fluctuation concept of fracture and deformation, is experimental testing. The experiments were carried out on a six-position testing stand (Fig. 1), which is based on a metal frame (1) with support platforms (2). The support rods (3) serve as

[1] Garant.ru. Rasporyazheniye Pravitelstva RF ot 31 dekabrya 2020 g. № 3684-r. Ob utverzhdenii Programmy fundamentalnykh nauchnykh issledovaniy v RF na dolgosrochnyy period (2021–2030 gg.) [Order of the Government of the Russian Federation of December 31, 2020 No. 3684-r. On approval of the Program of Fundamental Scientific Research in the Russian Federation for the long-term period (2021–2030)]. URL: https://www.garant.ru/products/ipo/prime/doc/400070256/ (date of application: 21.01.2026).

supports for the specimen (4), with the distance between them adjustable depending on the specimen length. To create the required stress in the specimens, a loading device (5) was used. Heating of the rod-type electric heaters (6), which provide the required temperature in the specimen loading zone, was achieved using a LATr 1M 220V-9A autotransformer. Temperature regulation was carried out with an EPV2-11A potentiometer, group XK, 0–300 °C, and monitored with a thermometer accurate to ±1 °C. To maintain the set temperature, a protective casing (7) was also used, which additionally serves to create a directed heat flow onto the specimens.

To eliminate the influence of mechanical vibrations during specimen fracture, a damping device was used – a container filled with sand, topped with a 20 mm thick rubber mat.

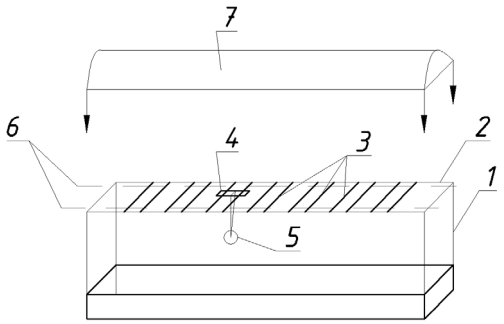

1 – metal frame; 2 – support platforms; 3 – support rods; 4 – specimen; 5 – load device; 6 – rod electric heaters; 7 – casing.

Figure 1. Schematic representation of the six-position stand for determination of short-term transverse bending strength and durability.

Durability (time to reach the ultimate state under the action of non-critical stresses) was determined at three different temperatures, with the specimens conditioned at the corresponding temperature for at least 2 hours prior to testing. For each temperature, durability was measured at five stress levels ranging from 0.70 to 0.98 of the ultimate strength, which was determined on the same six-position testing stand using the standard procedure: calculation scheme – simply supported single-span beam, load – centrally applied concentrated force. The required load to achieve the specified stress in each specimen was calculated based on the condition of pure bending according to the single-span, simply supported beam model with a centrally applied concentrated load. Between 6 and 12 specimens were tested under identical conditions for each data point, and the obtained results were subjected to statistical processing.

Based on the obtained experimental data, methodologies for determining the durability of building materials within the framework of the thermal fluctuation concept of fracture and deformation of solids were developed and tested for adequacy.

The developed methodologies for determining the durability of building materials within the framework of the thermal fluctuation concept of fracture and deformation of solids are based on a previously proven hypothesis regarding the linearity of the variation of the angular coefficients of the temperature-dependent straight lines describing the relationship between the logarithm of durability and stress [19].

3. Results and Discussion

One of the thermal fluctuation constants of the generalized Zhurkov equation – specifically, the limiting temperature of solid-state existence – can be obtained outside the framework of the thermal fluctuation concept of fracture and deformation of solids by alternative methods. For example, it can be determined from a derivatogram, which in turn is the result of differential thermal analysis.

The remaining three thermal fluctuation constants of the generalized Zhurkov equation can be found mathematically by solving a certain system of equations based on an experimentally determined dependence of the logarithm of durability on voltage at a selected temperature and an experimentally determined control point (the dependence of the logarithm of durability on voltage) at a different temperature. Based on the proven hypothesis of the linearity of the change in the angular coefficients of the direct temperatures of the dependence of the logarithm of durability on voltage, while the line of the limiting temperature of the existence of a solid body is parallel to the stress axis of the graph of the dependence of the logarithm of durability on voltage and the presence of a limit temperature of the existence of a solid body determined in another way, a linear equation of the dependence of the change in the logarithm of durability on voltage at the temperature of the reference point is found. The ordinate of the intersection point of the equations of direct temperatures gives the value of the constant $\lg \tau_0$. The

remaining two constants are determined from solving a system of equations based on the generalized Zhurkov equation, in which two of the four constants are already known, as well as the values of the logarithm of durability under specific operating conditions (voltage and temperature).

Thus, when determining the thermal fluctuation constants of the generalized Zhurkov equation using the described method, the number of experiments is reduced by almost 3 times, which makes it possible to increase the number of studies per point. This technique can be used only if the material does not change its structure in the temperature range under consideration (the thermal fluctuation constants remain constant).

An analysis of the fundamental principles of the thermal fluctuation concept of fracture and deformation of solids, along with a comparative analysis of the experimentally obtained relationships between the logarithm of durability and both stress and ambient temperature, as well as the corresponding thermal fluctuation constants, suggests that the values of these constants depend on the coordinates of the pole point and on the rate of change of the slope coefficient of the temperature-dependent straight lines in the $\lg\tau-\sigma$ relationship. The variation of the constants as a function of changes in the pole point coordinates and the slope coefficient of the temperature lines should follow certain defined dependencies.

According to the classical principles of the thermal fluctuation concept of fracture and deformation of solids, which have been confirmed in practice, when the rate of change of the slope coefficient of the temperature-dependent lines is maintained, a shift of the pole point solely along the ordinate axis results in a linear change only in the constant $\lg\tau_0$ among the thermal fluctuation constants. Conversely, when the pole point is shifted solely along the abscissa axis, only the constant U_0, associated with the bond rupture energy, changes linearly.

To simplify calculations, and relying on the proven hypothesis of the linear variation of the slope coefficients of the temperature-dependent lines describing the relationship between the logarithm of durability and stress, one can refer to the change in the limiting temperature of solid-state existence, which will also exhibit a linear character. A change in the limiting temperature of solid-state existence leads to a linear change in the slope coefficients of the temperature lines. Considering that, in the classical case, the thermal fluctuation constants U_0 and γ are determined from a graph plotted in $U-\sigma$ coordinates, their variation is likewise linear, as has been experimentally confirmed.

The described dependencies make it possible to determine the thermal fluctuation constants of a material without reconstructing the obtained experimental graph in $\lg\tau-\sigma$ coordinates, as required in the classical methodology, but instead through manipulation of a reference bundle. This method has been named “Determination of Thermal Fluctuation Constants by the Reference Bundle Method.” As the reference bundle, the set of lines shown in Fig. 2 is proposed, for which the thermal fluctuation constants have the values presented in Table 1. These values were obtained based on the experimentally determined constants of polyvinyl chloride plates tested under transverse bending: $\lg\tau_0$ = –2.34; γ = = 43.85 kJ/(mol·MPa); T_m = 437.95 K, U_0 = 313.85 kJ/mol.

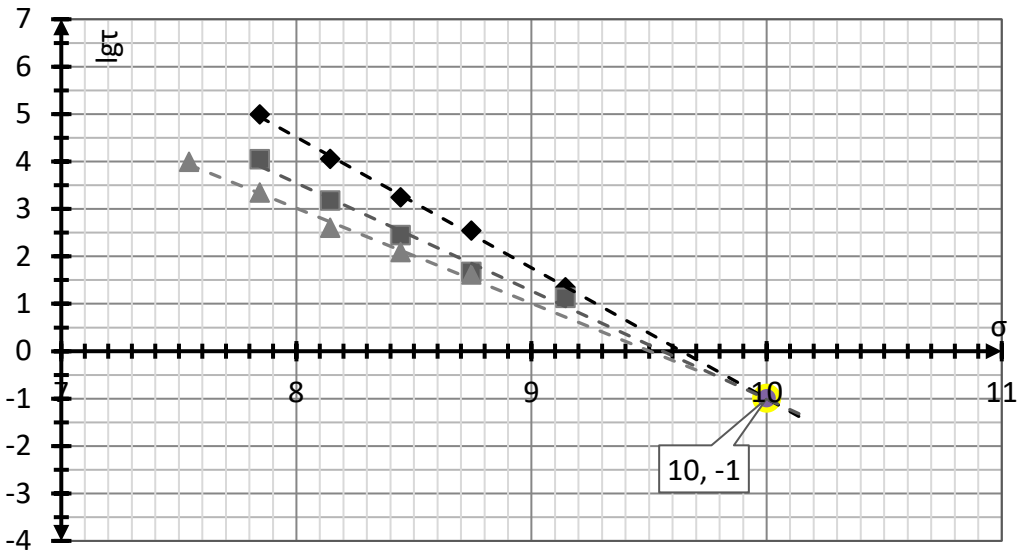

Figure 2. Reference beam.

Table 1. Thermal fluctuation constants of the reference beam.

γ, kJ/(mol·MPa)	U_0, kJ/mol	T_m, K	$\lg\tau_0$
50	500	500	–1

To find the thermal fluctuation constants using the reference beam method, the reference constants of Table 1 must be multiplied by the conversion coefficients (a system of coefficients). To do this, initially, based on the experimental dependences of the logarithm of durability on stresses and temperature, a family of fan-shaped straight lines is constructed in $\lg\tau-\sigma$ coordinates and the coordinates of the pole point are determined, as well as the value of the angular coefficient c^* of the equation of dependence of the angular coefficients of the forward temperatures of the graph in $\lg\tau-\sigma$ coordinates on the reverse temperature. Next, the conversion coefficients k_q and k_k are determined:

$$k_\sigma=\frac{\sigma}{\sigma_e}, \tag{1}$$

where σ – the point of the abscissa pole of the obtained graph of direct temperatures; σ_e – the points of the abscissa pole of the reference graph of direct temperatures;

$$k_k=\frac{c^*}{c_e^*}, \tag{2}$$

where c^* – the angular coefficient of the equations of dependence of the angular coefficients of the direct temperatures of the graph in coordinates $\lg-\sigma$ on the inverse temperature of the experimental graph; c_e^* – the angular coefficient of the equations of dependence of the angular coefficients of the direct temperatures of the graph in coordinates $\lg-\sigma$ on the inverse temperature of the reference graph.

For the accepted reference beam, c_e^* = –2.619.

The constant $\lg\tau_0$ is determined by the ordinate of the pole point of the obtained bundle of lines. The limiting temperature of solid-state existence is found from the linear relationship describing the variation of the slope coefficients of the equations.

The thermal fluctuation constant U_0 is determined by multiplying the reference constant $U_{0,e}$ by a system of coefficients k_σ and k_k :

$$U_0=k_\sigma\cdot k_k\cdot U_{0,e} \tag{3}$$

The structural-mechanical constant γ_e is determined by multiplying the reference constant γ_e by the coefficient k_k :

$$\gamma=k_k\cdot\gamma_e. \tag{4}$$

Compared to the classical approach, the methodology is less labor-intensive and also allows one to avoid errors and inaccuracies that may arise during graphical constructions. The adequacy of the methodology has been verified on a range of building materials.

To derive a formula for determining the durability of solids without the need to determine the thermal fluctuation constants of the generalized Zhurkov equation, one can use the known mathematical relationships for calculating the thermal fluctuation constants. By introducing, for convenience, a set of notations and conditions, as presented in Fig. 3, it is possible to arrive at the following formulas for determining durability:

$$\tau=\tau_0\cdot\exp\left[2.3\cdot k\cdot10^3\cdot\left(\sigma_m-\sigma\right)\cdot\left(\mathrm{T}^{-1}-\mathrm{T}_m^{-1}\right)\right] \tag{5}$$

and

$$\lg \tau = \lg \tau_0 + 2.3 \cdot k \cdot 10^3 \cdot (\sigma_m - \sigma) \cdot \left(T^{-1} - T_m^{-1} \right). \quad (6)$$

In Fig. 3, the equation of the straight line corresponding to temperature T_1 is given by $\lg \tau = a_1 \sigma + b_1$, and the equation of the straight line corresponding to temperature T_2 is given by $\lg \tau = a_2 \sigma + b_2$. The notation of points is adopted as follows: $\lg \tau_n^m$, where n corresponds to the index of the selected stress level, and m corresponds to the index of the selected temperature.

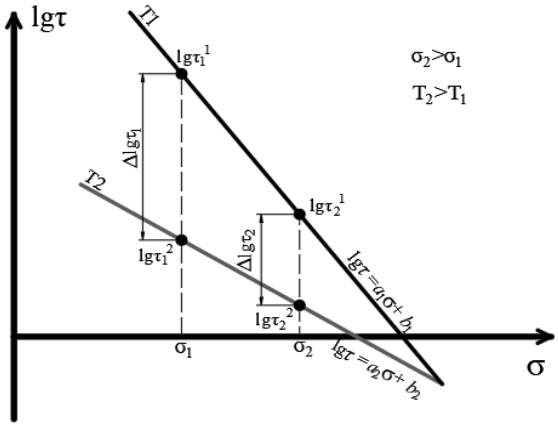

Figure 3. Graph of the dependence of the decimal logarithm of durability on voltage at a given temperature.

The obtained formulas (5) and (6) make it possible to determine the durability of solids without calculating the thermal fluctuation constants γ and U_0, which in turn eliminates the need for additional graph reconstructions, thereby increasing the accuracy of the calculations.

The presented methods are original and were developed relatively recently; therefore, at the present time, no independent validations by other researchers have been reported. However, their application using experimental data obtained by other authors for wood-composite materials [20–22] and bitumen-based materials [23, 24] demonstrates a high degree of agreement with the results of determining thermal fluctuation constants by classical methods.

4. Conclusion

The proposed methodology for determining the thermal fluctuation constants of the generalized Zhurkov equation based on a single temperature line and one control point (a total of six points) makes it possible to reduce the labor intensity of their determination. However, its main drawback is the reduced accuracy of determining the thermal fluctuation constants. Therefore, it is recommended for cases where only approximate values are required with minimal labor costs. To simplify the determination of thermal fluctuation constants from experimentally obtained data, a computer program titled “Calculation of Thermal Fluctuation Constants of the Generalized Zhurkov Equation” was developed and officially registered.

The proposed reference bundle method improves the accuracy of determining the thermal fluctuation constants of the generalized Zhurkov equation by eliminating the need to reconstruct the original experimentally obtained graph in logarithm of time vs. stress coordinates into a graph in logarithm of time vs. inverse temperature coordinates, as required in the classical methodology. To automate the calculations, a computer program titled “Determination of Thermal Fluctuation Constants by the Reference Bundle Method” was developed and officially registered. In addition, Patent for Invention No. 2763483 was obtained for this method.

The proposed method for determining the durability of solids also improves the accuracy of durability assessment by completely eliminating the need for graph plotting and transitioning to a mathematical determination of durability. To automate the calculations, a computer program titled “Determination of the Durability of Solids” was developed and officially registered. In addition, Patent for Invention No. 2760177 was obtained for this method.

Further development of the thermal fluctuation concept of fracture and deformation of solids may proceed through the consideration of operating conditions as well as the prediction of durability from the standpoint of the loss of the material's thermophysical properties.

References

1. Suleymanov, A.M. Eksperimentalno-teoreticheskiye osnovy prognozirovaniya i povysheniya dolgovechnosti materialov myagkikh obolochek stroitelnogo naznacheniya [Experimental and theoretical foundations for predicting and increasing the durability of soft shell materials for construction purposes]: abstract of a dissertation for the degree of Doctor of Technical Sciences. Kazan State University of Architecture and Engineering. Kazan, 2006.
2. Shelikhov, N.S., Sagdiev, R.R., Timirgaliev, M.M. Design of a method for assessing the durability of building materials in aggressive environments. News of the Kazan State University of Architecture and Engineering. 2019. 4(50). Pp. 394–400.
3. Osipov, S.N., Zakharenko, A.V., Pozdnyakov, D.A. (2018) On Longevity of Solid Construction Materials. Science and Technique. 17 (4). Pp. 278–287. DOI: 10.21122/2227-1031-2018-17-4-278-287
4. Abdrahimova, N. Experimental and theoretical studies of plug joints reinforced concrete columns under transverse force. IOP Conference Series: Materials Science and Engineering. 890. Article no. 012053. DOI: 10.1088/1757-899X/890/1/012053
5. Temikeev, K., Abdykalykov, A., Zulpuev, A.M. Temir Bolot, Meshcheriakov, A.A. Estimation of the operation resource level of the load bearing structures of buildings and facilities during design and operation period. The Herald of Kyrgyz State Technical University. 2023. 65(1). Pp. 551–557. DOI: 10.56634/16948335.2023.1.551-557
6. Kashlev, Y.A., Maslyaev, S.A. The Rate of Fast Particles Leaving a Planar Channeled Regime in a Quasiclassical Approach. Inorganic Materials: Applied Research. 2020. 11(3). Pp. 514–519. DOI: 10.1134/S207511332003020X
7. Bescher, E., Vallens, K., Kim, J. Belitic calcium sulfoaluminate cement and its use in the United States. Cement and its Applications. 2020. 6. Pp. 90–95.
8. Pichugina, A.S., Vakhovskaya, R.V. Appliance of biomineralization in phosphogypsum roadbed compaction. Aktual'nye nauchnye issledovanija v sovremennom mire. 2021. 11-9(79). Pp. 25–31.
9. Rykunova, M.D. Svoystva tsementnogo testa i kamnya v prisutstvii glutarovogo aldegida [Properties of cement paste and stone in the presence of glutaric aldehyde]. Energosberezheniye i innovatsionnyye tekhnologii v toplivno-energeticheskom komplekse [Energy conservation and innovative technologies in the fuel and energy complex]. Industrial University of Tyumen. Tyumen, 2022. Pp. 50–53.
10. Korikov, D.V. Asymptotic Description of Fast Thermal Processes in Scalar Harmonic Lattices. Physics of the Solid State. 2020. 62(11). Pp. 2232–2241. DOI: 10.1134/S1063783420110177
11. Regel', V.R., Slutsker, A.I., Tomashevskiĭ, É.E. Reviews of Topical Problems: the Kinetic Nature of the Strength of Solids. Soviet Physics Uspekhi. 1972. 15(1). Pp. 45–65. DOI: 10.1070/PU1972v015n01ABEH004945
12. Tomashevskii, E.E., Zakrevskii, V.A., Novak, I.I., Korsukov, V.E., Regel, V.R., Pozdnyakov, O.F., Slutsker, A.I., Kuksenko, V.S. Kinetic micromechanics of polymer Fracture. International Journal of Fracture. 1975. 11(5). Pp. 803–815.
13. Yartsev, V.P., Voronkov, A.G. Influence of temperature on the range of energy of polymeric material activation under desctruction and strain. Bulletin of Volgograd State University of Architecture and Civil Engineering Series: Civil Engineering and Architecture. 2013. 31-2(50). Pp. 223–226.
14. Makarova, T.V., Potapov, Yu.B. Prognostication of Durability the Rubber Polymeric Concrete Based on Termofluctuation Theory of Destruction and Straining of Solid Bodies. Kompozitsionnye stroitelnye materialy i konstruktsii [Composite building materials and structures]. Voronezh State University of Architecture and Civil Engineering. Voronezh, 2014. Pp. 156–159.
15. Petrov, M.G. Investigation of the longevity of materials on the basis of the kinetic concept of fracture. Journal of Applied Mechanics and Technical Physics. 2021. 62(1). Pp. 145–156. DOI: 10.15372/PMTF20210118
16. Kovshov, A.G. Kinetic, Thermofluctuation Nature Friction Surfaces of Solid Friction during Wear. Izvestiya Samarskogo nauchnogo tsentra Rossiyskoy akademii nauk [News of the Samara Scientific Center of the Russian Academy of Sciences]. 2020. 22(3). Pp. 37–43. DOI: 10.37313/1990-5378-2020-22-3-37-43
17. Kienzler, D., Wan, Y., Erickson, S.D., Wu, J.J., Wilson, A.C., Wineland, D.J., Leibfried, D. Quantum Logic Spectroscopy with Ions in Thermal Motion. Physical Review X. 2020. 10(2). Article no. 021012. DOI: 10.1103/PhysRevX.10.021012
18. Gorokhov, T.I., Yerofeyev, A.V. Sravnitelnyy analiz pogreshnostey grafoanaliticheskogo i matematicheskogo metoda opredeleniya termofluktuatsionnykh konstantobobshchennogo uravneniya Zhurkova [Comparative Analysis of Errors in the Graphical-Analytical and Mathematical Method of Determining Thermal-Fluctuation Constants of the Generalized Zhurkov Equation]. Molodyye uchenyye – razvitiyu Natsionalnoy tekhnologicheskoy initsiativy (POISK) [Young scientists – for the development of the National Technology Initiative (POISK)]. 2020. 1. Pp. 142–144.
19. Yerofeyev, A.V., Gorokhov, T.I., Gorokhov, S.I. Gipoteza o lineynosti izmeneniya uglovykh koeffitsiyentov pryamykh temperatur zavisimosti logarifma dolgovechnosti ot napryazheniya [Hypothesis of the Linearity of Change in the Angular Coefficients of Direct Temperatures of the Dependence of the Logarithm of Durability on Voltage]. Aktualnyye voprosy arkhitektury i stroitelstva [Current issues in architecture and construction]. Ogarev Mordovia State University. Saransk, 2021. Pp. 291–295.
20. Pakhomova, E., Emelyanov, S., Yartsev, V., Danilov, V., Monastyrev, P. The Influence of Climatic Aging on the Performance of Wood-Based Panels. Civil Engineering Journal. 2023. 9(6). Pp. 1491–1508. DOI: 10.28991/cej-2023-09-06-015
21. Yarcev, V.P., Danilov, V.M. Influence of climatic aging on operating properties of fiberboard. Russian Journal of Building Construction and Architecture. 2023. 1(57). Pp. 66–76. – DOI: 10.36622/VSTU.2023.57.1.005
22. Mamontov, S., Mamontov, A., Monastyrev, P., Emelianov, S., Pahomova, E. Aging and Long-Term Mechanical Impact in the Durability of Wood Composites. Lecture Notes in Civil Engineering. 287. Modern Problems in Construction. Springer. Cham, 2023. Pp. 57–66. DOI: 10.1007/978-3-031-12703-8_7
23. Yarcev V. P., Danilov V. M. Thermal Fluctuation Regularities of the Fracture of Bituminous Composites. Russian Journal of Building Construction and Architecture. 2025. 1(77). Pp. 70–80. DOI: 10.36622/2541-7592.2025.77.1.007
24. Yarcev, V.P., Danilov, V.M., Suchkov, K.O. The Effect of Fillers on the Durability of Bitumen Composites. Stroitelnyye materialy, oborudovaniye, tekhnologii XXI veka [Construction materials, equipment, technologies of the 20th century]. 2025. 1(288). Pp. 62–65.

Information about the authors:

Alexander Erofeev, *PhD in Technical Sciences*
ORCID: https://orcid.org/0000-0002-1035-887X
E-mail: AV.Erofeev@yandex.ru

Received 03.08.2025. Approved after reviewing 09.10.2025. Accepted 18.10.2025.

Magazine of Civil Engineering

ISSN 2712-8172

journal homepage: http://engstroy.spbstu.ru/

Research article

UDC 624

DOI: 10.34910/MCE.139.10

Implementation of geopolymer for stabilizing granular soil

B.Z. Raoof ✉, ***A.H. Abdulkareem***, ***A.R. Rajab***

University of Anbar, Ramadi, Iraq

✉ *ban22e1008@uoanbar.edu.iq*

Keywords: Granular soil, geopolymer, soil stabilization, sustainable material.

Abstract. River sand, despite being an available material, a low-cost, but loose sandy soil, cannot be used as a construction material in civil engineering works due to its poor grain size distribution and low bearing capacity. Geopolymer is recently considered a novel eco-friendly alternative to conventional soil enhancement and stabilization materials, such as ordinary Portland cement (OPC) and lime, which harm the environment in terms of high CO_2 emissions and energy consumption. Hence, this study investigated the potential strengthening of loose sandy soil using geopolymer. Different alkaline activator (AA) solution ratios were used with varying curing temperatures for producing the river-sand geopolymer. The river sand-geopolymer specimens were matured in the oven at different temperatures for 48 hours. A series of unconfined compressive strength (UCS) tests were carried out on the 3, 7, 14, and 28 days of curing. The results show that the UCS of the river-sand geopolymer matrix significantly increased with increasing the main ingredient of its activator solution (sodium silicate) as well as the temperature. The UCS reached 13.42 MPa when the AA solution ratio was 0, whereas it decreased up to 1.15 MPa when the AA solution ratio became 1.5 at a temperature of 60 °C and 28 days of curing. Therefore, geopolymer is feasible and sustainable material to improve problematic soil for different applications.

Citation: Raoof, B.Z., Abdulkareem, A.H., Rajab, A.R. Implementation of geopolymer for stabilizing granular soil. Magazine of Civil Engineering. 2025. 18(7). Article no. 13910. DOI: 10.34910/MCE.139.10

1. Introduction

River sands, or loose sand, are cohesion-less soils that have a consistent and uniform dispersion of particles with no sharp edges. They are classified as poorly graded. The material's gradation characteristics pose substantial challenges when employed for construction projects, such as the construction of road and railway embankments or fills. Moreover, the compaction of this material presents significant challenges because its compaction curves have no clearly defined ideal moisture content. At very low moisture content, a minimum dry density value may be observed [1].

Furthermore, the load-bearing capacity of on-site river sand is generally insufficient for most geotechnical engineering applications. Therefore, it is necessary to utilize alternate materials. The use of alternative materials is sometimes impossible since there are no suitable alternative materials available on-site. Therefore, several techniques for enhancing soil quality and optimizing its workability for engineering applications can be investigated. Apply material processing procedures to improve the geotechnical characteristics of the flawed soil, such as durability, resistance to erosion, compressibility, permeability, physical qualities, and mechanical properties [2]. Soil stabilization refers to the method of improving the physical or chemical characteristics of soil. Techniques including mechanical compaction and the use of calcium-rich compounds can achieve this [3]. In the last three decades, notable advancements have been made in developing and broadly adopting different ground stabilization techniques in industrial projects [4]. Recycling crushed concrete is a sustainable way to improve soft soils' chemical and geotechnical properties

[5]. Numerous techniques, such as mechanical stabilization (stone columns, preloading, dynamic compaction, or vibroflotation), chemical stabilization (using ordinary Portland cement (OPC), cement kiln dust (CKD), or lime), or geotextile stabilization have been used to improve the characteristics of weak soil [6]. The process of stabilizing weak soil generally involves chemical treatment, which requires chemical binders like OPC [7, 8]. Conventional soil stabilizers, such as cement and lime, undergo thermal breakdown of calcium carbonate found in limestone during production. This process leads to significant emissions of greenhouse gases and energy. Manufacturing each ton of cement leads to the release of about ton of carbon dioxide. The global production of CO_2 amounts to around 1 %, with an average emission of 0.95 tons of CO_2 per 1 ton of lime processing [9, 10]. The method necessitates a substantial amount of energy to sustain the elevated temperatures necessary for the manufacture of OPC, which range from 450 to 1550 °C, as well as temperatures between 100 and 1000 °C for lime production. During cement manufacturing, the raw ingredients are rapidly exhausted. According to the report, the production of 2 billion tons of cement necessitates over 3 billion tons of raw materials, with limestone accounting for 70 % of the total [11].

Therefore, it is necessary to develop innovative soil stabilizers that may function as a viable and ecologically sustainable alternative to cement in many civil engineering projects. The advancements in geopolymerization have gained significant attention as a feasible substitute for handling solid waste and by-products. These developments provide a sophisticated and economical method for dealing with various problems, especially those related to the treatment and storage of hazardous waste in environmentally sensitive circumstances [12]. The term geopolymer was initially coined in the 1970s to describe inorganic alkaline aluminosilicate-activated materials [13, 14]. This compound's synthesis occurs at ambient or slightly higher temperatures, utilizing raw materials rich in alumina and silica, such as fly ash (FA), slag, metakaolin, and calcined clay, in the presence of alkaline activators (AA). Geopolymers are becoming increasingly attractive as an alternative to soil stabilization due to their ability to address the environmental issues connected with traditional binders by producing less quantities of CO_2 during the stabilization process. On average, producing one 1 of geopolymer generates a mere 0.19 to 0.24 tons of CO_2 emissions and moderately affects global warming [15].The researcher investigated using geopolymers, specifically sodium-based AAs and FA class F, to stabilize sandy clay soil.

Cristelo et. al. [16] studied involved a comparison with a binder that is based on cement. The ratio of activators to FA (A/FA) ranged from 1 to 2.5, whereas the ratio of FA varied between 20, 30, and 40 % of the total solids. Unconfined compressive strength (UCS) samples were created and tested after curing for 7, 28, 90, and 365 days. The results showed a significant improvement in strength when using a lower A/FA ratio, leading to a 43.4 MPa rise after 365 days of curing. The UCS results of the cement and geopolymer samples showed a significant resemblance after 28 days of curing [16]. Geopolymer treatment significantly improved the properties of medium and high plastic soils in a separate investigation. The UCS of the medium plastic soils, which included 5 % of FA, was 1.0 MPa. The pressure later rose to 2.6 MPa when the FA level was raised to 25 %. However, the UCS did not experience any changes due to the inclusion of up to 20 % FA in high plastic soil. But when the concentration of FA reached 30 %, the UCS exhibited a substantial and rapid increase of 400 % [17]. Moreover, the strength of soft soil experienced a substantial enhancement with the application of a geopolymer consisting of granulated blast furnace slag (GBFS) and basic oxygen furnace slag (BOFS). It was shown that exposing samples to temperatures between 20 and 45 °C resulted in a 42 time increase in the UCS compared to untreated soil [18]. Other researchers had utilized the geopolymer that was derived from ground-GBFS as an environmentally friendly alternative to cement in deep soil mixing applications. Their study analysed the cement-treated specimens vs. GGBS-based geopolymer samples. The analysis considered the varying levels of GGBS content, ranging from 10 to 30 %, and the activator ratio, which ranged from 0.5 to 1.0. The results showed that specimens treated with geopolymer had a greater UCS compared to those treated with cement at the exact dosage, except for the mixture with an Alkaline/Binder (A/B) ratio of 0.5; this is a consequence of the development of increased pozzolanic and geopolymeric mechanisms [19].

For silty sand soil type, Rios et al. [20] examined the characteristics of stabilized this soil type using alkali-activated cement. The researchers employed sodium hydroxide (SH) (NaOH) and sodium silicate (SS) (Na_2SiO_3) as the alkali activator solution and FA as the precursor material. The strength and stiffness tests reveal substantial enhancement beyond the 28 days of the curing process, although the short-term strength was deemed sufficient. Recent research suggests that its capacity to endure immersion and wetting-drying cycles is consistent with the existing standards for soil cement, thereby supporting its potential as a viable alternative to soil cement. In the study conducted by Hai-yan et al. [21], a geopolymer was synthesized through the combination of alkali-activated saline soil with FA, resulting in the development of environmentally sustainable construction materials. The researchers observed that the mixing of saline soil with FA resulted in enhanced mechanical and physical properties, as well as increased durability. The aforementioned attributes are further augmented as the percentage of FA rises from 20 to 60 %. Based on the findings of the study, it has been determined that the most optimal parameters for the dissolution of

SiO_2 and Al_2O_3 involve the utilization of a 5 M NaOH solution at a temperature of 60 °C over a period of 24 hours. Moreover, the use of FA significantly improves water's resilience and resistance to permeation. Their investigation uncovered that exclusively stimulating saline soil as a precursor has restricted advantages. Adding extra chemical components like alumina and silica to the product is required to get the desired characteristics [21]. The use of FA-based geopolymer as an additive in organic soils is advantageous due to its strong bonding properties, resulting in enhanced strength and long-term stability [22]. The use of FA-based geopolymer significantly increases the stiffness of soil-reclaimed asphalt pavement-fly ash (soil-RAP-FA) mixtures, with higher FA content leading to higher equivalent modulus M_{equ} [23]. The loose sand geopolymer matrix's, USC showed a significant increase within the range when the main ingredient of the geopolymer, i.e., FA, was increased. The compressive strength of the soil-geopolymer matrix was observed to increase when the FA content was 5–15 % but decreased when the FA content was 20–30 % [24]. Geopolymer, like Rafsangan natural pozzolan, CKD, and an activator, such as calcium carbide residue or NaOH, were combined to stabilize sandy soil with poor grading. The research showed that the addition of CKD and NaOH considerably improved the UCS of the soil samples [25].

Most literature, as per our knowledge, that dealt with enhancing soil characteristics or improving its stabilization conditions by applying an alkali-geopolymer approach has an inevitable need for adding fine materials enriched with alumina and silica like FA, furnace slag, etc. Despite the growing interest in using geopolymer as sustainable materials, there is a lack of studies on their application in the field of geotechnical aspects. Therefore, this work investigated the feasibility of employing geopolymer for geotechnical stabilization of loose sandy soil as an alternative to cement, lime, or any other pozzlanic additives. The river sand soil has many pozzolanic chemical components, including silica and alumina, which make it an excellent raw material for geopolymer. This study investigated the impact of mixing river sand with varied proportions of AA solution ratios at varied temperatures on the UCS at different curing times. The aim of this work is to develop a substance that increases soil particles' adhesion and solidity (i.e., enhances its geotechnical characteristics). The produced substances might be utilized as a building material in engineering applications and infrastructure projects, as well as for impeding the displacement of sand dunes. A thorough series of laboratory tests were conducted to evaluate the strength and stiffness of the geopolymer-loose sand matrix. In addition, the sand's microstructure enhancement was analysed using scanning electron microscopy (SEM).

2. Material and Methods

2.1. Soil Properties

The river sand-soil utilized in this work was obtained from a location near the Euphrates River within Ramadi city and classified as SP by unified soil classification system ASTM D2487-2017 [26]. Fig. 1 depicts the grain size distribution of the river sand-soil according to ASTM D422-2007 [27]. Table 1 gives a summary of the physical and chemical characteristics of the river sand soil. The chemical components of the river sand soil as identified by X-ray fluorescence analysis is showed in Table 2.

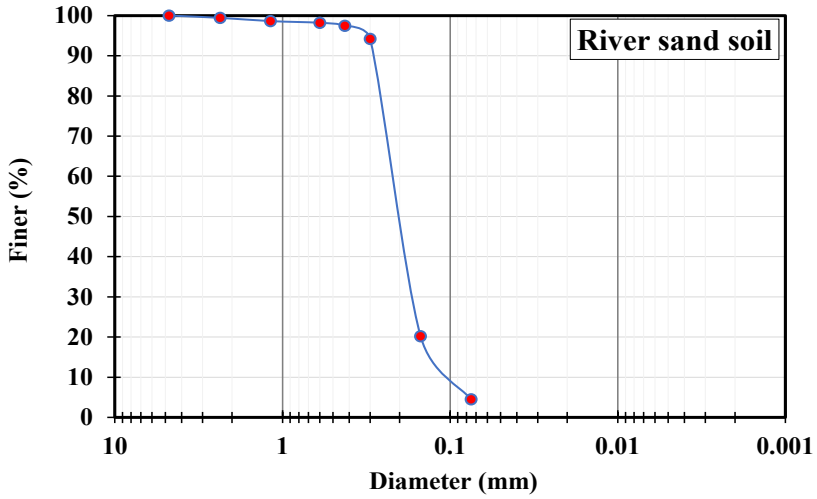

Figure 1. Grain size distribution curve of river sand.

Table 1. The properties and classification of river sand soil.

Soil property	Value
Specific gravity, G_s	2.7
Uniformity coefficient	2.3
Coefficient of curvature	1.25
D10 (mm)	0.1
D30 (mm)	0.17
D60 (mm)	0.23
Sand %	95.4
Silt & clay (%)	4.52
Plasticity	NP
pH	8
OC (%)	3.4

2.2. AA Solution

In this study, the activator used was a combination of SH and SS that was purchased from a local vendor in Baghdad. According to the product specifications, NaOH, used in the work was a white colored flake-like shell with 98 % purity, as obtained by the chemical analysis. It was characterized by its rapid dissolution in distilled water with continuous stirring. It has a molecular weight of 40 g/mol and this substance is preferred for producing geopolymer because of its abundance and higher alkalinity compared to other components. On the other hand, the specifications for SS indicate that it is in a liquid state and contains SiO_2 (32.5 %), Na_2O (13.4 %), and water (54 %). The materials are illustrated in Fig. 2.

Table 2. Chemical compositions of soil (X-ray fluorescence) analysis.

Chemical composition	Elemental Oxide
SiO_2	6.659
Al_2O_3	0.577
Fe_2O_3	4.681
Cao	7.165
K_2O	0.583
Na_2O	0.26
Mgo	0.117
SO_3	0.0005
MnO	0.0692
SiO_2	6.659

(a) **(b)** **(c)**

Figure 2. Materials: (a) Na_2SiO_3 (SS), (b) NaOH flakes (SH), c) river sand soil.

2.3. Compaction Test

Many laboratory tests were conducted to examine geopolymers made from river sand. The standard Proctor test, as outlined in ASTM D698-12 [28], determined the maximum unit weight and optimum moisture content (OMC) of the untreated river sand soil. Fig. 3 demonstrates that the maximum unit weight is 15.59 KN/m^3 and the OMC is 9.36 %. The moisture-density curve is not as distinct when compared to the compaction curve for cohesive soils. When compacting coarse-grained cohesionless soils (such as sands and gravels) using a standard or modified Proctor's technique, the shape formed is referred to as a humpback or camelback [29].

2.4. Sample Preparation

To create SH, 320 g of appropriate NaOH flakes were dissolved in 1 l of distilled water. The solution was mixed until it reached the desired 8 molarity (M) of concentration. It is important to note that when NaOH is added to water, it generates an exothermic reaction. Therefore, it is necessary to wait for a specific time before using the solution. This ensures that the solution does not generate heat during the mixing process, which could negatively affect its workability. To prepare the river sand geopolymer, the required amount of SS was added to the SH at least 2 hours prior its use. The amount of alkaline solution added to the dry materials was calculated based on the OMC percentage obtained from the standard Proctor test, which was approximately 9.34 %. The manufacture of the river sand-geopolymer involved the utilization of three different ratios of SH to SS (SH:SS). Additional 10 % of extra water was added to achieve the desired water content and suitable workability. Three ratios of SH:SS were used in the production of the river-sand geopolymer, these ratios of SH:SS were 0, 0.75, and 1.5 %.

The process began by combining the AA solution with dry river sand soil and stirring thoroughly for 6 to 10 min until a homogenous mixture was achieved. Table 3 provides a detailed description of the components used in the blend. The mixture was poured evenly in 3 layers into PVC molds, which were cylindrical with dimensions of 100 mm in height and 50 mm in diameter. A longitudinal incision was made on the side of the molds to make specimen extraction easier. The uppermost portions of each layer were scraped to ensure contact between the three levels. To achieve homogeneity among the three layers, a plastic rod was employed to remove any air bubbles or voids that may have formed during the pouring procedure. The entire mold was placed on a vibration plate to achieve densification. After vibrating, the specimens were cured in the oven at designated temperatures of 30, 45, and 60 °C for 48 hours. The specimens were extracted from the molds, enveloped in plastic sheets, and placed back in the oven at a temperature of 30 ° for curing until the time of testing. The UCS of each specimen was assessed at age of 3, 7, 14, and 28 days. In accordance with ASTM D2166-2006 [30], the UCS specimens were fabricated using cylindrical PVC tubes with a height-to-diameter (h:d) aspect ratio of 2:1, measuring 100:50 mm. A uniaxial machine with a loading capacity of 50 kN and a displacement rate of 0.1 mm/min was utilized to conduct the UCS test on the specimen.

The UCS may not be the best method to assess the bearing capacity of sandy soil because of its poor ability to sustain lateral pressure. This can be attributed to the lack of cohesion in the soil. As a result, the study lacks reference samples to compare with samples treated with an activated alkali solution.

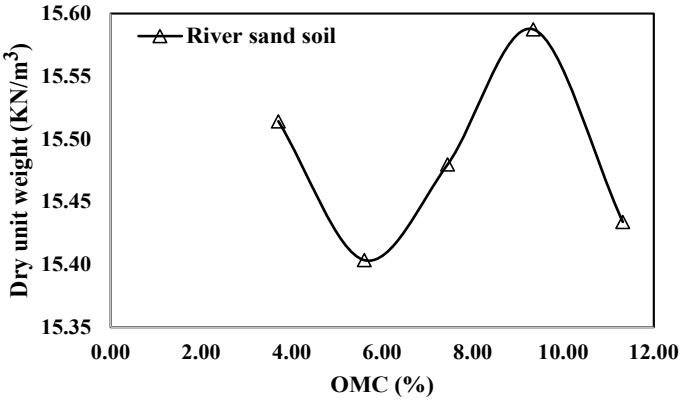

Figure 3. Compaction curve of river sand soil.

Table 3. Details of mixture used.

Sample	Soil (%)	AA	SH:SS	Temperature (°)
S-AA 0 T30°	100	0	0:100	30
S-AA 0 T45°	100	0	0:100	45
S-AA 0 T60°	100	0	0:100	60
S-AA 0.75 T30°	100	0.75	43:57	30
S-AA 0.75 T45°	100	0.75	43:57	45
S-AA 0.75 T60°	100	0.75	43:57	60
S-AA 1.5 T30°	100	1.5	60:40	30
S-AA 1.5 T45°	100	1.5	60:40	45
S-AA 1.5 T60°	100	1.5	60:40	60

Sample codes: SH:SS(SH = NaOH, SS= Na_2SO_3)

3. Results and Discussion

3.1. UCS

3.1.1. Effect of Curing Time of Soil –Geopolymer

The UCS of river sand-geopolymer tends to increase with the passing of time. This trend was observed across different temperatures and curing durations of 3, 7, 14, and 28 days for soil stabilization with AAs. Several researchers have found similar observations regarding the impact of cure time on geopolymer [18, 31–33] . In this study, the highest UCS values were recorded for stabilized soil specimens that had been incorporated with all ratios of AAs at different temperatures after 28 days of testing. For example, for an AA of SH:SS = 0:100 at 60°C, the UCS values increased from 5 to 13.42 MPa over a period of 28 days, with intermediate readings of 9 MPa at 7 days and 12.39 MPa at 14 days. This increasing trend was observed across all other mixtures as well. The strength of the geopolymer material increases over time, indicating a continuous build-up of bonding as the polymerization process progresses, as demonstrated in Fig. 4.

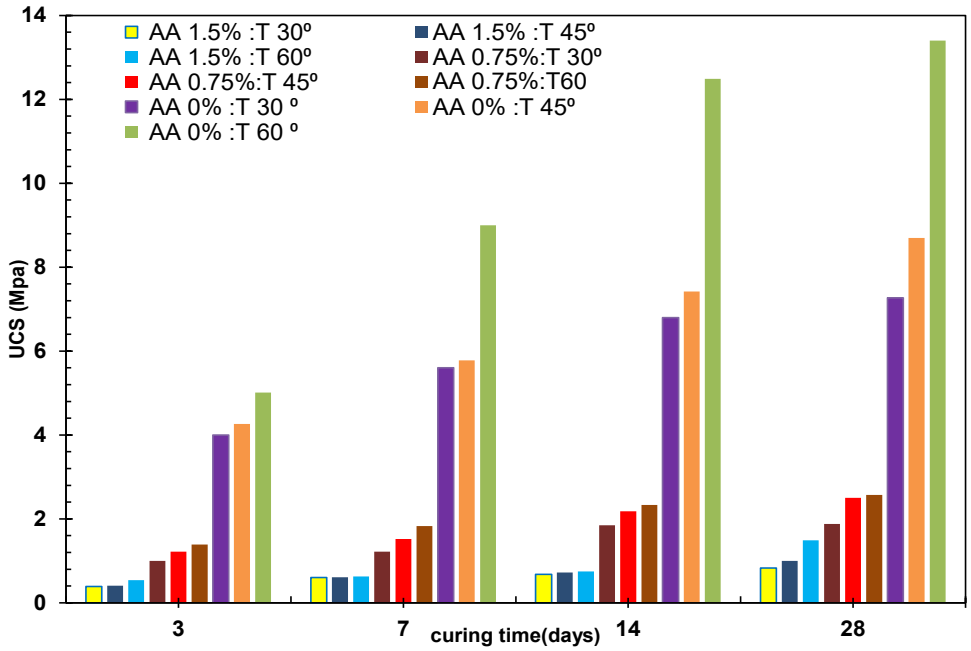

Figure 4. The effect of curing time on UCS of the river-sand geopolymer.

3.1.2. Effect of curing temperature of geopolymer

The UCS of stabilized soil mixed with an AA (river-sand geopolymer) improves significantly with an increase in the curing temperature. Many researchers have also studied the effect of temperature on geopolymers [18, 31–33]. The observed enhancement in strength with increasing curing temperature can be attributed to the dehydroxylation, disintegration, and polycondensation mechanisms of the aluminosilicate polymer that take place between the soil-precursor particles and the alkaline solution. The present investigation provides confirmation that elevated curing temperatures have a positive impact on the dissolution of aluminosilicate, resulting in a homogeneous dispersion of gel formation. This results in a bridging of the gaps between interface transition zones and an increase in compressive strength as in the previous studies [34,35] , as shown in Fig. 5. For example, the UCS of mixture AA of SH:SS = 0:100 increased from 6.81 to 8.69 and 12.39 MPa with increasing curing temperature from 30 to 45 and 60 °C, respectively. Thus, higher temperatures enhanced the effectiveness of dissolving features in aluminosilicate precursors, which could explain the significant increase in strength [36].

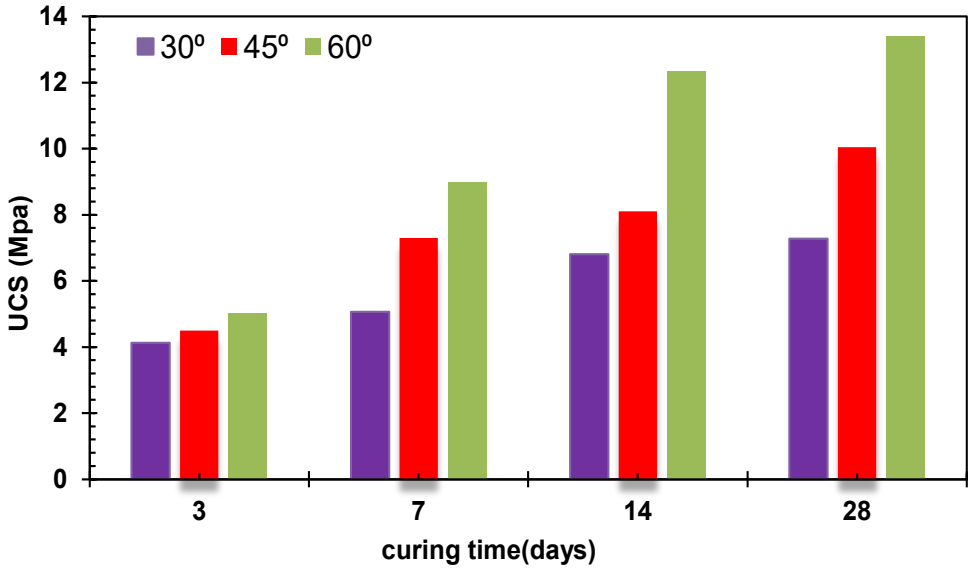

Figure 5. Effect of temperature on UCS of the river-sand geopolymer.

3.1.3. Effect of AA ratio of geopolymer

The type of activator, the ratio of SH: SS, immediately affect the UCS value of stabilized soil. The AA solution is prepared mixed from SH with SS. The solution of SH with 8 M concentration and the ratio of SH:SS 0, 0.75, and 1.5 % was used. Moreover, in this study, the AA ratio (SH:SS = 0:100) gives the highest UCS value at 28 days and 60 °C of curing as shown in Fig. 6. Soluble silica increases the condensation activity and promotes the growth of more silica in the polymeric chain, hence enhancing its strength characteristics [37, 38]. Increasing the activator content resulted in an increase in the leaching of silicon and aluminium from amorphous phase in river-sand geopolymer. The strength geopolymer materials prepared by SS was improved at room temperature [39].

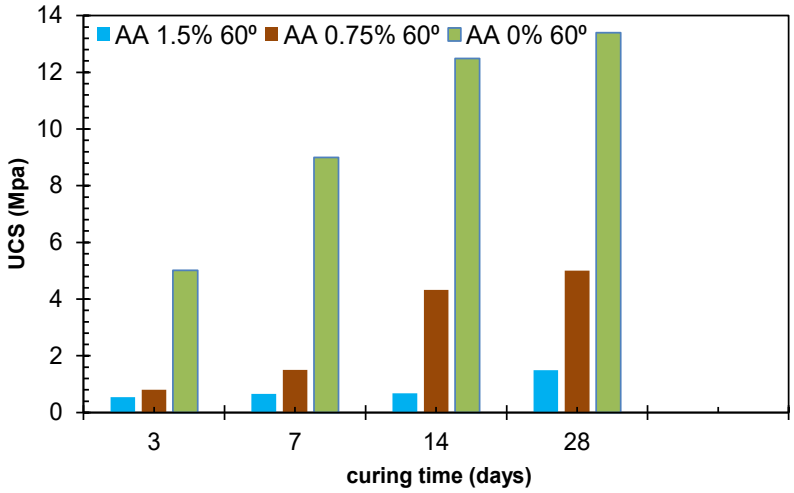

Figure 6. Effect of AA on UCS of the river-sand geopolymer.

3.2. Stress-strain curve

The experiment involved testing stabilized soil-geopolymer specimens containing an AA ratio (SH:SS = 0:100) from SS only, and other specimens containing an AA (SH:SS = 43:57, 60:40) at 8 M concentration of SH. The specimens were kept to mature for 48 hours and were subjected to curing temperatures of 30, 45, and 60 °C. After that, they were left in the oven until the time of the test at 3, 7, 14, and 28 days. The stress-strain relationship between the specimens is shown in Fig. 7. The results showed that as curing time and temperature increased, the stress increased, and the strain decreased as the results displays in [40, 41]. The stress-strain curve of the river-sand geopolymer specimens showed a clear peak stress, followed by a gradual decrease in strain. This indicates inherent brittleness under shearing. In comparison, shear failure occurred in specimens (S-AA 0) at a relatively lower strain compared to the specimens of (S-AA 0.75) and (S-AA 1.5) at all curing temperatures in different ages of the test. This is because the addition of SS improves the strength between soil particles, provides a uniform distribution,

and reduces the average pore size. The decrease in the percentage of SS in the AA solution negatively affects the strength of the geopolymer.

3.3. Microstructure Characteristic

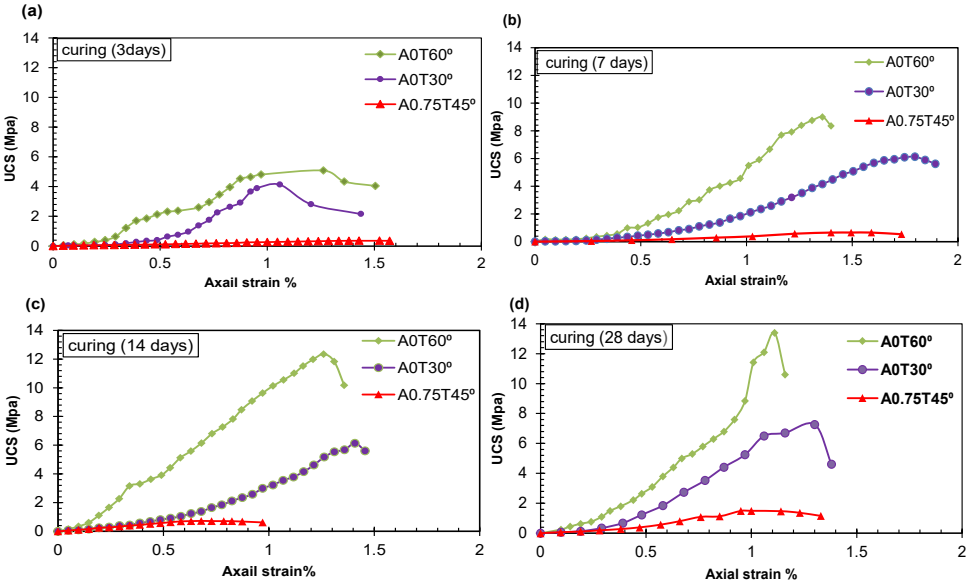

Figure 7. Stress-strain curve for the specimen with test time of: (a) 3 days; (b) 7days; (c) 14 days; (d) 28 days.

A SEM investigation was conducted on river-sand geopolymer specimens with two different AA ratios: 100:0 (0 %) and 60:40 (1.5 %). All specimens were allowed to be cured for 28 days before conducting the SEM test. The geopolymer mixtures were polymerized for 48 hours at 60 °C. Fig. 8 displays the SEM images of river-sand geopolymer. The SEM test was conducted on samples identical to those used for the UCS test. The chosen activated solution ratio filled the pores of the loose river sand and created thick formations. Furthermore, a noticeable alteration took place in the composition of sandy soil because of the introduction of an AA and the polymerization process, causing partial dissolving of aluminosilicate and activation of sand particles effectively. The stabilized sand particles were tightly connected by a geopolymer connection within a highly cross-linked 3D network, forming a solid crystalline composite. This aligns with the substantial improvements in soil stability. The polymerization process occurred due to the addition of an activator solution (SS) to the alkaline nature of selected river sand, which resulted in the formation of sodium aluminium silicate hydrate (N-A-S-H) gel in conjunction with the partial dissolution of activated soil sand with an AA ratio of 0 more than the specimens of AA = 1.5. The results match the findings of the studies on the effect of the geopolymer on the microstructure of the improved soil as a binder [22, 24].

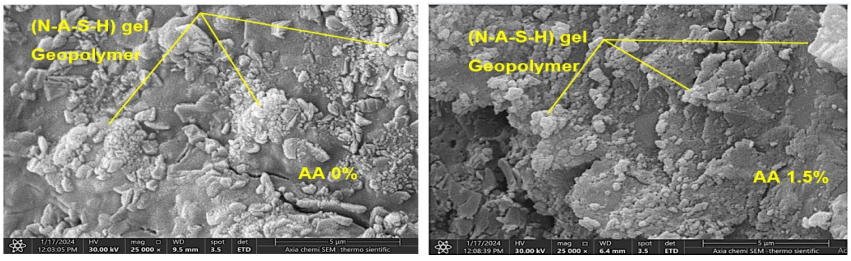

Figure 8. SEM images (9.5 X: 5 un) of geopolymer (a) AA 0 % (SH:SS = 0:100), (b) AA 1.5 % (SH:SS = 43:57), at 60° and 28 days. Sodium aluminate silicate hydrate gel (N-A-S-H).

4. Conclusion

The study investigated the significance of using geopolymer based on river sand soil (granular soil) merely without the addition of any fine pozzolanic materials such as FA, volcanic ash, etc.

Sandy soil stabilization by geopolymer showed a promising eco-friendly, economically viable, and sustainable alternative to OPC and lime.

The geopolymer could enhance the mechanical properties of soil, where the strength of river-sand geopolymer, measured as UCS, significantly increased with the AA = 0 (SH:SS = 0:100) ratio (high concentration of activator solution (SS)).

The highest value of UCS (13.42MPa) was at AA ratio = 0, 60 °C, and 28 days curing time. This result might be attributed to the existence of soluble silica that enhanced the condensation activity and developed more silica in the polymeric chain, which improved the strength property of the soil matrix.

Furthermore, under UCS, the dominant stress-strain reaction for geopolymer-based river sand soil was brittle yield, with stress peaking before sudden failure. When the geopolymer stress ratio increases, the response becomes stiffer. The SEM images revealed a homogeneous, denser, and very stiff structure.

The geopolymer gel improved the soil particles. The images indicated that the pores in the texture surrounding the geopolymer gel were evenly distributed and that the geopolymer behaved as a binder among the soil particles.

References

1. Elipe, M.G.M., López-Querol, S. Aeolian sands: Characterization, options of improvement and possible employment in construction – The State-of-the-art. Construction and Building Materials. 2014. 73. Pp. 728–739. DOI: 10.1016/j.conbuildmat.2014.10.008
2. Flodin, N., Broms, B. Historical development of civil engineering in soft clay. Soft Clay Engineering. Elsevier. Amsterdam, 1981. Pp. 27–133.
3. Sherwood, P. Soil Stabilization with Cement and Lime. Transport Research Laboratory, 1993. 153 p.
4. Huat, B.B.K., Prasad, A., Kazemian, S., Anggraini, V. Ground Improvement Techniques. CRC Press. London, 2019. 316 p. DOI: 10.1201/9780429507656
5. Karkush, M.O., Yassin, S. Using sustainable material in improvement the geotechnical properties of soft clayey soil. Journal of Engineering Science and Technology. 2020. 15(4). 2208–2222.
6. Dhowian, A.W. Laboratory simulation of field preloading on Jizan sabkha soil. Journal of King Saud University – Engineering Sciences. 2017. 29(1). Pp.12–21. DOI: 10.1016/j.jksues.2015.09.001
7. Al-Amoudi, O.S.B. Characterization and chemical stabilization of Al-Qurayyah sabkha soil. Journal of Materials in Civil Engineering. 2002. 14(6). Pp. 478–484. DOI: 10.1061/(ASCE)0899-1561(2002)14:6(478)
8. Al-Homidy, A.A., Dahim, M.H., Abd El Aal, A.K. Improvement of geotechnical properties of sabkha soil utilizing cement kiln dust. Journal of Rock Mechanics and Geotechnical Engineering. 2017. 9(4). Pp.749–760. DOI: 10.1016/j.jrmge.2016.11.012
9. Khedari, J., Watsanasathaporn, P., Hirunlabh, J. Development of fibre-based soil–cement block with low thermal conductivity. Cement and Concrete Composites. 2005. 27(1). Pp.111–116. DOI: 10.1016/j.cemconcomp.2004.02.042
10. Provis, J.L., Van Deventer, J.S.J. Alkali Activated Materials: State-of-the-Art Report, RILEM TC 224-AAM. Springer. Dordrecht, 2013. XIV, 388 p. DOI: 10.1007/978-94-007-7672-2
11. Garcia-Lodeiro, I., Palomo, A., Fernández-Jiménez, A. An overview of the chemistry of alkali-activated cement-based binders. Handbook of Alkali-Activated Cements, Mortars and Concretes. Woodhead Publishing, 2015. Pp.19–47. DOI: 10.1533/9781782422884.1.19
12. Hamzah, H.N., Al Bakri Abdullah, M.M., Heah, C.Y., Arif Zainol, M.R.R., Kamarudin, H. Review of soil stabilization techniques: Geopolymerization method one of the new technique. Key Engineering Materials. 2015. 660. Pp. 298–304. DOI: 10.4028/www.scientific.net/KEM.660.298
13. Davidovits, J. Geopolymer Chemistry and Applications. 2nd edn. Geopolymer Institute, 2008. 585 p.
14. Provis, J.L. Activating solution chemistry for geopolymers. Geopolymers: Structures, Processing, Properties and Industrial Applications. Woodhead Publishing, 2009. Pp. 50–71. DOI: 10.1533/9781845696382.1.50
15. Papadopoulos, A.M., Giama, E. Environmental performance evaluation of thermal insulation materials and its impact on the building. Build Environ. 2007. 42(5). Pp. 2178–2187. DOI: 10.1016/j.buildenv.2006.04.012
16. Cristelo, N., Glendinning, S., Fernandes, L., Pinto, A.T. Effects of alkaline-activated fly ash and Portland cement on soft soil stabilisation. Acta Geotechnica. 2013. 8. Pp. 395–405. DOI: 10.1007/s11440-012-0200-9
17. Adhikari, B., Khattak, M.J., Adhikari, S. Mechanical and durability characteristics of flyash-based soil-geopolymer mixtures for pavement base and subbase layers. International Journal of Pavement Engineering. 2021. 22(9). Pp. 1193–1212. DOI: 10.1080/10298436.2019.1668562
18. Alimi, M., Ghorbani, A. Mechanical and compressibility characteristics of a soft clay stabilized by slag-based mixtures and geopolymers. Applied Clay Science. 2020. 184. Article no. 105390. DOI: 10.1016/j.clay.2019.105390
19. Bhavita Chowdary, V., Ramanamurty, V., Pillai, R.J. Experimental evaluation of strength and durability characteristics of geopolymer stabilised soft soil for deep mixing applications. Innovative Infrastructure Solutions. 2021. 6. Article no. 40. DOI: 10.1007/s41062-020-00407-7
20. Rios, S., Ramos, C., Viana da Fonseca, A., Cruz, N., Rodrigues, C. Mechanical and durability properties of a soil stabilised with an alkali-activated cement. European Journal of Environmental and Civil Engineering. 2019. 23(2). Pp. 245–267. DOI: 10.1080/19648189.2016.1275987
21. Hai-yan, Y., Juan, Z., Jiu-jun, Y., Yong-qiang, L. Research on the mechanical properties and mechanism of alkali-activated saline soil composite materials. Ferroelectrics. 2018. 529(1). Pp. 49–58. DOI: 10.1080/00150193.2018.1448195
22. Ameen, S.K., Abdulkareem, A.H., Mahmood, N.S. Shear strength behavior of organic soils treated with fly ash and fly ash-based geopolymer. Journal of the Mechanical Behavior of Materials. 2023. 32(1). Article no. 20220264. DOI: 10.1515/jmbm-2022-0264
23. Abdulwahed, H.S., Aljanabi, K.R., Abdulkareem, A.H. Optimization of equivalent modulus of RAP-geopolymer-soil mixtures using response surface methodology. Journal of King Saud University – Engineering Sciences. 2024. 36(6). Pp. 375–384. DOI: 10.1016/j.jksues.2022.06.005

24. Al-Rkaby, A.H.J., Katea, A. Improvement the Strength Characteristics of Loose Sandy Soil Using Sustainable Geopolymer. Math Stat Eng Appl. 2023. 72(1). Pp. 660–667. DOI: 10.17762/msea.v72i1.1975
25. Nabizadeh Mashizi, M., Bagheripour, M.H., Jafari, M.M., Yaghoubi, E. Mechanical and Microstructural Properties of a Stabilized Sand Using Geopolymer Made of Wastes and a Natural Pozzolan. Sustainability. 2023. 15(4). Article no. 2966. DOI: 10.3390/su15042966
26. D2487-17 A. Standard Practice for Classification of Soils for Engineering Purposes (Unified Soil Classification System). ASTM International. West Conshohocken, PA, 2017. 10 p. DOI: 10.1520/D2487-17
27. D422-07. Standard Test Method for Particle-Size Analysis of Soils. West Conshohocken, PA, 2007. 8 p.
28. D698-12. Standard Test Methods for Laboratory Compaction Characteristics of Soil Using Standard Effort. ASTM International. West Conshohocken, PA, 2007. 13 p.
29. Iowa Statewide Urban Design and Specifications. Chapter 6: Geotechnical. URL: https://www.iowasudas.org/wp-content/uploads/sites/15/2022/12/Chapter_06-2022.pdf (date of application: 10.02.2026).
30. D2166-06 A. Standard Test Method for Unconfined Compression Strength of Cohesive Soil. ASTM Standards. West Conshohocken, PA, 2006. 6 p.
31. Yu, J., Chen, Y.-H., Chen, G., Wang, L. Experimental study of the feasibility of using anhydrous sodium metasilicate as a geopolymer activator for soil stabilization. Engineering Geology. 2020. 264. Article no. 105316. DOI: 10.1016/j.enggeo.2019.105316
32. Abdullah, H.H., Shahin, M.A., Sarker, P. Use of Fly-Ash Geopolymer Incorporating Ground Granulated Slag for Stabilisation of Kaolin Clay Cured at Ambient Temperature. Geotechnical and Geological Engineering. 2019. 37. Pp. 721–740. DOI: 10.1007/s10706-018-0644-2
33. Dungca, J.R., Codilla II, E.E.T. Fly-ash-based geopolymer as stabilizer for silty sand embankment materials. International Journal of GEOMATE. 2018. 14(46). Pp. 143–149. DOI: 10.21660/2018.46.7181
34. Leong, H.Y., Ong, D.E.L., Sanjayan, J.G., Nazari, A. Strength development of soil–fly ash geopolymer: Assessment of soil, fly ash, alkali activators, and water. Journal of Materials in Civil Engineering. 2018. 30(8). Article no. 4018171. DOI: 10.1061/(asce)mt.1943-5533.0002363
35. Tian, X., Xu, W., Song, S., Rao, F., Xia, L. Effects of curing temperature on the compressive strength and microstructure of copper tailing-based geopolymers. Chemosphere. 2020. 253. Article no. 126754. DOI: 10.1016/j.chemosphere.2020.126754
36. Lopes, A., Lopes, S., Pinto, I. Influence of Curing Temperature on the Strength of a Metakaolin-Based Geopolymer. Materials (Basel). 2023. 16(23). Article no. 7460. DOI: 10.3390/ma16237460
37. Duan, P., Yan, C., Zhou, W. Compressive strength and microstructure of fly ash based geopolymer blended with silica fume under thermal cycle. Cement and Concrete Composites. 2017. 78. Pp. 108–119. DOI: 10.1016/j.cemconcomp.2017.01.009
38. Rangan, B.V., Hardjito, D., Wallah, S.E., Sumajouw, D.M. Studies on fly ash-based geopolymer concrete. Proceedings of the world congress geopolymer, Saint Quentin, 2005. Pp. 133–137.
39. Alrefaei, Y., Wang, Y.S., Dai, J.G. The effectiveness of different superplasticizers in ambient cured one-part alkali activated pastes. Cement and Concrete Composites. 2019. 97. Pp. 166–174. DOI: 10.1016/j.cemconcomp.2018.12.027
40. ASTM D1633-00. Standard test methods for compressive strength of molded soil-cement cylinders. ASTM International. West Conshohocken, PA, 2007. 4 p.
41. Association BS. Mortar and concrete – Test method for splitting tensile strength of cylindrical specimens. NBR, 1983.

Information about the authors:

Ban Z. Raoof,
E-mail: ban22e1008@uoanbar.edu.iq

Ahmed H Abdulkareem, *PhD*
E-mail: ahm1973ed@uoanbar.edu.iq

Ahmed Rahomi Rajab, *PhD*
ORCID: https://orcid.org/0000-0003-4420-0576
E-mail: ahmed.rahomi2@uoanbar.edu.iq

Received 06.06.2024. Approved after reviewing 05.05.2025. Accepted 05.06.2025.